
Introduction to Colloidal (Dusty) Plasmas

Lecture Notes

André Melzer

Institut für Physik
Ernst-Moritz-Arndt-Universität Greifswald

Version of: October 26, 2016
(2nd Edition)

Contents

1. Introduction	1
2. Charging of Dust Particles	6
2.1. Outline	6
2.2. OML Charging Currents	7
2.2.1. Derivation of the OML Currents	7
2.2.2. Discussion of the OML Model	11
2.2.3. Streaming Ions	12
2.2.4. Collisions	12
2.3. Other Charging Currents	13
2.3.1. Photoelectron Emission	13
2.3.2. Secondary Electron Emission	14
2.4. The Particle as a Floating Probe	15
2.4.1. OML Currents	15
2.4.2. The Capacitance Model	16
2.4.3. Floating Potential with Streaming Ions	17
2.4.4. Floating Potential with Collisions	18
2.4.5. Floating Potential with Secondary Electron Emission	19
2.5. Temporal Evolution of the Particle Charge	21
2.5.1. Charging in the rf Sheath	22
2.5.2. Stochastic Fluctuations	23
2.6. Influence of Many Particles and Electron Depletion	24
3. Forces and Trapping of Dust Particles	27
3.1. Gravity	27
3.2. Electric Field Force	27
3.2.1. Shielding	27
3.2.2. Polarization Forces	29
3.3. Ion Drag Force	30
3.3.1. Qualitative Discussion: Barnes model	31
3.3.2. Quantitative Discussion: Hutchinson/Khrapak model	33
3.4. Neutral Drag Force	35
3.5. Thermophoresis	35
3.6. Laser Forces	36
3.7. Compilation of Forces, Dust Levitation and Trapping	38
3.8. Vertical Oscillations	40
3.8.1. Linear Resonance and Charge Measurement	41
3.8.2. Parametric Resonances	45

3.8.3. Nonlinear Resonances	47
4. Coulomb Crystallization	51
4.1. The One-Component Plasma (OCP)	51
4.2. Yukawa Systems	52
4.3. Coulomb Crystallization in Dusty Plasmas	54
4.4. Crystallization in Bounded Systems	55
4.5. Structural Information	57
4.5.1. Wigner-Seitz Cells	57
4.5.2. Pair Correlation Function	57
4.5.3. Structure Factor	59
4.5.4. Angular Correlation Function	59
4.5.5. Example	60
4.6. 3D Crystals	60
5. Dust Particle Interaction	63
5.1. Interaction in the Horizontal Plane	63
5.2. Vertical Interaction	65
5.2.1. The wakefield potential (wave model)	65
5.2.2. The ion focus (particle model)	68
5.2.3. Non-reciprocal attraction	70
5.3. Measurement of the Attractive Force	72
5.4. Oscillatory Instability of the Vertical Alignment	75
5.4.1. Solution of the Coupled Oscillations	76
5.4.2. General Analysis of the Instability	78
5.4.3. Conditions for the Instability	79
5.5. The Phase Transition of the Plasma Crystal: Experiment	81
5.6. The Phase Transition of the Plasma Crystal: Simulations and Theory	84
6. Waves in Weakly Coupled Dusty Plasmas	87
6.1. Dust-Acoustic Waves	87
6.2. Ion-Flow Driven Dust Acoustic Waves	92
6.3. Dust Ion-Acoustic Wave	94
6.4. Other Wave Types	96
7. Waves in Strongly Coupled Dusty Plasmas	100
7.1. Compressional Mode in 1D	101
7.2. Dust Lattice Waves in 2D	104
7.3. Compressional 1D Dust Lattice Waves: Experiment	107
7.4. Compressional 2D Dust Lattice Waves: Experiment	110
7.5. Shear 2D Dust Lattice Waves: Experiment	111
7.6. Mach Cones	111

7.7. Transverse Dust Lattice Waves	114
7.8. Dispersion Relation from Thermal Particle Motion	116
7.9. A Note on Shielding	117
8. Finite Dust Clusters	120
8.1. Formation of Finite Dust Clusters	120
8.2. Structural Transitions in 1D Dust Clusters	121
8.3. Structure of 2D Finite Dust Clusters	122
8.3.1. Example of 2D Cluster Configurations: Configuration (0,6)	123
8.3.2. Example of 2D Cluster Configurations: Configuration (1,5)	127
8.4. Structure of 3D Finite Dust Clusters	128
8.5. Normal Modes in 2D Finite Clusters	130
8.6. Modes from Thermal Particle Motion	133
8.7. Stability	134
8.8. Phase Transitions	136
9. Technical Applications of Dusty Plasmas	140
9.1. Particle Growth Mechanisms	140
9.1.1. Cluster Formation	141
9.1.2. Agglomeration Phase	144
9.1.3. Accretion Phase	146
9.2. Technological Impacts of Dusty Plasmas	146
9.2.1. Surface Contamination by Dust	147
9.2.2. Flue Gas Cleaning	148
9.2.3. Dust in Fusion Devices	149
9.2.4. Formation of New Materials	150
9.2.5. Polymorphous Silicon Films	151
10. Astrophysical Dusty Plasmas	154
10.1. Noctilucent Clouds and PMSE	154
10.2. Dust Streams From Jupiter	156
10.2.1. Model	157
10.2.2. Model and Experiment	158
10.3. Dust Orbits at Saturn	159
10.4. Spokes in Saturn's Rings	161
10.5. Mach Cones in Saturn's Rings	164
11. Summary	166

Preface to the Second Edition

The field of dusty plasmas has continued to grow over the last years. In the light of new developments I felt that some parts of this Introduction needed to be revised.

While I still tried to stick to the basic concepts of dusty plasmas I tried to mention some recent progress. Some of the questions declared as open in the first edition have been settled, some new questions have arisen.

Changes include, to name a few, the role of collisions in the charging, the state of understanding of the ion drag force, driven dust-acoustic waves, three-dimensional dust systems and many more. Further many figures have been revised (not only changed to color).

Suggestions, comments and improvements are still welcome.

Enjoy!

Preface to the First Edition

This manuscript has emerged from lectures held by the author at the Ernst-Moritz-Arndt-University Greifswald and the Christian-Albrechts-University Kiel in the years 2002 to 2005. It covers the topics in the field of dusty plasmas for a course of 2 to 3 semester hours.

It is intended as an introductory course into the novel and fascinating field of complex plasmas. The reader should have a background of general plasma physics on an introductory level. Dusty plasmas shed a new and different light on various aspects of plasma physics like the problem of shielding or the mechanism of acoustic waves in plasmas. The study of dusty plasmas thus provides new insight into plasma physics and substantiates, revises and strengthens its concepts. The author hopes that these lecture notes will drive the reader's interest into this growing and interesting field of physics.

At the University Greifswald, the manuscript can serve as a companion to the Course "Colloidal Plasmas" which is a compulsory one-hour course for students who have specialized into plasma physics and to the Course "Colloidal Plasmas II", a voluntary two-hour course for students interested in dusty plasmas.

I would like to thank Yuriy Ivanov, Sebastian Käding and Matthias Wolter for proofreading. Additional errors that I left in the manuscript can be reported to me under melzer@physik.uni-greifswald.de. Suggestions, comments and improvements are welcome.

Enjoy!

1. Introduction

Colloidal (or dusty or complex) plasmas are a new and fascinating field of plasma physics. Colloidal plasmas enable to study basic plasma properties on an “atomic” kinetic level and they allow to visualize collective plasma phenomena, like oscillations and waves. Moreover, a vast number of novel phenomena are found in these systems. New features in colloidal plasmas range from Coulomb crystallization to new types of forces and waves. In these lecture notes, a general introduction to this active and growing field will be given. Areas of special interest are covered in a few monographs [1, 2, 3, 4].

Dusty plasmas share a number of physical concepts and similarities with non-neutral plasmas, like pure ion plasmas in Paul or Penning traps, as well as with colloidal suspensions, where charged plastic particles are immersed in an aqueous solution. In analogy to these systems, the terms “colloidal plasmas” or “complex plasmas” are frequently used for dusty plasmas more or less as synonyms. Here, we will mainly use “colloidal plasmas” for strongly coupled dust systems with micrometer sized particles. When referring to particles in astrophysical or technological plasmas, the term “dusty plasmas” will be used.

Colloidal and dusty plasmas consist of macroscopic solid particles immersed in gaseous plasma environment of electrons, ions and neutrals. The particles are charged by the inflow of electrons and ions or by other means. Thus, the dust particles act as an additional plasma species. Hence, the study of the plasma-particle and particle-particle interaction, their fundamental properties and their collective effects open up new and interesting visions on plasma physics.

Dusty plasmas are ubiquitous in astrophysical situations, like interstellar clouds, the rings of the great planets or comet tails. In his book [1], Verheest characterizes dusty plasmas by: “If the claim is made that more than 99 % of the observable universe is in the plasma state then it could be jokingly asserted that the remainder is dust”. For instance, Saturn’s B-ring consists of micron and submicron dust particles (and larger boulders) in the plasma environment of Saturn. There, peculiar features have been observed by the Voyager spacecraft (see Fig. 1.1a): Radially extended structures (“spokes”) develop within minutes and last for hours. This behaviour cannot be explained by pure gravitational interactions. Other examples of dusty astrophysical plasmas include comets and interstellar clouds. Comets are “dirty (dusty) snowballs” that evaporate under the influence of the solar wind. Comets usually form a plasma tail and the bright curved dust tail. Cometary dust generally has a size distribution with high abundance of small grains (0.1 μm diameter) and a smaller number of larger particles which then can interact with the plasma tail near the comet head and the solar wind (see Fig. 1.1b). Finally, in interstellar clouds, dust particles of 0.01 to 10 μm are found. One of the interesting questions, here, is the influence of charged particles on star and planet formation.

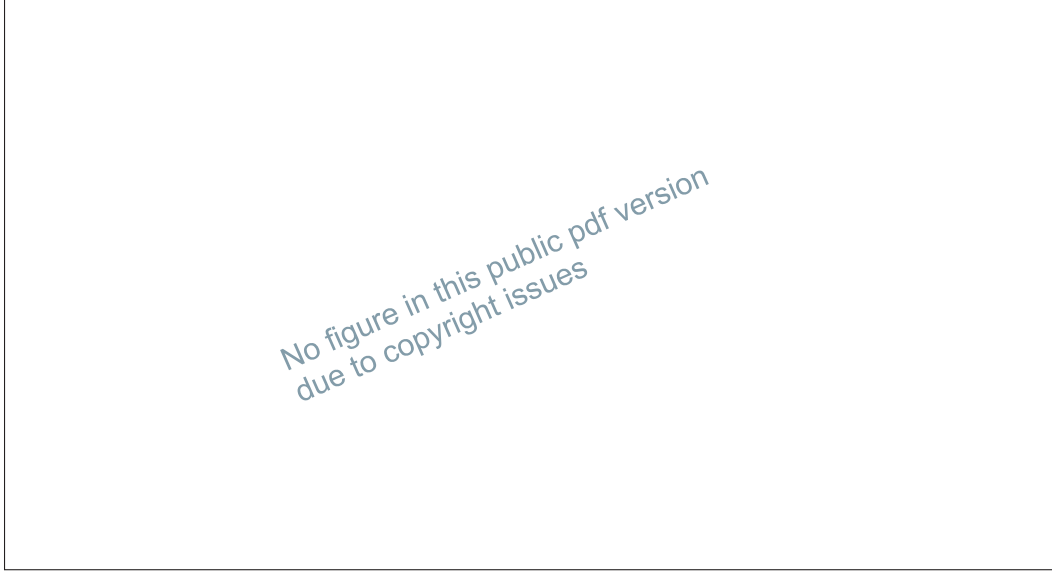


Figure 1.1: (a) *Spokes in Saturn's rings. The spokes are the radially extended dark features.* (b) *Plasma and dust tail of comet Hale-Bopp (1994).*

In microchip manufacturing about 70 % of the production steps require plasma processing techniques for etching or thin film deposition. Plasma processing allows to manufacture multi-layer devices and fine vertical structures that help to increase packing density (see Fig. 1.2). However, it was found in the end of the 1980's that in reactive gases used for chip processing also small dust particles can grow due to polymerization. The grown particles are trapped in the plasma near the wafers (see Fig. 1.3). It is obvious that dust particles falling on the etched structures can lead to severe damages and malfunctions of the chips ("killer particles"). Thus, here the removal of dust particles from the discharge is a crucial issue. Similarly, particles can also grow in fusion devices and its implication for operational performance is currently discussed. On the other hand, the incorporation of submicron dust particles in thin films leads to new materials, like self-lubricating films with small embedded MoS_2 particles or the manufacturing of polymorphous solar cells with increased efficiency.

In typical laboratory experiments on fundamental aspects of colloidal plasmas monodisperse spherical particles of 1 to 10 micrometer diameter are trapped in gas discharges. The microspheres attain high negative charges of the order of 10^3 to 10^5 elementary charges due to the inflow of plasma electrons and ions. However, due to the extreme mass the charge-to-mass ratio that determines the dynamic properties is by orders of magnitude smaller than that of ions, not to mention electrons.

In colloidal plasmas the microspheres can be viewed individually due to their comparatively large size. Due to the very low charge-to-mass ratio the spatial and time scales

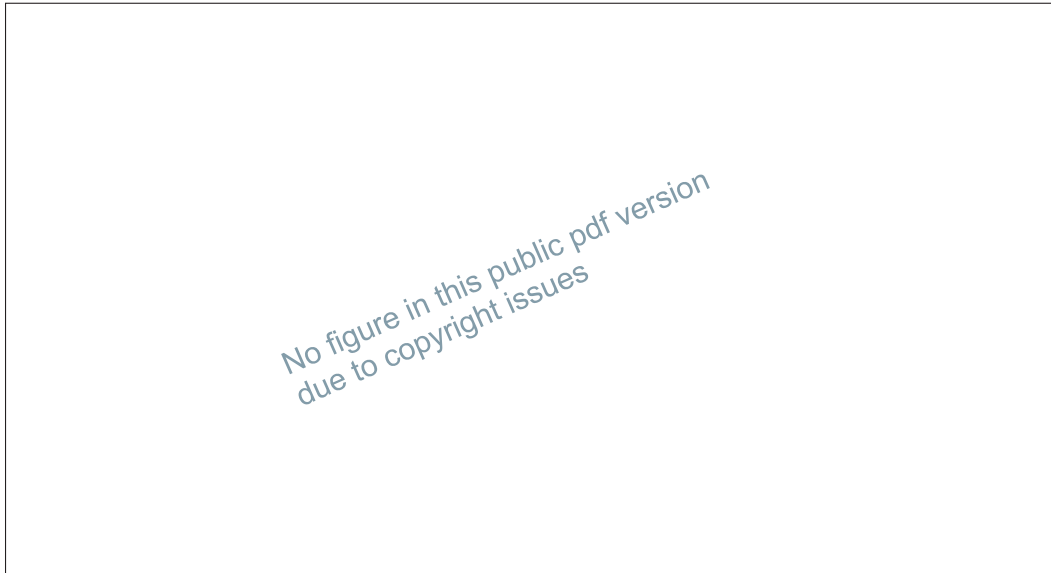


Figure 1.2: (a) 300 mm wafer (Infineon), (b) deep silicon etching for MEMS Micro-Electro-Mechanical Systems (Surface Technology Systems Plc)

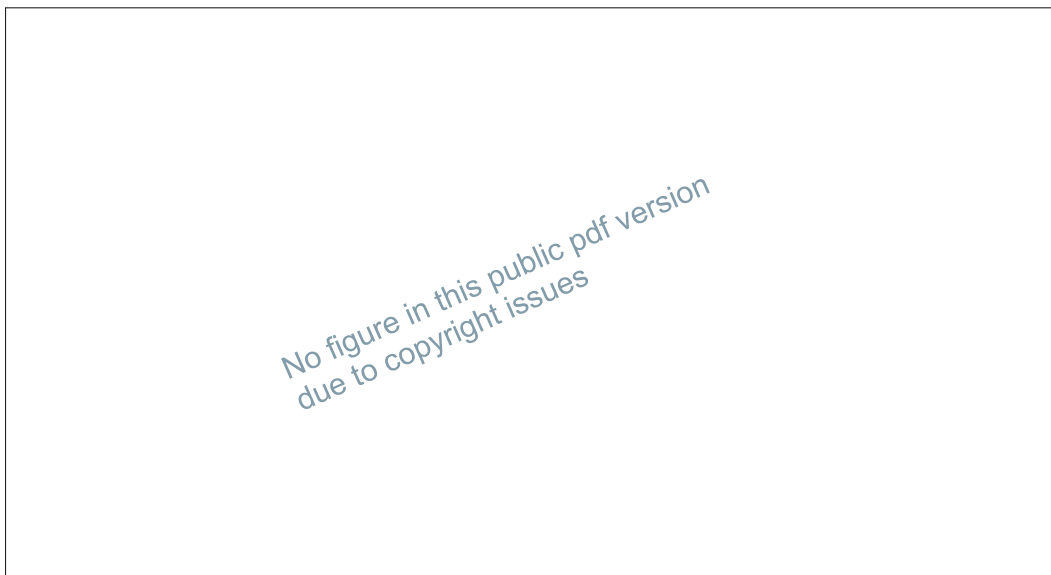


Figure 1.3: (a) Dust particles trapped above silicon wafers in a plasma processing discharge [5]. (b) Micrograph of a “killer particle”.

for particle motion are ideal for studying the dynamics of complex plasmas by video

microscopy, e.g. interparticle distances are of the order of hundreds of microns, typical frequencies of the order of a few Hertz.

Due to the high charges the electrostatic potential energy of the dust particles by far exceeds the thermal energy of the microspheres which are effectively cooled to room temperature by the ambient neutral gas: the system is said to be strongly coupled. The strong-coupling regime is hardly reached in ordinary plasmas. In colloidal plasmas, the dust particles can arrange in ordered crystal-like structures, the plasma crystal (see Fig. 1.4).

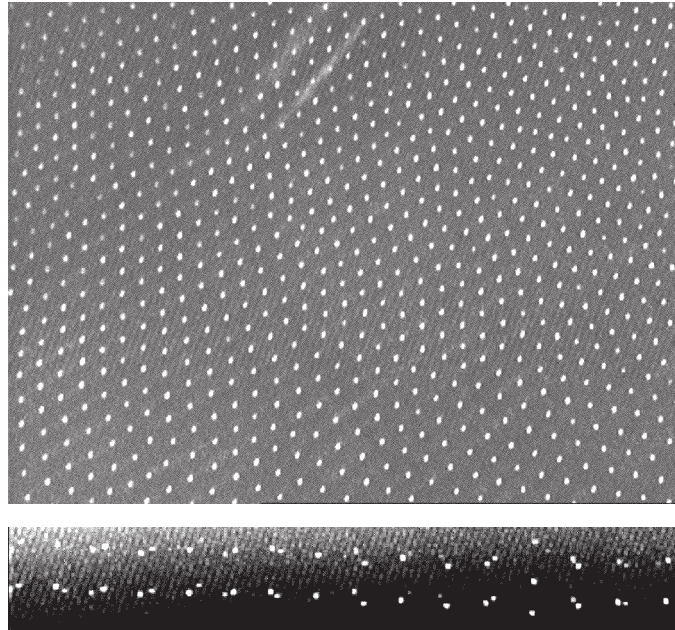


Figure 1.4: *The plasma crystal with two layers, top and side view.*

Colloidal plasmas therefore enable to study a vast variety of novel phenomena, like fluid and crystalline plasmas, phase transitions, strong-coupling effects, waves and Mach cones in condensed matter and many more. They provide a unique system bridging the fields of plasma physics, condensed matter and material science. Thus, the leading motive for the enormous research activity in this field is that dynamic processes of strongly coupled systems can be investigated on the kinetic level of individual particles.

The above mentioned properties set the stage for the physics of colloidal plasmas. The topics presented in the Lecture notes are guided by the available experiments on colloidal and dusty plasmas. The theoretical concepts are developed to a depth necessary to understand the experimental findings. A complete theoretical description is not intended, here. In these Lecture notes, I will first give an introduction to the fundamental properties of dusty plasmas which include particle charging, which is treated in Chapter 2, and forces

on the dust particles in Chapter 3. Strongly coupled systems together with the particle-particle interaction and phase transitions are described in Chapter 4 and 5. Thereafter, collective effects like waves in weakly and strongly coupled systems will be discussed in Chapters 6 and 7, respectively. The above concepts will then also be applied to systems consisting of only a small number of particles, so-called dust clusters, in Chapter 8. Finally, in Chapter 9 and 10 I will present phenomena in technological and astrophysical dusty plasmas that have already been briefly mentioned in this Introduction.

2. Charging of Dust Particles

The charge a particle attains in a plasma is certainly the most fundamental parameter. Unlike for electrons or ions, the particle charge is not fixed, but determined by the ambient plasma parameters. The charge may thus change on the particle trajectory which results in a number of new and interesting phenomena.

2.1. Outline

The particle charging is, from the theoretical point of view, one of the most interesting but also difficult questions when all the peculiarities of the charging process of a dust particle are taken into account including trapping in the highly non-neutral, non-equilibrium sheath environment of a plasma with the presence of streaming ions and ion-neutral collisions. Hence, here, the charging model will be developed in steps starting from idealized cases to more complex analyses.

The problem of particle charging is closely related to the theory of electrostatic probes (Langmuir probes) in plasmas. There, the task is to determine electron and ion densities, electron temperature etc. from the current-voltage characteristic of the probe. For particle charging, we assume that these plasma parameters are known and the question is which potential on the dust grain is established by the currents onto the particle.

The particle attains a potential, the so-called floating potential ϕ_{fl} which is determined from the condition that at floating potential the sum of all currents to the particle vanishes, i.e.

$$\sum_{\ell} I_{\ell}(\phi_{\text{fl}}) = \frac{dQ_{\text{d}}}{dt} = 0 \quad (2.1)$$

where I_{ℓ} denotes the different currents to the probe at the floating potential. Since we are interested in the equilibrium charge (at least at the moment), the first task will be to determine this floating potential from the particle currents.

Currents to the particle may arise from the inflow of plasma electrons and ions or from the emission of secondary electrons and photoelectrons. One can think of many other charging currents, like electron emission due to strong electric fields etc., which however are considered unimportant in most cases and which will not be discussed here. Electron and ion collection will dominate in laboratory plasmas whereas secondary electron and photoelectron emission are considered important under astrophysical conditions.

2.2. OML Charging Currents

We will start the discussion with electron and ion collection in the ideal case of an isotropic Maxwellian plasma environment at rest. The currents to the particle can be described by the OML (“orbital motion limit”) model first derived by Mott-Smith and Langmuir in 1926 [6]. There, it is assumed that electrons and ions move towards the dust particle from infinity on collisionless orbits subject only to the electrostatic interaction with the dust particle. The OML problem is exactly equivalent to Kepler dynamics or Rutherford scattering.

Since the electrons are much more mobile than the ions the particle will generally charge negatively. In the calculation of the currents we will adopt that view and assume that the particle potential is negative with respect to the plasma potential, i.e. $\phi_p < 0$. Thus, the ions are the attracted and the electrons are the repelled species. The ion and electron OML currents are given by the following expressions (given here in advance for reference, they will be derived in the following section)

$$\begin{aligned} I_i &= \pi a^2 n_i e \sqrt{\frac{8kT_i}{\pi m_i}} \left(1 - \frac{e\phi_p}{kT_i} \right) \\ I_e &= -\pi a^2 n_e e \sqrt{\frac{8kT_e}{\pi m_e}} \exp\left(\frac{e\phi_p}{kT_e}\right) , \end{aligned} \quad (2.2)$$

where a is the particle radius, n_i, n_e are ion and electron densities, T_i, T_e the respective temperatures and m_i, m_e their masses. For the sake of completeness, the OML currents for positive particle potentials $\phi_p > 0$ read as

$$\begin{aligned} I_i &= \pi a^2 n_i e \sqrt{\frac{8kT_i}{\pi m_i}} \exp\left(-\frac{e\phi_p}{kT_i}\right) \\ I_e &= -\pi a^2 n_e e \sqrt{\frac{8kT_e}{\pi m_e}} \left(1 + \frac{e\phi_p}{kT_e} \right) . \end{aligned} \quad (2.3)$$

2.2.1. Derivation of the OML Currents

Ion Current

As mentioned above, we will study here the usual case of $\phi_p < 0$ to derive the OML currents of Eq. (2.2). We start with the ion species that is attracted by the dust. Possible ion trajectories are depicted in Fig. 2.1. Ions with impact parameters smaller than a critical parameter b_c , i.e. $b < b_c$, will hit the particle, those with $b > b_c$ will only be deflected in the electric field of the dust. The critical parameter b_c is defined by the condition that the ion will hit the dust particle with grazing incidence.

At infinity the angular momentum of such an ion with the critical impact parameter b_c is

$$L = |\vec{r} \times \vec{p}| = m_i v_{i,0} b_c .$$

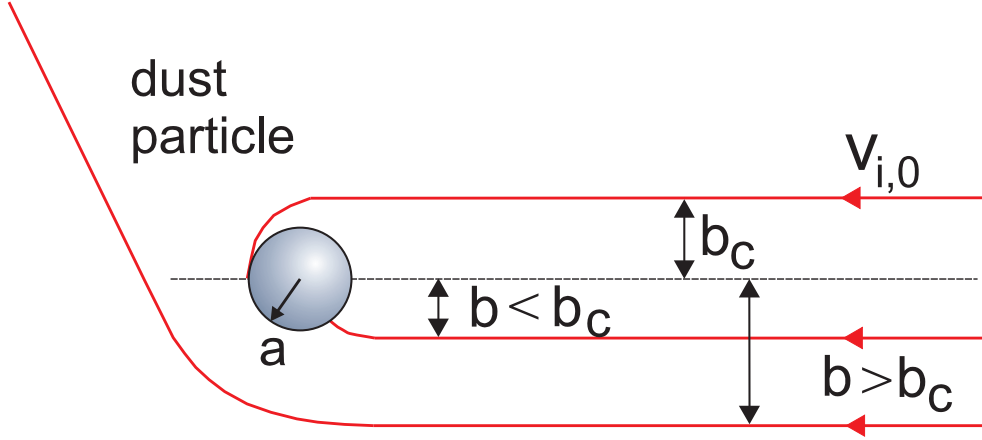


Figure 2.1: Ion trajectories with different values of the impact parameter b .

Since this ion hits the dust at grazing incidence its angular momentum at the particle surface is

$$L = m_i v_i a \quad .$$

When there are no collisions the angular momentum of the ion is conserved.

The energy balance of the ions is the sum of kinetic and potential energy in the electrostatic potential of the dust particle

$$\frac{1}{2} m_i v_{i,0}^2 = \frac{1}{2} m_i v_i^2 + e\phi_p \quad .$$

Here, the energy of the ion at infinity and when arriving on the particle are balanced. Using the conservation of angular momentum the energy balance can be written as

$$\frac{1}{2} m_i v_{i,0}^2 = \frac{1}{2} m_i v_{i,0}^2 \left(\frac{v_i^2}{v_{i,0}^2} + \frac{e\phi_p}{(1/2) m_i v_{i,0}^2} \right) = \frac{1}{2} m_i v_{i,0}^2 \left(\frac{b_c^2}{a^2} + \frac{e\phi_p}{(1/2) m_i v_{i,0}^2} \right)$$

and thus

$$b_c^2 = a^2 \left(1 - \frac{2e\phi_p}{m_i v_{i,0}^2} \right) \quad . \quad (2.4)$$

We can then easily define the cross section for ion collection as

$$\sigma_c \equiv \pi b_c^2 = \pi a^2 \left(1 - \frac{2e\phi_p}{m_i v_{i,0}^2} \right) \quad . \quad (2.5)$$

It is seen that the cross section σ_c for ion collection is larger than the particle's geometric cross section $\sigma = \pi a^2$. Of course, this is due to the attraction by the dust (Remember: $\phi_p < 0$) as also easily seen from Fig. 2.1.

Now, the charging current to the particle by ions is given by

$$dI_i = \sigma_c(v_i) dj_i = \sigma_c(v_i) n_i e v_i f(v_i) dv_i \quad ,$$

where $j_i = n_i e v_i$ is the ion current density. The ion current has to be integrated over the ion velocity distribution function $f(v_i)$ that is assumed to be an isotropic Maxwellian in the following, i.e.

$$f(v_i) = 4\pi v_i^2 \left(\frac{m_i}{2\pi k T_i} \right)^{3/2} \exp\left(-\frac{1}{2} \frac{m_i v_i^2}{k T_i}\right) \quad \text{with} \quad \int_0^{\infty} f(v_i) dv_i = 1 \quad ,$$

where T_i is the ion temperature and k is Boltzmann's constant. The charging current is then obtained by integration over the Maxwellian velocity distribution

$$I_i = 4\pi^2 a^2 n_i e \left(\frac{m_i}{2\pi k T_i} \right)^{3/2} \int_0^{\infty} \left(1 - \frac{2e\phi_p}{m_i v_i^2} \right) v_i^3 \exp\left(-\frac{1}{2} \frac{m_i v_i^2}{k T_i}\right) dv_i \quad . \quad (2.6)$$

By rearranging we have

$$I_i = 4\pi^2 a^2 n_i e \left(\frac{m_i}{2\pi k T_i} \right)^{3/2} \left[\underbrace{\int_0^{\infty} v_i^3 \exp\left(-\frac{1}{2} \frac{m_i v_i^2}{k T_i}\right) dv_i}_{F_1} - \underbrace{\int_0^{\infty} \frac{2e\phi_p}{m_i} v_i \exp\left(-\frac{1}{2} \frac{m_i v_i^2}{k T_i}\right) dv_i}_{F_2} \right] \quad .$$

These two integrals can be easily evaluated resulting in*

$$F_1 = \frac{2(kT_i)^2}{m_i^2}$$

$$F_2 = \frac{2(kT_i)^2}{m_i^2} \frac{e\phi_p}{kT_i} \quad .$$

Finally, collecting all terms the OML ion current is

$$I_i = \pi a^2 n_i e \sqrt{\frac{8kT_i}{\pi m_i}} \left(1 - \frac{e\phi_p}{kT_i} \right) \quad . \quad (2.7)$$

This relation can be interpreted as a product of the ion current density $j_i = n_i e v_{th,i}$ at the ion thermal velocity $v_{th,i} = (8kT_i/\pi m_i)^{1/2}$ onto a dust particle and an effective cross section. The term $\pi a^2 (1 - e\phi_p/kT_i)$ describes the increased cross section of the dust particle at the ion thermal energy kT_i (which is not exactly the "real" ion thermal energy $(3/2)kT_i$).

*The definite integral is given by

$$\int_0^{\infty} x^n e^{-ax^2} dx = \frac{k!}{2a^{k+1}} \quad \text{for odd} \quad n = 2k + 1 \quad .$$

Electron Current

The electron current can be calculated in complete analogy to the ion's. The cross section of the dust particles for electrons is

$$b_c^2 = a^2 \left(1 + \frac{2e\phi_p}{m_e v_{e,0}^2} \right) .$$

The difference to the ionic cross section is the “+”-sign in the bracket. This results in a reduction of the effective cross section compared to the dust particle area since the electrons are the repelled species (still $\phi_p < 0$). The electron current (with Maxwellian electrons) is then determined by

$$I_e = -4\pi^2 a^2 n_e e \left(\frac{m_e}{2\pi k T_e} \right)^{3/2} \int_{v_{\min}}^{\infty} \left(1 + \frac{2e\phi_p}{m_e v_e^2} \right) v_e^3 \exp \left(-\frac{\frac{1}{2} m_e v_e^2}{k T_e} \right) dv_e . \quad (2.8)$$

Here, the lower bound of the integral is $v_{\min} = \sqrt{-2e\phi_p/m_e}$ instead of “0” in the ion current since only electrons that are energetic enough to overcome the electrostatic repulsion can reach the dust particle, i.e. electrons with $m_e v_e^2/2 > m_e v_{\min}^2/2 = -e\phi_p$ are able to hit the dust.

For the electron currents the analogous integrals I_1 and I_2 result in[†]

$$\begin{aligned} I_1 &= \frac{2(kT_e)^2}{m_e^2} \exp \left(\frac{e\phi_p}{kT_e} \right) \left(1 - \frac{e\phi_p}{kT_e} \right) \\ I_2 &= \frac{2(kT_e)^2}{m_e^2} \frac{e\phi_p}{kT_e} \exp \left(\frac{e\phi_p}{kT_e} \right) \end{aligned}$$

The electron current finally is

$$I_e = -\pi a^2 n_e e \sqrt{\frac{8kT_e}{\pi m_e}} \exp \left(\frac{e\phi_p}{kT_e} \right) . \quad (2.9)$$

One could have obtained the same result for the electron current from a statistical description by arguing that the thermal electron flux onto the dust particle will be reduced by a Boltzmann factor $n_e \rightarrow n_e \exp(e\phi_p/kT_e)$ for the repelled electrons: Only the electrons of the high-energy tail of the Maxwellian distribution will reach the particle.

[†]The following integrals result in

$$\int_v^{\infty} x e^{-ax^2} dx = \frac{1}{2a} e^{-av^2}$$

and

$$\int_v^{\infty} x^3 e^{-ax^2} dx = \frac{1}{2a^2} (1 - av^2) e^{-av^2} .$$

2.2.2. Discussion of the OML Model

General: Our derivation was based on the assumption of **collisionless** ion trajectories. This is an essential ingredient in view of conservation of angular momentum. Further, the calculations were done for an **isotropic** situation where we have used the isotropic form of the Maxwell velocity distribution function. Another assumption is that the distribution function for the electrons and ions is **Maxwellian** in the first place.

However, all of these conditions are often violated in plasma discharges. Typically, the ion mean-free path is often not much larger than the Debye length, especially in discharges in noble gases that have very large cross sections for ion-neutral charge exchange collisions. Moreover, the particles are trapped in the space charge sheath of a plasma discharge (as we will see below) where the ion motion is directed towards the electrodes. Finally, the distribution functions of electrons in plasma discharges are often better characterized by a bi-Maxwellian or Druyvesteyn-like distribution rather than a pure Maxwellian. Hence, especially the high-energy tail of the electron distribution that determines the particle charge can strongly deviate from the Maxwellian assumption. For a full treatment of all these processes, thorough numerical simulations [7] are required. However, the effect of streaming ions and ion-neutral collisions will be further discussed below to get a feeling for these effects.

Energy barrier in the OML model: An interesting point is that for the OML motion an angular momentum barrier exists: Certain ions that from energy balance considerations should fall onto the particle will actually not reach the particle [8]. The reason is that the effective potential $U_{\text{eff}} = e\phi - L^2/2mr^2$ has a “hump” at distances $r > a$ where the ions are already reflected. Their distance of closest approach thus is not the particle surface. They do not come close to the region near the particle where the above discussed energy and angular momentum balance hold. This hump in the effective potential appears only for a small range of angular momenta and energies. For particles much smaller than the Debye length ($a \ll \lambda_D$) that fraction of reflected ions is negligible and the OML results are still valid [9, 10].

Radial motion theory: In Langmuir probe theory a number of other models are available to describe the current to a (spherical) probe, like e.g. the radial motion theory (ABR) by Allen, Boyd and Reynolds [11] where the ions start from infinity with no kinetic energy and are accelerated radially towards the probe (or the dust particle). However, it has been shown [12] that in the ABR model the particle floating potential tends to zero for $a \ll \lambda_D$ which is unphysical. On the contrary, OML gives a finite particle potential independent of particle size (see Sec. 2.4.1.).

2.2.3. Streaming Ions

In many cases, like in the sheath environment of a discharge, the ions have a drift velocity \mathbf{u}_i that can be much larger than the thermal ion velocity $\mathbf{v}_{th,i}$. Thus, the ion species is no longer described by an isotropic Maxwellian distribution. In that case, the ion current is modified. The ion current to a dust particle can then be written in the form

$$I_i = \pi a^2 n_i e v_{th,i} f(\mathbf{u}_i), \quad (2.10)$$

where $f(\mathbf{u}_i)$ is a (rather complicated) function of the ion drift velocity [13]

$$f(x) = \sqrt{\frac{\pi}{4}} x \left[\left(1 + \frac{1}{2x^2} - \frac{e\phi_p}{kT_i x^2} \right) \text{erf}(x) + \frac{1}{\sqrt{\pi} x} e^{-x^2} \right]$$

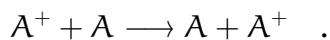
where $x = \mathbf{u}_i / \sqrt{2kT_i/m_i}$ and $\text{erf}(x)$ is the error function[‡]. For ions with high streaming velocity $\mathbf{u}_i \gg \mathbf{v}_{th,i}$ the ion current reduces to

$$I_i = \pi a^2 n_i e \mathbf{u}_i \left(1 - \frac{2e\phi}{m_i \mathbf{u}_i^2} \right), \quad (2.11)$$

which is obtained by replacing the thermal ion energy kT_i in Eq. (2.2) by the kinetic energy of the drifting ions $m_i \mathbf{u}_i^2 / 2$. The effect of streaming ions is further discussed in Sec. 2.4.3.

2.2.4. Collisions

Ion-neutral collisions considerably modify the ion current onto the dust since the ion loses its kinetic energy in that collision and is subsequently accelerated towards the dust. Further, the presence of collisions will lead to ions trapped in the electrostatic potential well performing Keplerian orbits around the dust [14]. In plasma discharges in noble gases ion-neutral collisions are predominantly charge-exchange collisions where an ion transfers its charge to a formerly neutral atom



In a weakly collisional regime one might estimate that every ion-neutral collision in a sphere of a certain radius R_0 around the dust leads to a collection of this ion. The probability of such a collision is roughly R_0/ℓ_{mfp} when independent collisions can be assumed. Here, $\ell_{mfp} = 1/(n_n \sigma_{in})$ is the mean free path for ion-neutral collisions, n_n is the

[‡]The error function is given by

$$\text{erf}(x) = \frac{2}{\sqrt{\pi}} \int_0^x \exp(-y^2) dy$$

neutral gas density and σ_{in} is the ion-neutral (charge-exchange) collision cross section. The thermal current of ions through a sphere of radius R_0 is simply $I = \pi R_0^2 n_i e v_{\text{th},i}$ yielding a collisional current of

$$I_{\text{coll}} = \pi R_0^2 n_i e v_{\text{th},i} \frac{R_0}{\ell_{\text{mfp}}}$$

Hence, the total ion current can be assumed [9] to be the sum of the ion collection current in Eq. (2.2) and the collision current

$$I_i = \pi a^2 n_i e v_{\text{th},i} \left(1 - \frac{e\phi_p}{kT_i} + \frac{R_0^3}{a^2 \ell_{\text{mfp}}} \right) . \quad (2.12)$$

A reasonable size R_0 would be where the ion-grain interaction energy is of the order of the ion thermal energy, i.e. using a Debye-Hückel interaction of shielding length λ_D

$$\frac{kT_i}{e} = \frac{Z_d e}{4\pi\epsilon_0 R_0} e^{-R_0/\lambda_D} .$$

To a good accuracy, one finds [15] that $(R_0/\lambda_D)^3 = 0.1(a/\lambda_D)^2(e\phi_p/kT_i)^2$ (thereby making also use of the capacitance model in Sec. 2.4.2.). Combining this all, the ion charging current including collisions can be written as

$$I_i = \pi a^2 n_i e v_{\text{th},i} \left(1 - \frac{e\phi_p}{kT_i} + 0.1 \left(\frac{e\phi_p}{kT_i} \right)^2 \frac{\lambda_D}{\ell_{\text{mfp}}} \right) . \quad (2.13)$$

The effect of collisions on the particle potential will be further discussed in Sec. 2.4.4..

2.3. Other Charging Currents

Two other possible charging mechanisms are described here which are considered important mostly for astrophysical situations [16]. These are charging by UV radiation and secondary electron emission. Both processes lead to electron emission from the dust particle and can thus be treated as a positive current to the particle.

Other possible charging mechanisms, like thermal emission, field emission, sputtering, or ion-induced electron emission are neglected, since they are usually not important for dusty plasmas in the laboratory or in space.

2.3.1. Photoelectron Emission

The absorption of UV radiation releases photoelectrons and hence constitutes a positive charging current. The magnitude of the current depends on the photoemission yield η which is specific for the dust material ($\eta \approx 1$ for metals and $\eta \approx 0.1$ for dielectrics). In

many cases the released photoelectrons can be described by a Maxwellian distribution with a temperature T_v . The charging current by photoemission is then given by [16]

$$\begin{aligned} I_v &= \eta\pi\alpha^2 eK & \phi_p \leq 0 \\ I_v &= \eta\pi\alpha^2 eK \exp\left(\frac{-e\phi_p}{kT_v}\right) & \phi_p > 0 \quad , \end{aligned} \quad (2.14)$$

where K is the flux of photoelectrons. Photoemission by UV radiation might be important for dust grains in astrophysical situations near stars. For example, this effect is made responsible for dust layers floating above the surface of the Moon.

2.3.2. Secondary Electron Emission

Secondary electron emission from the impact of energetic electrons might also be important under certain conditions in astrophysical situations. The secondary electron emission coefficient $\delta(E_e)$ describes the number of released electrons per incoming electron. It strongly depends on the energy of the impinging electron E_e and is described by the empirical formula

$$\delta(E_e) = 7.4\delta_m \frac{E_e}{E_m} \exp\left(-2\sqrt{\frac{E_e}{E_m}}\right)$$

that has the maximum yield of δ_m at $E_e = E_m$. Here, δ_m and E_m are material-dependent quantities that are in the range of $\delta_m = 0.5 \dots 30$ and $E_m = 0.1 \dots 2$ keV. Since the maximum yield δ_m can be much larger than 1, many more electrons can be released for each incoming electron. This may even lead to positively charged dust grains.

Meyer-Vernet has calculated the current from secondary electron emission: Integrating the secondary yield over a Maxwellian distribution of incoming electrons leads to the following expression of the charging current

$$\begin{aligned} I_s &= 3.7\delta_m\pi\alpha^2 n_e \sqrt{\frac{8kT_e}{\pi m_e}} \exp\left(\frac{e\phi_p}{kT_e}\right) F_{5,0}(E_m/4kT_e) \quad \text{for } \phi_p < 0 \\ I_s &= 3.7\delta_m\pi\alpha^2 n_e \sqrt{\frac{8kT_e}{\pi m_e}} \left(1 + \frac{e\phi_p}{kT_e}\right) \exp\left(\frac{e\phi_p}{kT_e} - \frac{e\phi_p}{kT_s}\right) F_{5,B}(E_m/4kT_e) \quad \text{for } \phi_p > 0 \end{aligned} \quad (2.15)$$

with T_s being the temperature of the released secondary electrons, $B = \sqrt{4e\phi_p/E_m}$ and

$$F_{5,Y}(x) = x^2 \int_Y^\infty u^5 e^{-(xu^2+u)} du \quad ,$$

which is an integral that can be evaluated numerically.

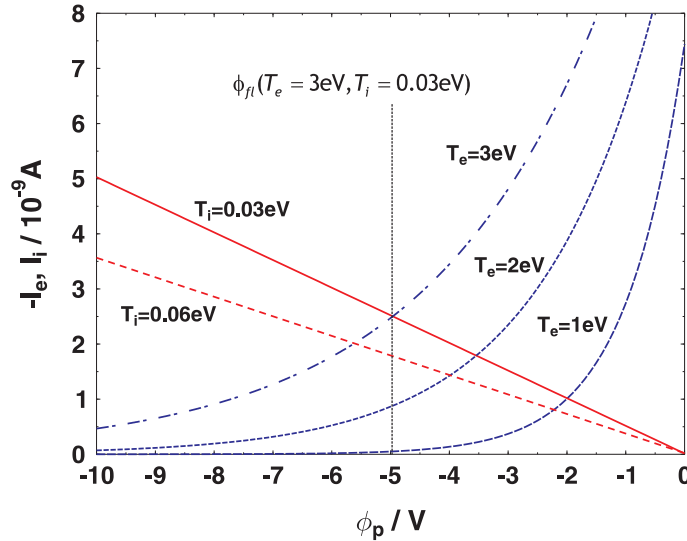


Figure 2.2: OML currents onto a dust particle for different values of electron and ion temperatures. The intersection of electron and ion current gives the floating potential (the negative electron current is plotted as positive, here). Other parameters used here are $\alpha = 4.7 \mu\text{m}$ and $n_i = n_e = 1 \cdot 10^9 \text{ cm}^{-3}$, which influence only the absolute magnitude of the currents, but not the floating potential. As an example, the floating potential $\phi_{fl} \approx -5 \text{ V}$ is indicated for the $T_e = 3 \text{ eV}$ and $T_i = 0.03 \text{ eV}$.

2.4. The Particle as a Floating Probe

2.4.1. OML Currents

As mentioned above, the floating potential of the particle is determined from the condition that all currents to the particle vanish, see Eq. (2.1). In laboratory discharges usually only the collection currents need to be considered. The OML electron and ion currents as a function of particle potential ϕ_p are shown in Fig. 2.2. The floating potential is then found from the intersection of the electron and ion currents.

T_e/T_i	1	2	5	10	20	50	100
H	-2.504	-2.360	-2.114	-1.909	-1.700	-1.430	-1.236
He	-3.052	-2.885	-2.612	-2.388	-2.160	-1.862	-1.645
Ar	-3.994	-3.798	-3.491	-3.244	-2.992	-2.660	-2.414

Table 2.1: Normalized floating potentials $e\phi_{fl}/kT_e$ in quasineutral plasmas $n_e = n_i$ in Hydrogen, Helium and Argon for different electron-to-ion temperature ratios.

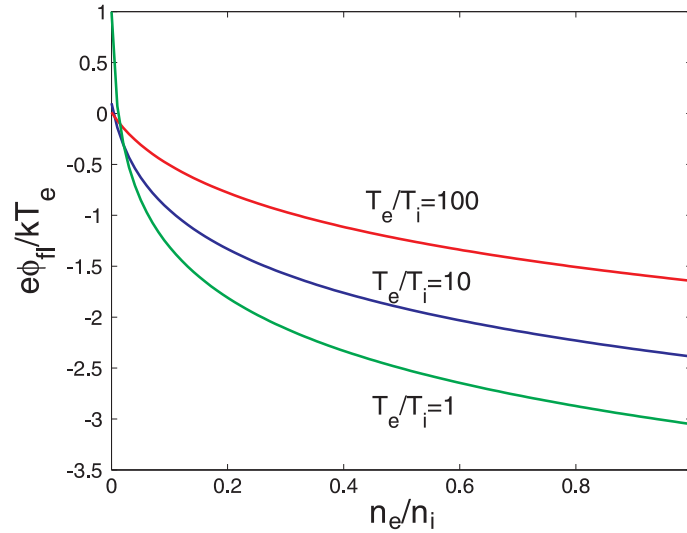


Figure 2.3: *Normalized floating potential of a dust particle for reduced electron density n_e/n_i .*

Analytically, the floating potential ϕ_f is obtained by equalizing the electron and ion currents resulting in

$$1 - \frac{e\phi_f}{kT_i} = \sqrt{\frac{m_i T_e}{m_e T_i}} \frac{n_e}{n_i} \exp\left(\frac{e\phi_f}{kT_e}\right) . \quad (2.16)$$

This equation can be easily solved numerically for ϕ_f for given values of the plasma parameters. In Table 2.1 the calculated floating potentials are shown for various discharge conditions. For the astrophysically important case of the isothermal ($T_e = T_i$) hydrogen plasma the well-known Spitzer value $\phi_f = -2.5kT_e/e$ is approached. Under typical laboratory discharges in heavier gases with $T_e \gg T_i$ a good rule-of-thumb approximation is $\phi_f \approx -2kT_e/e$. However, for electron energy distributions with even a small suprathermal electron component the floating potential will be decisively different.

If the electron density is reduced with respect to the ion density $n_e < n_i$, e.g. in the sheath of a discharge, the electron charging current is reduced and the particle attains a more positive floating potential. This is shown in Fig. 2.3 where the floating potential is shown for reduced electron density $n_e/n_i = 0 \dots 1$. For $n_e/n_i = 1$ the above value is retrieved (see Table 2.1), for $n_e/n_i \rightarrow 0$ even positively charged dust is found.

2.4.2. The Capacitance Model

After having determined the floating potential on the particle (at least in the case of pure OML currents) the charge on the particle has to be found. Therefore, the dust particle is

considered as a spherical capacitor of capacitance C . The particle charge is then given by

$$Q_d = Z_d e = C \phi_f \quad , \quad (2.17)$$

where Z_d is the number of elementary charges on the dust. In the vacuum case the capacitance of a sphere is

$$C = 4\pi\epsilon_0 a \quad .$$

In an ambient plasma with shielding length λ_D the capacitance is

$$C = 4\pi\epsilon_0 a \left(1 + \frac{a}{\lambda_D} \right) \quad ,$$

which for the typical case of $a \ll \lambda_D$ reduces to the vacuum value.

That means that a particle of $a = 1 \mu\text{m}$ radius attains $Z_d = 695$ elementary charges per volt floating potential. With the above mentioned rule-of-thumb estimation of the floating potential $\phi_f = -2kT_e/e$ an approximate formula of the dust charge is given by

$$Z_d = (-)1400 a_{\mu\text{m}} T_{e,\text{eV}} \quad (2.18)$$

with $T_{e,\text{eV}}$ being the electron temperature in electron volts and $a_{\mu\text{m}}$ the particle radius in microns. We will often treat Z_d as a positive number and deal with the fact that the dust (usually) is negatively charged by a minus sign for the elementary charge.

2.4.3. Floating Potential with Streaming Ions

For streaming ions, the floating potential is obtained from the equality of the electron current and the ion current for drifting ions according to Eq. (2.10). For this case, the floating potential is shown in Fig. 2.4. One can see that for small drift velocities up to the thermal velocity the floating potential is nearly unchanged and equal to the case without drift. Then, first a decrease of floating potential is observed (by about a factor of two) and after that a strong increase. Thus the particle first becomes more negative with respect to the OML case. The minimum floating potential is observed when the ions have approximately Bohm velocity $u_i \approx v_B = (kT_e/m_i)^{1/2}$. With further increased drift velocity the particles become less negatively charged. The first decrease of the potential is due to the reduction of the collection cross section $(1 - 2e\phi/m_i u_i^2)$ with increasing drift velocity. The increase of the potential at high drift velocities finally is due to the increased ion flux $n_i e u_i$. Moreover, it is seen that the approximated ion current according to Eq. (2.11) already works for relatively low drift velocities $u_i > v_{\text{th},i}$.

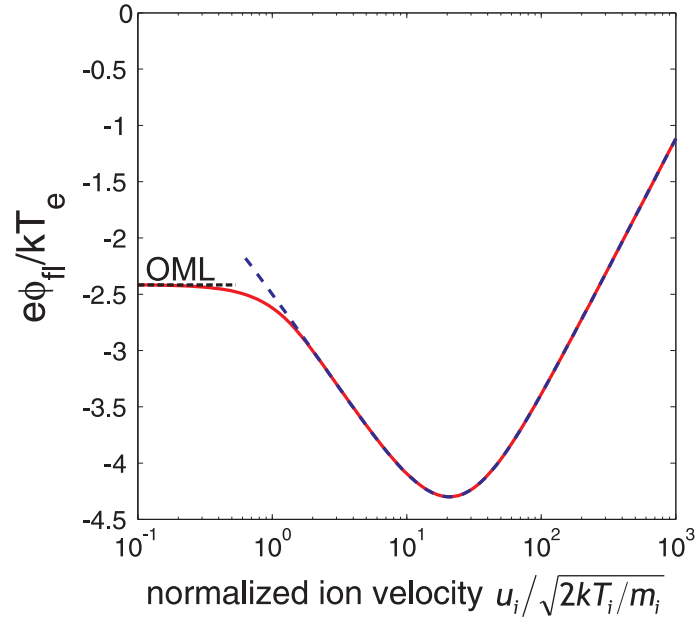


Figure 2.4: Particle floating potential as a function of the streaming velocity of the ions. The floating potential has been normalized to the electron temperature, the drift velocity to the ion thermal velocity. The classical OML result is also indicated. The solid line is the full Eq. (2.10), the dashed line is the approximation of Eq. (2.11). Parameters: $T_e/T_i = 100$ in argon.

2.4.4. Floating Potential with Collisions

In the case of collisions, the particle floating potential is derived by balancing the electron current and the collisional ion current according to Eq. (2.13). Figure 2.5 shows the floating potential of a dust particle in a collisional plasma background as a function of the mean free path ℓ_{mfp} . The constant OML result $e\phi_{\text{fl}}/kT_e = -2.414$ (compare Tab. 2.1) is shown as the dotted line. The red solid line indicates the influence of collisions using the collisional ion current of Eq. (2.13). For low collisionality (large mean free path) the OML result is retrieved. With shorter mean free path the particle potential becomes substantially less negative, the charge number substantially reduces. This is due to the collision-enhanced ion current to the particle.

For comparison, the results of a more sophisticated calculation and fitting procedure by Zobnin et al. [17] are also shown (see also [18]). Zobnin revealed two effects: first, the floating potential depends on particle size (which is not found for OML or the collisional current). Second, at very small mean free path the particle potential again becomes more negative. This is due to the effect that there the ion motion towards the dust is effectively hampered by the very frequent ion-neutral collisions (hydrodynamic limit). However, the

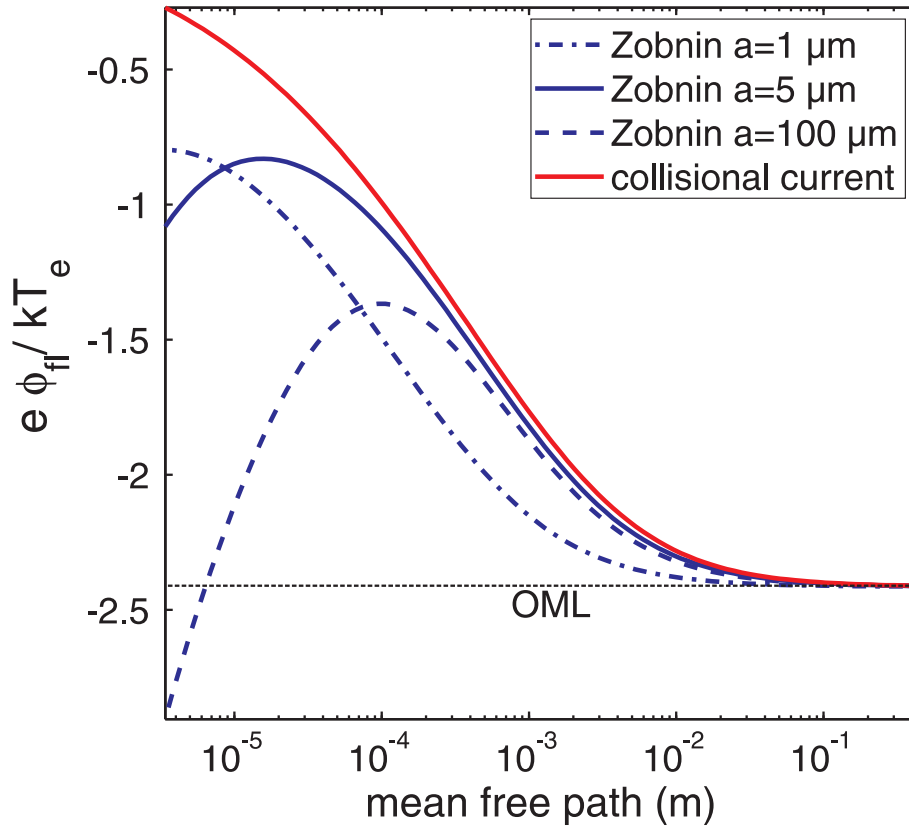


Figure 2.5: Particle floating potential as a function of ion mean free path. Parameters: $n_i = n_e = 2 \cdot 10^8 \text{ cm}^{-3}$, $T_e = 3 \text{ eV}$, $T_i = 0.03 \text{ eV}$ in argon. The dotted line is the OML result. The solid red line indicates the result from the collisional ion current according to Eq. (2.13). The blue lines indicate the results of more sophisticated calculations by Zobnin et al. [17] for different particle sizes.

floating potential derived from our collisional ion current of Eq. (2.13) is in good agreement with the more sophisticated results down to mean free paths of the order of millimeter or even sub-millimeter for particle sizes in the micrometer range. Hence, collisions effectively reduce the particle floating potential and dust charge (up to a factor of 2) compared to the OML results.

2.4.5. Floating Potential with Secondary Electron Emission

If secondary electron emission is important, as for cosmic grains, the floating potential is determined from the condition

$$I_e + I_i + I_s = I_{\text{tot}} = 0 \quad .$$

Such a situation is shown in Fig. 2.6, where the secondary electron emission current I_s together with the OML charging currents I_e and I_i are shown as a function of the particle potential ϕ_p . Under the conditions chosen here the total current vanishes for three values of the floating potential. The floating potential thus is not a unique value, but is multivalued [19].

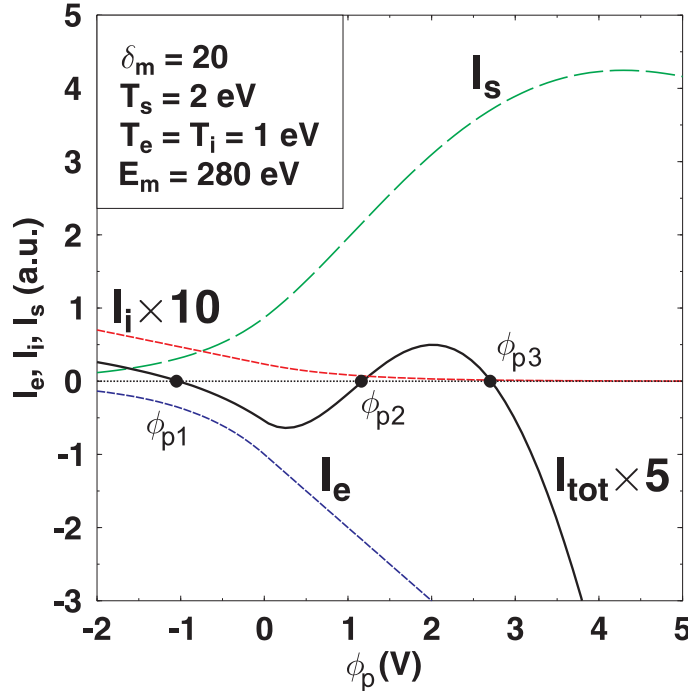


Figure 2.6: Secondary electron emission current I_s , the OML charging currents I_e and I_i as well as the total current I_{tot} as a function of grain potential. The total current vanishes for three values of the floating potential, where the middle root is unstable, but the two extreme roots are stable. Hence, positive and negative grains can exist under the same plasma conditions. Parameters are as indicated in the inset.

The two outer values of the floating potential ϕ_{p1} and ϕ_{p3} are stable roots, the middle ϕ_{p2} is unstable. The first stable root is always negative $\phi_{p1} < 0$, the second stable is always positive $\phi_{p3} > 0$. For these two outer roots

$$\left. \frac{dI_{\text{tot}}}{d\phi} \right|_{\phi_{p1,3}} < 0 \quad .$$

Thus, if a positive charge $+\Delta Q$, e.g. an ion, is added to the dust at the floating potential $\phi_{p1,3}$ the particle potential gets more positive $\phi_{p1,3} \rightarrow \phi_{p1,3} + \Delta\Phi_p$ which results in a negative total current to the particle that compensates the positive charge $+\Delta Q$. Therefore,

$\phi_{p1,3}$ are stable roots. Correspondingly, ϕ_{p2} is unstable. Any fluctuation of the particle charge near ϕ_{p2} will switch the potential to either ϕ_{p1} or ϕ_{p3} .

That means that in the *same* plasma negatively as well as positively charged dust grains can exist. The oppositely charged particles can then immediately coagulate in the plasma. This process might have an enormous influence on the growth mechanism of planetesimals in astrophysical dusty plasmas where secondary electron emission is present.

2.5. Temporal Evolution of the Particle Charge

So far, the particle charge has been considered as static. However, the temporal behavior of the dust charge can have a significant influence on the dynamic properties of the dust. The time scale for OML charging by ions τ_i is found from Eq. (2.1) by considering the ion charging current only

$$\frac{dQ}{dt} = I_i = \pi a^2 n_i e \sqrt{\frac{8kT_i}{\pi m_i}} \left(1 - \frac{e\phi_p}{kT_i} \right) .$$

Replacing the particle potential using the capacitor model this results in the differential equation

$$\frac{dQ}{dt} = \pi a^2 n_i e \sqrt{\frac{8kT_i}{\pi m_i}} \left(1 - \frac{Qe}{4\pi\epsilon_0 a kT_i} \right) . \quad (2.19)$$

This equation has the solution

$$Q(t) = Q_0 e^{-t/\tau_i} + 4\pi\epsilon_0 a \frac{kT_i}{e}$$

with the charging time scale

$$\tau_i = 4\pi\epsilon_0 a \frac{kT_i}{e} \frac{1}{\pi a^2 e n_i v_{th,i}} . \quad (2.20)$$

This time scale can be interpreted as the charging time $\tau = RC$ of the particle capacitance $C = 4\pi\epsilon_0 a$ through the resistance $R = U/I$, where $U = kT_i/e$ is the typical electric potential of thermal ions and $I = \pi a^2 e n_i v_{th,i}$ is the typical thermal OML ion current to the particle. Or, alternatively from Eq. (2.7), $R = dU/dI$ at the floating potential. The electron charging time is given by the same formula where the ion quantities are replaced by those of the electrons:

$$\tau_e = 4\pi\epsilon_0 a \frac{kT_e}{e} \frac{1}{\pi a^2 e n_e v_{th,e}} . \quad (2.21)$$

Due to the higher electron mobility it follows that $\tau_e \ll \tau_i$, and the overall charging time is dominated by the slower ions. Typical charging times in laboratory discharges are of the order of microseconds (see also Fig. 2.7 and 2.8). This is still typically much faster than the dynamical time scale of the particles, so the particle charge should always be in equilibrium with the plasma conditions. However, we will find some exceptions from that reasoning in the following.

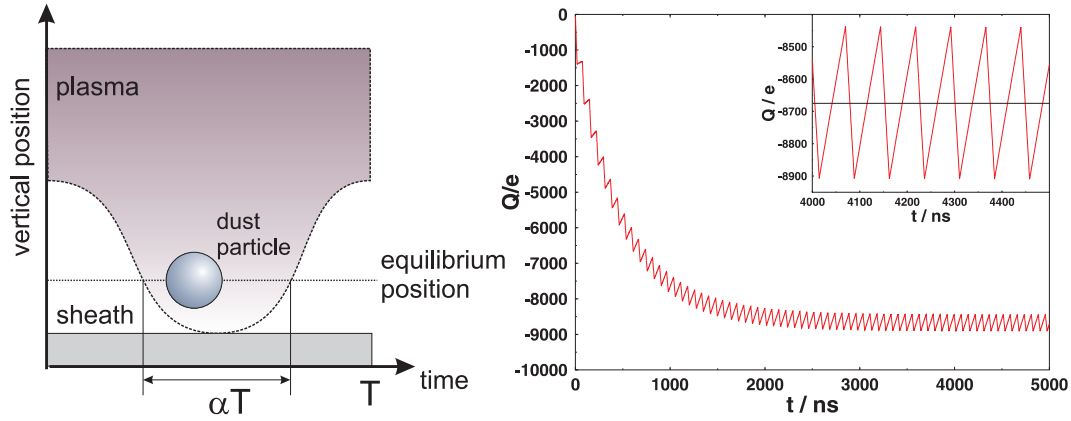


Figure 2.7: *Temporal evolution of a dust particle in the rf sheath. The inset is a magnification of the oscillating particle charge. Parameters: $a = 4.7 \mu\text{m}$, $kT_e = 3 \text{ eV}$, $kT_i = 0.03 \text{ eV}$, $n_i = 1 \times 10^9 \text{ cm}^{-3}$, and the electron flooding is assumed as $\alpha = 25 \%$ of the rf period. The equilibrium charge then is $Z_d = 8610$ negative elementary charges. After [20].*

2.5.1. Charging in the rf Sheath

In laboratory investigations on colloidal plasmas the particles are usually trapped in the sheath of rf discharges, where the (time averaged) electric field force on the particle balances gravity (see Sec. 3.7.). In the rf discharge, the electrons are able to follow the instantaneous rf voltage (which typically oscillates at 13.56 MHz), whereas the ions and the dust grains only react to the time averaged fields. In a simplified picture, the electron component of the plasma can be described as oscillating back and forth between the electrodes leading to a periodically increasing and collapsing sheath at the electrodes. A dust particle trapped in the sheath therefore periodically “sees” a quasineutral plasma environment, when the sheath is flooded by electrons, and a pure ion sheath, when the sheath is expanded. Hence, the electron charging current to the dust particle will also be modulated by the rf frequency, thus

$$\begin{aligned} \dot{Q} &= I_i + I_e & \text{for } 0 < t < \alpha T \\ \dot{Q} &= I_i & \text{for } \alpha T < t < T \end{aligned}$$

where $\alpha = 0 \dots 1$ is the fraction of the rf period $T = 75 \text{ ns}$ when the dust particle is in the “flooded” sheath (see Fig. 2.7a).

The temporal behavior of a dust particle in the sheath is shown in Fig. 2.7b for a particle immersed into the sheath starting from zero charge. In accordance with the charging time scale, see Eq. (2.20), the steady state charge is reached after a few microseconds.

Due to the periodic oscillation of the electron component, the dust particle charge is also modulated with the applied frequency of 13.56 MHz leading to a sawtooth behavior

of the dust charge. In the inset one can see the steep electron charging towards more negative charge numbers and the slower ion discharging. After long times the particle charge is modulated by few hundred elementary charges at a mean particle charge of a few thousand. Hence, the charge modulation is a few percent at a high frequency. These modulations should not affect the particle dynamics on the time scale of the dust particle motion.

2.5.2. Stochastic Fluctuations

Besides the periodic modulation of the dust charge due to the rf sheath, the particle charge experiences stochastic fluctuations due to the discreteness of the charge carriers – electrons and ions. This effect has been investigated by Cui and Goree as well as Matsoukas and Russel [21, 22] simulating the collection of individual electrons or ions according to the OML currents. The probability of collecting an ion p_i or electron p_e is taken proportional to the ion (electron) current to the particle. The collection of electrons and ions is treated as a stochastic process. At the floating potential, obviously $p_i = p_e$. In Fig. 2.8 the temporal behavior of the dust charge due to stochastic charging processes starting from zero charge is shown.

In the beginning at zero charge the probability of collecting an electron is much, much higher than collecting an ion due to the higher mobility of the electrons. The particle gets negatively charged. After a certain time, the charging time according to Eq. (2.20), the probability of electron or ion collection becomes more and more equal

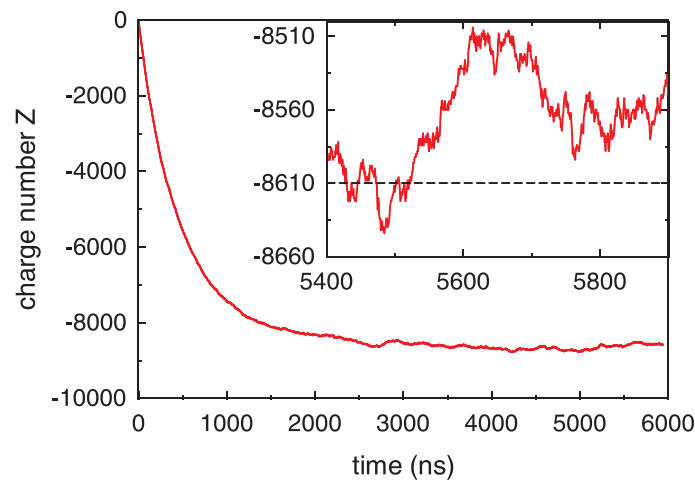


Figure 2.8: *Temporal behavior of the dust charge by stochastically collecting individual electrons and ions. The inset is a magnification of the dust charge fluctuations around equilibrium $Z_{\text{eq}} = 8610$. Parameters are the same as in Fig. 2.7.*

to each other. After having reached the equilibrium value the dust charge fluctuates around this value with an amplitude of about 100 elementary charges. The equilibrium value found in the stochastic approach is the same as for the static approach according to Eq. (2.16). It has been shown from simulations and analytical calculations that the charge fluctuations are $\delta Z_{\text{rms}} \approx 0.5\sqrt{Z_{\text{eq}}}$. These fluctuations are small and quite high-frequency so that an influence on the particle dynamics is not to be expected for micron sized particles. However, nanometer sized grains have equilibrium charges of the order of $Z_{\text{eq}} = 1$. Charge fluctuations can cause the particles to be charged even positively. Then one could also find positively and negatively charged dust in the same plasma which can lead to fast particle coagulation. This process might be of interest for particle growth in technological discharges (see Chapter 9).

2.6. Influence of Many Particles and Electron Depletion

So far, only the charging of single dust particles has been considered. Now, we would like to investigate the behavior of many dust particles. When the dust density n_d is high, a considerable amount of electrons is bound to the dust. Thus, the density of free electrons in the plasma might be drastically reduced due to the presence of the dust which in turn influences the charging behavior of the dust [24].

For a quantitative description we consider a situation as described in Fig. 2.9a) where a finite dust-containing plasma region is embedded in an infinite dust-free plasma. In the outer plasma, we find the undisturbed plasma density $n_{i,0} = n_{e,0}$, the dust density is zero ($n_d = 0$) and also the plasma potential ψ is defined as zero. In the dust-containing plasma cloud the plasma potential ψ differs from that in the outer plasma due to the presence of the charged dust particles [Fig. 2.9c)]. The electron and ion density in the dust cloud is assumed to adjust to the change in potential with a Boltzmann factor, which might be justified in astrophysical situations where $T_e \approx T_i$,

$$\begin{aligned} n_e &= n_{e,0} \exp\left(\frac{e\psi}{kT_e}\right) \\ n_i &= n_{i,0} \exp\left(-\frac{e\psi}{kT_i}\right) \quad . \end{aligned}$$

The influence of the dust becomes noticeable when the quasineutrality condition

$$n_e e = n_i e - n_d Z_d e = n_i e - n_d C \phi_d \quad (2.22)$$

is affected by the dust. The negative charge is either due to free electrons or due to electrons bound on the dust particles. If the dust density is high then there are not enough electrons present to charge the particles to their single-particle floating potential. The particles thus acquire a more positive potential. This effect is called electron depletion.

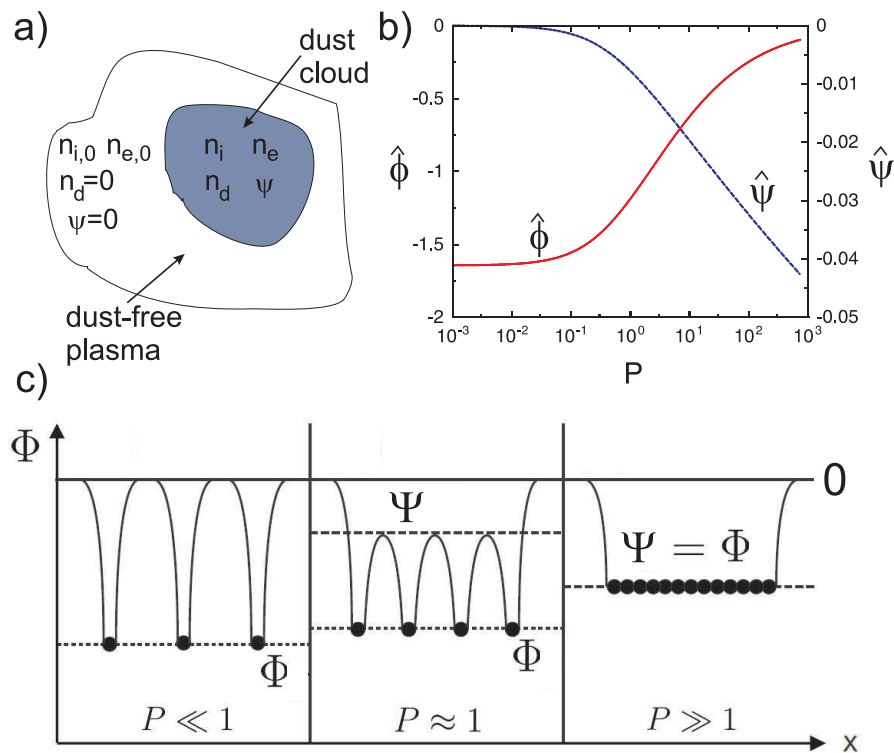


Figure 2.9: a) Sketch of the dust cloud in an extended pristine plasma. b) Particle floating potential $\hat{\phi}_f$ and cloud potential $\hat{\psi}$ as a function of the Havnes parameter P . Parameters: $T_e/T_i = 100$ in Helium. c) A one-dimensional section through the dense dust cloud. The particle potential ϕ and the cloud potential ψ in different regimes of the parameter P . After [23].

Hence, the quasineutrality condition has to be coupled to the charging equation. Using the normalized dust floating potential $\hat{\phi}$ and plasma potential $\hat{\psi}$ with

$$\hat{\phi} = \frac{e\phi_{fl}}{kT_e} \quad \text{and} \quad \hat{\psi} = \frac{e\psi}{kT_e}$$

the quasineutrality condition and the charging equation are written as

$$\exp(\hat{\psi}) - \exp\left(-\frac{T_e}{T_i}\hat{\psi}\right) - \underbrace{\frac{4\pi\epsilon_0 a kT_e n_d}{e n_{e,0}}}_{\mathbf{P}} \hat{\phi} = 0 \quad (2.23)$$

$$\left(1 - \frac{T_e}{T_i}\hat{\phi}\right) - \sqrt{\frac{T_e m_i}{T_i m_e}} \exp\left[\left(1 + \frac{T_e}{T_i}\right)\hat{\psi}\right] \exp(\hat{\phi}) = 0 \quad . \quad (2.24)$$

The terms containing $\exp(\hat{\psi})$ and $\exp(T_e/T_i\hat{\psi})$ are the normalized electron and ion densities, respectively. The Eqs. (2.23) and (2.24) have to be solved simultaneously for $\hat{\psi}$ and $\hat{\phi}$, i.e. for the floating potential of the dust and the local plasma potential in the dust cloud. The dust influence is described in terms of the so-called Havnes parameter

$$\mathbf{P} = \frac{n_d Z_d}{n_{e,0}} = \frac{4\pi\epsilon_0 a kT_e n_d}{e n_{e,0}} = 695 T_{e,\text{eV}} a_{\mu\text{m}} \frac{n_d}{n_{e,0}} \quad ,$$

where $T_{e,\text{eV}}$ is the electron temperature in electron volts and $a_{\mu\text{m}}$ is the particle radius in microns. Figure 2.9b) illustrates the influence of the electron depletion with increasing Havnes parameter \mathbf{P} . The single particle limit is obtained for $\mathbf{P} \rightarrow 0$. Near $\mathbf{P} = 0.1$ the floating potential on the particle increases considerably towards more positive values and approaches $\hat{\phi}_{fl} \rightarrow 0$ for $\mathbf{P} \rightarrow \infty$. This reflects the electron depletion. There are not enough electrons present as to charge all dust particles to the full single-particle potential, thus, the available electrons are distributed among the dust particles, i.e. the free electron density $n_e = 0$ and $Z_d = n_i/n_d$.

3. Forces and Trapping of Dust Particles

In this part we will discuss the main forces acting on dust particles in a plasma discharge. These forces are gravity, electric field force, ion drag force, thermophoresis and neutral drag. After analysis of the forces under plasma conditions the trapping of dust particles in the laboratory, under microgravity and in plasma processing devices will be described. We are then in a position to derive a method for the charge measurement in the sheath of a plasma and to discuss vertical oscillations in the plasma sheath.

3.1. Gravity

The gravitational force simply is

$$\vec{F}_g = m_d \vec{g} = \frac{4}{3} \pi a^3 \rho_d \vec{g} \quad , \quad (3.1)$$

where \vec{g} is the gravitational acceleration and ρ_d is the mass density of the dust grains. Since this force scales with a^3 it is the dominant force for large particles in the micrometer range and becomes negligible for particles in the nanometer range.

3.2. Electric Field Force

Obviously, the electric field force due to an electric field \vec{E}

$$\vec{F}_E = Q_d \vec{E} = 4\pi\epsilon_0 a \phi_d \vec{E} \quad (3.2)$$

is the governing force for charged particles. With the applied capacitor model this force scales linearly with the particle size. In the plasma sheath strong electric fields prevail that exert an electric field force that is large enough to levitate large micron-sized grains against gravity. In the plasma volume, due to quasineutrality, only small electric fields exist. Thus, in the plasma volume, particles can be trapped only when gravity is not important as for nanometer particles or for large particles under microgravity conditions.

3.2.1. Shielding

One subtle problem should be discussed in more detail, here: Since in a plasma the (negative) dust particle is surrounded by a (positive) shielding cloud of ions (see Fig. 3.1a), one might think that the electric field force acts individually on the dust and on the shielding cloud in opposite directions, thereby canceling each other. In other words: the entire system of dust and shielding cloud is neutral and thus no net electric field force

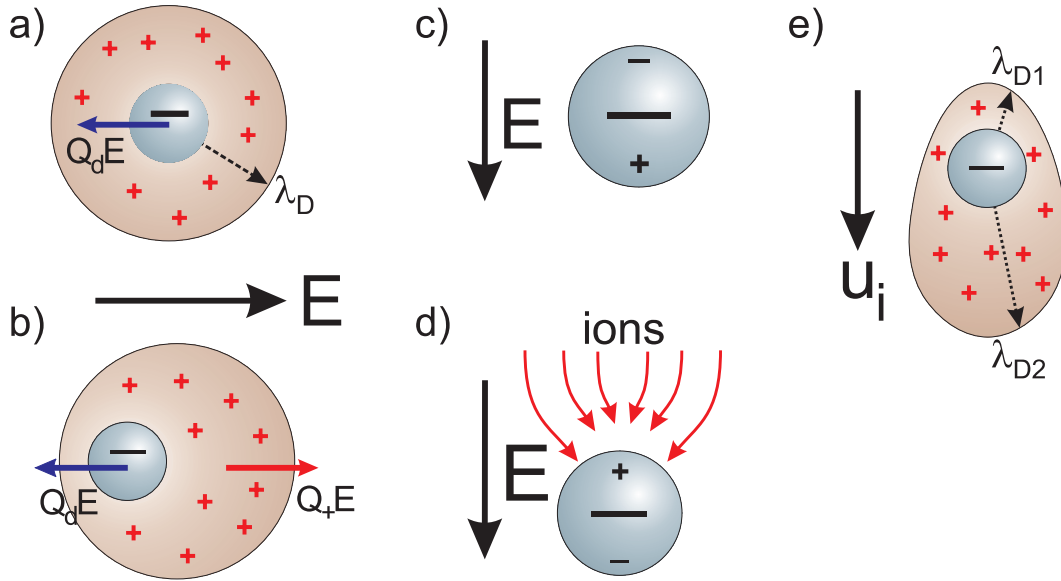


Figure 3.1: *Electric field force and polarization forces: a) “right” and b) “wrong” picture of the dust particle and its shielding cloud under the influence of an external field E . Formation of a dipole moment on the dust particle induced by an electric field (c) or by directed charging (d). Polarization of the dust cloud due to an ion streaming motion.*

should exist, see Fig. 3.1b. If this reasoning was true there would be no action of the electric field force on the dust particle.

Hamaguchi and Farouki [25] have discussed that point in detail: To understand the behavior of the dust one has to carefully distinguish between the source and the effect. The shielding cloud is formed due to the presence of the electric field of the dust particle (and the external field). The shielding cloud reacts according to these fields. Hence, the shielding cloud is a response to the presence of the dust. When the dust moves from a place A in the plasma to a place B, the shielding cloud is not pushed from A to B by the dust. Rather, the ion cloud decays at A and re-forms at B. The shielding cloud is not “attached” to the dust by a force and thus there is no counterforce from the cloud onto the dust.

Consequently, the full force of Eq. (3.2) acts on the dust particle, the dust particle is moved by this force and the shielding cloud is formed according to the electric fields near the dust. The shielding cloud does not hinder the action of the electric field force on the dust. This reasoning holds for spherically symmetric shielding clouds. If the spherical symmetry of the shielding is distorted by the external field, additional polarization forces exist, that will be described now.

3.2.2. Polarization Forces

Polarization forces arise from dipole moments on the particles or the shielding cloud. In general, the polarization force on a dipole is

$$\vec{F}_{\text{dip}} = \vec{\nabla}(\vec{p} \cdot \vec{E}) \quad , \quad (3.3)$$

where \vec{p} is the dipole moment. Dipole moments on the particles can either be influenced by an external electric field or generated by directed charging processes (for dielectric particles).

The dipole moment on a dielectric particle by an external electric field \vec{E} (see Fig. 3.1c) is given by

$$\vec{p} = 4\pi\epsilon_0\alpha^3 \frac{\epsilon - 1}{\epsilon + 2} \vec{E} \quad ,$$

where ϵ is the dielectric constant of the dust material. Due to the α^3 scaling the force due to an induced dipole becomes relevant only for extremely large particles.

Dipole moments may also arise from a directed charging (Fig. 3.1d) due to streaming ions where one side of the particle is hit more frequently by ions than the other side. For the case of a particle in the plasma sheath the top side is expected to be more positive than the bottom. Note, that the dipole moments by directed charging and the induced dipole are opposite.

Hamaguchi and Farouki [25] have analyzed a situation which is close to that found in a plasma sheath. In the sheath there is a difference in electron and ion density which is sustained by an electric field \vec{E} . Consequently, the plasma densities can change over the size of the shielding cloud, thus a spatially dependent shielding length $\lambda_D(\mathbf{r})$ is considered in the model (see Fig. 3.1e). In the lower sheath of a discharge the electric field usually points downward from the positive plasma towards the negative electrodes. Near the plasma edge the electron and ion densities are larger than at the electrode. Thus, the shielding length on the top side λ_{D1} of a dust particle in the sheath is smaller than that on the bottom λ_{D2} .

The authors have solved the Debye-Hückel equation for the electrostatic potential $\phi(\mathbf{r})$ in this situation

$$\Delta\phi(\mathbf{r}) - \frac{\phi(\mathbf{r})}{\lambda_D(\mathbf{r})^2} = \frac{Q_d}{\epsilon_0}\delta(\mathbf{r})$$

and found the electric force on the dust particle including the contribution of the distorted shielding cloud as

$$\mathbf{F}_E = Q_d\vec{E} - \frac{Q_d^2}{8\pi\epsilon_0} \frac{\vec{\nabla}\lambda_D(\mathbf{r})}{\lambda_D^2} \quad . \quad (3.4)$$

The force has two components. The first one is just the usual electric field force as in Eq. (3.2). The direction of the force is determined by the charge. The second term is due to

the deformation of the shielding cloud. It is always in the direction of decreasing shielding length λ_D . The total force might thus be increased or decreased by the deformation. According to Hamaguchi and Farouki the shielding length to be used in Eq. (3.4) depends on the ion streaming velocity \mathbf{u}_i . For subthermal ion drifts (i.e., $\mathbf{u}_i < \mathbf{v}_{th,i}$) ions can contribute to shielding and the relevant shielding length is the ion Debye length $\lambda_D = \lambda_{D,i}$. For supersonic ion streams ($\mathbf{u}_i \gg \mathbf{v}_{th,i}$) the ions are too fast to contribute to shielding and thus the relevant shielding length is the electron Debye length $\lambda_D = \lambda_{D,e}$ (see also Sec.7.9.). In most cases, however, the polarization forces are negligible, except for very large particles.

3.3. Ion Drag Force

The next two forces to be discussed are drag forces which arise from a relative motion of a plasma species relative to the dust particle. In the case of the ion drag force there is an ion stream relative to the dust particle and the interaction is electrostatic, whereas for the neutral drag atoms or molecules of the neutral gas background drift past the dust and interact by direct collisions. The number of particles interacting with the dust per time interval dt is given by $dN = n\sigma\vec{v}_{rel}dt$, where n is the density of the streaming species, σ is the cross section for interaction and \vec{v}_{rel} is the relative velocity (see Fig. 3.2). Then,

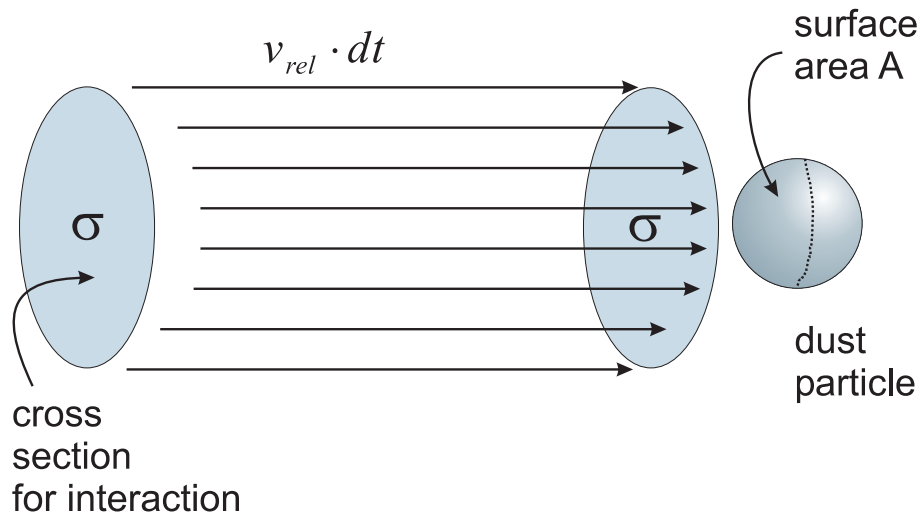


Figure 3.2: Sketch to determine the number of plasma particles per unit time moving relative to the dust particle and interacting with it. Here, σ indicates the cross section for the relevant interaction of the plasma species with the dust.

the drag force is given from the momentum transfer $\Delta\mathbf{p}$ per time interval as

$$\vec{F}_{\text{drag}} = \frac{dN\Delta\mathbf{p}}{dt} = \Delta\mathbf{p}n\sigma\vec{v}_{\text{rel}} \quad . \quad (3.5)$$

Now, we start with the ion drag force. The ion drag is due to streaming ions. The streaming motion can arise from ambipolar diffusion or supersonic motion in the sheath. The ion drag consists of two parts, the collection force \vec{F}_{dir} due to ions directly hitting the dust and the Coulomb force \vec{F}_{Coul} due to Coulomb scattering of the ions in the electric field of the dust particle (see Fig. 2.1). The ion drag force will be discussed in two steps using, first, a simplified model for a qualitative understanding of the processes before, second, a more quantitative description is given. The ion drag force can have significant contributions in dusty plasmas. For example, the ion drag force is made responsible for the formation of the “void” (see Sec. 3.7.).

3.3.1. Qualitative Discussion: Barnes model

In this first qualitative model, we note that the collection part of the ion drag force is just due to those ions which are also responsible for the ion charging of the dust and is thus given by

$$\vec{F}_{\text{dir}} = \pi a^2 m_i v_s n_i \vec{u}_i \left(1 - \frac{2e\phi_{\text{fl}}}{m_i v_s^2} \right) \quad . \quad (3.6)$$

Here, $m_i v_s$ is the momentum transfer of the ion at the mean velocity $v_s = (\mathbf{u}_i^2 + v_{\text{th},i}^2)^{1/2}$ given by the ion thermal velocity $v_{\text{th},i}$ and the ion drift velocity \mathbf{u}_i . The interaction cross section is that for ion collection defined in Eq. (2.5).

The Coulomb force is exerted by those ions which are not collected by the dust, but are deflected in the electric field of the dust grain. From plasma physics textbooks it is known that

$$\sigma = 4\pi b_{\pi/2}^2 \ln \Lambda = 4\pi b_{\pi/2}^2 \ln \frac{\lambda_D}{b_{\pi/2}}$$

is the cross section for ion-electron Coulomb collisions, where $b_{\pi/2} = e^2/(4\pi\epsilon_0 m_i v^2)$ is the impact parameter for 90° deflection and $\ln \Lambda$ is the Coulomb logarithm. The Coulomb logarithm is due to truncation of the intrinsically infinite Coulomb collision cross section at the Debye length λ_D , i.e. Coulomb collisions outside the screening cloud are regarded unimportant. A cut-off towards small impact parameters is not necessary since electrons and ions are considered point-like.

For collisions with finite-sized dust particles the above Coulomb cross section has to be modified. The minimum collision parameter is b_c since ions with $b < b_c$ are absorbed

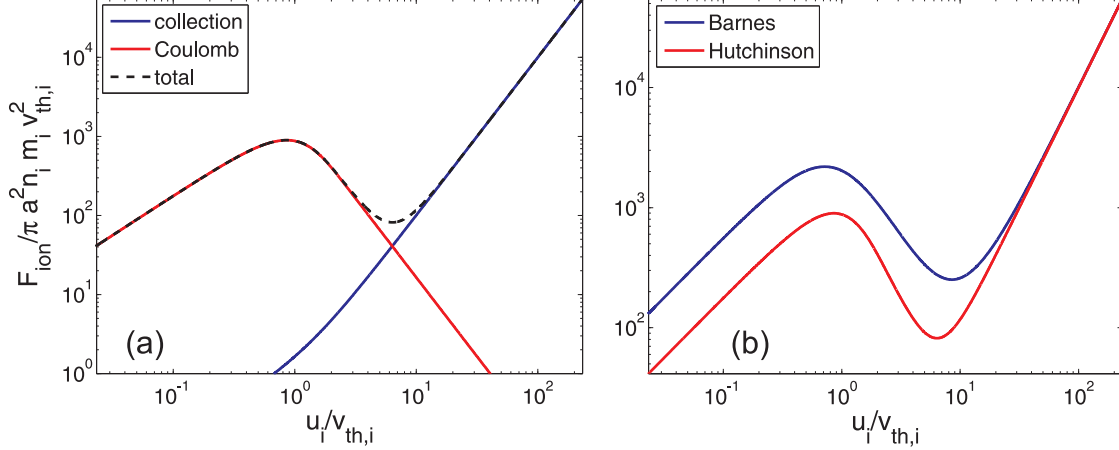


Figure 3.3: Calculated ion drag force on a double-logarithmic scale. In (a) the total force and contribution of the ion collection and the Coulomb scattering are shown using the Hutchinson/Khrapak model. (b) Comparison of the qualitative Barnes model (using $\lambda_{D,e}$) with the sophisticated Hutchinson/Khrapak model.

by the particle and contribute to the direct force. Integrating the Coulomb collision cross section from b_c to λ_D yields [26]

$$\sigma = 4\pi b_{\pi/2}^2 \ln \left(\frac{\lambda_D^2 + b_{\pi/2}^2}{b_c^2 + b_{\pi/2}^2} \right)^{1/2} .$$

with the slightly modified 90° collision parameter

$$b_{\pi/2} = \frac{Q_d e}{4\pi\epsilon_0 m_i v_s^2} = \frac{a e \phi_p}{m_i v_s^2} .$$

In the last equation we have used the capacitor model to replace the dust charge Q_d .

Thus, finally, the Coulomb force on a dust particle from streaming ions is

$$\vec{F}_{\text{Coul}} = 4\pi b_{\pi/2}^2 m_i n_i v_s \vec{u}_i \ln \left(\frac{\lambda_D^2 + b_{\pi/2}^2}{b_c^2 + b_{\pi/2}^2} \right)^{1/2} = 2\pi \frac{a^2 e^2 \phi_p^2}{m_i v_s^3} n_i \vec{u}_i \ln \left(\frac{\lambda_D^2 + b_{\pi/2}^2}{b_c^2 + b_{\pi/2}^2} \right) \quad (3.7)$$

In this force calculation, still only ion trajectories within one Debye length λ_D around the dust are considered. An open question so far is which Debye length has to be used, the electron or the ion Debye length. As a crude estimate Eq. (3.7) with the electron Debye length $\lambda_{D,e}$ can be used [27].

Finally, the total ion drag force is just the sum of the direct and the Coulomb collision force

$$\vec{F}_{\text{ion}} = \vec{F}_{\text{dir}} + \vec{F}_{\text{Coul}} \quad (3.8)$$

and is directed along the ion streaming motion. The ion drag force is shown in Fig. 3.3. The ion drag shows a pronounced S-shape. For small drift velocities the force first increases, then decreases and finally increases again. The first maximum is obtained when the drift velocity is of the order of the thermal velocity of the ions. For small drift velocities only the Coulomb force needs to be considered. The increase of the force at very low velocities is due to the increase of the Coulomb logarithm (due to the decrease of $b_{\pi/2}$) with velocity. After the maximum the Coulomb force decreases approximately as $1/u_i^2$. For $u_i \gg v_{\text{th},i}$ the collection force becomes dominant and increases as u_i^2 .

3.3.2. Quantitative Discussion: Hutchinson/Khrapak model

There are, however, some difficulties associated with the Barnes model. First, for the highly charged dust grains also Coulomb collisions outside the Debye sphere have to be included [28] since the ions feel the electrostatic potential of the dust far further than just one Debye length, hence the Coulomb logarithm has to be modified. As already became obvious in the above discussion a second problem is associated with the correct Debye length at the different ion streaming velocities. Finally, especially at low ion streaming velocities one has to consider that the ion velocity is a combination of the ion thermal velocity and the drift velocity which is adequately described by a shifted Maxwellian distribution function.

The collection force with a shifted Maxwellian ion distribution is then written as (see e.g. [29, 30])

$$F_{\text{dir}} = \pi a^2 m_i n_i v_{\text{th},i}^2 H(u) \quad , \quad (3.9)$$

where $H(u)$ which is a function of the normalized ion drift velocity $u = u_i / \sqrt{2kT_i/m_i}$ and the normalized particle potential $\chi = -e\phi_p/kT_i$ is given by *

$$H(u) = \frac{\sqrt{\pi}}{8} \left[u \left(2u^2 + 1 + 2\chi \right) e^{-u^2} + \left(4u^4 + 4u^2 - 1 - 2(1 - 2u^2)\chi \right) \frac{\sqrt{\pi}}{2} \text{erf}(u) \right] \frac{1}{u^2}.$$

The function scales as $H(u) \rightarrow (\pi/4)u^2 = u_i^2/v_{\text{th},i}^2$ for $u \gg 1$, hence $F_{\text{dir}} = \pi a^2 m_i n_i u_i^2$ which corresponds to the Barnes expression in Eq. (3.6) at high drift velocities. Hence, as shown in Fig. 3.3(b), for $u \gg 1$ the two models agree.

*The different prefactor given here compared that in Ref. [30] is due to the different normalizations of the thermal velocity.

Similarly, the Coulomb force is now given by

$$F_{\text{Coul}} = 32 \frac{\alpha^2 e^2 \phi_p^2}{m_i v_{\text{th},i}^2} n_i G(\mathbf{u}) \ln \Lambda \quad (3.10)$$

with the Chandrasekhar function $G(\mathbf{u}) = [\text{erf}(\mathbf{u}) - (2/\sqrt{3})\mathbf{u}e^{-u^2}]/(2u^2)$. For strong ion drifts $\mathbf{u} \gg 1$ the Chandrasekhar function scales as $G(\mathbf{u}) \rightarrow 1/(2u^2) = (\pi/16)v_{\text{th},i}^2/u_i^2$ yielding the same functional form as the Barnes expression in Eq. (3.7).

However, the strongest difference to the qualitative discussion above lies in the determination of the Coulomb logarithm $\ln \Lambda$. It has been shown by Khrapak et al. and Hutchinson [29, 30] that the Coulomb logarithm in the modified form

$$\ln \Lambda = \ln \frac{b_{\pi/2} + \lambda_s}{b_{\pi/2} + \alpha} \quad (3.11)$$

with a velocity dependent screening length already yields quite accurate results. The screening length

$$\lambda_s^2 = \frac{\lambda_{D,e}^2}{1 + 2kT_e/(m_i v_s^2)} + \alpha^2 \quad (3.12)$$

interpolates between the linearized Debye length at thermal ion velocities and the electron Debye length at high ion streaming velocities. This is reasonable since at higher streaming velocities the ions cannot participate in shielding (see Sec. 7.9. and also Sec. 3.2.2.).

Extensive numerical calculations by Hutchinson [30] have revealed that for evaluating $b_{\pi/2} = \alpha e \phi_p / (m_i v_{\text{eff}}^2)$ in the Coulomb logarithm of Eq. (3.11) and for the velocity dependent screening length λ_s in Eq. (3.12) an effective ion velocity of the form

$$v_{\text{eff}}^2 = 2 \frac{kT_i}{m_i} + u_i^2 \left(1 + \left[\frac{u_i / \sqrt{kT_e/m_i}}{0.6 + 0.05 \ln \mu + (\lambda_{D,e}/5\alpha)(\sqrt{T_i/T_e} - 0.1)} \right]^3 \right)$$

should be used. Here, μ is the atomic mass number of the ion.

The Hutchinson/Khrapak model yields highly accurate quantitative results for the ion drag force. For a particular case the total ion drag and its collection and Coulomb contribution using this model is shown in Fig. 3.3(a) as already discussed above. Fig. 3.3(b) shows the comparison of the Hutchinson/Khrapak and the Barnes model indicating substantial differences of the order of a factor of 2 and more, especially for the slow ion drift velocities that are relevant in experiments.

As complicated as the above discussions and equations already seem, they still refer to the case of collisionless ion trajectories. Simulations of the ion drag including ion-neutral collisions indicate a certain influence of collisions on the ion drag force [31, 32]. A “simple” treatment of collisions is, however, not available.

3.4. Neutral Drag Force

The neutral drag is a friction force due to neutral gas atoms hitting the dust particle. Neutral gas atoms or molecules that hit the dust lead to a slowing of the dust particle motion (when the dust is moving). Using Eq. (3.5) the force on a moving dust grain with velocity \vec{v}_d is readily given as [33]

$$\vec{F}_n = -\delta \frac{4}{3} \pi a^2 m_n v_{th,n} n_n \vec{v}_d \quad , \quad (3.13)$$

where m_n , n_n and $v_{th,n}$ are the mass, the density and the thermal velocity of the neutral gas atoms, respectively. The cross section for interaction is just the geometrical particle cross section πa^2 . The momentum transfer of the neutral gas onto the dust is of the order of $m_n v_{th,n}$ and slightly depends on how the gas atoms are reflected from the particle surface, e.g. diffuse, by specular reflection, isotropic etc. These differences are attributed to the parameter δ which lies in the range between 1 (for specular reflection) and 1.44 (for diffuse reflection). Experiments [34] on plastic microspheres in a plasma revealed a value of $\delta = 1.26 \pm 0.13$ and $\delta = 1.44 \pm 0.19$ using two different methods of measuring the drag force.

This neutral drag force was calculated by Epstein in 1924 for the analysis of the friction force in Millikan's famous oil drop experiment. We will often use that neutral drag in the form of a friction force , i.e.

$$\vec{F}_n = -m_d \beta \vec{v}_d \quad \text{with} \quad \beta = \delta \frac{8}{\pi} \frac{p}{a \rho_d v_{th,n}} \quad . \quad (3.14)$$

Here, β is the (Epstein) friction coefficient and linearly depends on the gas pressure p . The friction coefficient is inversely proportional to the particle radius a which means that in relation to their mass smaller particles experience stronger damping than larger particles.

3.5. Thermophoresis

The thermophoretic force acts on a dust particle due to a temperature gradient in the neutral gas. In an (over)simplified picture, it can be argued that neutral gas atoms from the "hotter" side hitting the dust grain have a larger momentum and thus exert a stronger force than atoms from the "colder" side. This leads to a force towards colder gas regions. However, the complete picture is more difficult and will not be discussed here. Following a rigorous treatment from gas kinetic theory, the thermophoretic force is found to be

$$\vec{F}_{th} = -\frac{32}{15} \frac{a^2 k_n}{v_{th,n}} \vec{\nabla} T_n \quad (3.15)$$

with T_n being the temperature of the neutral gas and k_n the thermal conductivity of the gas. The thermophoretic force is considered to be important for sub-micron particles due to heating of the gas by the plasma discharge. It has been intentionally applied for levitation of particles using strong temperature gradients by Rothermel et al. [35] and to the formation of 3D Yukawa balls (see Sec. 8.4.).

3.6. Laser Forces

In dusty plasmas focused laser beams are used to manipulate dust particles. The origin of the laser-particle manipulation goes back to the pioneering works of Ashkin [36] who has confined particles in optical traps. These works also have led to the techniques of laser-cooling of ions which is needed to form, e.g. Bose-Einstein condensates.

The laser beam interacts with the dust particle and pushes the particle in the direction of the beam. The origin of this laser force in dusty plasmas can be due to two sources, the radiation pressure or the so-called photophoretic force.

The force exerted by radiation pressure is just the momentum transfer of the laser photons p_{ph} that hit the dust particle. The radiation pressure can be written as [36]

$$P_{rad} = \frac{dp_{ph}}{A\Delta t} = \frac{dN_{ph}}{A\Delta t} \frac{h}{\lambda} = \frac{\Delta N_{ph}}{A\Delta t} \frac{h\nu}{c} = \frac{I}{c} . \quad (3.16)$$

Here, N_{ph} is the number of photons hitting the dust particle and λ and ν are the laser wavelength and frequency, respectively. The intensity I of the laser beam is just the number of photons of energy $h\nu$ per time interval focused onto the cross section A

$$I = \frac{N_{photon}h\nu}{A\Delta t} .$$

The force exerted by the radiation pressure then is

$$F_{rad} = \gamma \frac{I}{c} A_d \quad (3.17)$$

where A_d is the geometric cross section of the dust particle $A_d = \pi a^2$ and γ is a coefficient that takes the kind of interaction of the photons with the particle into account, i.e. $\gamma = 2$ for total reflection of the photons or $\gamma = 1$ for pure absorption.

For transparent particles, the radiation force also has a component perpendicular to the beam when the intensity profile of the beam is taken into account (see Fig. 3.4). Typically, a laser beam has a profile that has maximum intensity in the center and then gradually decreases outward. For a dust particle in the laser beam, this means that more photons go through the side of the particle that is closer to the center of the beam (the upper side in Fig. 3.4) compared to the other side (the lower side). The photons are deflected by the particle due to refraction. Since more photons on the upper side of the particles are deflected downwards than vice versa, an upward force (towards the center)

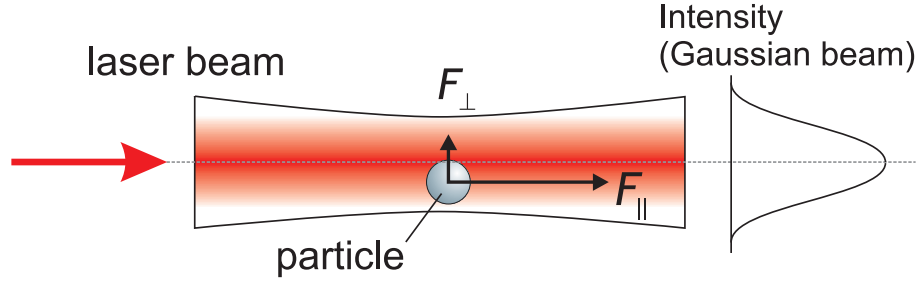


Figure 3.4: *Scheme of the laser-particle interaction due to radiation pressure.*

arises. This means, the particle is “sucked” into the beam in the direction perpendicular to the beam. This of course helps in the application of laser manipulation in dusty plasmas. This “trapping” of particles in the beam has been applied in the optical trap experiments of Ashkin and has also been observed in dusty plasma experiments.

The second mechanism that yields a force from laser beam interaction is much more difficult to analyze quantitatively. There it is assumed that the laser heats the illuminated particle surface. Similar to the thermophoretic force discussed above, neutral particles that impinge on the “hot” side of the dust are reflected at higher velocities than on the cold side. This leads to a force away from the “hot” side of the particle.

Now, the temperature distribution across the particle is very difficult to determine. When the particle is strongly absorbing, the photons are absorbed at the illuminated surface. The hot side is the illuminated side and the particles are pushed in the direction of the beam. If the particle is less absorbing the photons may be absorbed near the back side of the particles. Then the back side is heated and the photophoretic force is opposite to the laser beam. Under idealized conditions (i.e. the particle is much smaller than the mean free path of the gas and the photon energy is absorbed on the front side) the photophoretic force can be written as [37]

$$F_{\text{photo}} = \frac{\pi a^3 p I}{6(p a v_{\text{th},n} + \kappa T)} \quad (3.18)$$

where p is the gas pressure, T is the gas temperature and κ is the thermal conductivity of the particle.

From the simple models, the photophoretic force should exceed the radiation force considerably. However, this is difficult to judge due to the very complicated nature of the photophoretic force. Thus, a final answer whether radiation pressure or photophoretic forces dominate under the conditions of the dusty plasma experiments cannot be given, here.

Irrespective of the exact mechanism, lasers have been successfully applied in dusty plasmas to drive and manipulate particles (see e.g. [38] and references therein). And in many cases, the radiation pressure force was sufficient to explain the particle motion.

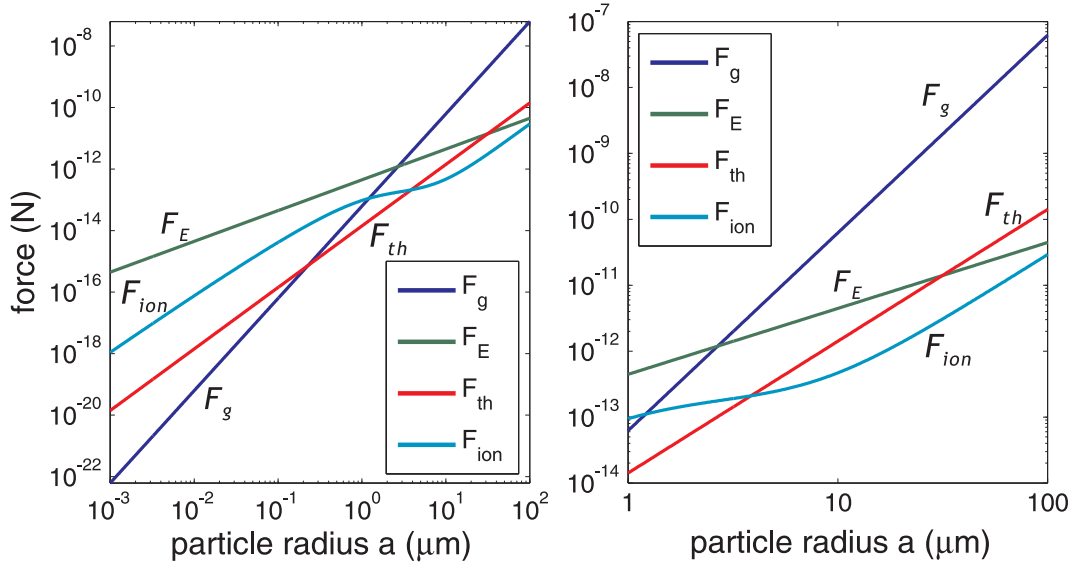


Figure 3.5: *Strength of the various forces as a function of dust particle radius. The employed parameters are: $\rho_d = 1500 \text{ kg/m}^3$, $T_e = 2 \text{ eV}$, $\phi_{fl} = -4 \text{ V}$, $E = 1000 \text{ V/m}$, $n_i = 10^{15} \text{ m}^{-3}$, $u_i = v_{th,i} = v_{th,n}$, $\nabla T_n = 200 \text{ K/m}$, $k_n = 0.016 \text{ kg m s}^{-3} \text{ (Ar)}$, $v_{th,n} = 400 \text{ m/s (Ar)}$.*

3.7. Compilation of Forces, Dust Levitation and Trapping

After the description of the relevant forces on the dust particles, now the question is how these forces can lead to particle levitation and trapping. Therefore, the strength of these forces as a function of particle size is calculated under the typical experimental conditions of a low-power Ar discharge (Fig. 3.5). For micron-sized dust particles (right panel) the dominant forces are gravity and electric field force. The thermophoretic force is already quite large when assuming a moderate temperature gradient of 200 K/m^\dagger . The ion drag force is smaller than the electric field force and gravity under the chosen conditions. Hence, for dust particles well above 1 micron in diameter and with small temperature gradients only electric field force and gravity are important. (Please note, that the electric field is considered as constant, here. In a discharge, the dust will move to a position, where the electric field force is large enough to balance the other forces.) The neutral drag is of interest only for moving particles and not for the identification of stable equilibria. Thus, the neutral drag is not considered, here.

For nanometer-sized dust particles (left panel of Fig. 3.5) gravity is negligible, as is for micron-sized dust under microgravity conditions. Then, ion drag force becomes the dominant force which has to be balanced by the electric field force.

[†]For a 3 cm electrode gap this corresponds to a temperature difference of 6°C , only.

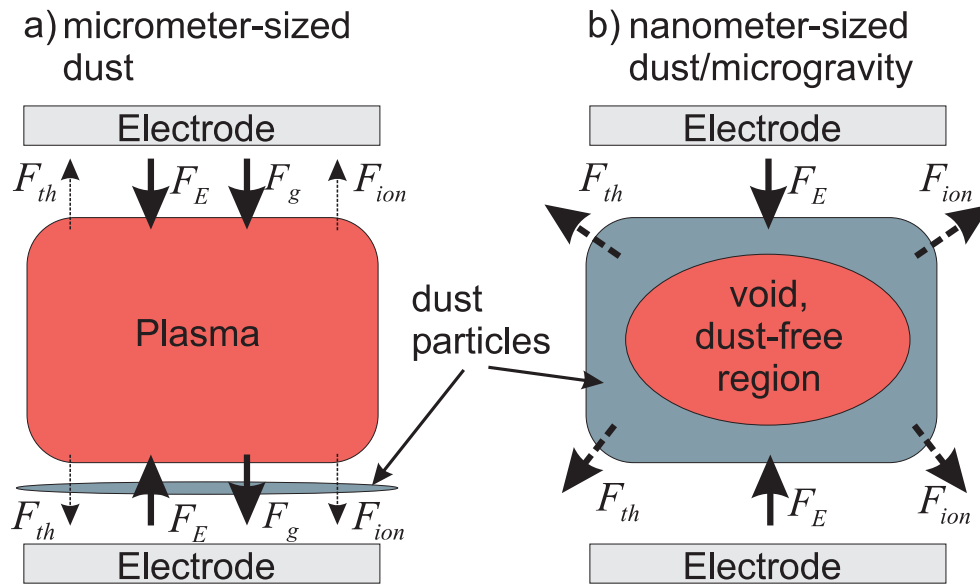


Figure 3.6: *Trapping and levitation of dust particles: a) large particles, gravity is dominant, b) small particles or microgravity conditions, gravity is unimportant*

Consequently, these relevant forces dominate the mechanism of particle trapping in plasma discharges. For large particles in the micrometer range where the dominant forces are gravity and electric field force a force balance is only obtained in the sheath of the lower electrode, where the upward electric field force is strong enough to balance the particles against gravity. Since the electric field in the sheath increases towards the electrode there typically is only a single position where electric field force and gravity balance. Thus, horizontally extended, but vertically restricted dust arrangements are possible (see Figs. 3.6a and 3.7a).

For smaller particles in the nanometer range or for large particles under microgravity conditions gravity is not important. Smaller electric fields are sufficient to levitate and trap the particles. Thus, particles can be trapped in the plasma bulk. There, the electric field force is pointing into the plasma bulk for negatively charged particles, whereas ion drag (and also the thermophoretic force) usually point outward. Thus, trapping of dust particles should be possible in the entire plasma volume and three-dimensional extended dust clouds should be formed (see Fig. 3.6b). However, it is found that for nanometer particles or under microgravity conditions large regions without dust particles, so-called “voids”, exist which are assumed to be due to the interaction of the ion drag and electric field force [39, 40, 41], see Fig. 3.7b,c). Recently, 3D spherical dust clouds have been formed in the laboratory by a combination of thermophoretic forces (to balance gravity) and a confinement by electric forces using dielectric materials (glass), see Sec. 8.4.

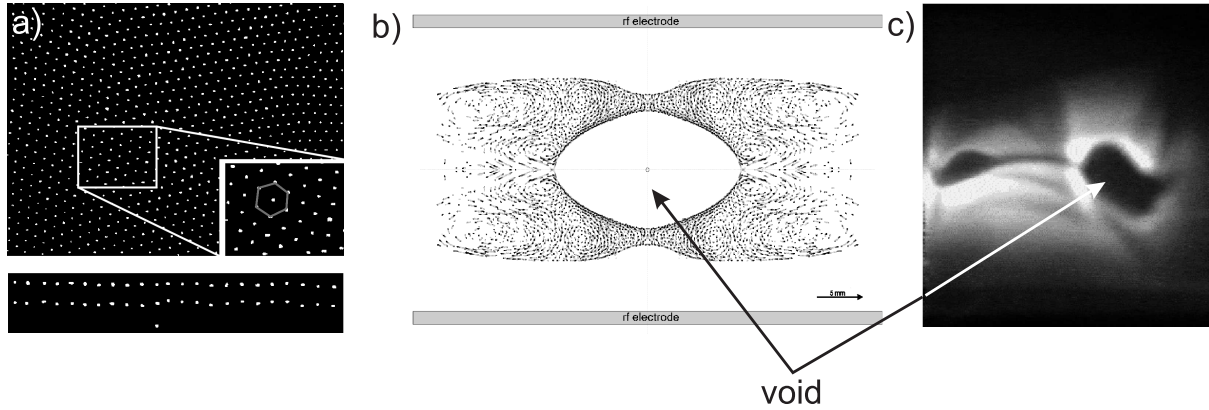


Figure 3.7: *a) Plasma crystal with two layers in the sheath of a gas discharge (top view and side view), (b) cross section through an extended 3D dust cloud of microspheres under microgravity conditions, and (c) dust clouds of nanometer-sized dust in a silane discharge (the dust appears as white clouds).*

3.8. Vertical Oscillations

We have seen that large, micron-sized particles are trapped in the plasma sheath due to a balance of electric force and gravity. However, the charging processes are often difficult to describe when all processes like the oscillating rf-sheath, ion-neutral collisions and all the various charging currents are taken into account. Here, vertical oscillations provide a useful and essential tool to measure the charge of the dust particles. Additionally, the oscillations allow to extract the electric environment of the plasma sheath.

In the sheath where the particles are trapped the electric fields are generally spatially dependent, i.e. $E = E(z)$. The electric field usually increases monotonously from the plasma-sheath boundary, where the electric field is small, towards the electrode where it is largest. The dust charge will also be spatially dependent due to the space-dependent densities and velocities of electrons and ions in the sheath. Typically, a unique equilibrium position z_0 exists where the particles are trapped (see Fig. 3.8c), i.e.

$$Q(z_0)E(z_0) = m_d g \quad . \quad (3.19)$$

The equation of motion for a particle in the vertical direction (relative to the equilibrium position) is then given by

$$\ddot{z} + \beta \dot{z} + \frac{Q(z)E(z)}{m_d} = F_{\text{ext}} \quad , \quad (3.20)$$

where β is the friction coefficient describing the neutral gas drag [Eq. (3.14)] and F_{ext} are other external forces applied to the particle. To solve this equation of motion, one has to

consider that the dust charge generally depends on the plasma conditions and therefore is itself a dynamic variable. In the following, we will investigate vertical oscillations of dust particles in the sheath for various situations.

3.8.1. Linear Resonance and Charge Measurement

In the most simple picture, vertical resonances can be treated in the following way: For small deviations from the equilibrium position the particle charge can be assumed to be spatially constant $Q(z) = Q_0$ and the electric field as linearly increasing $E(z) = E_0 + E_1(z - z_0)$. Here,

$$E_1 \equiv \frac{\partial E}{\partial z} = \frac{e}{\epsilon_0} (n_i - n_e)$$

is the slope of the electric field (neglecting any horizontal variations). When the charge density difference $n_i - n_e$ is constant (the so-called “matrix” sheath model) the slope of the electric field is constant. (see Fig. 3.8c). Such a linear electric field model is supported by a number of simulations of rf discharges [42] and theoretical analysis [43]. Under these assumptions the equation of motion reads

$$\ddot{z} + \beta \dot{z} + \frac{Q_0 E_1}{m_d} z = F_{\text{ext}} \quad .$$

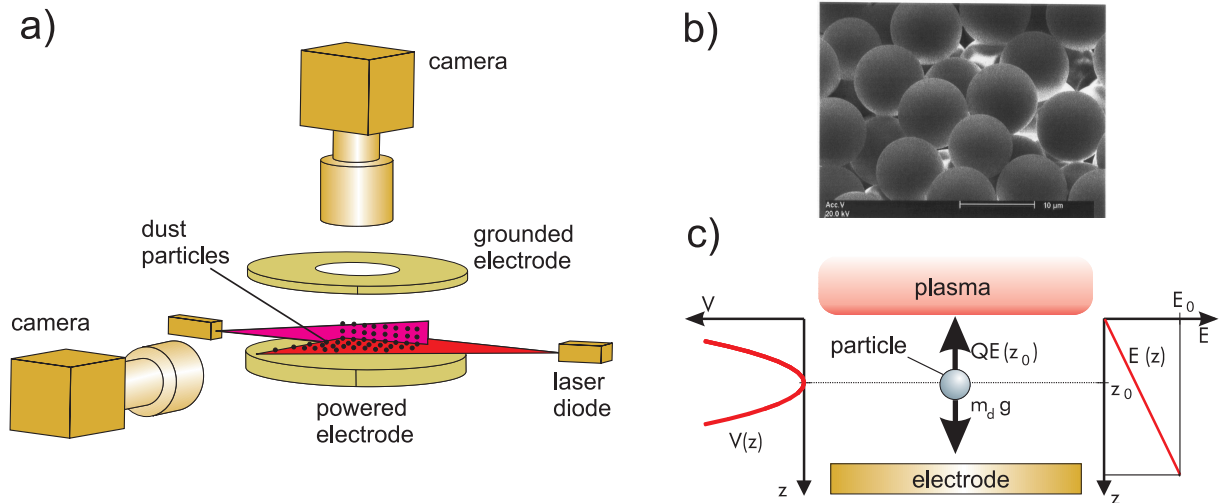


Figure 3.8: a) Scheme of the experimental setup in a typical experiment on complex plasmas. The particles are illuminated by vertical and horizontal laser sheets. The particle motion is recorded from top and from the side with video cameras. b) Electron micrograph of the MF particles typically used in the experiments. c) Trapping of the particles in the sheath of an rf discharge. See text for details.

This equation is just that of a damped harmonic oscillator where the microspheres are trapped in the harmonic potential well [44, 45]

$$\frac{1}{2}m_d\omega_{\text{res}}^2(z-z_0)^2 = \frac{1}{2}Q_0E_1(z-z_0)^2 \quad (3.21)$$

with the resonance frequency of

$$\omega_{\text{res}}^2 = \frac{Q_0}{m_d}E_1 \quad . \quad (3.22)$$

With external periodic excitation the resulting resonance curve is known from the damped oscillator as

$$A(\omega) = A_0 \frac{1}{\sqrt{(\omega_{\text{res}}^2 - \omega^2)^2 + \beta^2\omega^2}} \quad , \quad (3.23)$$

where $A_0/\omega_{\text{res}}^2$ ist the oscillation amplitude of the particle for $\omega \rightarrow 0$. The measurement of the vertical resonance of a trapped particle gives us a handle on the determination of the charge-to-mass ratio and allows to determine the particle charge Q_0 , if the mass of the particles is known [44, 45].

The assumption of a constant space charge density $e(\mathbf{n}_i - \mathbf{n}_e) = \epsilon_0 E_1$ models the linearly increasing electric field (with the slope E_1) in agreement with simulations of the rf sheath [42]. This allows the connection of the sheath electric field to the ion density measured by Langmuir probes in the bulk plasma. For a high voltage sheath the time averaged electron density $n_e = \alpha n_i$ is just the fraction α of the rf period where the particle “sees” a quasineutral environment due to the periodic rf oscillation of the plasma sheath, as discussed in Section 2.5.1.. For the condition of micron-sized particles in an rf sheath a rough estimate is $\alpha \approx 1/3$ [45]. This results in the following form of the resonance frequency used to analyze the experiments

$$\omega_{\text{res}}^2 = \frac{Qn_i(1-\alpha)e}{\epsilon_0 m_d} \quad . \quad (3.24)$$

The charge measurements have been performed using monodisperse MF (melamine formaldehyde) microspheres (see Fig. 3.8b), which are perfectly spherical and have a very low mass dispersion. Therefore, the particles have the same charge and are trapped at the same height in the sheath. A number of vertical resonance measurements have been made using these particles [45, 46]. The vertical oscillations were driven by applying a very low-frequent modulation of the electrode rf voltage, see Fig. 3.9a. In doing so, the sheath width is modulated and the particle is forced to oscillate vertically in the trapping potential well.

From a frequency scan, a resonance in oscillation amplitude was obtained near 20 Hz for dust particles of $2a = 9.47 \mu\text{m}$ diameter, see Fig. 3.9b. The measured data points are fitted with a resonance curve according to Eq. (3.23). From the fit the parameters A_0 ,

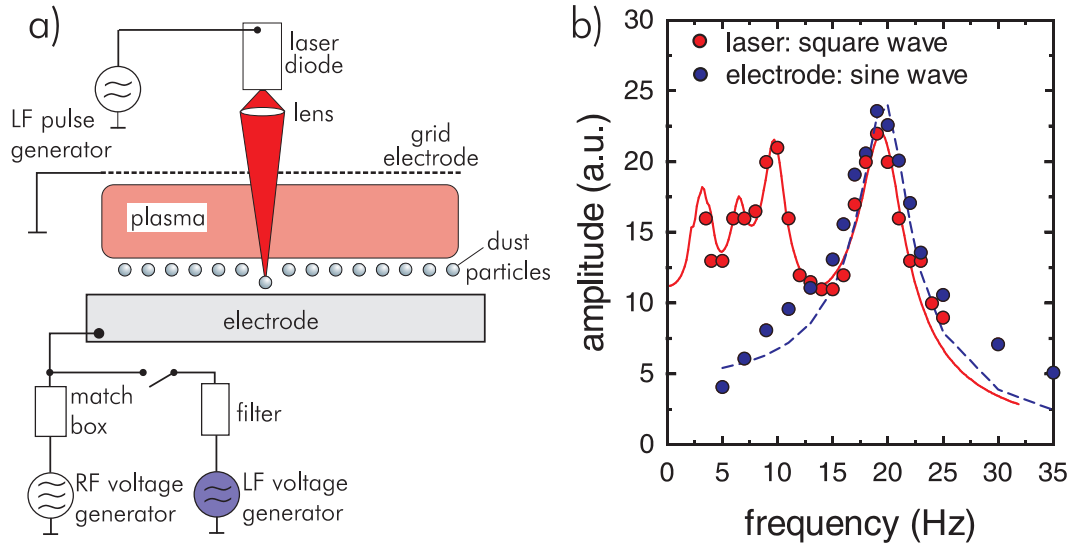


Figure 3.9: *Measuring the charge on MF microspheres. a) Experimental setup for excitation of resonances by rf voltage modulation and laser manipulation. b) Resonance curves obtained for a $9.47 \mu\text{m}$ MF particle for excitation by electrode voltage modulation and by laser pressure.*

the amplitude at very low frequencies, β and ω_{res} are obtained (Here: $A_0 = 5\omega_{\text{res}}^2$ a.u., $\beta = 26 \text{ s}^{-1}$ and $\omega_{\text{res}}/(2\pi) = 19.9 \text{ Hz}$). Applying this technique under different plasma conditions, from Eq. 3.22 the corresponding particle charges are found to be about 10 000 elementary charges and the floating potential is about 3 V (see Fig. 3.10). Estimations based on OML charging according to Eq. (2.16) result in charges that agree with the measured values within a factor of 2-3. It is seen that the dust charge slowly increases from about 6000 to 11000 elementary charges with decreasing pressure (120 to 40 Pa). This cannot be explained by pure OML charging, since the defining quantity, the electron temperature, is nearly constant ($T_e = 2.2 \text{ eV}$) in that pressure range. Rather, it is the charge reduction due to the ion-neutral collisions as described in Sec. 2.4.4.

The width of the measured vertical resonance peak is determined by the neutral gas drag on the particle and is in quantitative agreement with the Epstein [33] friction coefficient β in Eq. (3.20). For the above mentioned experiment (at a gas pressure of 70 Pa) the expected friction coefficient is calculated to be in the range between $\beta = 20 \text{ s}^{-1}$ and 29 s^{-1} , depending on the parameter δ , the measured value is $\beta = 26 \text{ s}^{-1}$.

An alternative, non-invasive technique to manipulate dust particles is by means of a focused laser beam as described in Sec. 3.6. in more detail. Here, one should note that the laser beam pushes the particle in the direction of the beam. By switching the laser “on” and “off” the vertical resonance curve of can be excited and measured (see Fig. 3.9). The resonance excited by the laser technique is nearly identical with the electrode manip-

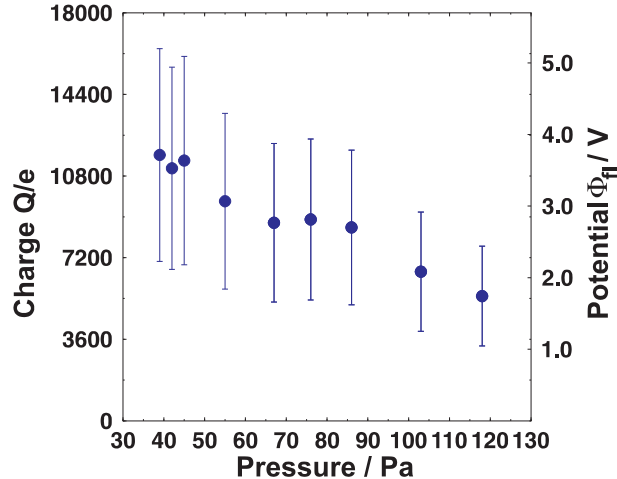


Figure 3.10: Measured dust charge as a function of discharge pressure. The uncertainty in the measured values is due to the uncertainty of the ion matrix sheath model, i.e. the uncertainty in the value α . From [46, 47].

ulation. With laser excitation additional spurious resonances at $\omega_{\text{res}}/2$, $\omega_{\text{res}}/3$ etc. are excited due to the square wave excitation (laser “on” and “off”) compared to the sinusoidal excitation at the electrode. Since the non-invasive laser technique and the electrode modulation give almost identical results it can be concluded that applying a small-amplitude potential modulation to the electrode does not lead to a severe disturbance of the plasma sheath environment.

Recently, the sensitivity of the vertical resonance method has been considerably improved by taking into account the phase relation between the exciting force F_{ext} and the particle oscillations [48].

Other Charge Measurements

Other in-situ charge measurements make use of the particle-particle interaction by the analysis of wave propagation or particle-particle collisions. These methods require a simultaneous measurement of the shielding length which also defines the interaction strength. The methods and their results will be presented in Sec. 5.1., but it should already be mentioned here that the charges obtained from particle-particle interaction are very similar to those of the resonance method.

In ex-situ charge measurements particles are dropped through a discharge into a Faraday cup where their charge is measured. In such experiments the influence of different charging mechanisms like electron beams or UV radiation was investigated, see Fig. 3.11. Indeed, with increased UV radiation positive dust is observed.



Figure 3.11: (right) Scheme of the experimental setup. The particles fall from the dropper into the Faraday cup, where the dust charge is measured. When the particles are irradiated by a strong UV source (left) the particles will charge positively. With a photoemitting cathode present, the particles are charged negatively due to the electrons released by this cathode (middle). From [49].

3.8.2. Parametric Resonances

The next type of vertical oscillations is given by parametric resonances. Parametric resonances occur when the confining potential is periodically modulated. A paradigm for parametric resonances is the children's swing.

Parametric resonances in dusty plasmas can be excited by placing a wire in the plasma sheath close to the dust particles. When applying sinusoidal electric potentials to the wire vertical oscillations are driven. The resulting resonance curve is shown in Fig. 3.12. It is seen that for small excitation voltages a single vertical resonance at ω_{res} as in the linear case is driven. At higher amplitudes, however, a second resonance at $2\omega_{\text{res}}$ suddenly appears. This second resonance is a clear indication of parametric resonance. Thus, driving the particles at double frequency also leads to large vertical particle oscillations [50].

Parametric resonances occur when the strength of the external confinement is modulated periodically. The equation of motion then reads

$$\ddot{z} + \beta\dot{z} + \omega_{\text{res}}^2 (1 + h \cos \omega t) = 0 \quad , \quad (3.25)$$

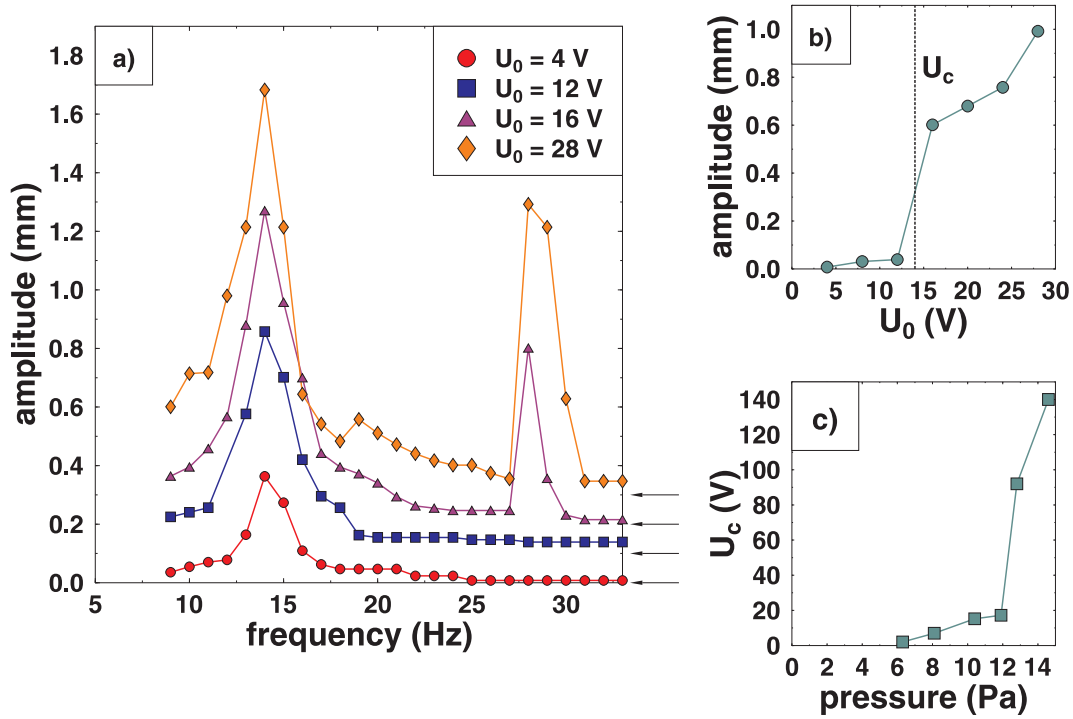


Figure 3.12: *Parametric excitation of the vertical resonance. (a) Resonance curves with the appearance of the second resonance at higher excitation voltages. (b) Amplitude of the second resonance versus excitation voltage and (c) critical excitation voltage as a function of gas pressure.*

where h is the modulation depth. That means that the strength of the confinement and thus the resonance frequency ω_{res} changes periodically with a frequency ω that generally is different from ω_{res} . In our case, the resonance frequency ω_{res} is due to the confinement of the particle in the sheath by gravity and electric field force as discussed above. The modulation at ω is due to the electrostatic potential on the wire.

This equation is known as Mathieu's equation in mechanics. It is known, that parametric resonances occur when the modulation frequency ω is close to ω_{res} or $2\omega_{\text{res}}$. When friction is present (i.e. $\beta > 0$) the second resonance occurs only when the modulation depth exceeds a threshold value. This is also seen in Fig. 3.12 where a certain excitation amplitude is needed to excite the second resonance. This excitation threshold also increases with increasing discharge pressure, i.e. gas friction. Such a behavior is expected from a parametric oscillator.

Following that reasoning, the occurrence of parametric resonances means that the external confinement is modulated and disturbed by applying an electrostatic potential to the wire, a situation that is not observed by modulation of the rf voltage. Thus, wire

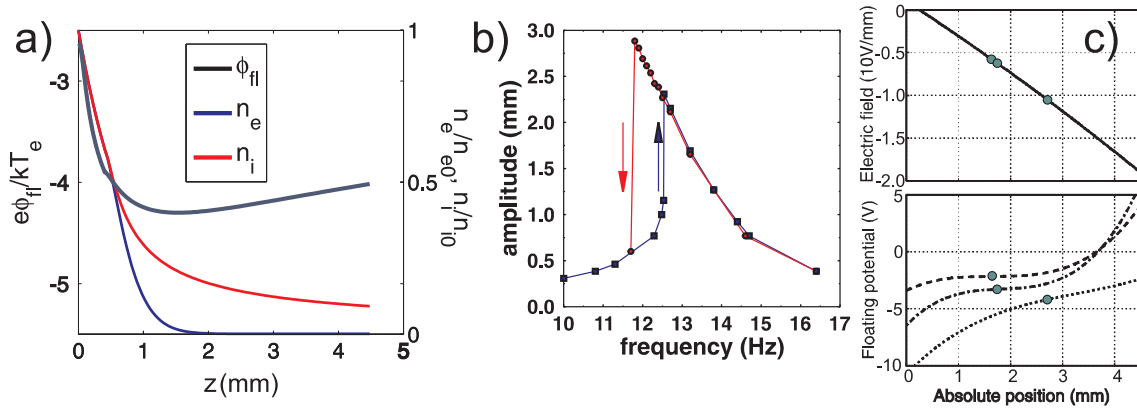


Figure 3.13: a) Calculated particle potential in the sheath using the OML model and a standard sheath model for the electron and ion densities and velocities, b) Nonlinear resonance curve for a $9.47 \mu\text{m}$ particle. Note the hysteresis in the resonance for increasing and decreasing frequency. c) Linear electric field and position dependent particle potential profiles that will lead to the observed nonlinear resonance for three different particle sizes. From [51].

excitation has to be used with great care in dusty plasma experiments.

3.8.3. Nonlinear Resonances

Now, we like to turn to nonlinear vertical particle oscillations. As outlined in Eq. (3.20) a position-dependent charge and/or higher than linear terms in the electric field mean nonlinear modifications to the harmonic potential well. Obviously a non-harmonic potential well leads to nonlinear resonances. The electric field is only linear when the difference in charge densities of electrons and ions is constant (matrix sheath). If that does not hold the electric field will vary in a nonlinear way.

The dust charge in the sheath can be position-dependent due to two counteracting effects, see Fig. 3.13a). As an illustration, the charge is calculated using the OML model with streaming ions according to Eq. 2.10 together with a simple dc model of a space charge sheath to account for varying electron and ion densities and velocities. In the presheath the ions are accelerated to Bohm velocity. At the sheath edge ($z \approx 0.5$ mm) the ion velocity further increases by acceleration in the sheath electric field. This leads to a less efficient decharging of the dust grains by the ions and thus a higher (negative) potential, i.e. charge, on the particle. On the contrary, deep in the sheath the electron density is considerably reduced leading to smaller electron current and, hence, less negative dust particles, see also Fig. 2.3.

To analyse nonlinear oscillations, we assume that $Q(z)$ and $E(z)$ can be expanded in

polynomials according to

$$\begin{aligned} E(z) &= E_0 + E_1z + E_2z^2 + E_3z^3 \dots \\ Q(z) &= Q_0 + Q_1z + Q_2z^2 + Q_3z^3 \dots \end{aligned} \quad (3.26)$$

Then, the equation of motion becomes nonlinear (up to 3rd order is considered, here, corresponding to a potential well of 4th order) with

$$\ddot{z} + \beta\dot{z} + C_1z + C_2z^2 + C_3z^3 = F_{\text{ext}} \quad . \quad (3.27)$$

The coefficients of nonlinearity are given by

$$\begin{aligned} C_1 &= \frac{1}{m} (Q_0E_1 + Q_1E_0) \\ C_2 &= \frac{1}{m} (Q_0E_2 + Q_1E_1 + Q_2E_0) \\ C_3 &= \frac{1}{m} (Q_0E_3 + Q_1E_2 + Q_2E_1 + Q_3E_0) \end{aligned} \quad (3.28)$$

The particle potential can then be written as

$$V(z) = \frac{1}{2}mC_1z^2 + \frac{1}{3}mC_2z^3 + \frac{1}{4}mC_3z^4 \dots \quad (3.29)$$

Here, C_1 corresponds to the (modified) linear resonance frequency, compare Eq. (3.21), C_2 to an up/down asymmetry of the vertical potential well and C_3 to a weakening/strengthening of the potential well with larger oscillation amplitudes. Nonlinear resonance curves have been excited in experiments at quite low gas pressure and high excitation amplitudes. In experiments of Ivlev et al. [52] the nonlinear oscillations were driven by applying a voltage to a wire placed below the dust particle. In contrast, Zafiu et al. [51] used the rf voltage modulation at the electrode.

The measured resonance curve shows distinct features of nonlinearity, see Fig. 3.13b. First, the resonance curve is not smooth. At certain excitation frequencies there is a jump in the oscillation amplitude from small to large values. Second, the resonance curve is bent towards lower frequencies and, third, there is a pronounced hysteresis in the resonance curve when going from smaller to larger frequencies or the opposite way.

The main resonance frequency is about 13 Hz, here, which corresponds to that of the linear resonance under these discharge conditions. The bending of the resonance towards lower frequencies is a clear indication that the potential well gets weaker with increasing amplitude, i.e. $C_3 < 0$. (For $C_3 > 0$ a bending towards higher frequencies would be expected.) This is easily seen from the following reasoning: Near the resonance the particle has a large oscillation amplitude and “feels” also the nonlinearity C_3 . When the potential gets weaker with increasing amplitude, the particle feels weaker restoring forces and the resonance frequency is then shifted towards lower frequencies. At lowered



Figure 3.14: *Self-excited vertical oscillations due to a position dependent charge and delayed charging.*

frequencies then again higher oscillation amplitudes can be sustained that further decrease the resonance frequency. In this way, a bending towards lower frequencies is observed.

By comparing the measured resonance curve with calculated resonances using the equation of motion (3.27) the coefficients of nonlinearity can be determined. These coefficients can then be related to position dependent dust charges or electric field profiles that may range from linear via parabolic to cubic. When using different particle sizes different regions of the sheath can be probed resulting in a more or less consistent set of parameters Q_i and E_i . Zafiu et al. found best agreement among experiments with different particle sizes for a linearly increasing electric field and a position dependent dust charge see Fig. 3.13c. As mentioned above, the position dependent dust charge is due to the increased ion stream and the reduced electron density in the sheath. Position-dependent dust charges have been reported recently in experiments using hypergravity conditions [53].

The idea of a time and space dependent charge is supported by the observation of self-excited vertical oscillations, see Fig. 3.14. There vertical particle oscillations have been observed that grow in time without external drivers [54]. The growth time is of the order of 10 s. The oscillations reach a large amplitude until the particles drop from the discharge. Such oscillations are only possible if a source of energy is provided that can overcome the energy loss by friction with the neutral gas. A possible energy gain mechanism can lie in the combination of a position-dependent dust charge and finite charging times. When during the oscillation the dust particle has an instantaneous charge $Q_t(z)$ which is different from the equilibrium charge $Q_{eq}(z)$ the restoring force $F = Q_t(z)E(z)$ and thus the restoring energy $\int F ds$ is different from the equilibrium situation. The difference is

illustrated by the shaded area in Fig. 3.14. Careful analysis [52] of this delayed charging has shown that indeed such a mechanism could overcome the energy loss by gas friction at low gas pressures. These self-excited oscillations and the nonlinear resonances clearly identify the dust charge as a dynamical variable.

4. Coulomb Crystallization

After identifying the basic mechanisms of charging and trapping of dust particles in a discharge, we now like to investigate the many-particle interaction of the dust in view of crystallization of the dust ensemble.

4.1. The One-Component Plasma (OCP)

At first, we like to investigate how systems of many charged particles behave under their mutual influence. The simplest situation that can be considered is that of point charges immersed in a homogeneous neutralizing background. As early as in the 1930s, Eugene Wigner [55] has discussed the situation of ions in a “sea” of electrons to study the crystalline order in metals. In dusty plasmas, we obviously identify the point charges with the dust particles and the neutralizing background with the plasma ions. In such a system with a homogeneous background the point charges interact by pure Coulomb repulsion. The background is only necessary to ensure overall charge neutrality.

Such a system of pure point charges is described by only a single parameter, the Coulomb coupling parameter

$$\Gamma = \frac{Q^2}{4\pi\epsilon_0 b_{\text{WS}} kT} \quad (4.1)$$

that describes the electrostatic interaction of neighboring dust particles in terms of their thermal energy. Here, T is the temperature of the point charges and Q is their charge. As a measure of the interparticle distance the Wigner-Seitz radius $b_{\text{WS}} = (3/4\pi n)^{1/3}$ is defined (n is the density of the point charges). For example, in a simple cubic structure with particle separation b the Wigner-Seitz radius is $b_{\text{WS}} = 0.62 b$.

A charged particle system is said to be strongly coupled when $\Gamma > 1$, i.e. when the electrostatic energy of neighboring particles exceeds the thermal energy. For a usual electron-ion plasma Γ is much smaller than unity, e.g. one finds $\Gamma = 8 \cdot 10^{-3} \ll 1$ for ions at $T_i = 0.03$ eV and $n_i = 1 \cdot 10^9$ cm⁻³ and even less for electrons due to their (typically) higher temperature.

From simulations of charged-particle systems it was found that the point charges arrange in ordered crystalline arrangements when the coupling parameter exceeds a critical value of $\Gamma_c = 168 \pm 2$ [56]. For $\Gamma < \Gamma_c$ the particles are in a fluid (= liquid or gas-like) state. Note, that a purely repulsive system has only a solid-fluid transition, there is no liquid-gas transition. A liquid-gas transition requires an attractive part in the interaction potential.

So, if the Coulomb energy by far dominates the thermal agitation the particles are forced to crystallize, a process known as Wigner or Coulomb crystallization. In 3D, the

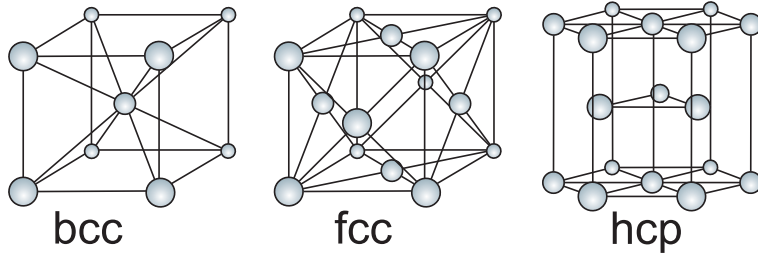


Figure 4.1: *Crystal structures in 3D (a) bcc, (b) fcc and (c) hcp*

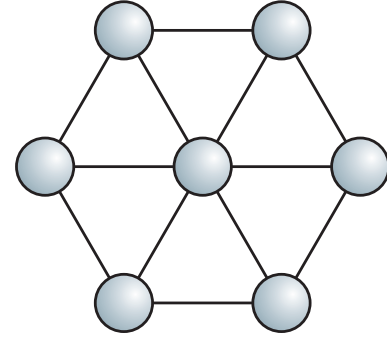


Figure 4.2: *Crystal structure in 2D: hexagonal structure*

particles arrange in a **bcc** lattice (see Fig. 4.1) which is the minimum energy configuration for pure Coulomb interaction.

The minimum energy configuration is determined from the sum of the electrostatic energies between all particles, the so-called Madelung energy,

$$u = \frac{1}{2N} \sum_{i \neq j}^N \frac{Q^2}{4\pi\epsilon_0 r_{ij}} \quad , \quad (4.2)$$

where r_{ij} is the relative distance between particle i and j . From detailed calculations the Madelung energy is found for pure Coulomb interaction as

$$\begin{aligned} u_{\text{bcc}} &= -0.895\,929\,255\,682 \quad \text{for the } \text{bcc} \text{ structure} \\ u_{\text{fcc}} &= -0.895\,873\,615\,195 \quad \text{for the } \text{fcc} \text{ structure} \\ u_{\text{hcp}} &= -0.895\,838\,120\,459 \quad \text{for the } \text{hcp} \text{ structure} \end{aligned}$$

in units of $\Gamma = Q^2/(4\pi\epsilon_0 b_{\text{WS}})$. The energies for the different lattice types are very close to each other, but the **bcc** structure is the one with the lowest energy (see Fig. 4.1 for the different lattice types).

In 2D systems crystallization takes place at the critical value $\Gamma_c = 125$ [56]. In 2D, the Wigner-Seitz radius is analogously defined as $b_{\text{WS}} = (\pi n)^{-1/2}$. The minimum energy configuration is the hexagonal structure as shown in Fig. 4.2. This is the structure you would expect from densely covering a table with coins.

4.2. Yukawa Systems

When shielding by the ambient plasma electrons and ions is taken into account the interaction potential between the point charges is usually described by the Debye-Hückel

potential (also named Yukawa potential, especially in the field of complex fluids)

$$\phi(r) = \frac{Q}{4\pi\epsilon_0 r} \exp\left(-\frac{r}{\lambda_D}\right) \quad , \quad (4.3)$$

where λ_D is the Debye shielding length

$$\lambda_D = \left(\frac{1}{\lambda_{D,e}^2} + \frac{1}{\lambda_{D,i}^2} \right)^{-1/2} \quad \text{with} \quad \lambda_{D,e,i} = \sqrt{\frac{\epsilon_0 k T_{e,i}}{n_{e,i} e^2}} \quad . \quad (4.4)$$

Besides the Coulomb coupling parameter Yukawa systems are characterized by a second parameter, the so-called screening strength, $\kappa = b_{WS}/\lambda_D$ which is the Wigner-Seitz distance b_{WS} in units of the Debye length. The OCP-limit is obtained again for infinite screening length, i.e. for $\kappa \rightarrow 0$.

The phase diagram of the Yukawa system is shown in Fig. 4.3. First, it is seen that the critical value for the solid-fluid transition strongly depends on the screening strength, i.e. $\Gamma_c = \Gamma_c(\kappa)$. The melting line increases almost exponentially with κ . Due to the exponential shielding a much higher Coulomb coupling parameter is required to enter the crystalline regime. For $\kappa = 0$ the OCP value of $\Gamma_c = 168$ is retrieved [58, 57].

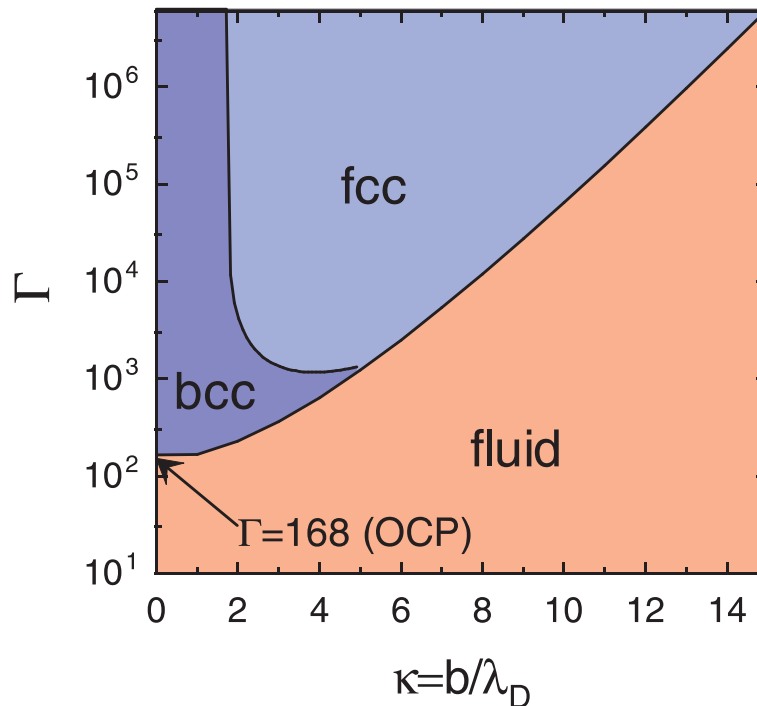


Figure 4.3: Phase diagram of the Yukawa system in the Γ - κ plane. The melting line increases almost exponentially with the screening strength. In the solid phase two different crystal structures, bcc and fcc are found. After [57].

The solid phase itself shows two different crystalline structures: for lower values of κ the bcc structure as in the OCP is found. For stronger screening the fcc structure is obtained. For increasing screening strength the Yukawa interaction becomes more and more like a hard-sphere potential. The packing density for spheres in the bcc structure is 68 % whereas it reaches 74 % in the fcc structure (the fcc structure is what one would obtain from stacking oranges into several layers). Thus at higher screening an increased packing density becomes more favorable.

4.3. Coulomb Crystallization in Dusty Plasmas

After the general introduction to strongly coupled systems we now investigate under which conditions Coulomb crystallization in dusty plasmas will be possible. The following ideas have already been presented in 1986 by Ikezi [59], years before plasma crystals have been discovered experimentally. Ikezi's model uses a few simplified assumptions which however capture the main features of the problem. First, the melting line of Yukawa systems is approximated by an effective Coulomb coupling parameter

$$\Gamma_{c,\text{eff}} = \frac{Z_d^2 e^2}{4\pi\epsilon_0 b_{\text{WS}} kT_d} \exp\left(-\frac{b_{\text{WS}}}{\lambda_D}\right) = \Gamma \exp(-\kappa) = 168 \quad ,$$

where it is assumed that the melting line exactly increases exponentially with increasing κ (Sometimes, the above definition is used as the coupling parameter, but usually Γ and κ are treated separately). Above $\Gamma_{c,\text{eff}} = 168$ crystallization is achieved in Ikezi's model. Since $\lambda_D \approx \lambda_{D,i}$ from Eq. (4.4) only ion screening is considered. The second assumption is concerned with the charging of the dust. For the dust charging the rule-of-thumb expression according to Eq. (2.18) is used. The dust charge, however, is limited when all electrons are bound to the dust (electron depletion), i.e.

$$Z_{d,\text{lim}} = e \frac{n_i}{n_d} \quad .$$

Now, under which parameters of ion and dust density, Wigner crystallization in dusty plasmas can occur? The ion density affects the screening length λ_D and the dust charge limit. High ion density means high dust charge limit, but strong screening. The dust density also affects the dust charge limit and the interparticle distance b . High dust densities mean low maximum dust charge, but small interparticle distance which results in high coupling. Both parameters thus have counteracting effects. From these considerations, Wigner crystallization should be possible in the dark area ABC in Fig. 4.4. The boundary of this region is dominated by different mechanisms. From A to B, the dust density is nearly constant. Also the charge Z_d is constant, there are no depletion effects due to the low dust density. On the entire upper boundary from A to C via B the particle is charged to its single particle value (here $\alpha = 10 \mu\text{m}$ is assumed). From A to B, the Debye length is much larger than the interparticle distance and screening effects are not important.

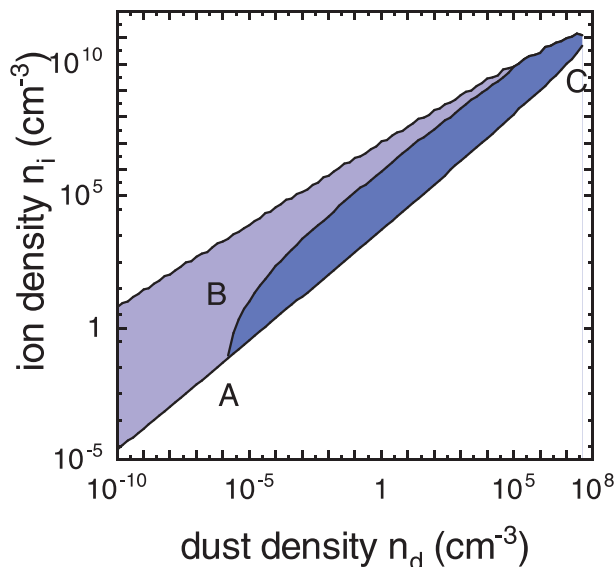


Figure 4.4: *Existence diagram of Wigner crystals in dusty plasmas. In the dark area Coulomb crystallization should be possible for a particle of $10\ \mu\text{m}$ radius. In the total shaded area crystallization can occur for arbitrarily sized particles. Note the wide logarithmic scale on both axes. After [59].*

Near B the situation changes. The ion density becomes so high that the Debye length is now of the order of the interparticle distance and screening becomes dominant. Thus the boundary bends towards much higher dust densities and thus smaller interparticle distances until point C is reached. On the boundary from C to A there are relatively large dust densities and low ion densities. Here, depletion effects become dominant. The charge on the dust is determined by the available free electrons thus limiting the coupling parameter.

Although this is a quite crude model it shows that Coulomb crystallization in dusty plasmas is possible in a range of ion and dust densities that is several orders of magnitude wide. For typical plasma discharges with $n_i = 10^9$ to $10^{10}\ \text{cm}^{-3}$ plasma crystals should exist for dust densities in the range from $n_d = 10^3$ to $10^5\ \text{cm}^{-3}$.

4.4. Crystallization in Bounded Systems

In the previous sections, the formation of Wigner crystals in extended 3D (and 2D) systems has been discussed. However, as we have seen, the plasma crystals in the experiments (see Fig. 3.7) are extended in the horizontal plane, but are confined in the plasma sheath by quite strong vertical fields. Similar confined systems are also found in ion trap experiments.

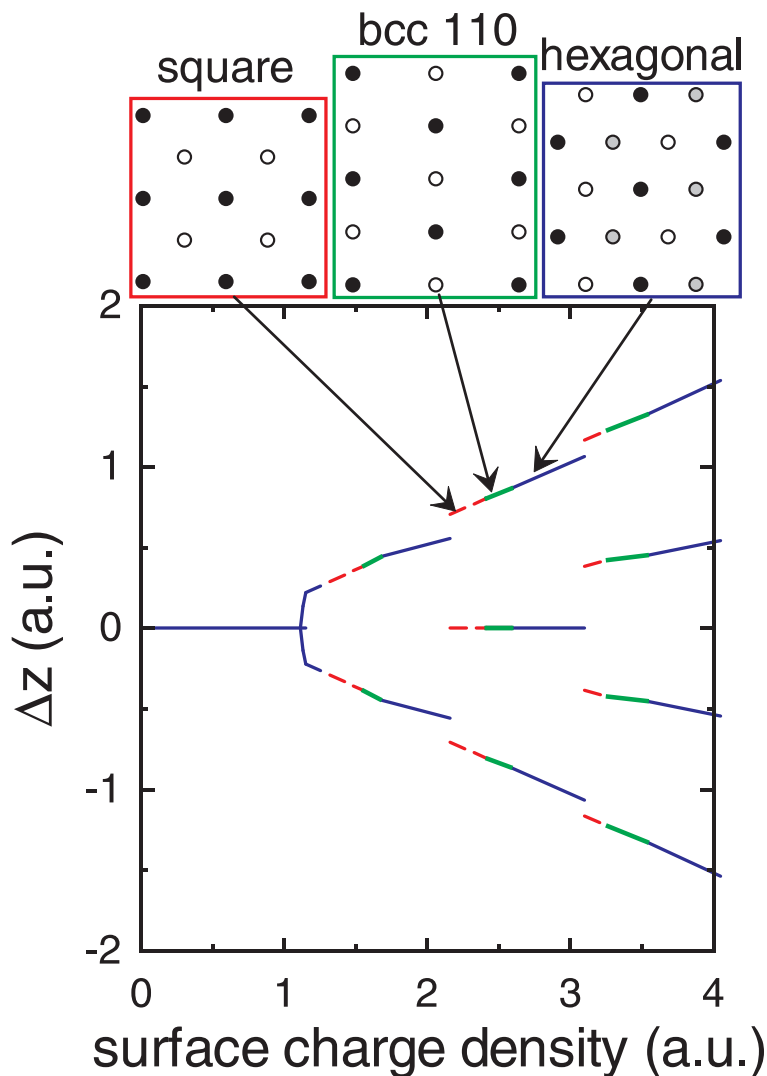


Figure 4.5: *Layer formation and crystalline structure in a confined system: Vertical position of the individual crystal layers. The respective crystal structure is indicated by the three inserts at the top, where the structure is viewed from top. Different shades of the circles denote different layers. After [60].*

The situation of confined OCP systems has to capture features of both 2D and 3D systems with competing planar hexagonal or volume bcc/fcc structures. To study possible crystal structures in bounded systems let us consider a system of point charges which is extended in the horizontal $x - y$ plane, but is confined by a parabolic potential in the vertical z -direction [60]. When the number of point charges is not too high the particles will arrange in a monolayer 2D crystal with hexagonal structure as discussed above. When

the density of charges is increased (or, equivalently, the vertical confinement is weakened) the monolayer system jumps to two layers, three layers and so on. This is an expected behavior of repulsive particles. It is interesting to note here that the crystal structure of the multi-layer system changes between square, bcc 110 and hexagonal (see Fig. 4.5). Thus the possible crystal structures of the infinite 3D systems are also found in a system with only a few layers.

The scenario is not much different if screening between the charges is taken into account [61, 62]. There, similar jumps to multi-layer systems with similar crystal structures are observed. However, the exact transition points, of course, depend on the screening strength.

Structures of systems confined in all spatial dimensions are described in Chapter 8.

4.5. Structural Information

To characterize the degree of order of the point charges and to define a system as fluid or solid it is necessary to have quantitative measures. Here, such techniques are presented with special emphasis on 2D systems, but they can be easily extended to 3D systems.

4.5.1. Wigner-Seitz Cells

One of the basic techniques to characterize a system of point charges is given by the Wigner-Seitz cell analysis. There, the 2D plane is covered with polygons where each particle is in the center of its own cell. The construction is as follows: for each particle the perpendicular bisector of the connection to neighboring particles is determined. The bisectors define a closed polygon around the particle of interest (see Fig. 4.6a). The main advantage of this procedure is that it determines which particles in the vicinity of the reference particle are the neighboring particles. Thus, the number of nearest neighbors is also determined. For a 2D system, the *mean* number of neighbors is 6. However, particles with 5 or 7 neighbors might exist which are termed defects. The relative abundance of 6-fold polygons is already a good qualitative hint whether a structure is crystalline or not. A structure with more than 90 % of hexagons can be called crystalline (see Fig. 4.8).

4.5.2. Pair Correlation Function

The pair correlation function $g(r)$ is the probability to find a particle at a distance r from a chosen particle. This is then averaged over all (chosen) particles. One finds that

$$g(r) \rightarrow 1 \quad \text{for } r \rightarrow \infty \quad ,$$

since one will always find a particle at large distances, and

$$g(r) \rightarrow 0 \quad \text{for } r \rightarrow 0 \quad ,$$

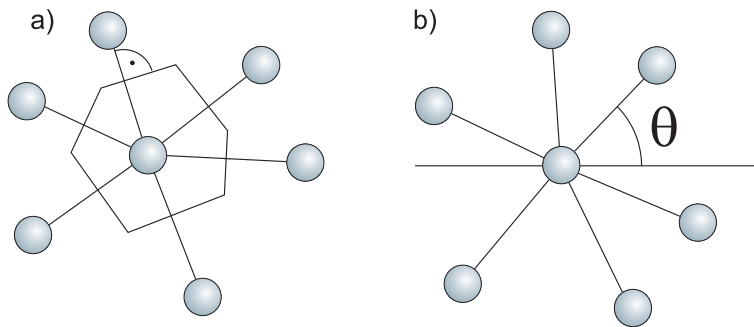


Figure 4.6: a) Sketch of the Wigner-Seitz cell construction. b) Definition of the angle θ

since the particles cannot come infinitely close to each other.

The pair correlation function gives the mean interparticle distance as well as the near and far order of the particle system. An example is shown in Fig. 4.7 for simulated OCP systems at different coupling strengths. The first peak in $g(r)$ is due to the neighboring particles, further peaks due to overnext neighbors and so on. For a hexagonal structure you would expect a peak at the interparticle distance b , the next peaks would be at $\sqrt{3}b$ and $2b$.

The more pronounced the peaks are and the more peaks can be identified the higher is the order of the system which also can be seen from Fig. 4.7. For small values of the coupling parameter ($\Gamma \approx 10$) there is only a very small hump at the nearest neighbor distance and the pair correlation function is nearly flat. This means that there is no strong order in the system and one can find particles at all distances larger than the

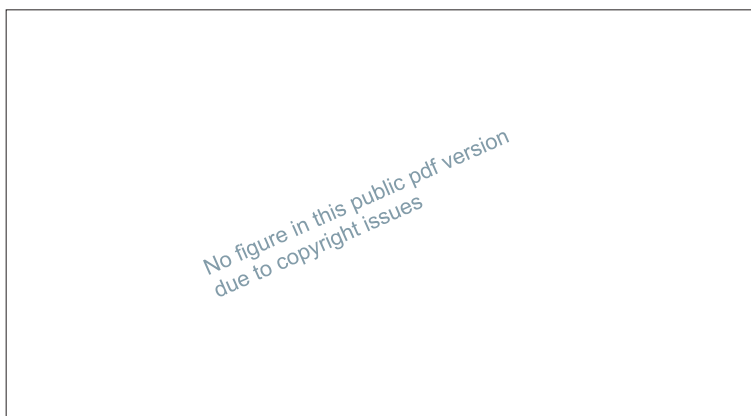


Figure 4.7: Pair correlation function $g(r)$ for various coupling parameters Γ of the OCP system. The nearest neighbor distance is found to be at $r \approx 1.7b_{ws}$. From [56].

interparticle distance. When Γ is increased the nearest neighbor peak grows and also the peaks of overnext neighbors (and so on) grow, indicating increased order of the system. This can also be easily seen in the comparison of solid, fluid and gas-like states in Fig. 4.8.

One might expect that at very high coupling parameters $\Gamma \gg \Gamma_c$ the particles should be at the exact lattice sites and the pair correlation function should collapse to single sharp δ -peaks. This is indeed true for 3D systems, but not for 2D. It was derived from very basic principles that there are always long-range fluctuations in 2D systems that destroy order over very long distances. The form of $g(\mathbf{r})$ can be analyzed more quantitatively which is of interest for the analysis of phase transitions in 2D systems, but that will not be explicated here.

4.5.3. Structure Factor

In condensed matter physics, the pair correlation function usually cannot be determined directly. Rather, the structure factor is determined from scattering of x-rays or neutrons. In dusty plasmas, we are able to measure the pair correlation function directly and to *calculate* the structure factor in order to compare with condensed matter experiments. The structure factor $S(\mathbf{q})$ is just the Fourier transform of the pair correlation function

$$S(\vec{q}) = 1 + n_d \int (g(\mathbf{r}) - 1) \exp(i\vec{q} \cdot \vec{r}) d\vec{r} \quad , \quad (4.5)$$

where \vec{q} is the wave vector of the scattered radiation. In 2D, this can be written as

$$S(q) = \frac{1}{N} \sum_{ij} \frac{1}{2\pi} \int_0^{2\pi} \exp(iqr_{ij} \cos \varphi) d\varphi = \frac{1}{N} \sum_{ij} J_0(qr_{ij}) \quad ,$$

where φ is the angle between \vec{r} and \vec{q} and J_0 is the zero-order Bessel function. The calculated structure factor is also shown in Fig. 4.8.

A large first peak in the structure factor means long-range periodicity of the pair correlation function. Thus, a peaked structure factor corresponds to long-range order.

4.5.4. Angular Correlation Function

Finally, the angular correlation will be discussed, here. Until now, only the translational order has been characterized. In contrast, the angular correlation function measures how the bond angles between nearest neighbors are oriented relative to each other as a function of distance between the bonds. The angular correlation is defined as

$$g_6(\mathbf{r}) = \langle \exp(6i[\theta(\mathbf{r}) - \theta(0)]) \rangle \quad , \quad (4.6)$$

where θ is the angle of a nearest neighbor bond relative to a fixed axis (see Fig. 4.6b). The factor 6 takes into account the presumed hexagonal order of the system and $\langle \cdot \rangle$

denotes the average over the particle arrangement. When $g_6(\mathbf{r})$ is close to 1 the nearest-neighbor bonds at a relative distance r are oriented along the same direction. The bond orientational order is destroyed by defects (particles with 5 or 7 neighbors). Behind defects the lattice orientation is different from the starting point. A value of g_6 close to 0 means that the bonds are randomly arranged (no correlation), a value of $g_6 = -1$ describes anti-correlation: the bonds have a relative orientation which differs by 30° which is the maximum difference in angle for a 6-fold symmetry. The angular correlation function of our model systems is also shown in Fig. 4.8. The angular correlation function also plays a large role in the identification of melting processes in 2D.

4.5.5. Example

The different techniques to characterize a particle arrangement is illustrated for three model systems (see Fig. 4.8) that reflect crystalline, fluid ($\Gamma > 1$) and gas-like ($\Gamma < 1$) order (it should be noted again, here, that for a system with only repulsive forces like OCP or Yukawa there is only a solid-fluid transition). In the solid state the pair correlation function is very pronounced. Pair correlation can be observed at least up to 7 interparticle distances. Correspondingly, the structure factor is large and sharp. The angular correlation function is large and decays only slowly with distance. In the fluid state, one can identify the nearest-neighbor and overnext-neighbor peak in $g(\mathbf{r})$. The structure factor thus is smaller and not that sharp. Also the angular correlation rapidly decreases. The gas-like state exhibits no correlation at all. The pair correlation is flat (compare Fig. 4.7 at $\Gamma = 10$), the structure factor is flat and there is no angular correlation, even for the smallest distances. This reflects the gas-like characteristics of this particle arrangement.

4.6. 3D Crystals

The previous discussions were related to some extent to 2D crystals (or crystals with a few layers) since they are easily produced in laboratory experiments. Nevertheless, three-dimensional dust crystals have been observed under microgravity conditions aboard the ISS [63] where the particles are not forced into the space charge sheath, but remain in trapped in the plasma volume. Figure 4.9 (a) shows the reconstruction of the 3D positions of about 10 000 particles forming an ordered arrangement. The order is illustrated by the pair correlation function in the inset indicating the strong peak of nearest neighbors and two subsequent peaks.

The identification of local order is much more difficult in 3D than in 2D due to the much more possibilities of particle arrangements. In this experiment, it was tried to identify the local crystal structure. For that purpose, for each particle of the crystal a local order parameter q_4 and q_6 was calculated that accounts for local 4- and 6-fold order using the

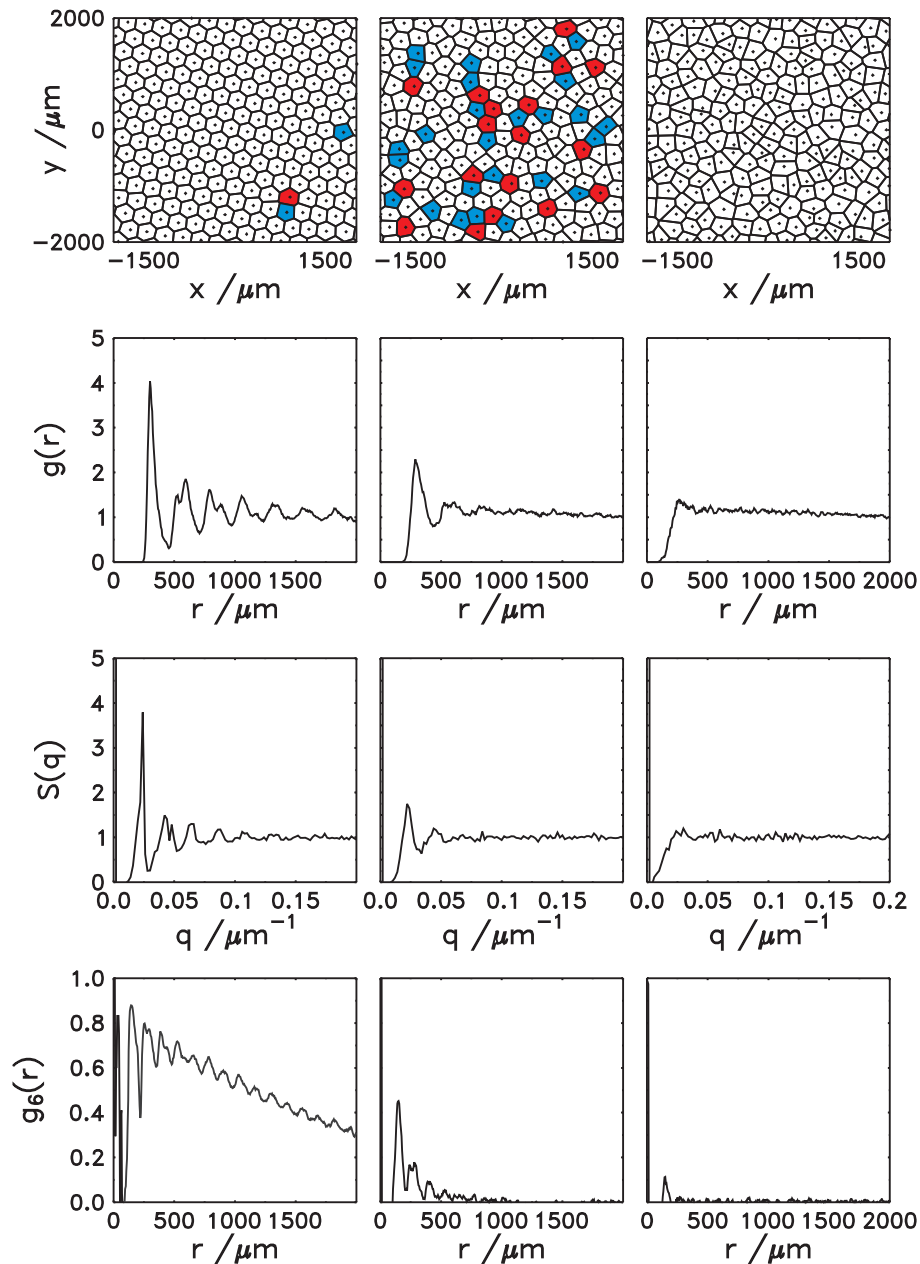


Figure 4.8: Structure of solid and fluid and gas-like structures, (a) Wigner-Seitz cell construction. For the solid and liquid state the defects are shaded (light grey: 5-fold defect, dark grey: 7-fold defect). (b) Pair correlation function $g(r)$, (c) structure factor $S(q)$ and (d) angular correlation function $g_6(r)$.



Figure 4.9: (a) 3D dust crystal under microgravity conditions aboard the ISS. The inset shows the pair correlation function before and after full crystallization (green and red curve, respectively). (b) Color-coded (from dark to light) is the number of particles with local order parameters q_4, q_6 indicating local 4- and 6-fold symmetry. From [63].

order properties of spherical harmonics [63]. The abundance of particles in the crystal with local order parameters q_4, q_6 is given in Fig. 4.9 (b) where also the order parameters of ideal hcp and fcc lattices (and also bcc which is not shown here) are indicated (compare also Fig. 4.1). It is seen that quite a substantial fraction of the particles are located close to the ideal hcp and fcc order parameters indicating high crystallinity (either as hcp or fcc lattice). However, also a certain fraction of the particles are randomly oriented showing that the particles are not fully crystallized.

In the plasma volume the forces acting on the particles are much smaller than in the sheath. Hence also the interparticle forces are usually much smaller since they have to compete with much smaller confining forces. Hence, such 3D crystals are usually much softer than those in the sheath (although those are already very soft). Hence, crystallization occurs on a very, very long time scale. Hence, formation (and observation) of 3D crystals is an interesting and difficult problem.

5. Dust Particle Interaction

In the previous chapters we have seen how a plasma crystal of microspheres trapped in the sheath of the discharge is formed. We have assumed that the interaction is described by a Coulomb or Debye-Hückel repulsion. Whether the interaction can really be described by such a shielded Coulomb potential will be discussed first for particles in the same horizontal layer. The vertical interaction will be discussed afterwards. We will learn that the interaction among dust particles trapped in the sheath of a discharge is dramatically different in the horizontal and in the vertical direction due to the dust particle environment.

5.1. Interaction in the Horizontal Plane

A close inspection of a 2D plasma crystal trapped in the sheath of a plasma discharge (see Fig. 3.7a) reveals very interesting details. In the horizontal plane, the particles arrange in a hexagonal structure (see inset), where each dust particle has six nearest neighbors. We have seen, that such a hexagonal structure is a minimum energy configuration in monolayer or few-layer systems for a repulsive Coulomb or Debye-Hückel interaction between the dust particles.

A direct experimental determination of the horizontal interaction potential V between microspheres has been achieved from central collisions of two particles by Konopka et al. [64]. For this purpose two microspheres ($2a = 8.9 \mu\text{m}$) are trapped in the sheath of an rf discharge. The horizontal confinement was due to a copper ring placed onto the electrode. The copper ring leads to an additional horizontal parabolic confinement (of strength ω_0) which was confirmed by the analysis of the motion of a single particle. One of the two microspheres was sitting at rest in the center of the confining potential, the other was pulled “uphill” by a positively biased probe wire and was subsequently released (see Fig. 5.1a).

The equation of motion for the two particles reads (using the relative coordinate x_r and the reduced mass $\mu = m_1 m_2 / (m_1 + m_2) = m_d / 2$)

$$\mu \ddot{x}_r + \mu \beta \dot{x}_r + \mu \omega_0^2 x_r = -\frac{\partial V(x_r)}{\partial x} \quad , \quad (5.1)$$

where V is the interaction potential to be determined. The integration of the equation of motion gives

$$V(x_r) = \frac{1}{4} m_d \dot{x}_r^2 + \frac{1}{4} m_d \omega_0^2 x_r^2 + \frac{1}{2} m_d \beta \int_0^t \dot{x}_r^2(\tau) d\tau \quad , \quad (5.2)$$

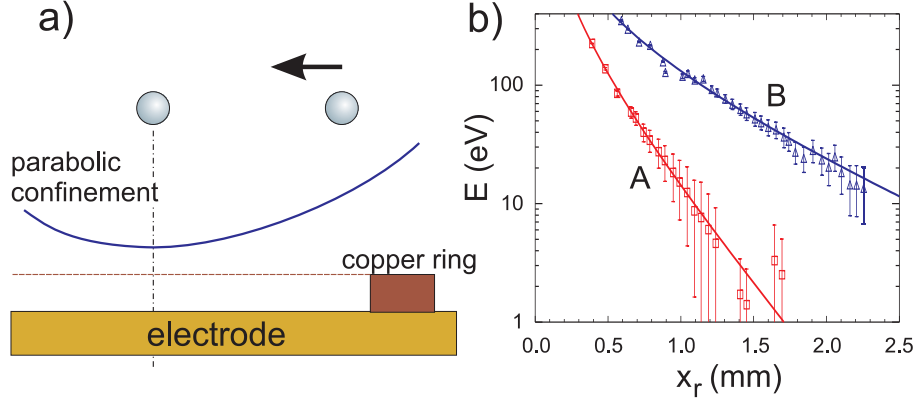


Figure 5.1: *Konopka's two-particle collision experiment: a) Scheme of the experimental arrangement, b) electrostatic interaction energy as a function of relative particle distance x_r . Symbols: experimental results, Lines: Best fits of a Debye-Hückel (Yukawa) potential. The two curves A and B correspond to different discharge conditions (see text). After [64].*

where the the first term is the kinetic energy of the two-particle system (using the reduced mass), the second describes the potential energy in the horizontal parabolic confinement and the third accounts for losses by friction with the neutral gas. The interparticle potential is measured from the relative particle positions and velocities which are easily determined from video data. This enables to reconstruct the interaction potential with good accuracy from the particle trajectories.

The experiments [64] show that the so obtained electrostatic energy directly reflects the interaction potential between the microspheres that can be described very accurately by a Debye-Hückel (Yukawa) type interaction

$$V(x_r) = Z_d e \phi(x_r) = \frac{Z_d^2 e^2}{4\pi\epsilon_0 x_r} \exp\left(-\frac{x_r}{\lambda_D}\right) \quad , \quad (5.3)$$

as shown in Fig. 5.1b, where a Debye-Hückel interaction was fitted to the experimental results. From the fit the following values of the charge and shielding length have been obtained: $Z_d = 13\,900$, $\lambda_D = 0.34$ mm (for case A at high discharge voltage $U_{pp} = 233$ V), $Z_d = 17\,100$, $\lambda_D = 0.78$ mm (case B, low voltage $U_{pp} = 64$ V). As expected the Debye length increases for lower plasma density (i.e., lower discharge voltage). The particle charges are in the range of the expected values from the charging theory and are comparable to the measurements using the resonance technique. The screening length is of the order of the electron Debye length in these discharges. This might be expected. However, that point has to be discussed in some more detail later.

The horizontal interaction can also be derived from wave experiments. The dispersion relation of waves contains the particle-particle interaction. Wave dispersion, and thus

particle interaction, will be discussed later in Chapters 6 and 7.

5.2. Vertical Interaction

When returning to the plasma crystal in Fig. 3.7, the side view reveals that the particles of different vertical layers are located directly atop of each other. They are vertically aligned. This unusual ordering is practically always observed for two or more vertical layers and has been recognized early after the discovery of the plasma crystal [65, 45]. The vertically aligned strings move as an entire chain in the crystal. This demonstrates that in the vertical direction additional attractive forces must be present. Possible sources and mechanisms for the formation of additional attractive forces will be described now.

Clearly, the observed vertical alignment of the microspheres certainly is not a minimum energy configuration for purely repulsive particle interactions. The fundamental reason for the difference between horizontal and vertical interactions lies in the fact that the main external forces on the microspheres – electric field force and gravity – act in the vertical direction. Due to gravity the microspheres are trapped in the non-neutral, non-equilibrium environment of the sheath which strongly influences the interaction between the microspheres.

For the very large and rod-like particles used in the experiment of Mohideen et al. [66] and Annaratone et al. [67] dipole moments on the particles might explain the observation of particle alignment along the electric field. However, these dipole effects are much too small to overcome the repulsion between the particles used in the experiments, here (see also Sec. 3.2.2.). Hence, other mechanisms have to be taken into account.

The ions in the sheath are the most obvious candidate as the source for the generation of attractive forces. Different mechanisms of ion-mediated attractive forces have been put forward in a number of theoretical models and simulations. Here, we will now discuss the formation of attractive forces from the viewpoints of a “wave” model and a “particle” model.

5.2.1. The wakefield potential (wave model)

In this class of models, the attraction is due to wakefield formation downstream the particles by a (supersonic $\mathcal{M} > 1$) ion flow [68]. Here, it is assumed that the dust particles excite ion-acoustic waves of all frequencies in the ion stream. The ion-acoustic waves superpose to form an attractive resonance below the dust particles where the ion density is increased with respect to the background level. In this approach the interaction between the ion flow and a single dust particle is described with the help of the dielectric function ϵ . Here, the ion flow velocity v_{i0} is assumed to be in the z direction with $\mathcal{M} = v_{i0}/v_B$ being the Mach number of the flow (v_B is the Bohm velocity). The electrostatic potential

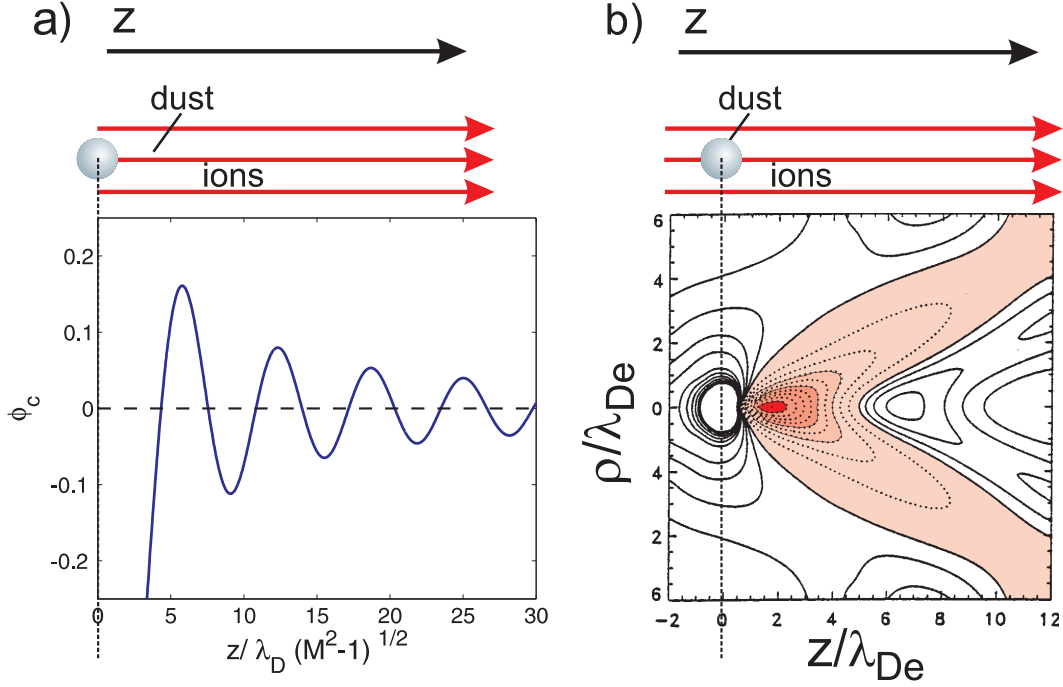


Figure 5.2: a) The ion wake potential in an ion flow. Downstream of the particle an oscillating potential is formed with alternating attractive ($\phi_c > 0$) and repulsive ($\phi_c < 0$) regions. After [68]. (b) Spatially resolved wakefield in the direction of the ion flow (z) and perpendicular to the flow (ρ). The potential contours are indicated (solid lines: negative potentials, dashed lines: positive potentials). The shaded area has a positive potential and is thus attractive for a second negative dust particle. Note the different axis scaling of z in panels (a) and (b).

around the dust particle is given from linear response theory in general terms by [69]

$$\phi(\vec{r}) = \int \frac{Z_d e}{8\pi^3 \epsilon_0 q^2} \frac{1}{\epsilon(\vec{q}, \omega - q_z v_{i0})} e^{i\vec{q}\cdot\vec{r}} d\vec{q} \quad , \quad (5.4)$$

where \vec{q} ($q = |\vec{q}|$) is the wave vector of the excited ion acoustic waves and $\epsilon(\vec{q}, \omega)$ is the dielectric response of the plasma. Eq. (5.4) is just the Fourier notation of the particle potential and the dielectric function describes the response of the plasma species (electrons and ions) to the electrostatic potential. Here, we use a moving frame with the velocity of the streaming ions. The frequencies are therefore Doppler shifted $\omega \rightarrow \omega - q_z v_{i0}$ (q_z is the z component of the wave vector).

The plasma dielectric response is given by

$$\epsilon(\vec{q}, \omega - q_z v_{i0}) = 1 + \frac{1}{q^2 \lambda_{D,e}^2} - \frac{\omega_{p,i}^2}{(\omega - q_z v_{i0})^2} \quad , \quad (5.5)$$

where the second term on the RHS describes the electron shielding and the third term is the ion response. For the electrons the low-frequency limit of the dielectric response is used due to the high mobility of the electrons. For the ions the (Doppler shifted) high frequency limit is taken.

After some algebra the inverse of the dielectric function is found as

$$\frac{1}{\epsilon(\vec{q}, \omega - q_z v_{i0})} = \frac{q^2 \lambda_{D,e}^2}{1 + q^2 \lambda_{D,e}^2} \left[1 + \frac{\omega_s^2}{(\omega - q_z v_{i0})^2 - \omega_s^2} \right], \quad (5.6)$$

where $\omega_s = q v_B / (1 + q^2 \lambda_{D,e}^2)^{1/2}$ is the frequency of oscillations in the ion flow. For comparison, the dielectric response of a Coulomb potential with screening by electrons (i.e. a Debye-Hückel potential) is simply given by

$$\frac{1}{\epsilon(\vec{q}, \omega)} = \frac{q^2 \lambda_{D,e}^2}{1 + q^2 \lambda_{D,e}^2}.$$

By substituting the dielectric function in Eq. (5.4) the total potential can be written as the sum of two potentials

$$\phi(\vec{r}) = \phi_D(\vec{r}) + \phi_c(\vec{r}) \quad (5.7)$$

where

$$\phi_D(\vec{r}) = \frac{Z_d e}{4\pi\epsilon_0 r} \exp\left(-\frac{r}{\lambda_{D,e}}\right)$$

is the usual Debye shielding potential and

$$\phi_c(\vec{r}) = \int \frac{Z_d e}{8\pi^3 \epsilon_0 q^2} \frac{q^2 \lambda_{D,e}^2}{1 + q^2 \lambda_{D,e}^2} \frac{\omega_s^2}{(\omega - q_z v_{i0})^2 - \omega_s^2} e^{i\vec{q}\cdot\vec{r}} d\vec{q}. \quad (5.8)$$

Using cylindrical coordinates $(x, y, z) \rightarrow (\rho, \varphi, z)$, an approximate solution on the vertical axis $\rho = 0$, i.e. behind the dust particle, is given by [68]

$$\phi_c(\rho = 0, z) = \frac{Z_d e}{4\pi\epsilon_0 z} \frac{2 \cos\left(z \lambda_{D,e} \sqrt{\mathcal{M}^2 - 1}\right)}{1 - \mathcal{M}^{-2}} \quad \text{for } z > 3\lambda_{D,e} \sqrt{\mathcal{M}^2 - 1}. \quad (5.9)$$

According to this model an oscillating ion wake potential ϕ_c downstream of the dust particle is created with an alternating sequence of regions with enhanced positive and negative potential (see Fig. 5.2a). For $z < 5\lambda_{D,e} \sqrt{\mathcal{M}^2 - 1}$ the potential is negative due to the presence of the negative dust particle at $z = 0$. The potential (and the corresponding ion density) then “overshoots” and forms an attractive potential between $5 < z/\lambda_{D,e} \sqrt{\mathcal{M}^2 - 1} < 8$. This wake potential is attractive to a second negatively charged particle when $\phi_c > 0$. This ion wake provides the attractive force necessary to explain the vertical ordering of the particles. This mechanism is similar to Cooper pairing in superconductors [70], in that the dust particle polarizes the surrounding medium, the plasma,

which in turn leads to attraction of other particles. In addition, it is reasoned that other dust particles will arrange in the areas of positive potential defined by the first particle. The vertical scales introduced by this collisionless model are different from those in the experiment: The model predicts that the lower particle would be found in the maximum of ϕ_c which is approximately at $z = 6\lambda_{D,e}\sqrt{\mathcal{M}^2 - 1} \approx 3000 \mu\text{m}$ when $\lambda_{D,e} = 500 \mu\text{m}$ is assumed. This is far from the observed vertical distances of $z = 400$ to $600 \mu\text{m}$.

Using a more advanced dielectric function including collisions (with the ion-neutral collision frequency ν_i) and Landau damping (through the application of a shifted Maxwellian velocity distribution f_{i0}) via

$$\epsilon(\vec{q}, \omega - q_z v_{i0}) = 1 + \frac{1}{q^2 \lambda_{D,e}^2} - \frac{\omega_{p,i}^2}{q^2} \int \frac{\vec{q} \partial f_{i0}(\vec{v}) / \partial \vec{v}}{q_z v_{i0} - \omega - i\nu_i} d\vec{v} \quad , \quad (5.10)$$

a more realistic wakefield potential is derived [69]. This wakefield potential is shown in Fig. 5.2b) in a plane parallel and perpendicular to the flow. The attractive potential maximum is shifted more closely to the particle and is now found at about $z \approx 2\lambda_{D,e}$ which agrees more closely with the experiment. The Landau and collisional damping also leads to a rapid decay of the oscillations along the flow so that generally only a single potential maximum behind the dust particle is obtained. Further, wake is V-shaped due to the Mach cone of the ion acoustic waves excited by the grain.

The above discussed wave model included the excitation of linear waves by a single dust particle. In a region near the dust the linear description might become invalid and further the effects introduced by the presence of a second particle in the wakefield are not addressed (which has been resolved in a recent article [71]).

5.2.2. The ion focus (particle model)

The problem of attraction will now be investigated on the microscopic particle (ion) level [73, 74, 32, 75]. For this purpose, the experimental conditions are closely mimicked in simulations: A two-layer plasma crystal in the sheath of an rf discharge is considered; the electric field and electron distribution are taken into account as time-averaged, but spatially dependent quantities.

The ion trajectories are calculated according to the following equation of motion in the electric field of the sheath $E_{\text{sheath}}(z)$ and of the dust particles

$$m_d \ddot{\vec{r}} = e \left(E_{\text{sheath}}(z) - \sum \nabla \phi_i(\vec{r}) \right) \quad ,$$

where $\phi_i(\vec{r})$ is the particle potential of particle i according to Eq. (4.3) and the sum is over all particles in the upper and lower layer. In the ion motion also collisions are taken into account. This is done the following way: The above equation of motion is solved between the collisions of the ions. The time between two collisions is chosen randomly in such a way that a defined ion mean free path λ_{mfp} is ensured (see Fig. 5.3a). In the

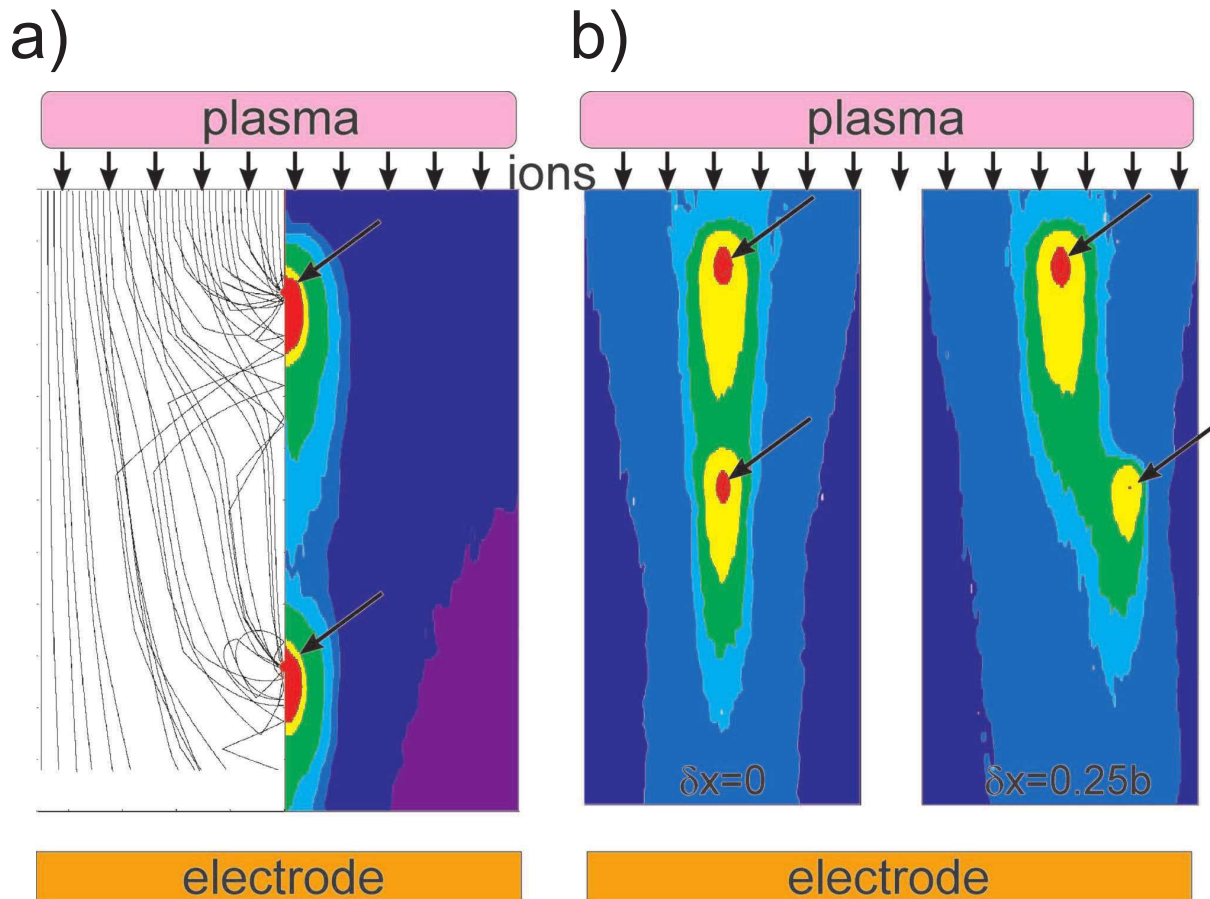


Figure 5.3: a) Ion density distributions calculated from the ion trajectories in the sheath for a vertically aligned pair of microspheres. Charge exchange collisions are included in this simulation as can be seen by abrupt changes in the particle trajectories. b) Ion density distribution for vertically aligned pairs (left, same as (a), but without the trajectories) and horizontally shifted crystal layers (right). The particle positions are indicated by the arrows. After [72, 73].

collision the ion loses its *kinetic* energy and starts again with a random *thermal* velocity. This is done until the ion hits the electrode or a dust particle. It is also assumed that the ions enter the plasma sheath with Bohm velocity.

The advantage of following the ion trajectories is that from the principle of *actio = reactio* the force exerted on the ion by the dust particle is the same force that acts on the dust by the ions. Thus the force on the dust due to the ions can be directly determined from the ion trajectories.

This experiment-related approach ensures that the forces on the particles can be calcu-

lated under very realistic conditions. Figure 5.3 shows the ion density distribution derived from the ion trajectories for the exact vertically aligned situation ($\delta x = 0$) and for the case that the lower layer is displaced by a quarter of the interparticle distance ($\delta x = 0.25b$). It is seen that the shielding ion cloud around each particle is extended downstream due to the ion flow. The ions are deflected below the dust by the Coulomb collisions with the particles. That results in a region of enhanced ion space charge density (“ion focus”) below each dust grain. The positive space charge is the reason for the attractive force on the particles. In this approach only a single attraction region is found in agreement with the more sophisticated wave model [69]. Hence, the wakefield (wave model) and the ion focus (particle model) can be considered as complimentary descriptions of the same phenomenon.

5.2.3. Non-reciprocal attraction

The ion trajectory simulations with a second dust particle, however, allow a deeper insight into the attraction [73]. Namely, one also finds surprisingly that the ion cloud of the upper particles is independent of the position of the lower particle. The upper half of Fig. 5.3b looks the same whether the lower particle is directly beneath the upper particle or whether it is shifted.

In a somewhat simplified picture the behavior can be described as following: Due to the supersonic ion flow the information on the location of the lower particles cannot be conveyed upstream. Since there is no reaction on the upper particles from the lower, the interaction between the particles is non-reciprocal: *the lower particles are attracted by the ion focus of the upper, but there is no attractive force acting on the upper particles*. This is an apparent violation of Newton’s third law *actio = reactio* when looking only at the dust particles. Although each single ion reacts with the dust particles by *actio = reactio* the collective ion population does not. This is an outcome of the supersonic ion flow that introduces a broken symmetry into the system. In other words, the steady ion flow puts energy into the system, thus, it is an *open* system where Newton’s third law does not necessarily hold [73].

The vertical particle interaction must therefore be described by a non-reciprocal attractive force. Due to the non-reciprocity of the interaction, we cannot assign a potential to this kind of interaction. We thus have non-conservative forces. Moreover, all techniques that rely on energy arguments, like OCP and Yukawa systems, cannot be directly applied to this situation.

The strength of the force acting on the lower particle in the horizontal direction F_x has been calculated from the ion trajectories as a function of the horizontal displacement δx . It is the restoring force that drives the lower particle back into the vertically aligned position. The strength of the force is shown in Fig. 5.4b. It is seen that the attractive, restoring force from the ion focus is decisively larger than the repulsion from the upper

particles. It is also seen that the force is linear in δx for small displacements, i.e.

$$F_x = -k_{\text{att}} \delta x \quad ,$$

which allows a linear stability analysis of the entire system (which is done in Sec. 5.4.).

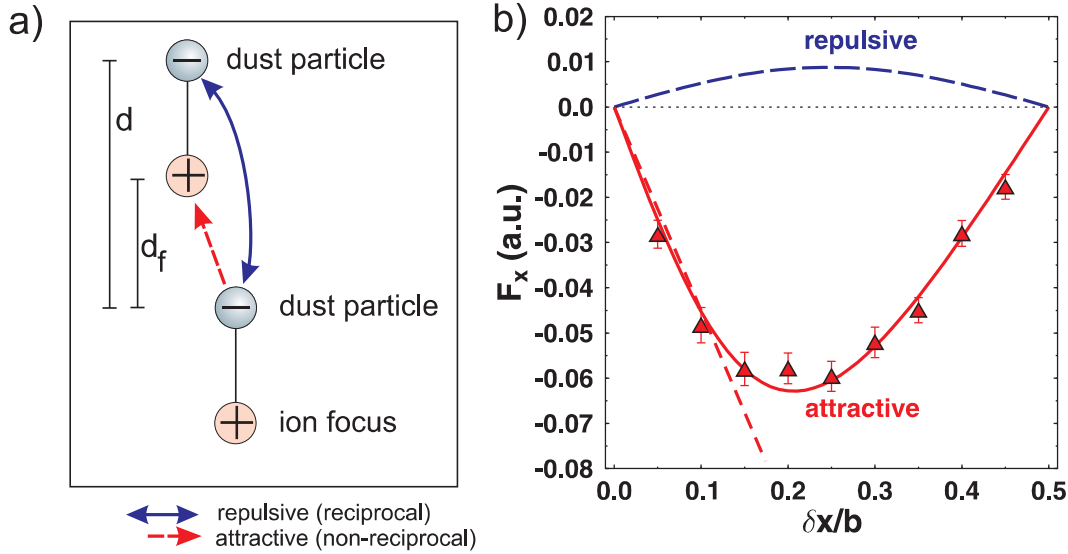


Figure 5.4: a) “Schweigert” model of the particle interaction derived from the simulation in Figure 5.3. The ion focus is mimicked by a positive point charge beneath a dust particle. The attractive force acts only on the lower particle. b) Strength of the attractive force (horizontal component) as a function of horizontal displacement. Symbols are results from the simulation, the solid line is from the model where the ion density distribution is replaced by a positive point charge. The dashed line indicates the linear behavior for small displacements. The repulsive force from the upper layer is shown for comparison. From [72].

This interaction can be translated into the “Schweigert” model presented in Fig. 5.4a. The distorted ion cloud around the dust, i.e. the ion focus, can be mimicked very accurately by replacing the ion cloud with a positive point charge Z_f at a distance $d - d_f$ directly below the upper particle (see Fig. 5.4b). Typical values are $Z_f = 0.5Z_d$ and $d_f = 0.4b$. The force exerted by this point-charge ion-focus exactly matches the forces determined from the full simulation, see Fig. 5.4b. This model system has the advantage that it can be analyzed quantitatively in view of stability and phase transitions.

5.3. Measurement of the Attractive Force

This peculiar type of particle interaction can be verified, also quantitatively, from experiments [76, 77, 78]. The non-reciprocal attractive forces can be probed experimentally in a very simple experiment. For this purpose, only two single particles are immersed into the plasma (see Fig. 5.5a). The first has a diameter of $3.47 \mu\text{m}$ (and a mass of $m_1 = 3.31 \times 10^{-14} \text{ kg}$) and the second one of $4.81 \mu\text{m}$ ($m_2 = 8.82 \times 10^{-14} \text{ kg}$). Due to their different masses the particles are trapped at different heights in the sheath, where the force balance is fulfilled for each of the particles. Thus, the vertical position of the particles is practically fixed. In the horizontal plane, the microspheres can move freely under the influence of the mutual interaction. From the response of one particle to the motion of the other particle the interaction between them can be directly extracted.

As in the case of the excitation of the vertical resonance, the focused beam of a manipulation laser (690 nm, 40 mW) is used to push the upper and lower particle individually and in a defined manner.

Without any laser force applied the two single microspheres are found vertically aligned as in the case of a plasma crystal. When now the upper particle is pushed by the radiation pressure of the laser beam *both* upper *and* lower particle move in the same way, their horizontal position is (nearly) identical, i.e. the particles stay vertically aligned (see Fig. 5.5b). That proves that the lower particle experiences an attractive force mediated by the upper particle.

When, however, the lower particle is pushed the two particles are separated horizontally, the alignment is broken (see Fig. 5.5c). The lower particle can be pushed far away from the upper ($t = 1 - 4 \text{ s}$). When the laser is switched off again, the lower particle approaches the aligned position below the upper one, whereas the upper (although being the lighter particle) does not move towards the lower. In contrast, shortly before the lower particle reaches the aligned position (around $t = 6 \text{ s}$) the upper particle experiences the repulsive force from the lower and moves away from the lower. This definitely demonstrates that the upper particle does not feel an attractive force mediated by the lower.

This confirms the fact that Newton's third law *actio = reactio* seems to be violated under these conditions. This is an outcome of the supersonic ion flow that introduces a preferred direction into the system. In addition, the ion stream introduces a source of free energy, thus the dust particle system and its environment is an open system where Hamiltonian dynamics does not hold. One of the main outcomes in connection with the theoretical analysis presented is that the interaction forces between the dust particles is non-reciprocal.

From the laser interaction with the two-particle dust system the horizontal attractive force component can also be derived quantitatively, see Fig. 5.6. By pushing the lower particle with the laser, the horizontal attractive force is balanced by the radiation pressure of the laser beam. By calibrating the laser force F_{laser} using experiments on single particles

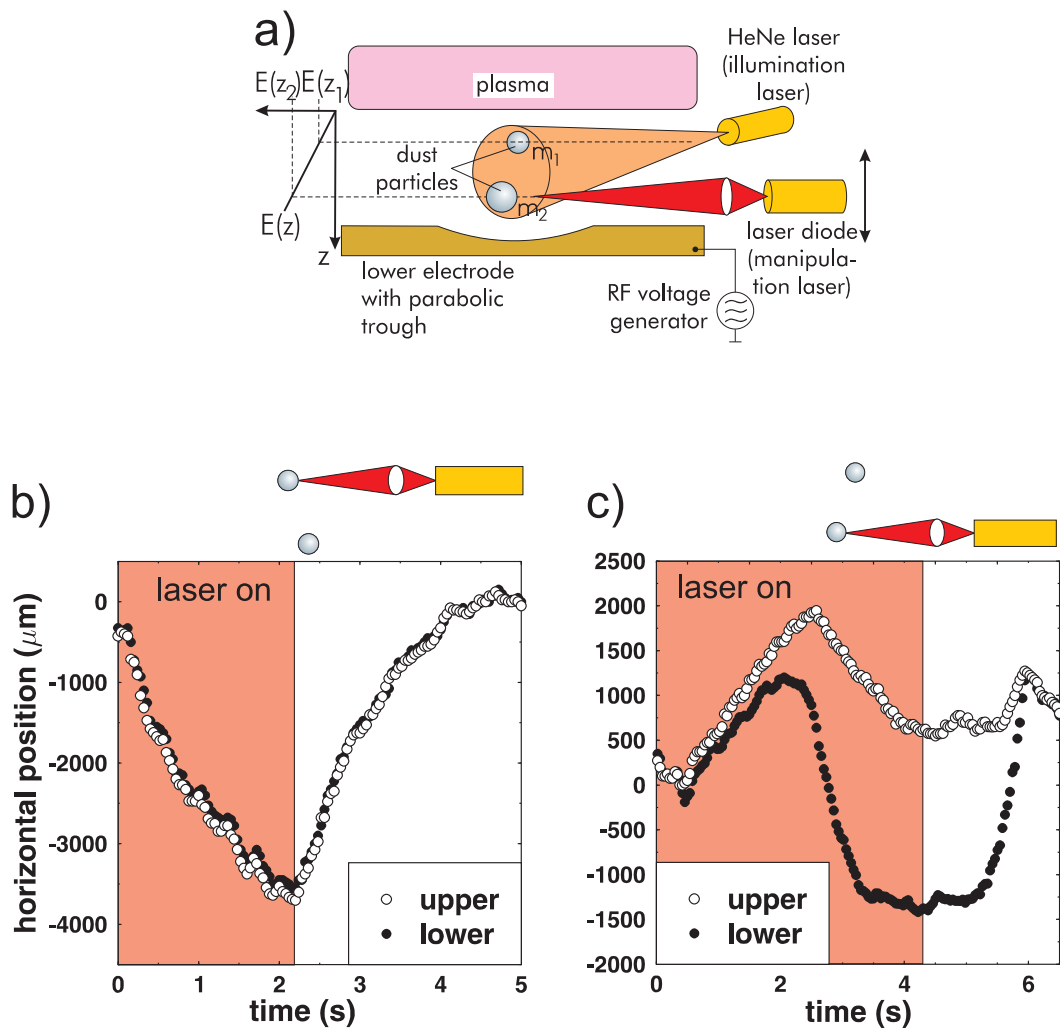


Figure 5.5: *Experiment on the non-reciprocity of the attractive force between two dust particles. a) Scheme of the experimental setup. Horizontal position of upper and lower particle when b) the upper particle is pushed and c) when the lower particle is pushed. After [77].*

we have determined the attractive force quantitatively. With increasing laser force the lower particle is shifted horizontally by a displacement Δx away from the aligned position.

Using the model of the positive point charge that mimics the ion focus the attractive force on the lower particle can be calculated. The horizontal component of the Coulomb force between the lower dust particle with charge Z_2 and the ion focus with charge Z_f is

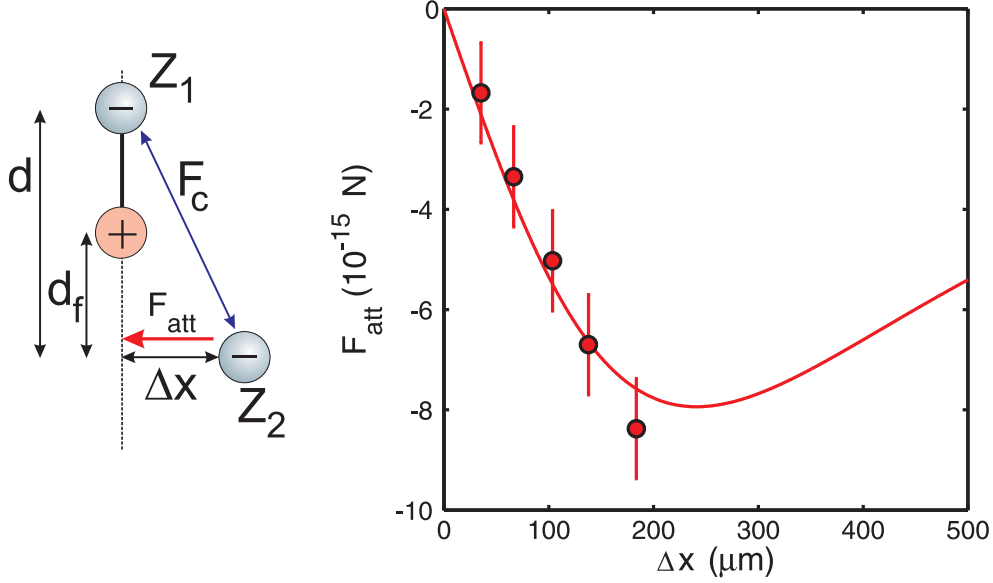


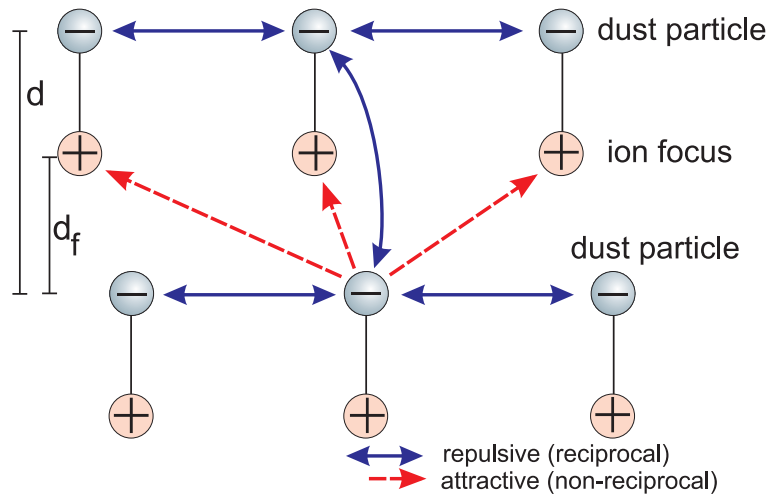
Figure 5.6: *Measurement of the attractive force between two dust particles. The measured magnitude of the attractive force (symbols) allows to derive the strength of the ion focus. The solid line is the calculated attractive force according to Eq. (5.11). After [78].*

given by

$$F_{\text{att}} = \frac{Z_f Z_2 e^2 \Delta x}{4\pi\epsilon_0 r_{f2}^2 r_{f2}} = \frac{Z_f Z_2 e^2 \Delta x}{4\pi\epsilon_0 (\Delta x^2 + d_f^2)^{3/2}} \quad , \quad (5.11)$$

where $r_{f2} = (\Delta x^2 + d_f^2)^{1/2}$ is the distance between the ion focus and the lower particle. In Fig. 5.6 the measured forces are shown in comparison to the above equation. The charge on the upper and lower particle was measured as $Z_1 = 2200$ and $Z_2 = 5900$, respectively, from the resonance method. Adjusting the values of Z_f and d_f in Eq. (5.11) agreement is found for $Z_f = 0.8Z_1$ and $d_f \approx 400 \mu\text{m}$. These values are in good agreement with the simulations.

This ‘‘Schweigert’’ model [73] of the ion focus with the non-reciprocal attraction due to the formation of the ion focus has hence been verified qualitatively and quantitatively by experiments. Moreover, this model is also able to explain the stability of plasma crystals and phase transitions from the ordered, solid phase to an unordered, fluid phase as described in the following. Moreover, this model has also been successfully applied to study mode-coupling instabilities [79].

Figure 5.7: *Forces in a two-layer plasma crystal.*

5.4. Oscillatory Instability of the Vertical Alignment

After having shown that the vertical interaction between the microspheres is indeed given by a non-reciprocal attractive force the question arises under which conditions the vertically aligned plasma crystal observed in the experiment is stable or unstable. Here, this analysis is performed for the simplest case of a two-layer chain of particles, see Fig. 5.7. There, the (reciprocal) repulsive forces between the negative dust particles and the (non-reciprocal) attractive forces on the lower layer particles towards the ion focus of the upper particles are indicated. From such a plasma crystal model the equations of motion in the horizontal plane for the n th particle in the upper (index 1) and lower (index 2) layer are

$$\ddot{x}_1^{(n)} + \beta \dot{x}_1^{(n)} = \frac{k_1}{m_d} (x_1^{(n-1)} - 2x_1^{(n)} + x_1^{(n+1)}) + \frac{Z_d^2 e^2}{4\pi\epsilon_0 m_d d^3} (x_1^{(n)} - x_2^{(n)}) \quad (5.12)$$

$$\begin{aligned} \ddot{x}_2^{(n)} + \beta \dot{x}_2^{(n)} = & \frac{k_2}{m_d} (x_2^{(n-1)} - 2x_2^{(n)} + x_2^{(n+1)}) + \frac{Z_d^2 e^2}{4\pi\epsilon_0 m_d d^3} (x_2^{(n)} - x_1^{(n)}) \\ & - \frac{Z_d Z_f e^2}{4\pi\epsilon_0 m_d d_f^3} (x_2^{(n)} - x_1^{(n)}) \quad . \end{aligned} \quad (5.13)$$

Here, a small horizontal elongation \mathbf{x} from the vertically aligned position is assumed. In addition, d and d_f are the vertical distance between the lower and upper layer and lower layer and ion focus, respectively, and Z_f the (positive) charge of the ion focus.

The first term on the RHS is the repulsive interaction between the particles of the same layer (upper or lower). This determines the horizontal oscillation frequency of the particles in the respective plane. The second term is the repulsion between upper and lower aligned particle (both taken as pure Coulomb forces for simplicity, here). The attraction

by the ion focus at the same horizontal position (\mathbf{n}) appears only in the equation of motion for the second layer due to the non-reciprocity of the attractive force. The final point to be addressed, here, is that in the lower layer the intralayer repulsion is assumed to be possibly different from that in the upper layer, which means $k_2 < k_1$. We will address this question in more detail below. The model presented here is simplified, it has, however, all the necessary ingredients to describe the physical mechanisms and to explain the experimental findings. A complete analysis taking into account a full 2D two-layer plasma crystal with hexagonal order and screened interaction is not much more difficult [73], but also does not include significant differences.

5.4.1. Solution of the Coupled Oscillations

To solve the equation of motion, first, we take the usual solution for waves on a linear chain $x_k^{(n)} = x_k \exp(i\mathbf{nq}\mathbf{b} - i\omega t)$, where \mathbf{q} is the wave vector and ω is the frequency of the wave. $\mathbf{n}\mathbf{b}$ is the equilibrium position of the \mathbf{n} -th particle in the chain. The equations then become

$$-\omega^2 x_1 - i\beta\omega x_1 = \frac{k_1}{m_d} x_1 (e^{i\mathbf{q}\mathbf{b}} - 2 + e^{-i\mathbf{q}\mathbf{b}}) + \frac{Z_d^2 e^2}{4\pi\epsilon_0 m_d d^3} (x_1 - x_2) \quad (5.14)$$

$$-\omega^2 x_2 - i\beta\omega x_2 = \frac{k_2}{m_d} x_2 (e^{i\mathbf{q}\mathbf{b}} - 2 + e^{-i\mathbf{q}\mathbf{b}}) + \frac{Z_d^2 e^2}{4\pi\epsilon_0 m_d d^3} (x_2 - x_1) \quad (5.15)$$

$$-\frac{Z_d Z_f e^2}{4\pi\epsilon_0 m_d d_f^3} (x_2 - x_1) \quad . \quad (5.16)$$

From trigonometric relations it is found that

$$e^{i\mathbf{q}\mathbf{b}} - 2 + e^{-i\mathbf{q}\mathbf{b}} = 2 \cos \mathbf{q}\mathbf{b} - 2 = 2 (\cos \mathbf{q}\mathbf{b} - 1) = -4 \sin^2 \left(\frac{\mathbf{q}\mathbf{b}}{2} \right) \quad .$$

Introducing the notations

$$\begin{aligned} \omega_d^2 &= \frac{Z_d^2 e^2}{4\pi\epsilon_0 m_d d^3} \\ \xi &= \frac{Z_f d^3}{Z_d d_f^3} \\ \omega_{1,2}^2 &= 4 \frac{k_{1,2}}{m_d} \quad , \end{aligned}$$

where ω_d is – apart from some multiplicative constants – the dust plasma frequency which is more rigorously defined in Sec. 6.1. and ξ is the relative strength of the attraction compared to the repulsive force. Since $Z_f \approx 0.5Z_d$ and $d_f \approx 0.4d$ the relative strength is $\xi \approx 8$ which indicates that the attraction by the ion focus is much stronger than the

repulsion by the upper particle. Finally, $\omega_{1,2}$ is the frequency of the interactions in the upper and lower layer.

The equation of motion for the upper and lower layer particle then reads

$$\left[\omega^2 + i\beta\omega - \omega_1^2 \sin^2 \left(\frac{qb}{2} \right) \right] x_1 = -\omega_d^2 (x_1 - x_2) \quad (5.17)$$

$$\left[\omega^2 + i\beta\omega - \omega_2^2 \sin^2 \left(\frac{qb}{2} \right) \right] x_2 = -(\xi - 1)\omega_d^2 (x_1 - x_2) \quad , \quad (5.18)$$

or, finally,

$$\left[\omega^2 + i\beta\omega - \omega_1^2 \sin^2 \left(\frac{qb}{2} \right) + \omega_d^2 \right] x_1 = \omega_d^2 x_2 \quad (5.19)$$

$$\left[\omega^2 + i\beta\omega - \omega_2^2 \sin^2 \left(\frac{qb}{2} \right) - (\xi - 1)\omega_d^2 \right] x_2 = -(\xi - 1)\omega_d^2 x_1 \quad . \quad (5.20)$$

This is now the standard form of the equations describing the interaction between the two layers. The non-reciprocal attraction can still be easily identified from the term containing the parameter ξ . The non-reciprocity becomes obvious from the fact that ξ only appears in the equation for the lower particle, but not for the upper.

This set of equations is of fourth order in ω , but can be solved analytically by multiplying the two equations yielding

$$\lambda^2 - \lambda (\tilde{\omega}_1^2 + \tilde{\omega}_2^2) + \tilde{\omega}_1^2 \tilde{\omega}_2^2 = -(\xi - 1)\omega_d^4 \quad , \quad (5.21)$$

where we have used the following abbreviations

$$\begin{aligned} \lambda &= \omega^2 + i\beta\omega \\ \tilde{\omega}_1^2 &= \omega_1^2 \sin^2 \left(\frac{qb}{2} \right) - \omega_d^2 \\ \tilde{\omega}_2^2 &= \omega_2^2 \sin^2 \left(\frac{qb}{2} \right) + (\xi - 1)\omega_d^2 \end{aligned}$$

Thus, the fourth-order equation actually is bi-quadratic. The solution is

$$\begin{aligned} \omega^2 + i\beta\omega = \lambda_{1,2} &= \frac{\tilde{\omega}_1^2 + \tilde{\omega}_2^2}{2} \pm \sqrt{\frac{(\tilde{\omega}_1^2 + \tilde{\omega}_2^2)^2}{4} - \tilde{\omega}_1^2 \tilde{\omega}_2^2 - (\xi - 1)\omega_d^4} \\ &= \frac{\tilde{\omega}_1^2 + \tilde{\omega}_2^2}{2} \pm \sqrt{\frac{(\tilde{\omega}_1^2 - \tilde{\omega}_2^2)^2}{4} - (\xi - 1)\omega_d^4} \end{aligned} \quad (5.22)$$

5.4.2. General Analysis of the Instability

Here, we should step back and have a look at this solution (5.22). We do not want to stick to the exact details of the equation, but to its general form

$$\lambda = D \pm \sqrt{E^2 - F} \quad .$$

There are two possibilities, namely that either the parameter λ is real or complex, i.e. that the expression under the square root is either positive ($E^2 > F \rightarrow \lambda = \lambda_{\text{real}}$) or negative ($E^2 < F \rightarrow \lambda = A \pm iB$). First, the case of a real $\lambda = \lambda_{\text{real}}$ will be discussed. Then, we have

$$\omega^2 + i\beta\omega - \lambda_{\text{real}} = 0$$

and we would get the complex solution

$$\omega = -i\frac{\beta}{2} \pm \sqrt{\lambda_{\text{real}} - \frac{\beta^2}{4}} \quad .$$

This means that the solution for $\mathbf{x} = \mathbf{x}_k \exp(i\mathbf{nq}\mathbf{b} - i\omega t)$ is a damped harmonic oscillation. There is nothing interesting about that. It does not lead to any instability. In this case, the vertical alignment is stable, both particles return with damped oscillations to their aligned state $\mathbf{x}_{1,2} = 0$.

On the other hand, when $\lambda = A \pm iB$ is complex, the situation is dramatically different. We get the same formal solution as above, namely,

$$\omega = -i\frac{\beta}{2} \pm \sqrt{A - \frac{\beta^2}{4} \pm iB} \quad , \quad (5.23)$$

but the imaginary contribution below the square root changes the solution drastically. There are four roots to this equation: a first pair is $\omega_{1,2} = \pm\omega_{r,1} - i\omega_{i,1}$, where the imaginary part is always negative. This also corresponds to a damped oscillatory motion, as above. The second pair of roots is $\omega_{3,4} = \pm\omega_{r,2} + i\omega_{i,2}$, where the imaginary part $\omega_{i,2}$ can be either negative or positive. The change from negative to positive imaginary part $\omega_{i,2}$ can be achieved by changing the value of β .

A solution with positive imaginary part of ω corresponds to an oscillatory instability with (exponentially) growing oscillations. Thus, such a solution would describe an instability of the vertically aligned pair of particles. The threshold value of the friction coefficient β^* for this change is found for the condition that the imaginary part is exactly zero, i.e. $\omega_{i,2} = 0$. We then have the condition that

$$\omega_{r,2}^2 + i\beta^* \omega_{r,2} = A + iB$$

which results in

$$\omega_{r,2} = \sqrt{A} \quad \text{and} \quad \beta^* = \frac{B}{\sqrt{A}} \quad . \quad (5.24)$$

The four roots of Eq. (5.22) are shown in Fig. 5.8. As described, two of the roots always have a negative imaginary part, even for $\beta = 0$. These would correspond to damped oscillations around the vertically aligned position. The two other roots cross the $\omega_{\text{imag}} = 0$ -line at the finite friction constant β^* . These correspond to oscillations with growing amplitudes rather than damped amplitudes. They thus are unstable oscillations. These unstable solutions are found in the entire range of the friction constant $0 < \beta < \beta^*$. This means that unstable oscillations occur *even though there is still friction of the dust particles with the background gas*. Thus energy has to be constantly supplied to the oscillation of the vertically aligned dust system. We will identify the energy source below.

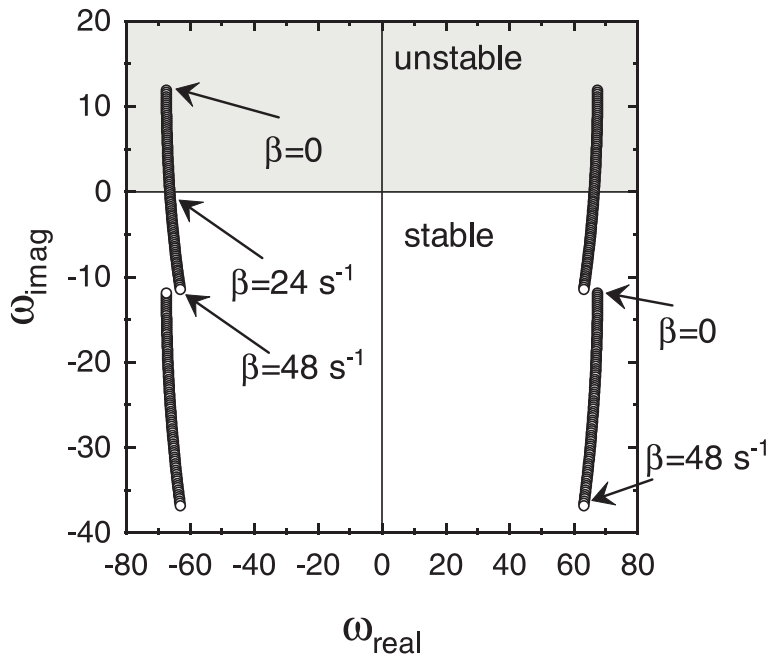


Figure 5.8: Roots of the instability equation (5.22) for assumed (but realistic) values of $A = 4400 \text{ s}^{-2}$ and $B = 1600 \text{ s}^{-2}$. When the imaginary part of the solution is larger than zero unstable oscillations with growing amplitude occur. Note, that this threshold is reached for finite values of the damping constant $\beta^* = B/\sqrt{A} = 24 \text{ s}^{-1}$.

5.4.3. Conditions for the Instability

Now, we have to identify under which conditions a complex $\lambda = A \pm iB$ is obtained in Eq. (5.22) which leads to the unstable oscillations. To obtain a complex λ the square root must be negative. A necessary (but not sufficient) condition obviously is that

$$\xi > 1 \quad .$$

This means that the attractive force due to the ion focus (which is represented by the parameter ξ) has to be larger than the repulsion by the upper particle. This is expected since without domination of attraction a vertical alignment would not be found in the first place.

From a more detailed analysis (that is not done here) one finds the more stringent conditions that

$$\xi > 2 \quad \text{and} \quad \omega_1^2 > \omega_2^2 \quad \text{i.e.} \quad k_1 > k_2 \quad .$$

First, the attraction must exceed the repulsion by at least a factor of two and, second, the spring constant reflecting the interlayer interaction must be weaker for the lower layer than for the upper. This second point can be understood from the fact that the lower layer particle does not only feel the attraction from the ion foci of the vertically aligned upper particle, but also the attraction from the other neighboring particles. The attraction to the neighboring upper particles then weakens the repulsion from the lower layer neighboring particles which results in $k_2 < k_1$.

The model presented here is simplified wherever possible, but it retains the main mechanisms. More sophisticated models exist that derive the above mentioned mechanism from a straightforward mathematical analysis. There, the somewhat ad hoc explanation of $k_1 > k_2$ is taken into account in a much more proper way. But in order not to focus on the mathematical details a “bare-bone” model is discussed here that allows to grasp the main ingredients of the instability.

From the physics point of view, this instability can be explained as follows: The streaming ions act as a source of free energy. The energy of the beam is transferred to the plasma crystal due to the Coulomb collisions of the ions with the dust. Above the critical value of damping the energy transferred by the ions can be dissipated by the friction of the dust particles with the neutral gas. Below the threshold the frictional losses cannot compensate the energy input and the ion energy piles up to drive the oscillatory instability.

On the level of the individual dust particles it looks like this: the lower layer particle feels an attractive force due to the ion wakefield of the upper particle. Hence it moves towards a position where it is aligned with the upper particle. However, the attractive force is non-reciprocal which means that the upper particles does *not* feel the attraction. In contrast, the upper particle feels the (screened) Coulomb repulsion from the negative charge of the lower layer particle. Hence, the upper particle tries to move away from the lower one. But the lower tries to follow the upper. The lower wants to be close to the upper, but the upper wants to escape. Due to the neighboring particles in the same layer, this type of unstable situation turns into an oscillatory instability. The neighbors of the upper particle provides a “cage” for the upper particle where it can basically oscillate at the dust plasma frequency. The lower particle tries to follow the oscillations of the upper, the upper tries to escape, and so, the oscillatory instability develops.

Summarizing, the linear stability analysis shows that a critical value of the friction coefficient $\beta^* > 0$, i.e. the gas pressure in the discharge, exists below which both upper and lower layer perform horizontal oscillations about the vertically aligned equilibrium position with exponentially increasing oscillation amplitude. These are short wavelength modes on the linear chain with $qb > 1$ with a frequency near the dust plasma frequency ω_{pd} . Moreover, from the stability analysis the relative phase and oscillation amplitude between particles of upper and lower layer can be derived. Above the critical pressure, the vertical alignment is found to be stable. This instability is directly connected to the frictional damping of the dust particles and not to a change of discharge parameters with changing pressure.

This theoretical description agrees very well with experimentally observed oscillations in two-layer plasma crystals near the melting transition [72], see Fig. 5.9. The calculated values for oscillation frequency, relative phase and amplitude as well as the pressure threshold for the onset of these oscillations are within a factor of two of the measured ones which gives this model a high credibility.

5.5. The Phase Transition of the Plasma Crystal: Experiment

We now will see what the effects of the above mentioned instability mechanism are. In the following, we will investigate the experimental melting transition of plasma crystals. The experiments have been performed with two-layer plasma crystals which are subject to the above mentioned instability. Mono-layer crystals do not show a melting scenario as described below.

Experimentally, the melting transition is observed when the gas pressure in the discharge is reduced [46, 80]. At high gas pressures (118 Pa in this particular experiment) well ordered crystalline structures are found (Fig. 5.10a). The particles do not move considerably, they stay in their respective Wigner-Seitz cells. At reduced pressure the particle arrangement undergoes a transition to a liquid and, finally, to an almost gas-like state. During this transition, at first, stream line particle motion around crystalline patches sets in, that gradually turns into a more and more irregular particle motion. This transition is also seen in the correlation function $g(r)$ and $g_6(r)$, see Fig. 5.10c,d. The translational as well as the orientational ordering is strongly decreased from the ordered state at high pressures to the completely disordered, gas-like state at 39 Pa.

The transition from the ordered to the liquid state is accompanied, and even driven, by the horizontal oscillations of the vertically aligned pairs that were discussed in the previous section. One can easily observe these oscillations around the equilibrium position by video microscopy. They are not visible in the trajectories since these are averaged over 10 seconds. The oscillations are, nevertheless, described in Fig. 5.9.

From the thermodynamic point of view, the transition is driven by a dramatic increase

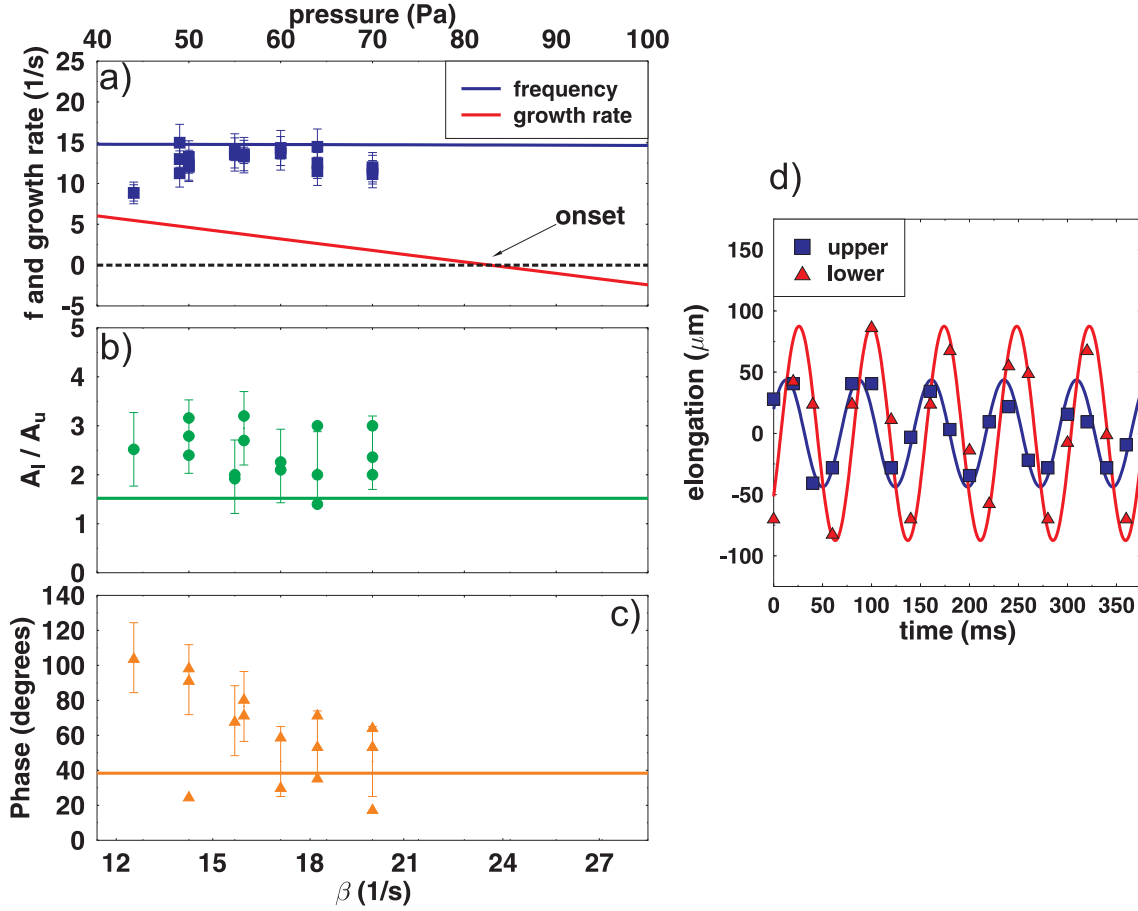


Figure 5.9: Comparison of experimental and theoretical oscillatory instability. a) Frequency of particle oscillations and growth rate of the instability, b) ratio of oscillation amplitudes A_l/A_u and c) phase difference of lower and upper particle. Symbols denote experimental values from oscillations during the melting transition and the lines correspond to the theoretical values from the stability analysis. d) One experimental example of horizontal oscillations of a vertically aligned pair. After [72].

of dust temperature from room temperature at 118 Pa to $T_d = 50$ eV at 39 Pa, see Fig. 5.10b. This high temperature is far above the energies of all other plasma species. This dramatic increase of dust temperature cannot be explained by simple changes in the discharge conditions with reduced pressure. In this pressure range of interest the densities of electrons and ions change by a factor about 3 and the electron temperature is nearly unaffected. These small changes cannot be made responsible for the change of dust temperature by a factor 1000.

Naturally, the previously described instability mechanism based on the non-reciprocal

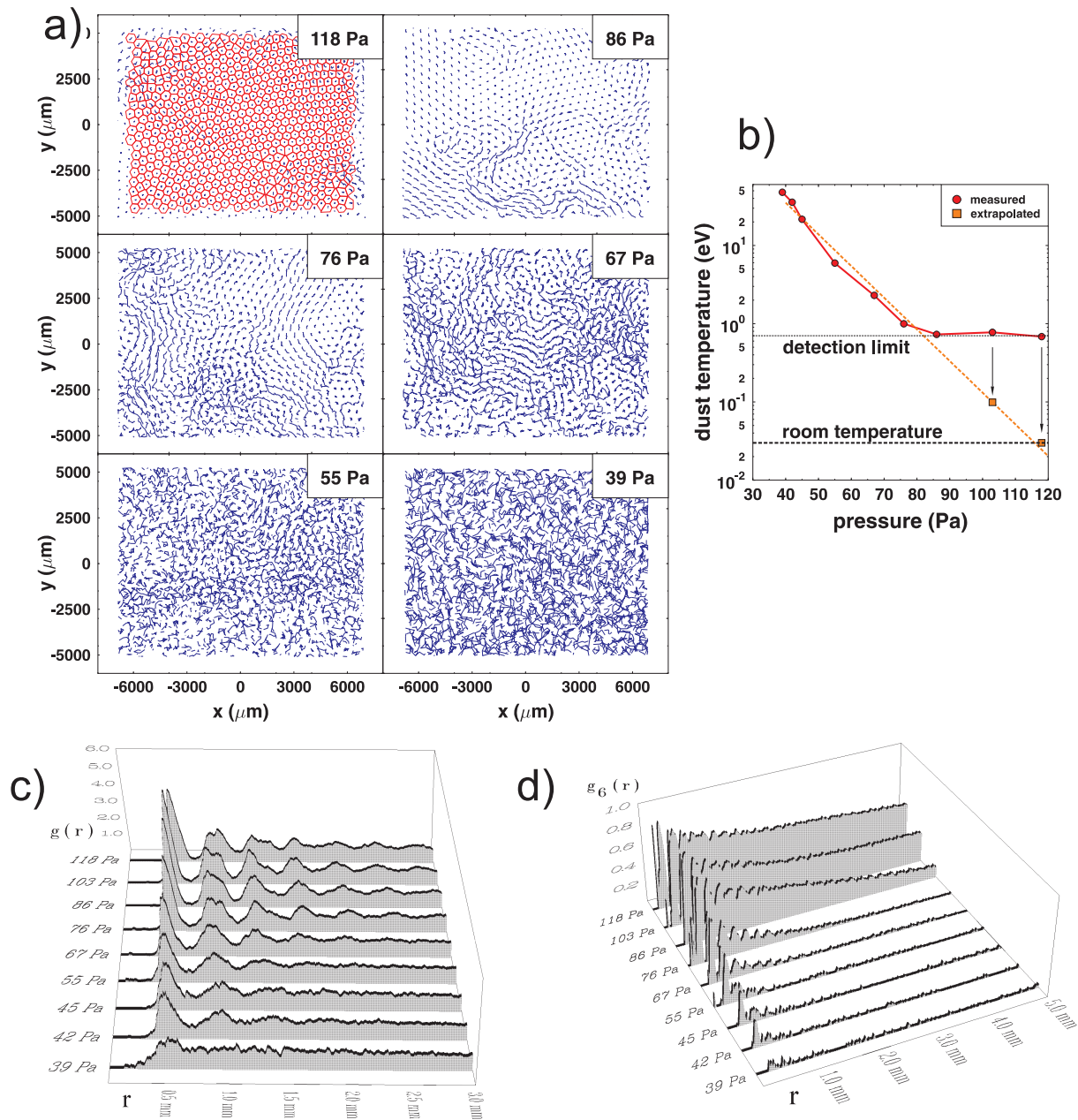


Figure 5.10: a) Trajectories of the dust particles over 10 seconds for decreasing discharge pressure, b) temperature of the dust particles as a function of discharge pressure. A temperature below 0.7 eV could not be detected due to the limited optical resolution, c) pair correlation and d) orientational correlation function versus pressure. After [46].

attraction is the source of energy input to the microspheres. The oscillatory instability sets in at about 80 Pa under the conditions of this experiment (see Fig. 5.9). This is exactly the pressure when fluid particle trajectories set in. The energetic oscillations are becoming more and more irregular and turn into a chaotic motion of the particles which can be interpreted as heating the dust particles to the high temperatures mentioned above.

One should note that very similar phase transitions have been observed in krypton at a lower gas pressure, but at nearly the same values for the frictional damping constant β [80].

5.6. The Phase Transition of the Plasma Crystal: Simulations and Theory

To identify the heating mechanism and melting dynamics of plasma crystals the melting transition was investigated in simulations in which the experimental conditions were mimicked in great detail [81]. Some of the interesting questions are how the instability mechanism drives the transition and how the oscillatory particle motion is randomized to heat the crystal.

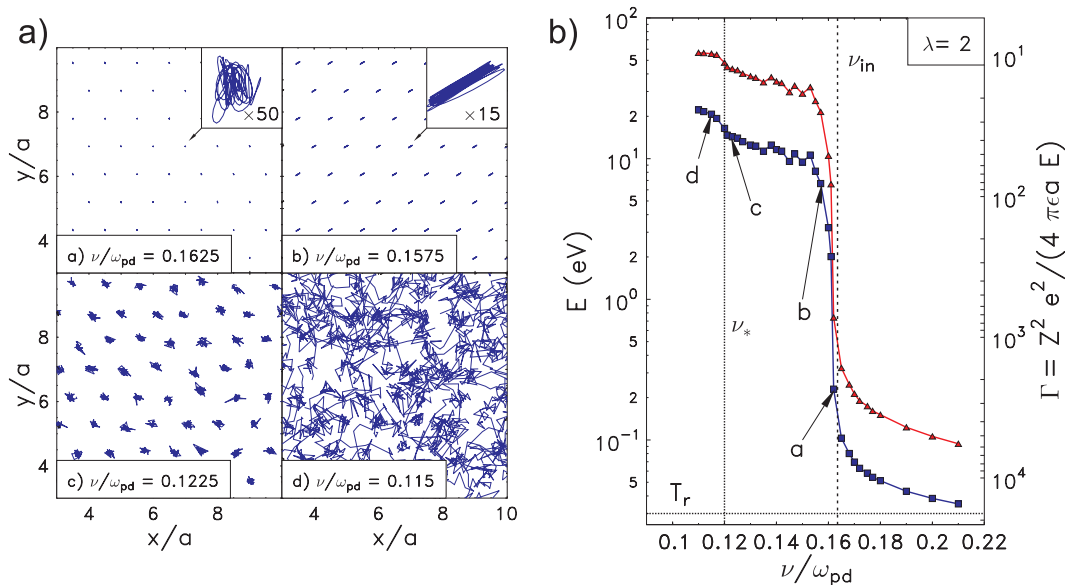


Figure 5.11: a) Particle trajectories for different friction coefficients during the melting transition. b) Particle energy of upper and lower layer versus friction coefficient. The points of which the trajectories are shown in a) are indicated by arrows. The two curves correspond to the energy of upper and lower layer, respectively. From [81].

In the simulations an ideal hexagonal two-layer plasma crystal is considered. The

negatively charged particles interact via a screened Coulomb repulsion and the particles of the lower layer experience the non-reciprocal, attractive force from the ion clouds of the upper particles. Here, the full horizontal dependence of the attractive force according to Fig. 5.3c is taken into account. In the simulation only horizontal displacements $\vec{\rho}_{jk} = (x_{jk}, y_{jk})$ from the equilibrium positions are taken into account ($k = 1, 2$ indicates upper and lower layer, respectively, and j denotes the number of the particle in that layer):

$$\frac{d^2\vec{\rho}_{jk}}{dt^2} + \beta \frac{d\vec{\rho}_{jk}}{dt} = \frac{1}{m_d} \vec{F}_{jk} + \frac{1}{m_d} \vec{F}_L. \quad (5.25)$$

The force acting on the particles \vec{F}_{jk} consists of two parts. The first describes the repulsion due to the other dust particles in the same or in the other layer. The second part describes the attractive force on the lower particles due to the ion focus (replaced by a single point charge). In addition, a Langevin force \vec{F}_L is applied to the particles to give them a finite temperature (room temperature) in the crystalline state at high pressure. This Langevin force is kept constant throughout the melting process leading to no additional heating.

This model is exactly the same as that used for the linear stability analysis in Section 5.4. with the exception of the Langevin force and the consideration of the full horizontal dependence, and not only the linear part for small elongations. As in the experiment, the gas pressure, i.e. the friction constant β , was slowly reduced in the simulation. The resulting energy of the dust particles as a function of gas pressure is shown in Fig. 5.11 together with the particle trajectories for different values of the friction coefficient.

For the melting transition of an ideal crystal a two-step melting scenario is obtained: Starting at high pressures the well ordered crystal is found. With decreasing friction the oscillatory instability described in Section 5.4. sets in at about $\beta_{in} = 0.165\omega_{pd}$. This leads to a dramatic increase of the dust kinetic energy from room temperature to about 10 eV. However, that does not lead to the melting of the crystal, instead, a hot crystalline state is found, here. With further reduction of friction ($\beta_* = 0.12\omega_{pd}$) the transition to a liquid state is observed.

The maximum energy of the dust particles and the overall melting scenario in the simulation agrees well with that obtained from experiments. However, some differences in comparison to the experiment are found in the simulation. First, the experimental melting transition takes place over a broader range of β than the simulation. Second, the two-step melting is not clearly observed in the experiment and, third, in the experiment characteristic stream line particle motions around crystalline patches are seen that are not present in the simulation.

This discrepancy is resolved when also defects in the plasma crystal are taken into account [82]. The crystal with defects shows a melting scenario that is very similar to the experimental: the increase of dust temperature with reduced pressure is slower, in overall quantitative agreement with the experiment. In addition, the two-step melting transition is “smeared out” over a broader range of β so that the melting is gradual and no sharp transition can be assigned. Finally, the particle trajectories show the streamline particle

motions that are characteristic for the experiment. The melting of a crystal with defects is shown in Fig. 5.12. Compare this simulated phase transition with the experimental one in Fig. 5.10. One can observe a deep agreement between the experimental and simulated phase transition. Since the simulations are only based on the non-reciprocal attraction as discussed above and no other heating mechanisms are taken into account this agreement gives strong confidence in the existence and relevance of these non-reciprocal forces.

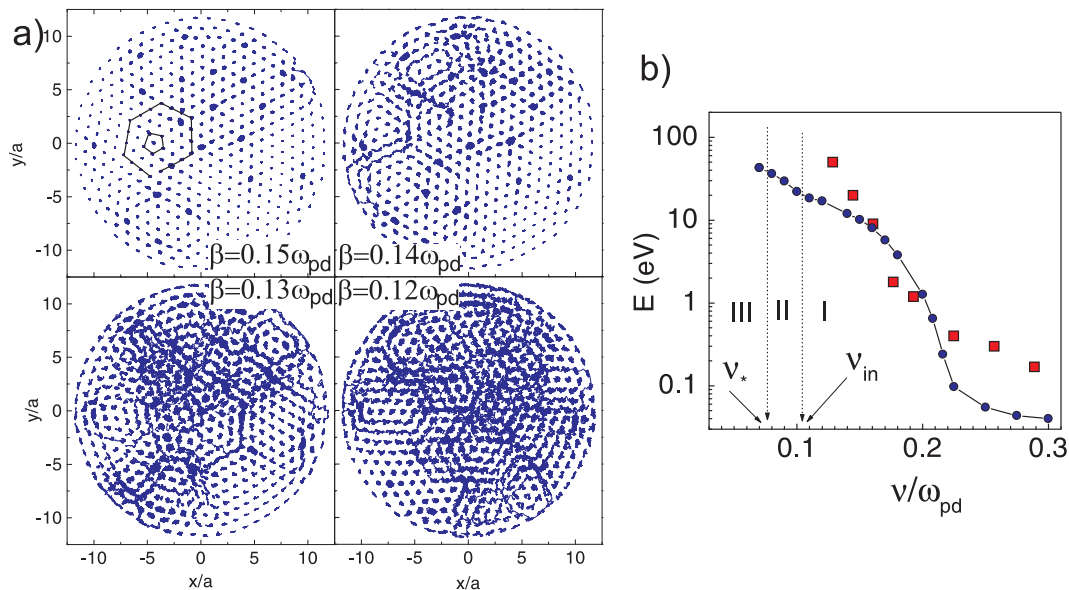


Figure 5.12: a) Particle trajectories for different friction coefficients during the melting transition. In the upper left panel the 5-fold defect is marked with a pentagon. b) Particle energy versus friction coefficient. Open circles (\circ): Two-step melting of a crystal with defects (simulation), squares (\blacksquare): Experimental results. After [82].

6. Waves in Weakly Coupled Dusty Plasmas

As another example of collective motions in dusty plasmas, we now turn to the topic of waves. For dusty plasmas, a number of wave modes exist that have been predicted theoretically and that will not be discussed entirely in these Lecture Notes. Instead, we will focus on a few fundamental wave types that have been observed in experiments. For a more detailed overview on waves the reader is referred to dedicated monographs [1, 3].

In general, two categories of waves can be identified, namely those which do not require strong coupling of the dust particles and those which rely on the strong coupling. In the first category, we find, e.g., the dust-acoustic (DAW) and dust ion-acoustic wave (DIAW). The dust lattice wave (DLW) with its different “polarizations” requires an ordered dust arrangement on lattice sites and thus belongs to the second category. Here, we start with the discussion of the weakly coupled waves, the DAW and the DIAW. The DAW is a wave where the dust particles are the moving species, the DIAW considers the dust as immobile, but the dust influences the wave propagation.

6.1. Dust-Acoustic Waves

The DAW is a complete analog to the ion-acoustic wave: The ion-acoustic wave is an electrostatic ion wave where the ions provide the inertia. In the DAW, the inertia is given by the dust.

The dust acoustic wave [83] is a very low-frequency wave with wave frequencies of the order of the dust plasma frequency ω_{pd} which, due to the high dust mass, is much less than the ion plasma and electron plasma frequency (ω_{pi}, ω_{pe}). Analogously to the electron and ion plasma frequency the dust plasma frequency is defined as

$$\omega_{pd} = \sqrt{\frac{Z_d^2 e^2 n_{d0}}{\epsilon_0 m_d}} \ll \omega_{pi}, \omega_{pe} , \quad (6.1)$$

where n_{d0} is the equilibrium (undisturbed) dust density.

Before the mathematical details of the wave motion are described, the wave mechanism is explained (see Fig. 6.1). Consider a wave-like disturbance of the dust density. The dust density disturbance is associated with an enhanced negative space charge due to the negative dust charge. This dust space charge $Z_d n_d$ will then be immediately shielded by the ambient plasma ions and (to a lesser extent) electrons. In contrast to the ion-acoustic wave, here the shielding is by both electrons and ions. However, the shielding is not complete, the dust charge density fluctuations $n_d Z_d$ are larger by a very small amount compared to that of electrons and ions $n_i - n_e$. However, this is enough to form negative and positive space charge regions which lead to electric fields that further drive the wave.

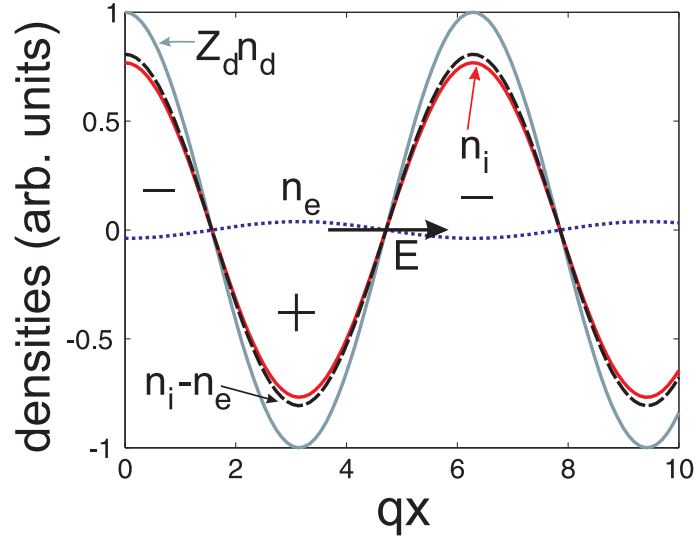


Figure 6.1: Comparison of the wave-like dust density disturbance with the ion and electron density fluctuations. It is seen that the dust density fluctuation $Z_d n_d$ is slightly larger than that of electrons and ions $n_i - n_e$.

The electric field is maximum near the zero-crossing of the dust density perturbations. Therefore, the electric field force pushes the fluctuations in the direction of the electric field and thus the wave propagates.

For the derivation of the DAW the equation of continuity, the momentum equation and Poisson's equation for the dust species are used which can be written as

$$\frac{\partial n_d}{\partial t} + \frac{\partial}{\partial x}(n_d v_d) = 0 \quad (6.2)$$

$$\frac{\partial v_d}{\partial t} + v_d \frac{\partial v_d}{\partial x} + \gamma_d \frac{kT_d}{m_d n_d} \frac{\partial n_d}{\partial x} = \frac{Z_d e}{m_d} \frac{\partial \phi}{\partial x} - \beta v_d \quad (6.3)$$

$$\frac{\partial^2 \phi}{\partial x^2} = -\frac{e}{\epsilon_0} (n_i - n_e - Z_d n_d) . \quad (6.4)$$

There are a few small differences to the usual ion-acoustic wave: the momentum equation (6.3) includes friction with the neutral gas (βv_d), and Poisson's equation (6.4) includes all three charged species, electrons, ions and dust. To solve these equations, the dust density and velocity as well as the electron and ion densities are considered as fluctuating quantities with

$$\begin{aligned} n_d &= n_{d0} + \tilde{n}_d \\ v_d &= 0 + \tilde{v}_d \\ \phi &= 0 + \tilde{\phi} . \end{aligned}$$

The fluctuations are considered to be wave-like, i.e. proportional to $\exp(i\mathbf{q}\mathbf{x} - i\omega t)$. The electrons and ions are assumed to have a Boltzmann distribution, namely

$$\begin{aligned} n_e &= n_{e0} \exp\left(\frac{e\tilde{\phi}}{kT_e}\right) \simeq n_{e0} \left(1 + \frac{e\tilde{\phi}}{kT_e}\right) = n_{e0} + \tilde{n}_e \\ n_i &= n_{i0} \exp\left(-\frac{e\tilde{\phi}}{kT_i}\right) \simeq n_{i0} \left(1 - \frac{e\tilde{\phi}}{kT_i}\right) = n_{i0} + \tilde{n}_i \end{aligned}$$

Here, n_{e0} and n_{i0} denote the equilibrium (undisturbed) values of the electron and ion density. For the undisturbed densities the quasineutrality condition is fulfilled, i.e.

$$n_{i0} = n_{e0} + Z_d n_{d0} \quad ,$$

where the dust is assumed to be negatively charged and adds to the electron charge density.

The above three equations can then be written as

$$-i\omega\tilde{n}_d + i\mathbf{q}n_{d0}\tilde{v}_d = 0 \quad (6.5)$$

$$-i\omega\tilde{v}_d + i\mathbf{q}\gamma_d \frac{kT_d}{m_d n_{d0}} \tilde{n}_d = \frac{Z_d e}{m_d} i\mathbf{q}\tilde{\phi} - \beta\tilde{v}_d \quad (6.6)$$

$$-q^2\tilde{\phi} = -\frac{e}{\epsilon_0} (n_i - n_e - Z_d n_d) \quad . \quad (6.7)$$

Here, as usual, we have used that for the wave-like fluctuations the spatial and temporal derivations can be replaced by the products with the frequencies and wave vectors ($\partial/\partial t \rightarrow -i\omega$; $\partial/\partial \mathbf{x} \rightarrow i\mathbf{q}$). The last equation then becomes

$$-q^2\tilde{\phi} = -\frac{e}{\epsilon_0} (n_{i0} - n_{e0} - Z_d n_{d0}) - \frac{e}{\epsilon_0} \left(n_{i0} \frac{e\tilde{\phi}}{kT_i} + n_{e0} \frac{e\tilde{\phi}}{kT_e} - Z_d \tilde{n}_d \right) \quad .$$

The first term is zero due to quasineutrality. Applying the quasineutrality again to replace $n_{e0} = n_{i0} - Z_d n_{d0}$ and using the relative dust density $\epsilon = n_{d0}/n_{i0}$ we get

$$-q^2\tilde{\phi} = \frac{e^2 n_{i0}}{\epsilon_0 kT_i} \left(1 + \frac{T_i}{T_e} [1 - Z_d \epsilon] \right) \tilde{\phi} + \frac{eZ_d}{\epsilon_0} \frac{\mathbf{q}}{\omega} n_{d0} \tilde{v}_d \quad ,$$

where we have used the first equation to replace \tilde{n}_d with \tilde{v}_d . From that we can write

$$\tilde{\phi} = -\frac{eZ_d}{\epsilon_0} \frac{\mathbf{q}}{\omega} n_{d0} \tilde{v}_d \frac{\lambda_{D,i}^2}{q^2 \lambda_{D,i}^2 + 1 + \frac{T_i}{T_e} [1 - \epsilon Z_d]} \quad .$$

Inserting this expression for ϕ and the first equation into the equation of motion we yield after a few rearrangements

$$\omega^2 + i\beta\omega = \left(\gamma_d \frac{kT_d}{m_d} + \epsilon Z_d^2 \frac{kT_i}{m_d} \frac{1}{\left(1 + \frac{T_i}{T_e} (1 - \epsilon Z_d) + q^2 \lambda_{D,i}^2 \right)} \right) q^2 \quad . \quad (6.8)$$

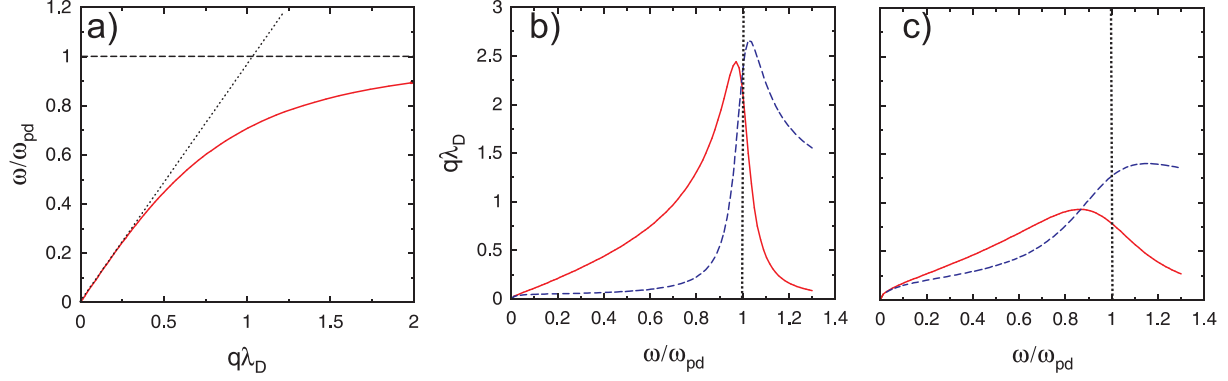


Figure 6.2: (a) Dispersion relation of the dust-acoustic wave without damping. The solid line is the full dispersion relation, the dotted line indicates the acoustic limit with the dust-acoustic velocity. (b) Dispersion relation with small friction ($\beta = 0.1 \omega_{pd}$) and (c) with large friction ($\beta = 0.5 \omega_{pd}$). Here, the solid line refers to the real part of the wave vector and the dashed line to the imaginary part. Note, that in (b) and (c) the axes have been exchanged compared to (a).

This is the full dispersion relation of the DAW. It contains a number of effects. The first term in the brackets is the dust thermal velocity and the second contains the influence of the electron and ion drive on the dust inertia. This is more clearly seen under the typical assumption of cold dust ($T_d = 0$) and cold ions ($T_i \ll T_e$). Then, the dispersion relation simplifies to

$$\omega^2 + i\beta\omega = \frac{\omega_{pd}^2 q^2 \lambda_{D,i}^2}{1 + q^2 \lambda_{D,i}^2} = \frac{\omega_{pd}^2 q^2 b^2}{\kappa^2 + q^2 b^2}, \quad (6.9)$$

which is the same as for the ion-acoustic wave where the ion properties are replaced by those of the dust and the electron properties by those of the ions. The second expression has been obtained by introducing the screening strength $\kappa = b/\lambda_{D,i}$. Thus the wave frequencies (and wave speeds) decrease with increasing κ .

The dispersion relation of the DAW is shown in Fig. 6.2a. For large wave numbers $q^2 \lambda_{D,i}^2 \gg 1$ the wave is not propagating and oscillates at the dust plasma frequency ω_{pd} . For small wave numbers $q^2 \lambda_{D,i}^2 \ll 1$ the wave is acoustic $\omega = qC_{DAW}$ with the dust-acoustic wave speed

$$C_{DAW} = \sqrt{\frac{kT_i}{m_d} \epsilon Z_d^2}. \quad (6.10)$$

As for the ion-acoustic wave, the wave speed is determined by the temperature of the lighter species (T_i) and the mass of the heavier (m_d). The dust-acoustic wave speed also includes the contribution of the dust charge Z_d and the relative dust concentration ϵ . It

is also interesting to note that the governing shielding length is the *ion* Debye length $\lambda_{D,i}$ as the ions are the oppositely charged fluid that shields the repulsion between the dust particles.

We now like to analyze the influence of friction on the wave motion. Before doing so we like to remind to how instabilities and waves are treated in “usual” plasma physics. There, the instability condition of a wave that is proportional to $\exp(\mathbf{i}\mathbf{q}\mathbf{x} - \mathbf{i}\omega\mathbf{t})$ is obtained when the imaginary part ω_I of the wave frequency $\omega = \omega_r + \mathbf{i}\omega_i$ becomes larger than zero. Naturally, the wave vector \mathbf{q} is a real value.

In contrast, when waves are excited in a frictional medium the wave frequency ω has to be taken as a real value and, consequently, the wave vector has to be treated as complex $\mathbf{q} = \mathbf{q}_r + \mathbf{i}\mathbf{q}_i$, where the real part $\mathbf{q}_r = 2\pi/\lambda$ is related to the wave length λ and the imaginary $\mathbf{q}_i = 1/L$ to the damping length L in the system. The damping length L is the distance where the wave amplitude is reduced to $1/e$. In this situation, we have to determine the real and the imaginary part of the wave vector for each value of the wave frequency. Thus, it is more convenient to plot the dispersion relation as $\mathbf{q}_r(\omega)$ and $\mathbf{q}_i(\omega)$ instead of the “usual” dispersion $\omega(\mathbf{q})$.

Figure 6.2b,c shows the DAW dispersion for small and large values of the friction coefficient β . For small friction the real part of the wave vector behaves similarly to the case of no damping. Close to $\omega = \omega_{pd}$ the wave vector turns over and decreases

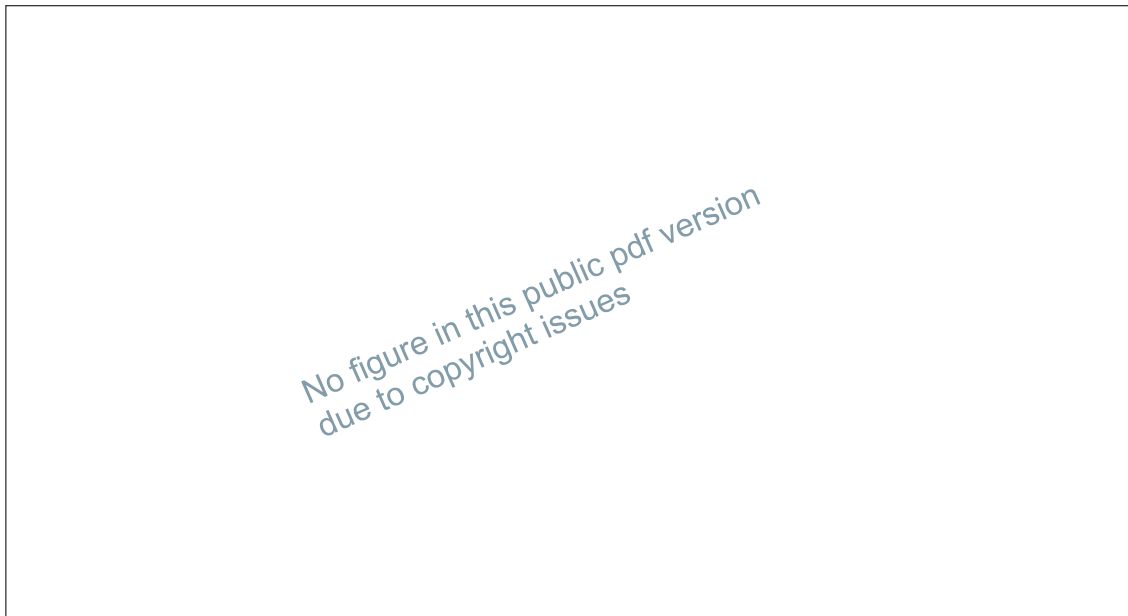


Figure 6.3: *Observation of the DAW in a dc discharge. (a) The DAW is seen as regions of high and low dust density in scattered light. (b) Measured dispersion relation of the DAW. From [84, 85].*

dramatically towards zero again. In this range the imaginary part of the wave vector jumps from small values, i.e. low damping, to large values. For $\omega > \omega_{pd}$ an overcritically damped DAW is found. This region with $\omega > \omega_{pd}$ was not accessible in the case of no damping. With damping present, this region can be entered, however only overcritically damped as an evanescent wave.

For larger friction constants (Fig. 6.2c) the wave speed ω/q increases and the maximum observable wave number decreases drastically. Moreover, the real and imaginary part of the wave vector are comparable over the entire range: the DAW is found to be strongly damped throughout.

Dust acoustic waves have been observed experimentally in weakly [84, 85] and strongly coupled dusty plasma systems [86]. In the weakly coupled system [84, 85], a dc discharge is driven between an anode disk and the chamber walls. The dust particles are accumulated from a dust tray placed below the anode region. The dust is found to form dust density waves with a certain wavelength and frequency (see Fig. 6.3a). By applying a sinusoidal voltage on the anode the wave can be driven and the dispersion relation is obtained (Fig. 6.3b). The wave shows a linear, acoustic dispersion in agreement with the DAW at long wavelengths.

In a different experiment [86], dust-acoustic waves have been driven in a plasma crystal by a sinusoidal voltage on a wire close to the crystal. The propagation of the wave in the crystal was observed by video cameras and the corresponding wave length and damping length are derived. The measured dispersion relation was found to be in close agreement with a damped DAW, although the system is strongly coupled. Compare the measured dispersion relation in Fig. 6.4b) with that of the calculated in Fig. 6.2c).

6.2. Ion-Flow Driven Dust Acoustic Waves

In a number of experiments under different conditions (dc or rf discharges in the laboratory or under microgravity) self-excited dust acoustic waves appear (e.g. [84, 87, 88, 89, 90, 91] to list a few), see also Fig. 6.5 and also Fig. 6.3. The ambipolar or sheath electric field that confines the dust usually also drives an ion flow. Hence, essentially every dust cloud in the experiment is penetrated by streaming ions. As the two-stream instability in “ordinary” plasmas excites slow space charge waves, here in a dusty plasma, the ion current excites the dust acoustic waves.

The dispersion relation of such a driven dust acoustic wave can be written in simplified form as

$$\epsilon(\omega, q) = 1 + \frac{1}{q^2 \lambda_{D,e}^2} - \frac{\omega_{pi}^2}{\Omega_i(\Omega_i + i\nu_i) - q^2 v_{th,i}^2} - \frac{\omega_{pd}^2}{\omega(\omega + i\beta)} = 0 \quad , \quad (6.11)$$

where

$$\Omega_i = \omega - q u_i$$

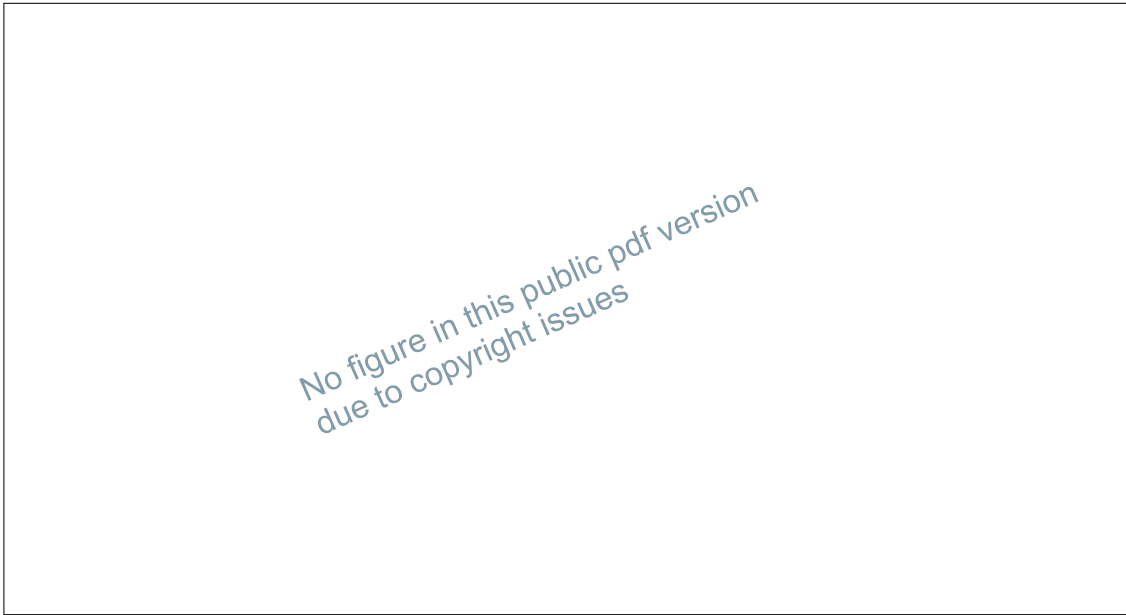


Figure 6.4: *a) Wire excitation of the DAW. The wave is driven by a sinusoidal voltage on the wire close to a plasma crystal. b) Measured dispersion of the DAW: real and imaginary part of the wave vector as a function of wave frequency. From [86].*

is the Doppler-shifted frequency that the drifting ion “see”. Hence, the ion term includes the drifting ions as well as ion-neutral collisions in form of the collision frequency ν_i . For the electrons, again, we have taken the low-frequency limit since we are interested in the very low-frequency dust acoustic waves [compare Eq. (5.5)]. For the dust, temperature is neglected (i.e. $v_{th,d} = 0$), but friction with the neutral gas is included by the Epstein friction coefficient β .

The dispersion relation has, in general, 4 complex roots for the frequency $\omega = \omega_r + i\omega_i$, but we are interested only in the very low frequency limit $\omega \leq \omega_{pd} \ll \omega_{pi}, \omega_{pe}$ (since we are dealing with self-excited waves here we analyze the situation with real and imaginary wave frequencies instead, as above, with complex wave vectors). Figure 6.6 shows the calculated real and imaginary parts of the frequencies for the ion-flow driven waves according to Eq. (6.11) in comparison to the undriven case according to Eq. (6.9). First, it is seen that the dispersion for the two cases look quite different. The attainable real wave frequencies are higher for the driven case. They can even exceed ω_{pd} . The imaginary part of the frequency for the driven wave is positive for a large range of wave vectors \mathbf{q} indicating that the wave is (exponentially) growing in time. Hence, the driven waves are unstable despite the presence of friction of the dust particles with the neutral gas (as accounted for by β). Only for very short waves ($q\lambda_{D,i} \approx 1$) wave damping occurs. The most unstable wave is found for $q\lambda_{D,i} \approx 0.5$ with $\omega_r \approx \omega_{pd}$ under the chosen conditions

(which are similar to that of Ref. [88]).

In contrast a wave without the ion-flow drive under the same conditions shows a slow increase of the wave frequency (real part) from zero towards the dust plasma frequency ω_{pd} . The imaginary part is almost constantly negative at $-\beta/2$ indicating the wave damping by neutral gas friction. Very long waves ($q \rightarrow 0$) are completely damped.

Hence, the (almost) omnipresent ion flow can excite dust acoustic waves against the neutral gas damping. The wave dispersion is accordingly modified and quantitatively differs from the simple undriven case. It has also been shown that the dust waves can be driven under an angle relative to the ion motion [90].

6.3. Dust Ion-Acoustic Wave

The next wave type to be discussed is the dust ion-acoustic wave. The dust ion-acoustic wave is the usual ion-acoustic wave where also the dust has been taken into account. In contrast to the DAW where the dust is the moving species, the dust particles are considered as immobile in the DIAW. The wave frequencies are of the order of the ion plasma frequency $\omega_{pi} \gg \omega_{pd}$. The influence of the dust lies only in the reduction of the free electron density since a certain fraction of the electrons is attached to the dust. We

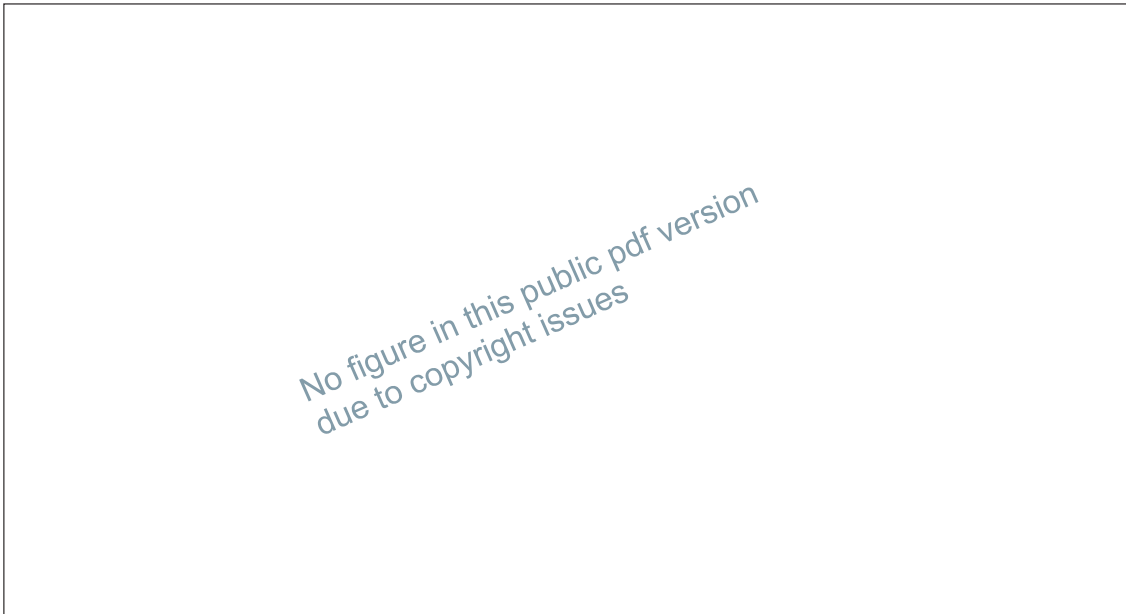


Figure 6.5: Snap shots of naturally excited DAWs. (a) DAW in a dc discharge in a glass tube, (b) DAW in a dc anodic plasma, (c) DAW in an rf discharge under microgravity. From [89, 88, 90].

apply the equation of continuity, the momentum equation and Poisson's equation for the ions

$$\frac{\partial n_i}{\partial t} + \frac{\partial}{\partial x}(n_i v_i) = 0 \quad (6.12)$$

$$\frac{\partial v_i}{\partial t} + v_i \frac{\partial v_i}{\partial x} = \frac{e}{m_i} \frac{\partial \phi}{\partial x} \quad (6.13)$$

$$\frac{\partial^2 \phi}{\partial x^2} = -\frac{e}{\epsilon_0} (n_i - n_e) . \quad (6.14)$$

These equations are exactly those which are used to derive the dispersion relation of the ion-acoustic wave. In comparison to the equations used to describe the DAW, here, in the momentum equation the kinetic pressure of the ions and the friction force are neglected. Poisson's equation does not include the dust since the dust is immobile. The electrons are treated as Boltzmann distributed

$$n_e = n_{e0} \exp\left(\frac{e\phi}{kT_e}\right) .$$

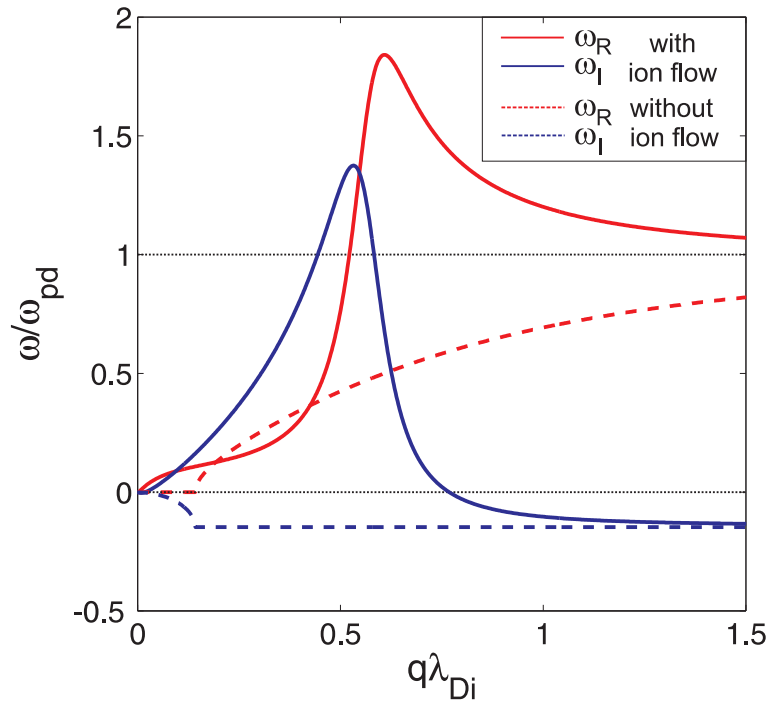


Figure 6.6: Dispersion relation of the dust acoustic wave excited by an ion flow (solid lines) according to Eq. (6.11). In comparison the dispersion of the undriven DAW according to Eq. (6.9) is also shown (dashed lines). The red and blue lines indicate the real and imaginary part of the wave frequency for a real wave vector \mathbf{q} , respectively.

The only place where the dust properties enter is the quasineutrality condition

$$\mathbf{n}_{i0} = \mathbf{n}_{e0} + Z_d \mathbf{n}_{d0} \quad .$$

Thus, here, the undisturbed electron and ion densities are different since a fraction of the electrons is bound on the dust. The equations are solved analogously as for the DAW. The dispersion relation of the DIAW is then given as

$$\omega^2 = \frac{\omega_{pi}^2 \lambda_{D,e}^2 q^2}{1 + q^2 \lambda_{D,e}^2} = \left(\frac{\mathbf{n}_{i0}}{\mathbf{n}_{e0}} \right) \frac{kT_e}{m_i} \frac{q^2}{1 + q^2 \lambda_{D,e}^2} \quad (6.15)$$

which is that of the pure ion-acoustic wave with the additional factor of $\mathbf{n}_{i0}/\mathbf{n}_{e0} > 1$. The dispersion relation of the DIAW is shown in Fig. 6.7 in comparison to the usual ion-acoustic wave. The sound speed of the DIAW (ω/q for $q \rightarrow 0$) is larger than that of the DIAW by the additional factor $(\mathbf{n}_{i0}/\mathbf{n}_{e0})^{1/2}$, namely

$$C_{\text{DIAW}} = \sqrt{\frac{\mathbf{n}_{i0}}{\mathbf{n}_{e0}}} \sqrt{\frac{kT_e}{m_i}} \quad . \quad (6.16)$$

Thus, with increasing dust charge density and thus reduced electron density the speed of the DIAW will increase in comparison to the pure ion-acoustic wave. The DIAW has the same maximum frequency, the ion plasma frequency ω_{pi} . The DIAW can be obtained from the ion-acoustic wave by rescaling the $q\lambda_{D,e}$ -axis since for the DIAW the electron Debye length differs from that of the IAW due to the reduced electron density.

Experimentally, the DIAW has been observed in a Q-machine plasma, where dust has been immersed [92]. It was found that the wave speed of the IAW increases when dust is present (see Fig. 6.8). The increase of the wave speed has been taken as an indication of the existence of the DIAW.

6.4. Other Wave Types

Theoretically, a number of additional waves types are discussed for weakly coupled dusty plasmas. Among those are the dust-cyclotron wave and the dust ion-cyclotron wave. Others are dust-Alfvén waves or the dust-Whistler waves.

The dust cyclotron wave and dust ion-cyclotron wave are again the exact twins of the ion-cyclotron waves. In the dust-cyclotron wave the dust is the mobile species. The ions in the “usual” ion-cyclotron wave are replaced by the dust and both electrons and ions take the role of the electrons. Consequently, the wave dispersion relation of the dust-cyclotron wave reads as

$$\omega^2 + i\beta\omega = \omega_{cd}^2 + \epsilon Z_d^2 \frac{kT_i}{m_d} q^2$$

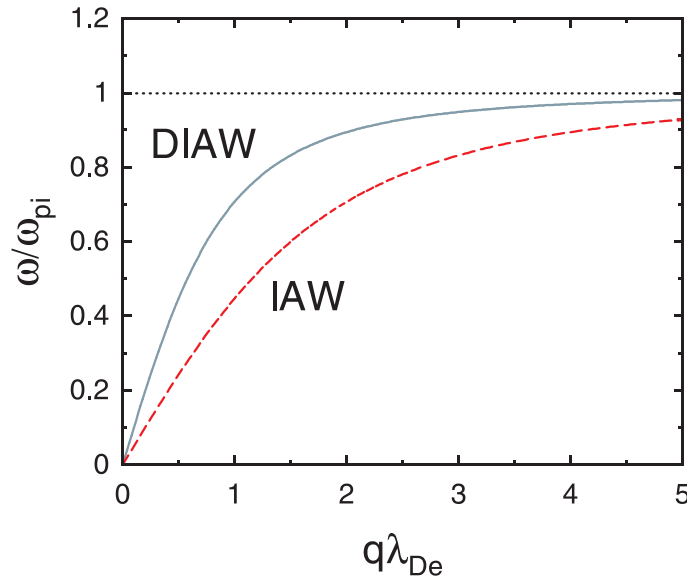


Figure 6.7: Dispersion relation of the DIAW in comparison to the usual ion-acoustic wave (IAW).

where $\omega_{cd} = Z_d e B / m_d$ is the cyclotron frequency of the dust at the magnetic field strength B . Obviously, it is the same dispersion relation as for the DAW, only shifted by the cyclotron frequency. The “usual” ion-cyclotron wave dispersion is known to be

$$\omega^2 = \omega_{ci}^2 + \frac{kT_e}{m_i} q^2$$

with the ion cyclotron frequency $\omega_{ci} = eB/m_i$. So, the ion-acoustic wave speed of the ion-cyclotron wave is replaced by the dust-acoustic wave speed for the dust-cyclotron wave.

Similarly, in the dust ion-cyclotron wave the dust is immobile and the ion-cyclotron dispersion includes only the term $n_{i0}/n_{e0} > 1$ to account for the electrons bound on the dust. The dispersion then is

$$\omega^2 = \omega_{ci}^2 + \left(\frac{n_{i0}}{n_{e0}} \right) \frac{kT_e}{m_i} q^2$$

Similar to the dust ion-acoustic wave, dust ion-cyclotron waves have been driven in a magnetized Q-machine plasma [92]. There, an increased amplitude of the ion-cyclotron wave is observed with increased dust charge density (see Fig. 6.9). This is not a direct measurement of the increased phase speed as in the case of the DIAW, but it demonstrates that the presence of dust allows an easier excitation of the ion-cyclotron wave.

Thus, the situation is completely analogous to the DAW/DIAW wave dispersion.



Figure 6.8: (a) *Experimental setup for the observation of the DIAW. The dust is immersed into the plasma by a rotating dust “drum”.* (b) *Measured velocity of the DIAW with increasing dust charge density ϵZ_D . From [92].*

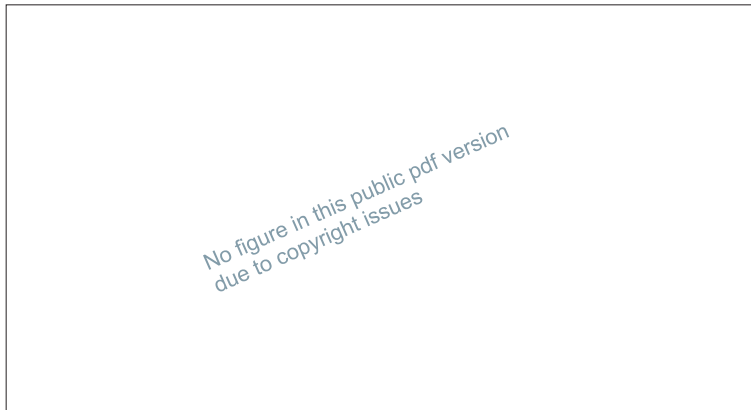


Figure 6.9: *Wave amplitude of the dust ion-cyclotron wave with increasing dust density. The wave amplitude is normalized to the case of no dust. From [92].*

Finally, a number of dust-influenced waves has been discussed theoretically. However, experimental measurements of such waves are rare. In addition, nonlinear properties of the

various wave types have also been analyzed theoretically. Again, only a few experiments are available. We thus limit the presentation of dust waves in weakly coupled systems to the examples mentioned here.

7. Waves in Strongly Coupled Dusty Plasmas

In this section, dust lattice waves (DLW) will be discussed. As the name suggests, the dust lattice wave requires the particles to be ordered in a crystal lattice. We thus need a strongly coupled dust system. The dust lattice waves will be treated here mostly for the 2D case.

In 2D systems, the dust lattice wave has three different “polarizations”. Compressional, shear and transverse modes will be discussed (see Fig. 7.1). For the compressional (longitudinal) mode, the particle motion is along the wave propagation direction and

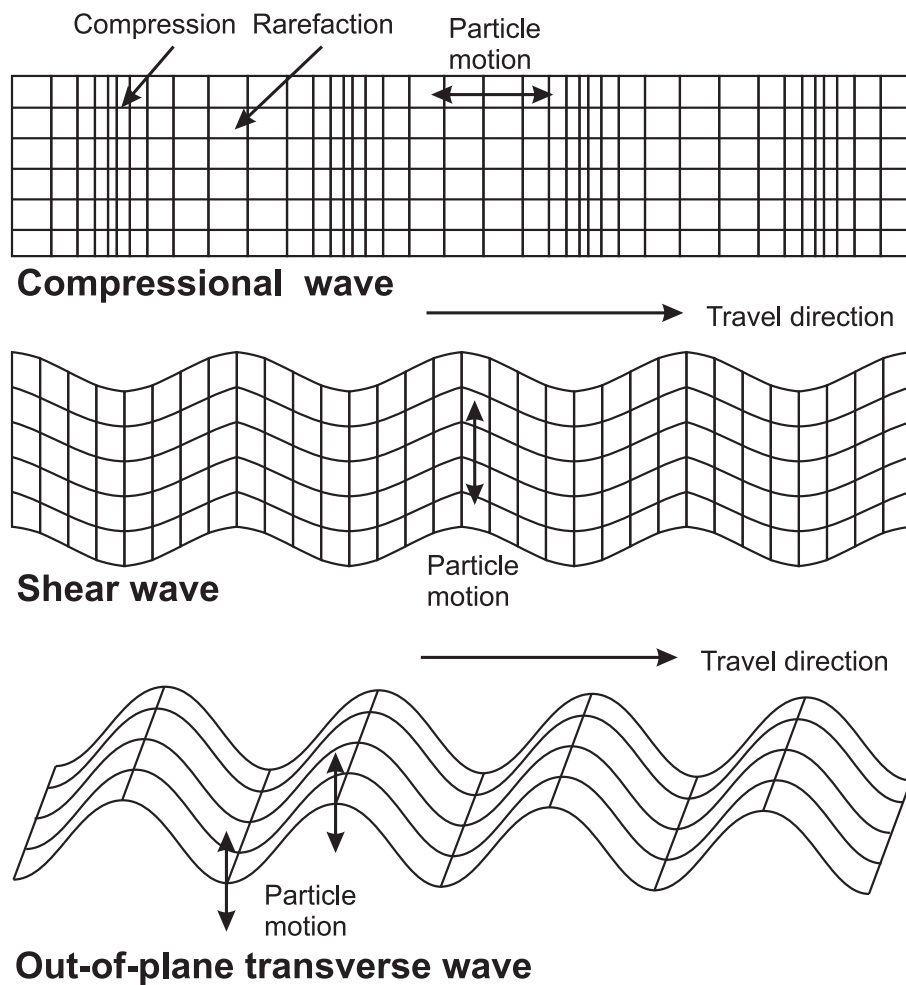


Figure 7.1: *Compressional wave, shear wave and transverse wave.*

leads to compression and rarefaction of the dust. In the shear mode, the dust motion is perpendicular to the wave propagation but inside the 2D crystal plane. The transverse mode also describes particle motion perpendicular to the wave propagation, but here the dust motion is an out-of-plane motion and thus requires the consideration of the vertical confinement of the dust. These three wave types have been observed in the experiment and will be presented in the following.

7.1. Compressional Mode in 1D

The dispersion relation of the 2D-DLW will be illustrated starting from the simpler model of a 1D chain of dust particles. On a linear chain the dust particles have equidistant equilibrium positions $X_n = nb$, where b is the interparticle distance. Neighboring dust particles are considered to be connected by springs of spring constant k . These “spring constants” are of course due to the repulsive interaction between the dust particles as described below. The force on the n -th particle is $F = k(x_{n-1} - x_n)$ due to the spring to the left neighbor and $F = k(x_{n+1} - x_n)$ due to the right neighbor. The equation of motion for the n -th particle then is

$$m_d \ddot{x}_n - m_d \beta \dot{x}_n = k(x_{n-1} - 2x_n + x_{n+1}), \quad (7.1)$$

where x_n is the elongation of the n -th particle from its equilibrium position X_n . Here, also friction with the neutral gas is included. Using the ansatz for waves on a linear chain $x_n = A \exp(i\mathbf{q}b - i\omega t)$ with wave vector \mathbf{q} and wave frequency ω the equation of motion becomes

$$-m_d \omega^2 - i m_d \beta \omega = k(e^{i\mathbf{q}b} + e^{-i\mathbf{q}b} - 2) = 2k(\cos \mathbf{q}b - 1)$$

and the dispersion relation (see also Sec. 5.4.)

$$\omega^2 + i\beta\omega = 4 \frac{k}{m_d} \sin^2 \left(\frac{\mathbf{q}b}{2} \right) \quad (7.2)$$

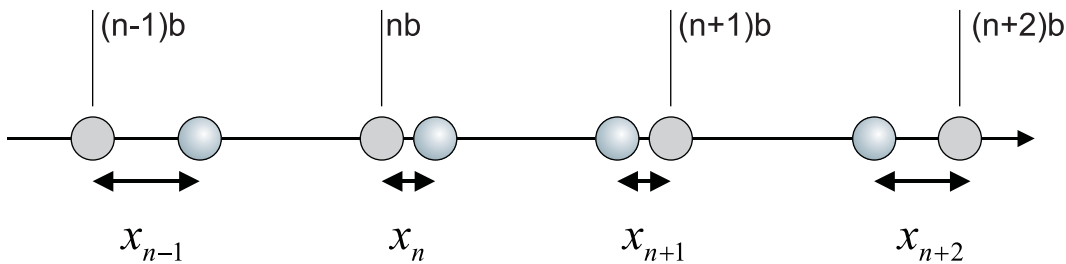


Figure 7.2: Sketch of a linear dust arrangement with longitudinal particle displacements. The grey circles indicate the equilibrium positions in the chain, the bluish the instantaneous positions in the traveling wave.

is obtained. This is the well-known dispersion relation of waves on a linear chain which is also very familiar in condensed matter physics.

Now, the spring constant k has to be related to the repulsive interaction between the dust particles. From mechanics it is known that the spring constant is just the second derivative of the interaction potential. This yields for a Debye-Hückel interaction at the interparticle distance b

$$k = \left. \frac{d^2\phi}{dx^2} \right|_{x=b} = \frac{Z_d^2 e^2}{4\pi\epsilon_0 b^3} e^{-\kappa} (2 + 2\kappa + \kappa^2) \quad , \quad (7.3)$$

where the screening strength $\kappa = b/\lambda_s$ has been used. The corresponding dispersion can then be written as

$$\omega^2 + i\beta\omega = \frac{Z_d^2 e^2}{\pi\epsilon_0 m_d b^3} e^{-\kappa} (2 + 2\kappa + \kappa^2) \sin^2 \left(\frac{qb}{2} \right) \quad , \quad (7.4)$$

Finally, the dispersion relation can be extended to include also the influence of many neighbors. Therefore, simply the “springs” to all other neighbors at distance ℓb have to be considered yielding [93]

$$m_d \ddot{x}_n - m_d \beta \dot{x}_n = \sum_{\ell=1}^{\infty} k(\ell b) (x_{n-\ell} - 2x_n + x_{n+\ell}) .$$

The full 1D dispersion relation then is given by [93]

$$\omega^2 + i\beta\omega = \frac{1}{\pi} \omega_{pd}^2 \sum_{\ell=1}^{\infty} \frac{e^{-\ell\kappa}}{\ell^3} (2 + 2\ell\kappa + \ell^2\kappa^2) \sin^2 \left(\frac{\ell qb}{2} \right) \quad , \quad (7.5)$$

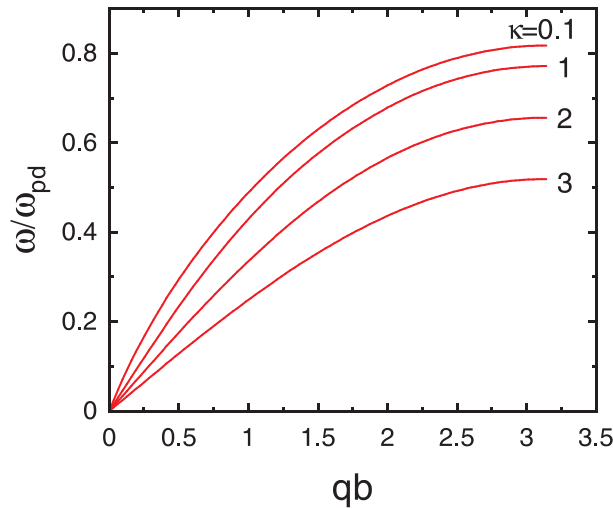


Figure 7.3: Dispersion relation of the 1D dust lattice wave for different values of the screening strength κ at zero damping.

where the dust plasma frequency

$$\omega_{\text{pd}}^2 = \frac{Z_d^2 e^2}{\epsilon_0 m_d b^3} \quad (7.6)$$

has been introduced for the strongly coupled case by identifying $\mathbf{n}_d \approx \mathbf{b}^{-3}$ in (6.1). It should, however, be noted that the dust plasma frequency is used here only because of the mathematical similarity. It does not correspond to a collective oscillation of the dust particles relative to a stationary background. Rather this frequency is related to the Debye frequency in solid-state physics.

The dispersion relation of the compressional 1D dust lattice wave is shown in Fig. 7.3 for different values of κ . The dispersion relation has approximately the form of a sine function. For small wave numbers (long wavelengths) the wave is acoustic ($\omega \propto q$), whereas the dispersion bends over for larger wave numbers and finally reaches a maximum where $\partial\omega/\partial q \approx 0$. The maximum wave number is given by $q\mathbf{b} = \pi$ which corresponds to a wave length $\lambda = 2\mathbf{b}$. This wavelength is the shortest possible wave length on a string of particles and corresponds to 180-degree out-of-phase motion between nearest neighbor particles. As for the DAW, the wave frequencies decrease with increasing κ .

The sound speed of the 1D compressional DLW is given by

$$c = \lim_{q \rightarrow 0} \frac{\partial\omega}{\partial q} = \lim_{q \rightarrow 0} \frac{\omega}{q} = \sqrt{\frac{Z_d^2 e^2}{\epsilon_0 m_d b}} \sqrt{\frac{1}{4\pi} \sum_{\ell=1}^{\infty} \frac{e^{-\ell\kappa}}{\ell} (2 + 2\ell\kappa + \ell^2\kappa^2)} = c_0 f(\kappa) \quad , \quad (7.7)$$

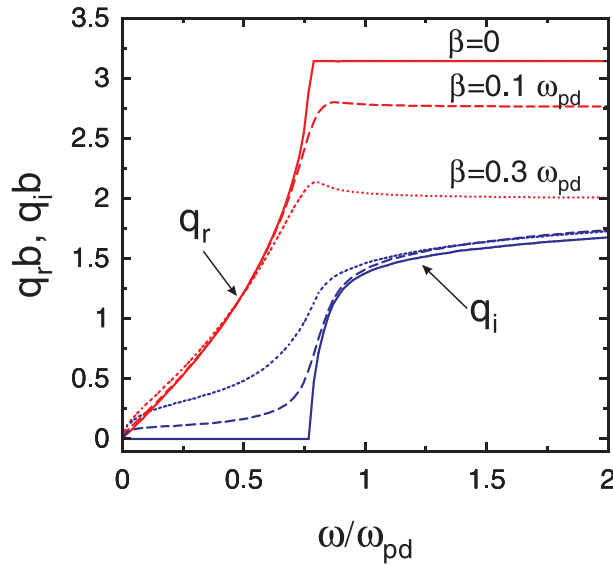


Figure 7.4: Dispersion relation of the 1D dust lattice wave for different values of the damping strength β at $\kappa = 1$.

where

$$c_0 = \sqrt{\frac{Z_d^2 e^2}{\epsilon_0 m_d b}} \quad (7.8)$$

is a measure of the sound speed of dust lattice waves in plasma crystals and

$$f(\kappa) = \sqrt{\frac{1}{4\pi} \sum_{\ell=1}^{\infty} \frac{e^{-\ell\kappa}}{\ell} (2 + 2\ell\kappa + \ell^2\kappa^2)} \quad (7.9)$$

is a function of κ only and takes into account the crystal order.

The effect of damping is shown in Fig. 7.4 where real and imaginary part of the wave vector are shown as a function of wave frequency. An analytical solution exists when only nearest neighbor interaction ($\ell = 1$) in Eq. (7.5) is taken account. Otherwise the solution has to be found numerically. Fig. 7.4 shows the case of many neighbor interaction. It can be seen that with increased damping the maximum real wave vector is reduced. In the same way, the imaginary part (corresponding to the inverse damping length) increases. Similar to the dispersion relation of the DAW, in the DLW the imaginary wave vector grows dramatically when the wave frequency comes close to the maximum wave frequency $\omega_{\max} \approx 0.8\omega_{\text{pd}}$ (compare Fig. 7.3). Heavily damped waves are found when the wave enters a frequency regime that was not accessible in the frictionless case where $\omega > \omega_{\max}$.

7.2. Dust Lattice Waves in 2D

The dispersion relation of 1D waves can be extended to the case of a two-dimensional lattice in a straightforward manner for the compressional mode as well as for the shear mode [94, 95].

There, one has to take into account the hexagonal order of the 2D lattice. For the compressional wave, the dispersion relation then reads

$$\omega^2 + i\beta\omega = \frac{1}{2\pi} \omega_{\text{pd}}^2 \sum_{\ell, m=1}^{\infty} \frac{e^{-\tilde{r}\kappa}}{\tilde{r}^5} \left(\ell^2 (3 + 3\tilde{r}\kappa + \tilde{r}^2\kappa^2) - \tilde{r}^2 (1 + \tilde{r}\kappa) \right) \sin^2 \left(\frac{\ell q b}{2} \right), \quad (7.10)$$

where $\tilde{r} = \sqrt{\ell^2 + m^2}$. The term after the sum is just the second derivative of the Yukawa potential in x -direction at the lattice site (ℓ, m) . Here, it is assumed that the wave propagates in x -direction (along \vec{a}_1 in Fig. 7.5). Thus, the force (related to the derivative) and thus the particle motion is in the same direction as the wave. Hence, this describes a compressional (longitudinal) wave mode.

For the shear wave one also has to take the second derivative, but in the y -direction (along \vec{a}_2), when the wave is propagating in the x -direction. The force and the motion are in the y -direction whereas the wave propagates in the x -direction. Hence, the wave is a shear wave. (Strictly speaking, this type of wave can be termed transverse wave.

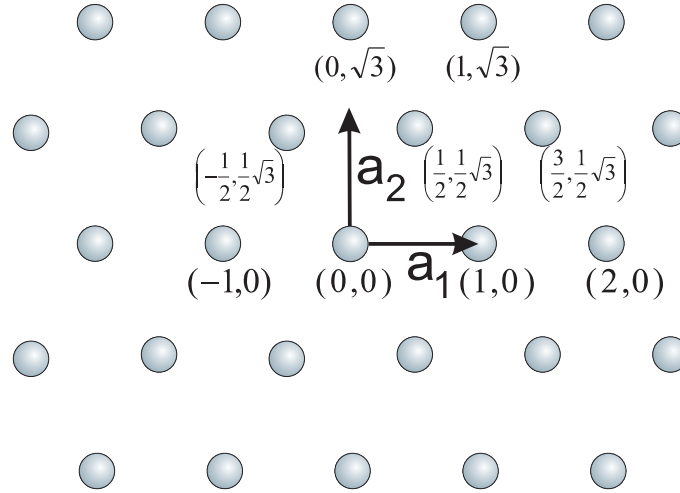


Figure 7.5: Hexagonal lattice with the lattice vectors \mathbf{a}_1 and \mathbf{a}_2 . The expression in brackets (ℓ, \mathbf{m}) gives the 2D particle position in units of the interparticle distance \mathbf{b} .

However, we like to reserve the term “transverse wave” for the out-of-plane wave discussed in Sec. 7.7.)

That yields

$$\omega^2 + i\beta\omega = \frac{1}{2\pi} \omega_{\text{pd}}^2 \sum_{\ell, \mathbf{m}=1}^{\infty} \frac{e^{-\tilde{r}\kappa}}{\tilde{r}^5} \left(m^2 (3 + 3\tilde{r}\kappa + \tilde{r}^2 \kappa^2) - \tilde{r}^2 (1 + \tilde{r}\kappa) \right) \sin^2 \left(\frac{\ell \mathbf{q} \mathbf{b}}{2} \right). \quad (7.11)$$

The shear wave character is seen from the fact that the term after the sum includes \mathbf{m} (denoting the \mathbf{y} -direction) whereas the sin-expression includes ℓ (denoting the \mathbf{x} -direction).

The computed dispersion relation of the compressional and shear 2D dust lattice wave is shown in Fig. 7.6. The compressional mode has a form that is very similar to the 1D-case: For long wavelengths $\mathbf{q} \mathbf{b} \ll 1$ the dispersion is acoustic. For shorter wave lengths the compressional mode becomes dispersive and attains a maximum near $\mathbf{q} \mathbf{b} = \pi$. In contrast, the shear mode is nearly acoustic for all wavelengths. Thus, the shear mode is only little dispersive.

It is readily seen here, that the sound speed of the compressional mode is much larger than that of the shear mode. The sound speeds of the compressional and shear mode are given by [94]

$$\mathbf{c}_{\text{comp}} = \mathbf{c}_0 \mathbf{f}_{\text{comp}}(\kappa) \quad \mathbf{c}_{\text{shear}} = \mathbf{c}_0 \mathbf{f}_{\text{shear}}(\kappa) \quad (7.12)$$

where

$$\mathbf{f}_{\text{comp}} = \sqrt{\frac{1}{4\pi} \sum_{\tilde{r}} \frac{e^{-\tilde{r}\kappa}}{\tilde{r}} \left(\frac{15}{8} (1 + \tilde{r}\kappa) + \frac{9}{8} \tilde{r}^2 \kappa^2 \right)}$$

and

$$f_{\text{shear}} = \sqrt{\frac{1}{4\pi} \sum_{\tilde{r}} \frac{e^{-\tilde{r}\kappa}}{\tilde{r}} \left(-\frac{3}{8}(1 + \tilde{r}\kappa) + \frac{3}{8}\tilde{r}^2\kappa^2 \right)}$$

where the summation is over all possible distances in the hexagonal lattice \tilde{r} . Comparing the sound speed of the compressional 1D and 2D waves one finds only slight differences, e.g. the factor $15/8$ instead of 2 and $9/8$ instead of 1. These factors are the effect of the hexagonal lattice structure. The sound speed of the shear mode contains a negative term which substantiates that the sound speed of the shear mode is smaller than that of the compressional.

This dispersion holds for finite values of the screening strength κ . For pure Coulomb interaction $\kappa = 0$ the sum in the compressional dispersion relation (7.10) would diverge. Thus, for pure Coulomb interaction it is found that $\omega \propto \sqrt{q}$ for long wavelengths (and thus the sound speed $c = \omega/q \rightarrow \infty$ for $q \rightarrow 0$).

Moreover, the wave dispersion has been discussed for a compressional wave propagating along \vec{a}_1 and a shear wave along \vec{a}_2 . In the general case there can be any arbitrary angle θ of the wave propagation \vec{q} relative to the lattice orientation \vec{a}_1 which has an influence on the dispersion relation [95]. However, that influence only manifests in the very short wavelength regime $qb > 2.5$ when the exact position of the nearest neighbors is probed by the wave.

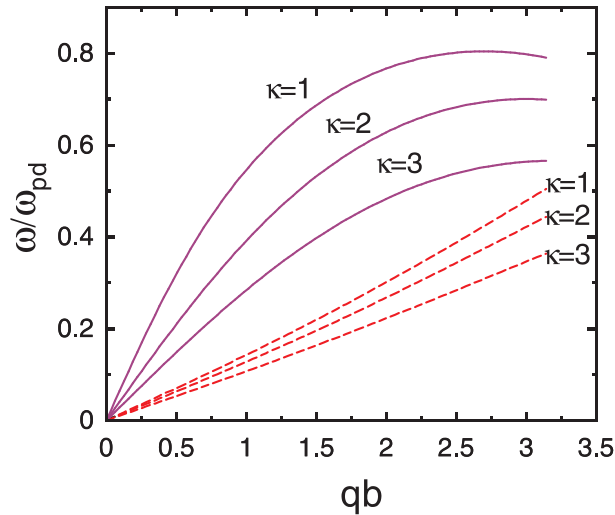


Figure 7.6: Dispersion relation of the 2D dust lattice wave for different values of the screening strength κ (without damping). The solid lines represent the compressional mode, the dashed lines the shear mode.

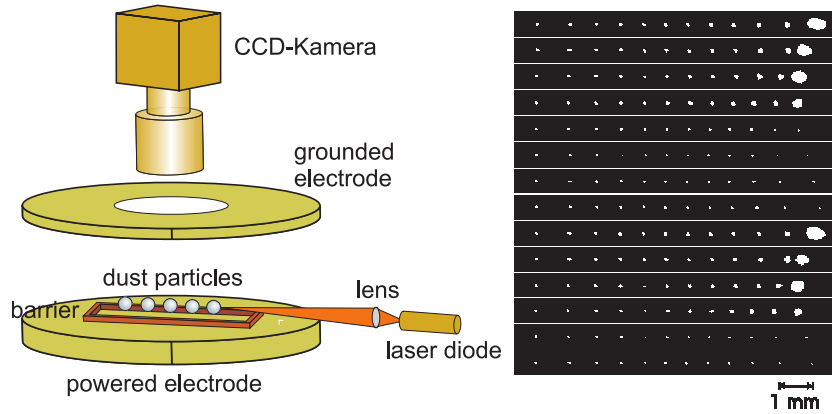


Figure 7.7: a) *Experimental setup for the excitation of 1D dust lattice waves in a chain of dust particles.* b) *Snap shots of the dust chain oscillation. The first particle shows strong “blooming” when hit by the laser beam. One can see that a wave is propagating into the dust chain. After [96].*

7.3. Compressional 1D Dust Lattice Waves: Experiment

Compressional dust lattice waves in 1D and 2D systems have been identified and measured by Homann et al. [96, 97]. Here, we start with the presentation of the 1D results.

A linear chain of dust particles has been realized by placing a rectangular barrier on the electrode (see Fig. 7.7a and Sec. 8.1.). Waves in the dust chain have been excited by focusing a laser beam onto the first particle. The laser beam is then switched “on” and “off” periodically and a wave is launched into the linear chain of dust particles. The oscillations are clearly seen in the video snap shots (Fig. 7.7b). It is also obvious that the amplitude of the wave decreases with distance in the chain due to friction with the neutral gas. The wave motion is then analyzed directly from the video data in terms of phase and amplitude. Therefore the oscillations of each particle in the chain relative to its equilibrium position is identified (see Fig. 7.8a). It is immediately seen that the phase of the oscillation progresses from one particle to next. Correspondingly also the oscillation amplitude decreases. The phases and amplitudes of all particles are then derived and analyzed as a function of equilibrium position (Fig. 7.8b,c). The observed linear dependence of the phase with particle position directly reflects the wave length λ and thus the real part of the wave vector $\mathbf{q}_r = 2\pi/\lambda$. The amplitude of the wave is found to decrease exponentially with distance from the first particle. This determines the damping length L and correspondingly the imaginary part of the wave vector $\mathbf{q}_i = 1/L$. Thus, the wave in the chain propagates as

$$\begin{aligned} x &= A \exp(iq_x - i\omega t) = A \exp(i(\mathbf{q}_r + i\mathbf{q}_i)x - i\omega t) \\ &= A \exp(i\mathbf{q}_r x - i\omega t) \exp(-\mathbf{q}_i x) \quad , \end{aligned}$$

where A is the oscillation amplitude of the first particle and x measures the distance from the first particle. The wave vector q_r and q_i depend on the wave frequency ω .

By measuring the imaginary and real part of the wave vector in such a way for different wave frequencies, the entire dispersion relation is identified. Fig. 7.9 shows the wave vectors as a function of wave frequency. The measured dispersion relation is then compared with the theoretical dispersion relation of the dust-acoustic wave according to Eq. (6.9) and of the dust lattice wave according to Eq. (7.5). It is clearly seen that the DAW does not match the measured dispersion relation whereas the DLW is in very good agreement. Thus, the 1D dust chain does not exhibit DAW-like wave motion in contrast to the finding of Section 6.1. where extended systems with DAW dispersion have been found. Here, the dispersion is clearly of DLW type.

The measured dispersion relation also allows to determine the screening strength κ . This is demonstrated in Fig. 7.9 where the measured dispersion is shown in comparison with theoretical curves for a range of κ -values. Best agreement between experiment and theory is obtained for a screening strength of $\kappa = 1.1$, reasonable agreement is found in

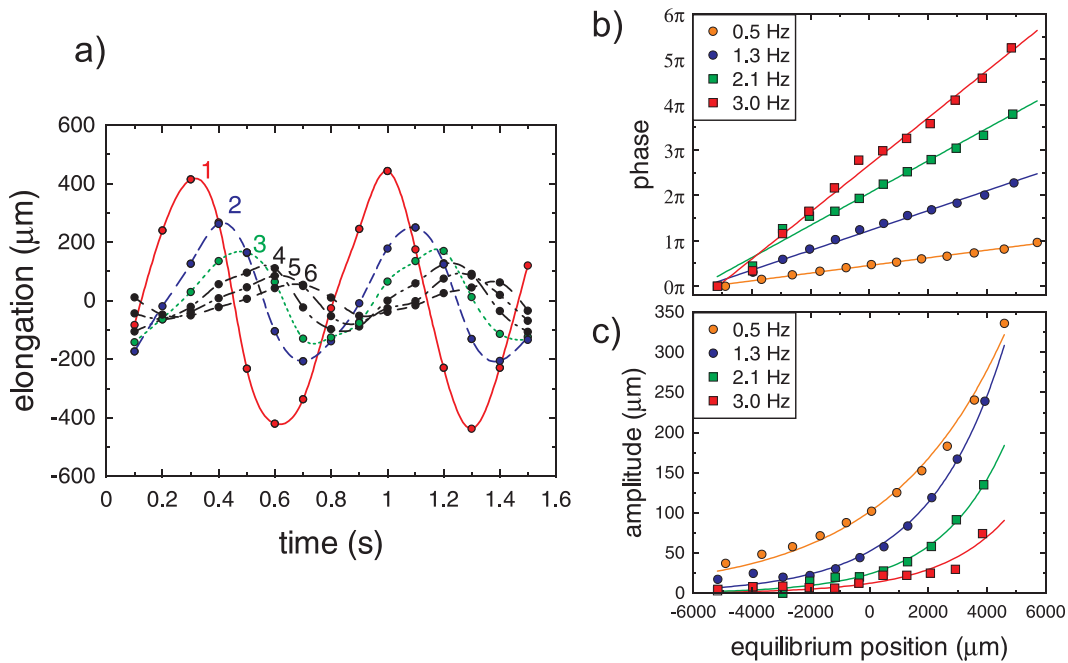


Figure 7.8: a) Particle oscillation relative to the equilibrium position as a function of time. The numbers denote the particle in the chain, where the first particle is the one hit by the beam. b) Phase and c) amplitude of the particle oscillation derived from a) as a function of position in the chain for different excitation frequencies. After [96].

the range between $\kappa = 0.7$ and 1.5, thus

$$\kappa = b/\lambda_s = 1.1 \pm 0.4 \quad . \quad (7.13)$$

This means that the screening length λ_s in the dust system is of the order of the interparticle distance b (or the other way round). In this case

$$\lambda_s \approx b = 930 \text{ } \mu\text{m} \quad .$$

This value of the screening length is of the order of the electron Debye length. We will return to the discussion of the screening problem below.

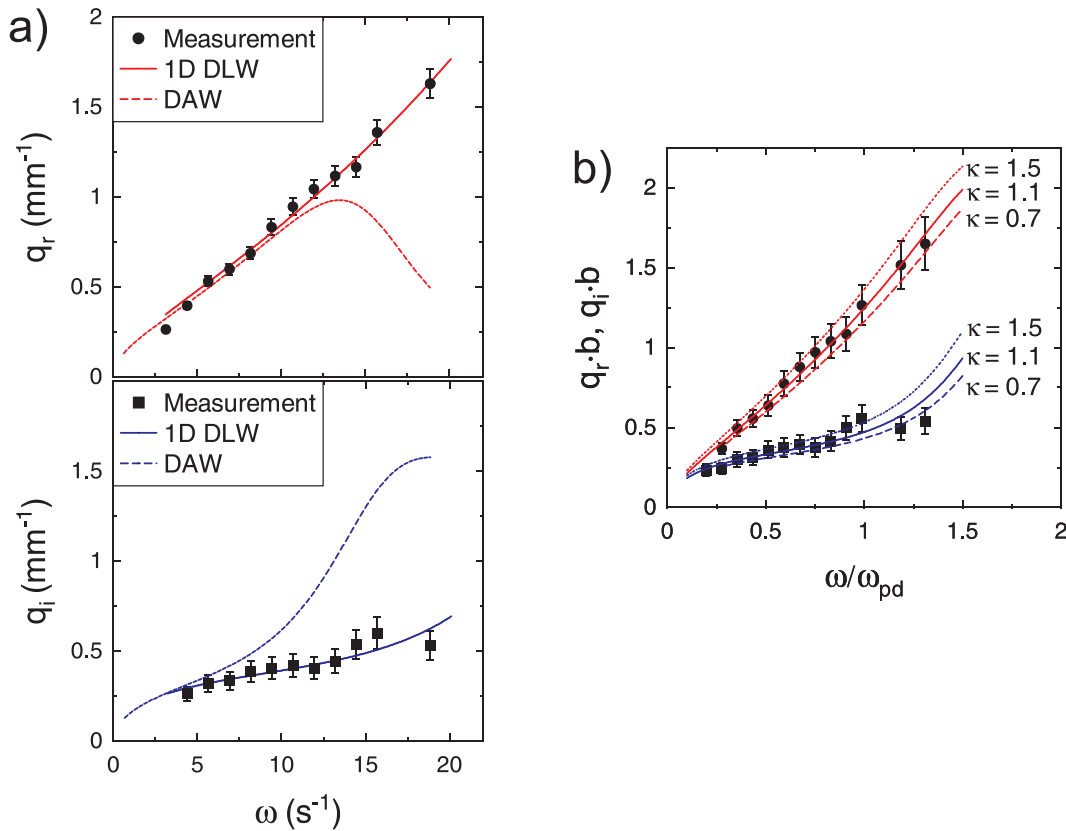


Figure 7.9: *a) Measured real and imaginary wave vectors as a function of wave frequency. The measured dispersion relation is compared to the theoretical dispersion relation of the DAW and DLW. b) Measured dispersion relation in comparison with theoretical DLW dispersions for various values of κ . In this Figure, normalized units ω/ω_{pd} (using the measured dust charge Z_d) and qb (using the measured interparticle distance b) have been used. After [96].*

7.4. Compressional 2D Dust Lattice Waves: Experiment

Experiments which are similar to those described above have been performed to measure the dispersion relation of the compressional DLW in two dimensions [97]. In the 2D case, the laser beam of an Argon ion laser was expanded into a line focus and directed onto the first row of particles in a 2D plasma crystal. By periodic modulation of the laser power a plane wave was launched in the plasma crystal (see Fig. 7.10a). Again, the wave motion of the dust was analyzed in terms of the phase and amplitude (Fig. 7.10b,c) as a function of distance from the excitation region. Similarly, the phase dependence directly reflects the wavelength λ and the amplitude decrease the damping length L for a given excitation frequency. In that way the dispersion relation of the wave has been measured (Fig. 7.10d,e). The measured dispersion was found to show good agreement with the 2D DLW dispersion. From this comparison the screening strength is determined to be $\kappa = 1 \pm 0.3$. So, also in 2D the interparticle distance b and shielding length λ_s are comparable and are found to be close to the electron Debye length.

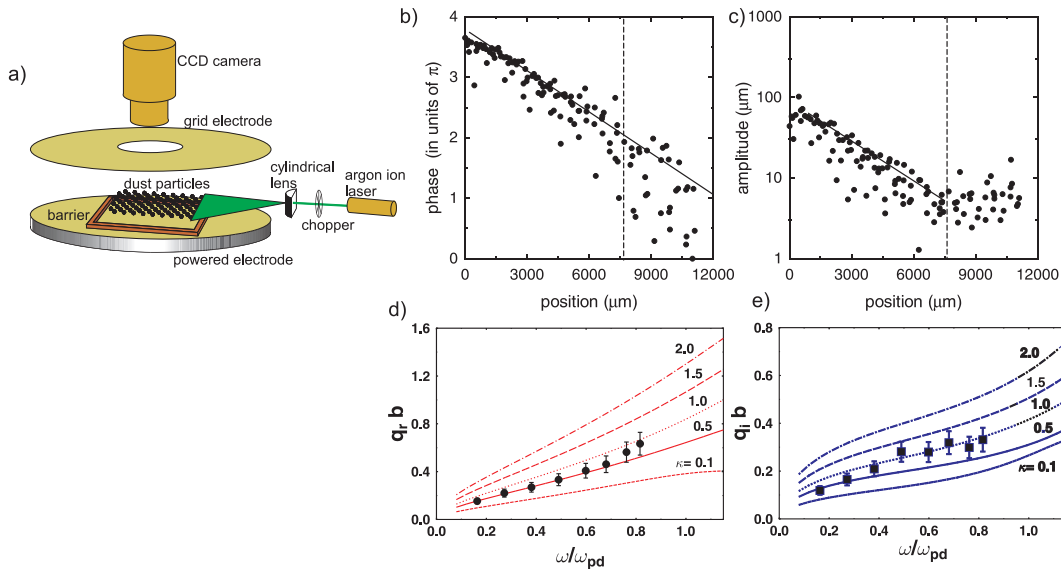


Figure 7.10: (a) Scheme of the experimental setup for the excitation of 2D dust lattice waves. (b) Phase and (c) amplitude of the dust particle motion as a function of distance from the excitation region for an excitation frequency of 2.8 Hz. (d,e) Real and imaginary wave vector as a function of frequency. The symbols denote the experimental data. The lines indicate the dispersion relation of the 2D DLW for various values of the screening strength κ . After [97].

7.5. Shear 2D Dust Lattice Waves: Experiment

Shear dust lattice waves have been observed by Nunomura et al. [98] also using laser beam excitation. There, a short pulse of a narrow laser beam excites a row of particles along the direction of the beam (see Fig. 7.11). The velocity pulse created by the beam propagates in a direction perpendicular to the beam. The dust particle motion and pulse travel direction are perpendicular, thus a shear wave is observed here. The outward velocity of the beam is much smaller than for a compressional pulse and in agreement with the acoustic velocity of the shear wave, see Eq. (7.12).

Recently, Nunomura et al. [99] have investigated shear and compressional waves in great detail by laser excitation. There, they also have studied the wave propagation along different lattice orientations and found reasonable agreement with the theoretical DLW dispersion relation.

7.6. Mach Cones

When an object moves through a medium with a velocity faster than the wave speed in that medium a V-shaped disturbance, the Mach cone, is excited. This phenomenon is

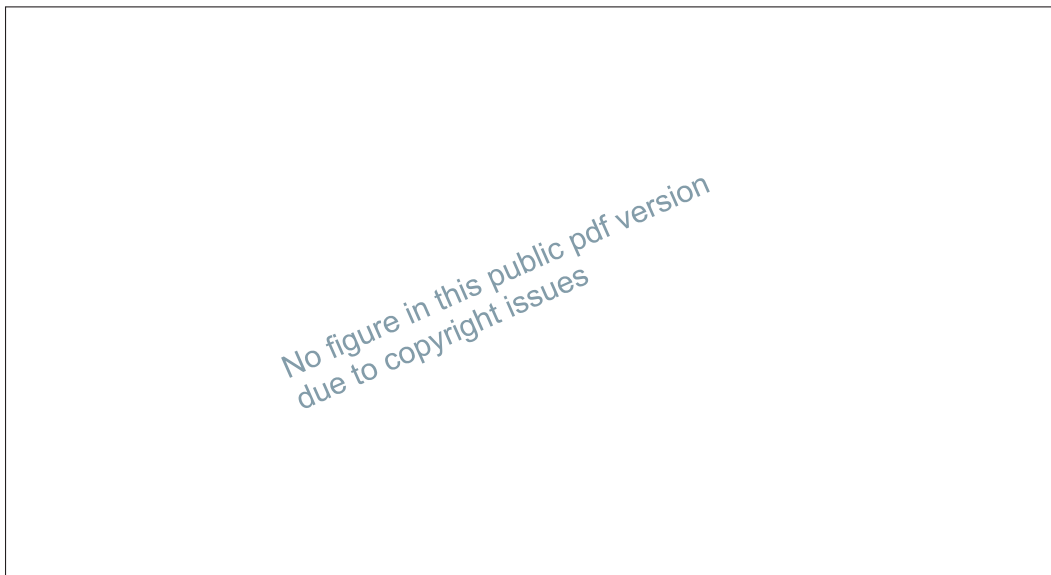


Figure 7.11: *Shear dust lattice waves. (a) Dust particle velocity vectors at certain time steps after a laser beam pulse. The initial laser beam pushed the particles in the central region from right to left. (b) Velocity profiles perpendicular to the beam direction. The central bar indicates the excitation region. From [98].*

well known, e.g. from the sonic boom behind a plane at supersonic velocity. Similarly, Mach cones can be observed in dusty plasmas using objects faster than the acoustic speed of the DLW.

The formation of a Mach cone is illustrated in Fig. 7.12e. The supersonic object moves at a velocity V that creates disturbances on its way at any instant. The disturbances propagate through the medium at the sound speed c . Since $c < V$ the front of the disturbance lags behind the object, thus forming the well-known V-shaped front, the Mach cone. The Mach cone has an opening angle μ that satisfies the relation

$$\sin \mu = \frac{c}{V} \quad . \quad (7.14)$$

Thus from a single measurement of the opening angle μ the sound speed of the DLW is readily obtained from which other parameters like particle charge or screening strength can be determined.

Mach cones in dusty plasmas have first been observed by Samsonov et al. [100, 101]. There, dust particles which accidentally are trapped below the actual 2D plasma crystal are found to move at large, supersonic, speeds at low gas pressure. The disturbance by these lower fast-moving particles excites a Mach cone in the upper plasma crystal.

In a different experiment [102] Mach cones in plasma crystals have been generated using the focal spot of a laser beam that was moved at supersonic speeds V through the crystal using a moving galvanometer scanning mirror (Fig. 7.12a). The laser technique allows the formation of Mach cones in a repetitive and controllable manner.

Figure 7.12b shows a video snap shot where the Mach cone created by the laser spot is easily seen. The opening angle here is about 45° . A more detailed picture is obtained when investigating the absolute values of the dust particle velocities. The particle speeds are shown in a gray-scale plot in Fig. 7.12c. Here, a strong first Mach cone is easily seen. However, additional secondary and tertiary Mach cones are also observable. The first strong cone is just the expected behavior for the Mach cone as described above. The additional features arise from the dispersive nature of the DLW at shorter wavelengths [103]. The laser spot creates wave disturbances at all wavelengths. Due to dispersion short wavelength waves travel at a different velocity than those at long wavelengths. This makes the picture described in Fig. 7.12e more complicated: Like the wave pattern of a moving ship (which is not a Mach cone as described above), the secondary and tertiary Mach cones can be interpreted as interference patterns of the waves launched by the moving laser beam.

From the measurement of the opening angle μ of the first Mach cone at various laser spot velocities the Mach cone relation is verified (see Fig. 7.12d). The sound speed measured here is about 20 mm/s. This is again a very small value which demonstrates that the dynamic processes in dusty plasmas occur on a long time scale.

The Mach cone in Fig. 7.12 is a compressional Mach cone due to excitation of compressional waves. Shear Mach cones by the excitation of shear waves have been demonstrated

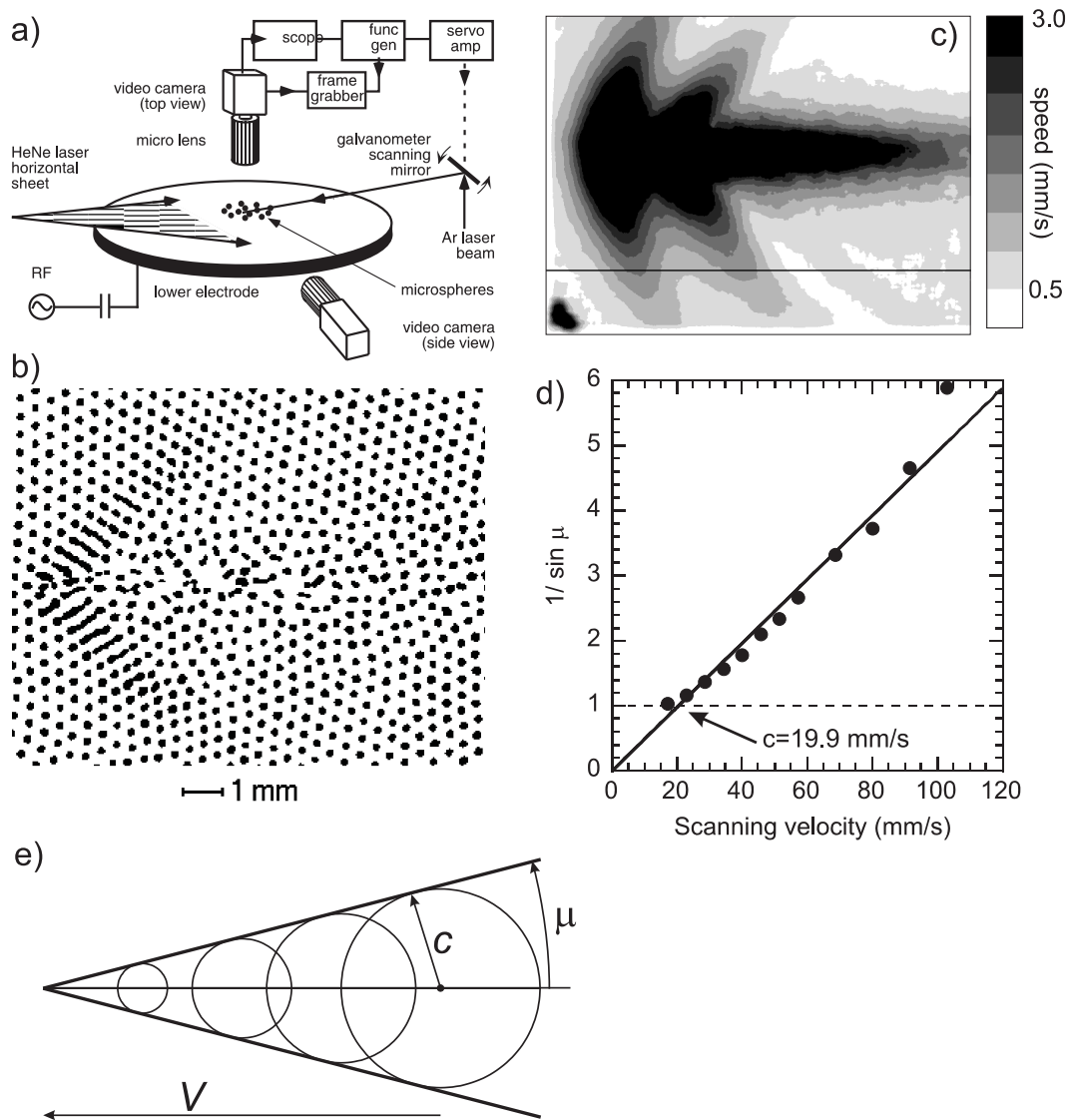


Figure 7.12: *Mach cones in dusty plasmas.* (a) *Scheme of the experimental setup.* (b) *Video snap shot of the dust crystal. The laser spot moves from right to left. A V-shaped disturbance is clearly observable.* (c) *Gray-scale map of the dust particle velocities.* (d) *Test of the Mach cone relation. Plot of $1/\sin \mu$ of the measured cone angle μ as a function of laser spot velocity V . From this, the sound speed is measured to be $c = 19.9$ mm/s.* (e) *Sketch of the Mach cone formation.*

by Nosenko et al. [104]. Shear Mach cones are observed at much lower laser spot velocities V due to the much smaller acoustic velocity of the shear waves.

Mach cones are discussed as a diagnostic tool: Mach cones are assumed to be observ-

able in the rings of Saturn by the Cassini spacecraft after its arrival at Saturn in 2004 [105]. In Saturn's rings, large boulders moving in Keplerian orbits have supersonic speeds relative to the smaller dust particles which move at speeds determined by their electrostatic interactions with Saturn's plasma environment (see Sec. 10.5.). The observation of Mach cones would allow detailed studies of the plasma conditions in the rings.

7.7. Transverse Dust Lattice Waves

All the above mentioned wave types and experiments have dealt with particle motions in the plane of the 2D plasma crystal. We now turn to the transverse dust lattice wave. There, an out-of-plane (vertical) particle motion perpendicular to the wave propagation is expected. Such vertical displacements are stabilized against the Coulomb repulsion of the particles by the vertical confinement potential. The external confinement is essential for this type of wave. Otherwise the wave would not be stable.

For the dispersion of the transverse DLW vertical displacements z_n in a 1D chain of particles are considered (see Fig. 7.13). The equation of motion then reads

$$m_d \ddot{z}_n - m_d \beta \dot{z}_n + m_d \omega_0^2 z_n = k_z (z_{n-1} - 2z_n + z_{n+1}), \quad (7.15)$$

where ω_0 is the strength of the vertical confinement [compare Eq. (3.22)] and k_z is the vertical "spring" constant. Using $\delta z = z_n - z_{n-1} \ll b$, the spring constant is given by

$$F_z = F(r) \frac{\delta z}{r} = F(\sqrt{\delta z^2 + b^2}) \frac{\delta z}{\sqrt{\delta z^2 + b^2}} \approx F(b) \frac{\delta z}{b} = \frac{Z_d^2 e^2}{4\pi\epsilon_0 b^3} e^{-\kappa} (1 + \kappa) \delta z = k_z \delta z, \quad ,$$

where F_z is the vertical component of the Coulomb force $F(\mathbf{r}) = -\partial\phi(\mathbf{r})/\partial\mathbf{r}$. The fact that here the spring constant involves the first derivative of the particle interaction ϕ (in contrast to the second derivative for the compressional and shear wave) states that the equilibrium situation is essentially unstable. For repulsive interaction the transverse elongations would grow indefinitely. The transverse oscillations are only stabilized by the additional counterforce due to the external confinement.

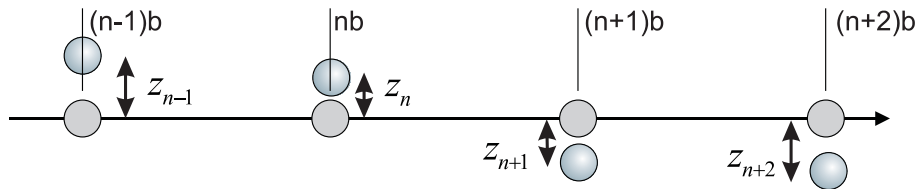


Figure 7.13: Sketch of a linear dust arrangement with transverse particle displacements.

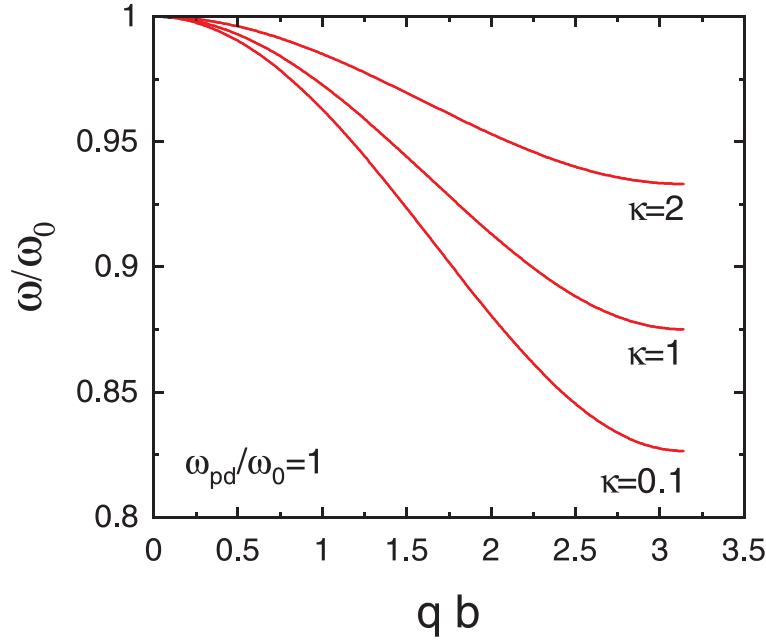


Figure 7.14: Dispersion of the transverse dust lattice wave for different values of κ without damping. The frequency scale, here, is normalized to ω_0 , not ω_{pd} . Also note the limited frequency scale.

Following the above procedure, the dispersion relation of the transverse DLW is given by [106]

$$\omega^2 + i\beta\omega = \omega_0^2 - \frac{1}{\pi}\omega_{\text{pd}}^2 e^{-\kappa} (1 + \kappa) \sin^2\left(\frac{qb}{2}\right). \quad (7.16)$$

One can see that the influence of the vertical confinement ω_0^2 is necessary to yield a stable dispersion relation.* It is interesting to note that this wave is a backward wave ($\partial\omega/\partial q < 0$), that is phase and group velocities move in opposite directions. In addition, the wave frequency approaches a finite value for long wavelengths ($\omega \rightarrow \omega_0$ for $q \rightarrow 0$). Such a type of wave is called “optical wave” in analogy to waves known from condensed matter. For $q \rightarrow 0$ this is a synchronous oscillation of all particles at the resonance frequency of the vertical potential well used for the determination of the dust charge (see Sec. 3.8.).

The calculated dispersion relation is shown in Fig. 7.14. Transverse dust lattice waves have been observed by Misawa et al. [107]. In their experiment, a linear chain of dust particles shows vertical oscillations (see Fig. 7.15) which propagate along the chain. From

*Otherwise $\omega^2 \propto -\omega_{\text{pd}}^2 \sin^2(qb/2)$ yielding a positive imaginary value for ω which indicates exponential growth.

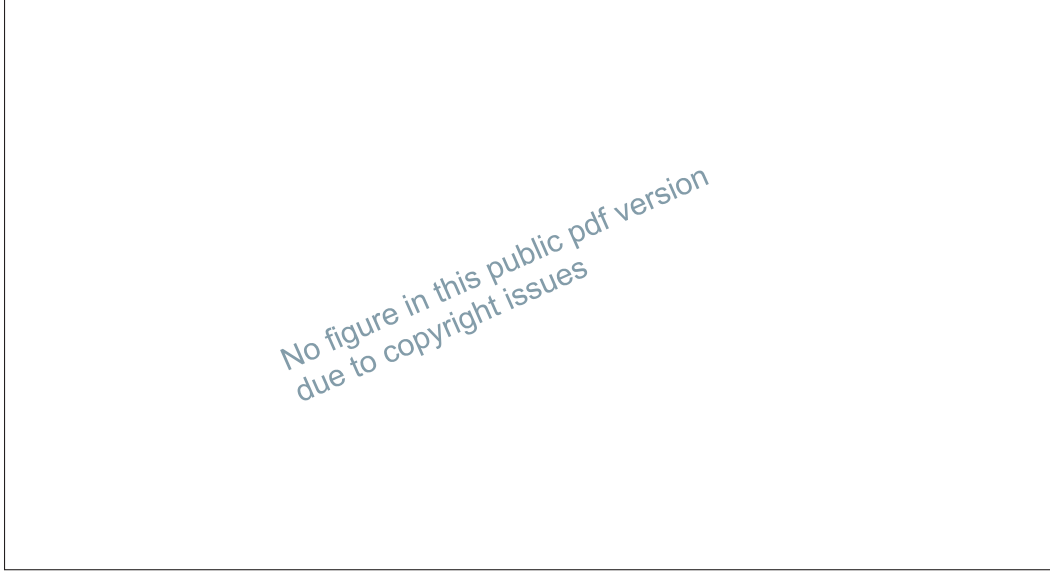


Figure 7.15: *Transverse dust lattice waves. (a) Still image of a 1D particle chain, (b) Grey scale image of the vertical displacement of the dust particles in the chain. The wave is seen to propagate backwards. (c) Measured dispersion relation of the transverse DLW. From [107].*

the time traces it is immediately seen that the wave is a backward wave (negative slope in the space-time diagram). The authors have measured a part of the dispersion relation where a finite frequency is found for $\mathbf{q} \rightarrow 0$ and the dispersion also has a negative slope, as expected for the transverse DLW. However, the overall agreement of the measured and the theoretical dispersion is not very satisfying.

7.8. Dispersion Relation from Thermal Particle Motion

Recently, a method was developed by Nunomura et al. to determine the dispersion relation of the various wave modes from the thermal Brownian motion of the dust particles in the plasma crystal [108, 109]. This powerful technique allows the measurement of the *entire* dispersion from a single video sequence.

To derive the dispersion relation from the Brownian motion, first the particle velocities $\vec{v}(\vec{r}, t)$ in the 2D particle plane are determined. From that the Fourier components of the velocity

$$\hat{v}(\vec{q}, \omega) = \frac{2}{TL} \int_0^T \int_0^L \vec{v}(\vec{r}, t) e^{(-i\vec{q} \cdot \vec{r} + i\omega t)} d\vec{r} dt \quad (7.17)$$

are determined. Here, L and T are the length and period over which the particle motion is integrated. The compressional mode is then obtained by taking the components of $\vec{v} \parallel \vec{q}$, only. The shear mode is derived from the components of $\vec{v} \perp \vec{q}$. This integral is evaluated for all wave vectors \vec{q} and frequencies ω . The square of the value of this integral is then proportional to the intensity of the wave at the chosen values of \vec{q} and ω .

Figure 7.16 shows the wave energy density of the Fourier components as a function of q and ω for the compressional and shear mode of an actual experiment. Following the above procedure the wave energy is large along distinct lines indicating the dispersion relation of the two wave modes. The dispersion relations obtained from this Brownian motion technique are in very good agreement with the theoretical predictions. This demonstrates the ability of this method to derive the dispersion relation from a single video sequence.

This method has also been applied to a linear chain of particles to measure the transverse mode dispersion (Fig. 7.16 bottom). Again good agreement with the theoretical dispersion is obtained. This powerful technique has also been applied to finite systems in the following chapter.

7.9. A Note on Shielding

At this point, a few words on the screening of dust particles in the sheath of rf discharges are appropriate. The above mentioned wave experiments (as well as the experiments on finite clusters in the following chapter) have revealed that the screening strength $\kappa = b/\lambda_s$ is of the order of 1. This means that the shielding length λ_s is of the order of

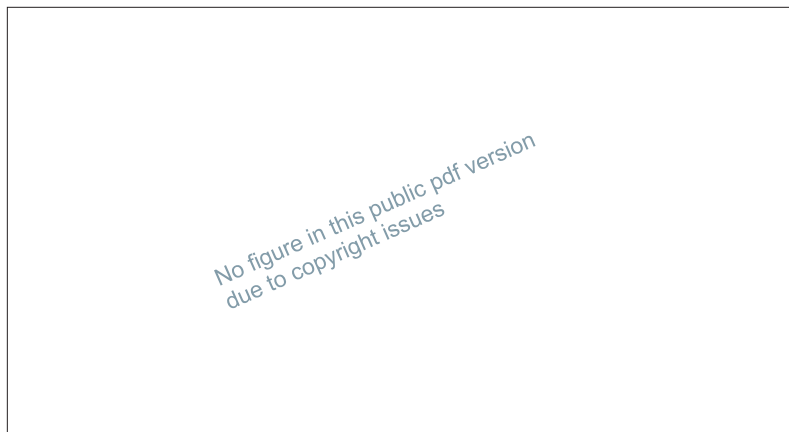


Figure 7.16: *Dispersion relation of the modes determined from the thermal Brownian motion. Top: compressional wave, middle: shear wave, bottom: optical wave. Note that in these figures the wave vector extends from $qb = -2\pi$ to $qb = +2\pi$, thus $qb = 0$ is in the center. After [108, 109].*

the interparticle distance b . The interparticle distance and thus the screening length is typically a few hundred microns for the experiments with micron-sized particles. Direct collision experiments in Sec. 5.1. also have revealed a screening length of the same size. We now would like to discuss the observed screening lengths in some more detail.

The observed shielding of a few hundred microns is close to the electron Debye length

$$\lambda_s \approx \lambda_{D,e} = \sqrt{\frac{\epsilon_0 k T_e}{n_e e^2}}$$

for typical plasma conditions of n_e around 10^8 to 10^9 cm^{-3} and T_e around 2 to 5 eV. In comparison, the ion Debye length

$$\lambda_{D,i} = \sqrt{\frac{\epsilon_0 k T_i}{n_i e^2}}$$

is about 60 to 100 μm due to the much smaller ion temperature $T_i \approx 0.05$ eV. The combination of these two Debye lengths, the linearized Debye length, is given by

$$\frac{1}{\lambda_D^2} = \frac{1}{\lambda_{D,i}^2} + \frac{1}{\lambda_{D,e}^2} .$$

Since the shorter length scale dominates the screening properties the linearized Debye length is very close to the ion Debye length $\lambda_D \approx \lambda_{D,i} \ll \lambda_s$. The observed screening length should be of the order of the linearized or ion Debye length if the ions are responsible for screening. Obviously, however, only the electrons contribute to screening, here.

This apparent paradox is resolved when ion streaming motion is taken into account. The experiments presented here have all been performed in the sheath of a plasma discharge. There, the ions stream with Bohm velocity v_B towards the electrode. Since the ion flow velocity is supersonic, one can argue that the ions cannot contribute to shielding. Khrapak et al. and Hutchinson [29, 30]) have given an expression for the shielding length with ions drifting at a velocity u_i , compare Eq. (3.12), as

$$\lambda_s^2 = \frac{\lambda_{D,e}^2}{1 + kT_e / (kT_i + (1/2)m_i u_i^2)} , \quad (7.18)$$

which is also shown in Fig. 7.17. For low drift velocities $u_i \rightarrow 0$ the screening length $\lambda_s = \lambda_D$ whereas for high drift velocities $\lambda_s = \lambda_{D,e}$. Hence, when the ion streaming velocity is below the ion thermal velocity the appropriate screening length is the linearized Debye length. If the ion streaming velocity is increased the ions cannot contribute to shielding since then the ion motion is dominated by the drift and not by the dust potential. For large drifts $u_i \gg v_{th,i}$ the appropriate screening length is the electron Debye length $\lambda_{D,e}$. Since the experiments are performed in the sheath where $u_i \geq v_B \gg v_{th,i}$ electron screening is dominating.

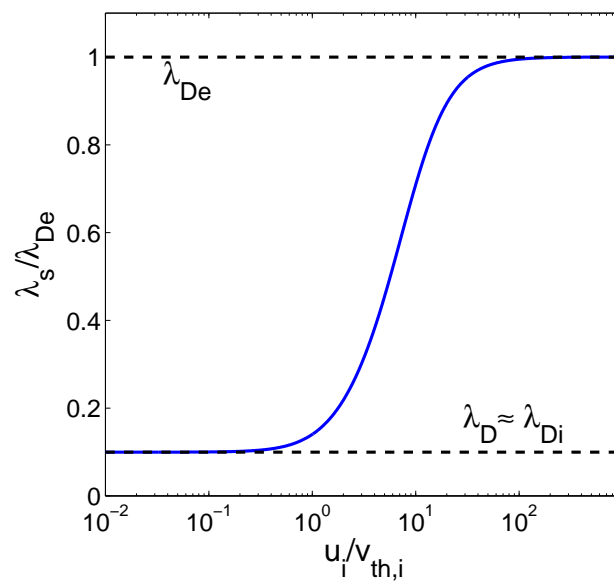


Figure 7.17: Screening length λ_s (in units of the electron Debye length $\lambda_{D,e}$) as a function of ion drift velocity u_i (in units of the ion thermal velocity).

8. Finite Dust Clusters

So far, waves in extended (1D and 2D) systems as well as crystalline structures in extended 2D and 3D systems have been presented. Now, we would like to draw the attention to collective effects in finite systems. Such Coulomb clusters are systems of a small number of charged particles trapped in an external potential. As early as 1904, such systems have been analyzed by J.J. Thomson as a model for the structure of the atom [110]. Nowadays, the structure and the dynamic properties of finite systems are easily modeled on a PC. Coulomb clusters are particularly appealing because of the interplay between the Coulomb repulsion among the particles and the confinement due to an external potential. This interplay determines the structure of a cluster and also its dynamics. Structure and dynamics dramatically depend on the exact particle number N , and the formation of highly symmetric configurations with “magic” particle numbers is observed in a wide variety of situations in the classical and quantum world.

Examples of charged-particle clusters of present-day interest are found as ions in Paul and Penning traps, ions in storage rings of accelerators, electrons on the surface of liquid helium, electrons in quantum dots, brown dwarf stars, charged particles in colloidal suspensions [111] or, as will be discussed here, charged dust particles in dusty plasmas [112, 113, 114].

8.1. Formation of Finite Dust Clusters

Finite dust Coulomb clusters are formed by trapping only a small number of dust particles into a confinement potential provided by a combination of forces described in Chapter 3.

The confinement potential energy V depends on the peculiarities of the setup and the exploited forces (see Fig. 8.1), but can often be considered as harmonic, i.e.

$$\begin{aligned} V(x_i, y_i, z_i) &= \frac{1}{2} m_d \omega_x^2 x_i^2 + \frac{1}{2} m_d \omega_y^2 y_i^2 + \frac{1}{2} m_d \omega_z^2 z_i^2 \\ &= \frac{1}{2} m_d \omega_0^2 (x_i^2 + \alpha_y y_i^2 + \alpha_z z_i^2) \quad . \end{aligned} \quad (8.1)$$

Here, $\omega_{x,y,z}$ is the confinement strength in x, y, z direction and $\alpha_{y,z} = \omega_{y,z}^2 / \omega_x^2$ is the relative strength of the confinement with respect to the confinement in x direction ($\omega_0 = \omega_x$). By changing the relative confinement strengths $\alpha_{x,y}$ various confinement geometries from 1D to 2D and 3D can be realized. How this is done in the experiment will be demonstrated below.

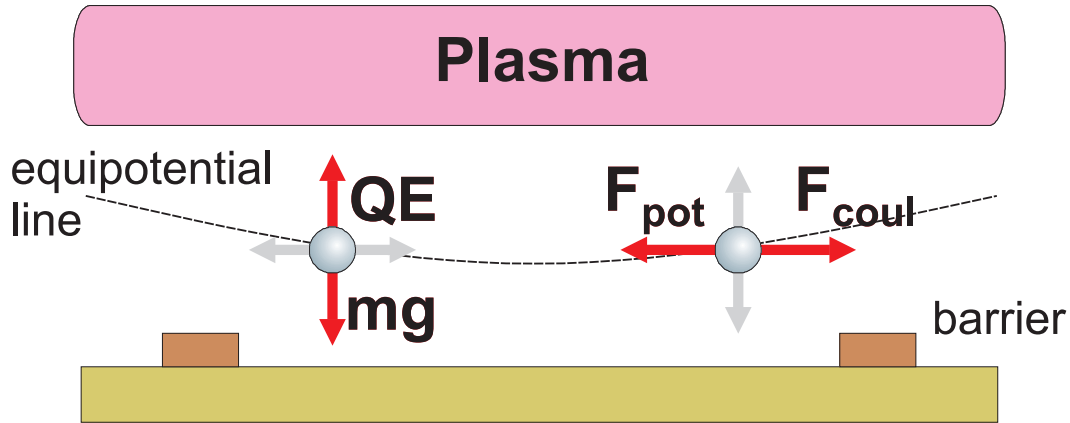


Figure 8.1: Sketch of the confinement of clusters in an rf discharge. In the vertical direction a very strong confinement is provided by the electric field force and gravity. In the horizontal direction a barrier on the electrode provides a shallow horizontal confinement. The force due to that potential energy F_{pot} balances the Coulomb repulsion F_{Coul} of the particles.

8.2. Structural Transitions in 1D Dust Clusters

Linear (1D) dust clusters are easily generated by placing a rectangular metal barrier (e.g. 6 mm height and $5 \times 40 \text{ mm}^2$ inner dimension) onto the lower electrode (see Fig. 8.2). A small number of particles ($N = 1$ to 20) are then dropped into the space charge sheath above the barrier [115], see also Fig. 8.1.

Vertically the particles are strongly confined due to the balance of electric field force and gravity (i.e. $\alpha_z \gg 1$). Horizontally the particles are confined due to the barrier on the electrode. Since the elongation of the barrier is much larger in y -direction than in x -direction the particles are only weakly confined along y . Thus, $\alpha_y \ll 1$ and the particles arrange along y in a linear 1D dust cluster.

Figure 8.2b) shows the arrangement of $N = 4$ to $N = 18$ particles in the barrier. It is seen that for $N = 4$ to $N = 9$ the particles strictly arrange in a linear arrangement. When, however, the particle number is increased from 9 to 10 a zigzag transition in the center of the chain occurs. For 18 particles a zigzag structure is seen nearly throughout the entire chain.

The reason for that is easily understandable: the confinement in the y -direction compresses the chain along its extension. The interparticle distance is smallest in the central part of the chain. When more and more particles are inserted into the chain the compression increases until it is easier for the central particles to make a transverse excursion (in the x -direction). Then, the force along y between neighboring particles due to compression exceeds the force in x from the confinement [115, 116].

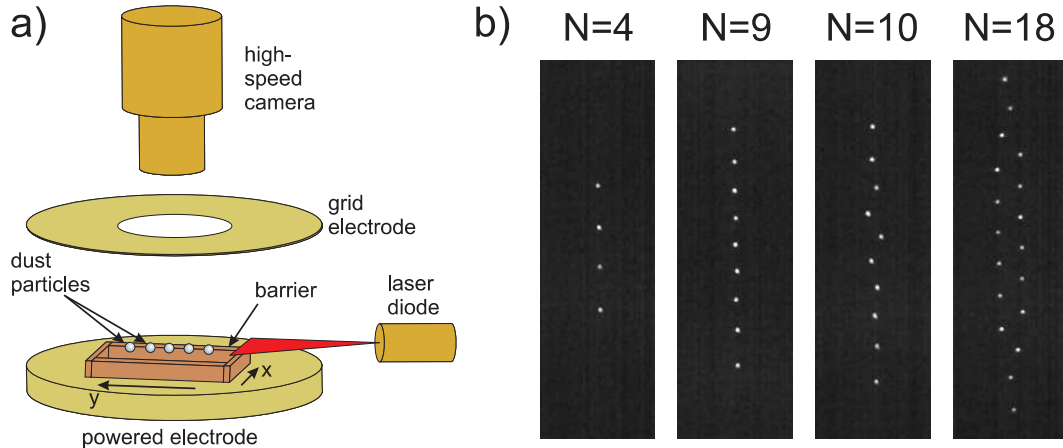


Figure 8.2: a) Scheme of the experimental setup for the confinement of 1D dust clusters. b) Snap shots of the 1D dust cluster for $N = 4, 9, 10$ and 18 . A structural transition in the cluster is seen by increasing the particle number. From 9 to 10 particles a zigzag transition occurs. From [115].

8.3. Structure of 2D Finite Dust Clusters

In 2D clusters, a small number of dust particles $N = 1$ to 1000, say, are trapped in the sheath above the lower electrode. Vertically, the particles are as usual strongly confined by the electric field force and gravity. Here, an additional weak parabolic confinement (of strength ω_0) is applied in the horizontal plane. Such a confinement can be realized by a shallow circular parabolic trough in the electrode (see Fig. 8.3). Hence, here, $\omega_x^2 = \omega_y^2 \ll \omega_z^2$ ($\alpha_y = 1$, $\alpha_z \gg 1$).

Under the interplay of the horizontal parabolic confinement and their Coulomb repulsion the particles arrange in concentric shells (see Fig. 8.4). The 2D clusters are sometimes said to form a “periodic table”. The structure and their dynamic properties dramatically depend on the particle number N . When changing from 5 to 6 particles (or from 15 to 16) a new shell opens up. Like in atomic and nuclear physics there exist “magic” particle numbers of high dynamic stability, e.g. the $N=19$ (1,6,12) cluster. The notation (N_1, N_2, N_3, \dots) refers to N_1 particles in the inner ring, N_2 in the second and so on. These clusters will be analyzed below in more detail.

These finite 2D clusters can be described in terms of their total energy

$$E = \frac{1}{2} m_d \omega_0^2 \sum_{i=1}^N r_i^2 + \frac{Z_d^2 e^2}{4\pi\epsilon_0} \sum_{i>j}^N \frac{\exp(-r_{ij}/\lambda_D)}{r_{ij}}, \quad (8.2)$$

where $\vec{r}_i = (x_i, y_i)$ is the 2D position of the i -th particle in the horizontal plane and $r_{ij} = |\vec{r}_i - \vec{r}_j|$. The strength of the horizontal confinement is denoted by the horizontal

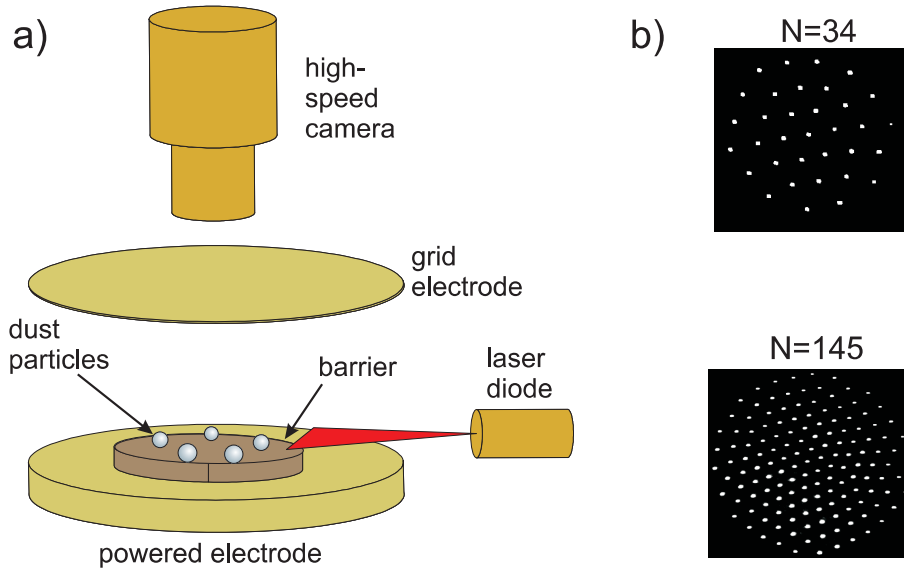


Figure 8.3: a) Scheme of the experimental setup for the confinement of 2D dust clusters. b) Snap shots of the 2D dust cluster for $N = 34$ and 145. From [117].

resonance frequency ω_0 . The first term is the potential energy due to the confinement in the horizontal plane and the second is the Coulomb repulsion of the particles.

The equilibrium structure of these systems is derived from the minimum of the total energy [118]. Experimentally they have been observed, e.g. by Juan et al. [112] and Klindworth et al. [113]. The observed cluster structures are in perfect agreement with the theoretical predictions. We will illustrate that in the following.

8.3.1. Example of 2D Cluster Configurations: Configuration (0,6)

The structure of a 2D cluster configuration will be illustrated using $N = 6$ particles under Coulomb interaction ($\lambda_D \rightarrow \infty$). We will study two possible configurations, namely the (0,6) and (1,5) configuration where either 6 particles are on a single ring or 5 particles are on the outer ring with a central particle (see Fig. 8.5). We assume that the particles are ordered in angular position and that only radial displacements can occur.

For the (0,6) configuration the potential energy is given by

$$E_{\text{pot}} = \frac{1}{2} m_d \omega_0^2 \sum_{i=1}^N r_i^2 = \frac{1}{2} m_d \omega_0^2 N r_6^2 \quad ,$$

where r_6 is the distance of the 6 particles from the center of the configuration. For the Coulomb energy we have to determine the distances between the different particles: They are $r_{ij} = r_6$ for $1 - 2, 2 - 3, 3 - 4, 4 - 5, 5 - 6$ and $1 - 6$ (since they form equilateral

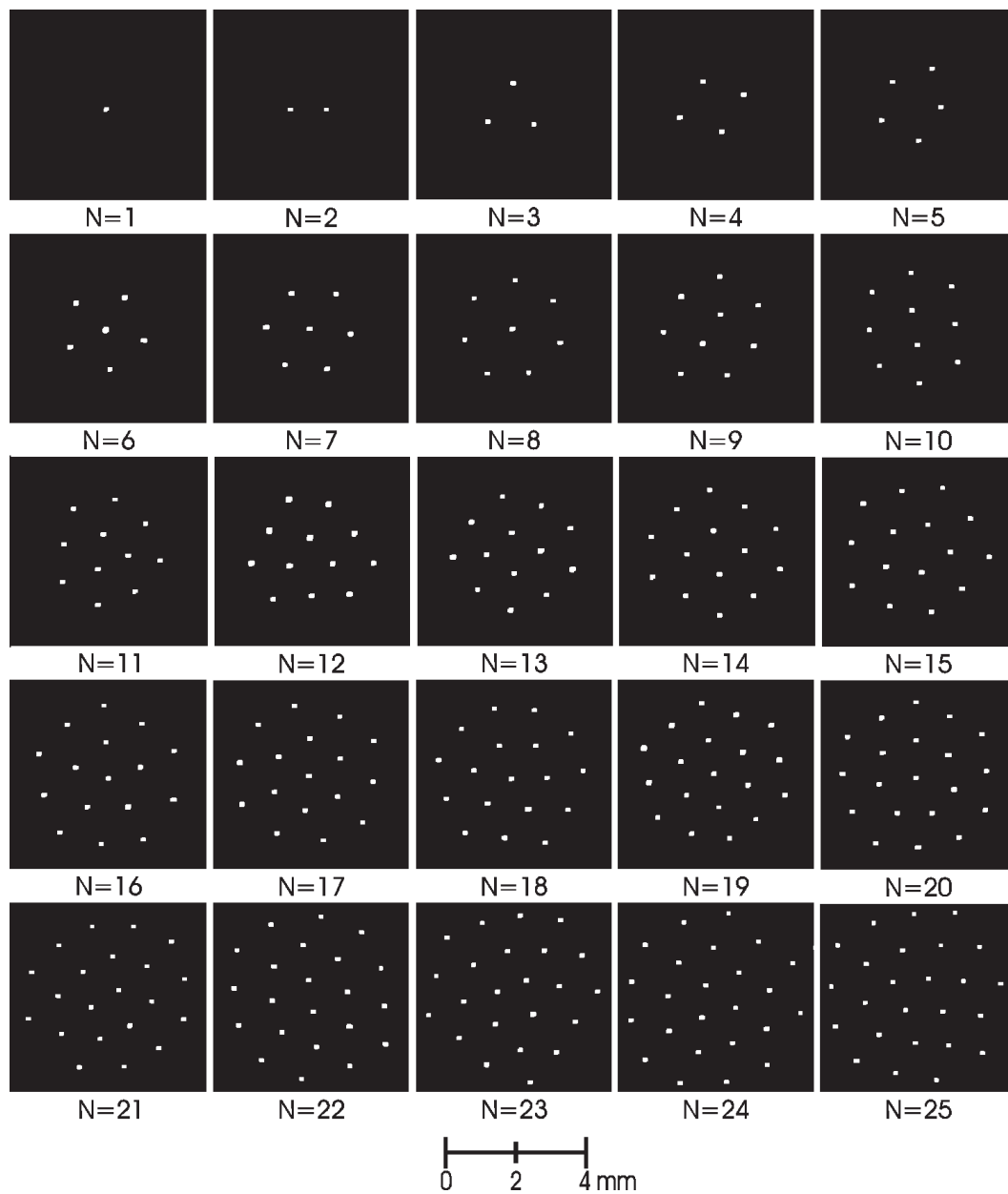


Figure 8.4: “Periodic table” of finite 2D clusters with $N = 1$ to $N = 25$ particles. These images are taken from the experiment.

triangles); in addition $r_{ij} = \sqrt{3}r_6$ for 1–3, 1–5, 2–4, 2–6, 3–5 and 4–6; finally, $r_{ij} = 2r_6$ for 1–4, 2–5, 3–6. These are the 15 possible combinations for $i > j$ at $N = 6$.

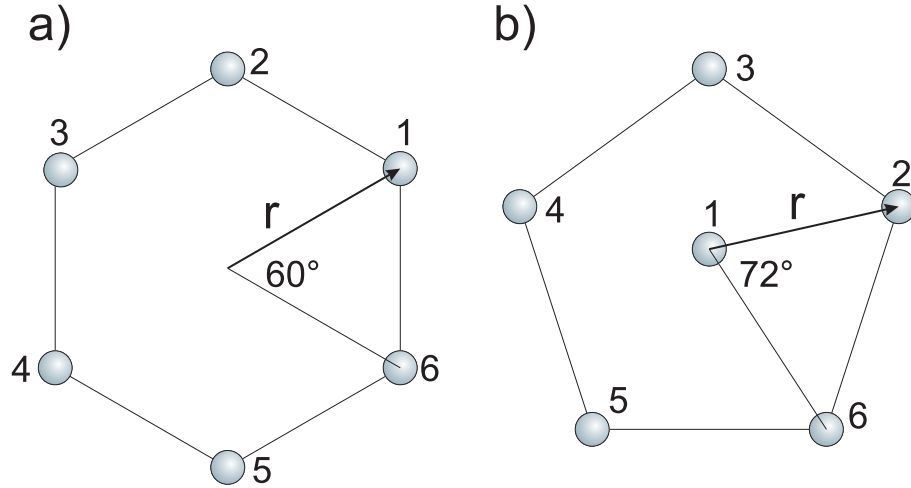


Figure 8.5: Two possible configurations of a 6-particle cluster: (a) (0,6) and (b) (1,5). The numbers denote the different particles.

Thus, the Coulomb energy is

$$E_{\text{Coul}} = \frac{Z_d^2 e^2}{4\pi\epsilon_0} \sum_{i>j}^N \frac{1}{r_{ij}} = \frac{Z_d^2 e^2}{4\pi\epsilon_0} \left(\frac{6}{r_6} + \frac{6}{\sqrt{3}r_6} + \frac{3}{2r_6} \right) = \frac{Z_d^2 e^2}{4\pi\epsilon_0 r_6} \underbrace{\left(6 + \frac{6}{\sqrt{3}} + \frac{3}{2} \right)}_{10.97} .$$

The total energy is then given by

$$E = \frac{1}{2} m_d \omega_0^2 N r_6^2 + \frac{Z_d^2 e^2}{4\pi\epsilon_0 r_6} 10.97 \quad (8.3)$$

The distance r_6 is undefined at the moment. It must be evaluated from the condition that r_6 is the equilibrium distance. For $r < r_6$ the Coulomb energy dominates, for $r > r_6$ the potential energy. The equilibrium is found from

$$\frac{\partial E}{\partial r} = 0 \quad \rightarrow \quad m_d \omega_0^2 N r_6 - \frac{Z_d^2 e^2}{4\pi\epsilon_0 r_6^2} 10.97 = 0 \quad \rightarrow \quad r_6^3 = \frac{Z_d^2 e^2}{4\pi\epsilon_0} \frac{2}{m_d \omega_0^2} \frac{10.97}{2N}$$

Inserting this into Eq. (8.3) yields

$$\begin{aligned} E_6 &= \left(\left(\frac{Z_d^2 e^2}{4\pi\epsilon_0} \right)^2 \frac{m_d \omega_0^2}{2} \right)^{1/3} \left(N \sqrt[3]{\frac{10.97^2}{(2N)^2}} + 10.97 \sqrt[3]{\frac{2N}{10.97}} \right) \\ &= 16.95 \left(\left(\frac{Z_d^2 e^2}{4\pi\epsilon_0} \right)^2 \frac{m_d \omega_0^2}{2} \right)^{1/3} . \end{aligned}$$

When measuring the distances and energies in units of

$$r_0 = \left[\frac{Z_d^2 e^2}{4\pi\epsilon_0} \frac{2}{m_d \omega_0^2} \right]^{1/3} \quad \text{and} \quad E_0 = \left[\left(\frac{Z_d^2 e^2}{4\pi\epsilon_0} \right)^2 \frac{m_d \omega_0^2}{2} \right]^{1/3} \quad (8.4)$$

the equilibrium distance and energy are found as

$$r_6 = \sqrt[3]{\frac{10.97}{2N}} = 0.97 \quad \text{and} \quad E_6 = 16.95 \quad .$$

In these normalized units the energy and the distances do not depend on the physical parameters like particle charge, mass etc. They only define the absolute values of the energy and the absolute size of the cluster, but they do not have an influence on the structure, on the dynamics and so on. Structure and dynamics are determined only by the particle number N .

When we analyze the confinement near the equilibrium position we can develop the energy into the different orders, like

$$E(\delta r) = E_6 + \frac{1}{2} \frac{\partial^2 E}{\partial r^2} \delta r^2 + \dots \quad .$$

The term linear in the displacement from the equilibrium position $\delta r = r - r_6$ is zero since r_6 is the equilibrium position where $\partial E / \partial r = 0$. The second order term results in

$$\begin{aligned} \left. \frac{\partial^2 E}{\partial r^2} \right|_{r=r_6} &= \frac{1}{2} m_d \omega_0^2 2N + 10.97 \frac{Z_d^2 e^2}{4\pi\epsilon_0} \frac{2}{r_6^3} = \frac{1}{2} m_d \omega_0^2 \left(2N + 10.97 \frac{2}{10.97/2N} \right) \\ &= \frac{1}{2} m_d \omega_0^2 6N \quad . \end{aligned} \quad (8.5)$$

Thus it is found that the 6 particles of the (0,6) configuration are experiencing a harmonic confinement. When identifying this confinement with a harmonic potential well of resonance frequency ω for N particles we find

$$\frac{1}{2} \frac{\partial^2 E}{\partial r^2} \delta r^2 = \frac{1}{2} N m_d \omega^2 \delta r^2 \quad \rightarrow \quad \omega^2 = 3\omega_0^2 \quad . \quad (8.6)$$

This means that the 6 particles experience a potential well of strength $\sqrt{3}\omega_0$. Since we have considered only radial displacements in this analysis the corresponding particle motion is a coherent radial oscillation of all 6 particles. Thus, the cluster grows and decreases in size periodically. Therefore, this type of motion is called breathing mode. The breathing mode is found to be at the fixed frequency given by Eq. (8.6). Moreover, it is found that the breathing mode *always* has the frequency $\omega = \sqrt{3}\omega_0$ independent of particle number N . This is a general result that holds for pure Coulomb interaction between the particles. When a screened interaction is taken into account the frequency of the breathing mode increases with increasing screening strength.

8.3.2. Example of 2D Cluster Configurations: Configuration (1,5)

The alternative configuration consists of one central particle surrounded by another 5. The potential energy is readily found as

$$E_{\text{pot}} = \frac{1}{2} m_d \omega_0^2 \sum_{i=1}^N r_i^2 = \frac{1}{2} m_d \omega_0^2 (N-1) r_5^2 \quad ,$$

where r_5 is the distance of the 5 outer particles from the center. The Coulomb energy is

$$E_{\text{Coul}} = \frac{Z_d^2 e^2}{4\pi\epsilon_0} \sum_{i>j} \frac{1}{r_{ij}} = \frac{Z_d^2 e^2}{4\pi\epsilon_0} \left(\frac{5}{r_5} + \frac{5}{1.18r_5} + \frac{5}{1.90r_5} \right) = \frac{Z_d^2 e^2}{4\pi\epsilon_0 r_5} \underbrace{\left(5 + \frac{5}{1.18} + \frac{5}{1.90} \right)}_{11.87} .$$

Here, the distance from the central particle to the other 5 is $r = r_5$, between particles 2–3, 2–6, 3–4, 4–5, and 5–6 it is $r = 1.18r_5$ and between 2–4, 2–5, 3–5, 3–6, and 4–6 it is $r = 1.90r_5$.

The equilibrium distance is found as

$$\frac{\partial E}{\partial r} = 0 \quad \rightarrow \quad m_d \omega_0^2 (N-1) r_5 - \frac{Z_d^2 e^2}{4\pi\epsilon_0 r_5^2} 11.87 \quad \rightarrow \quad r_5^3 = \frac{Z_d^2 e^2}{4\pi\epsilon_0} \frac{2}{m_d \omega_0^2} \frac{11.87}{2(N-1)}$$

Inserting this into the total energy, one obtains in normalized units

$$r_5 = 1.059 \quad \text{and} \quad E_5 = 16.82 \quad .$$

Hence, the cluster configuration (1,5) has a lower energy than (0,6) and thus is energetically favored. This is also seen in Fig. 8.4 where the (1,5) configuration is found for 6 particles.

Finally, the radial confinement is given by

$$\begin{aligned} \left. \frac{\partial^2 E}{\partial r^2} \right|_{r=r_5} &= \frac{1}{2} m_d \omega_0^2 2(N-1) + 11.87 \frac{Z_d^2 e^2}{4\pi\epsilon_0} \frac{2}{r_5^3} \\ &= \frac{1}{2} m_d \omega_0^2 \left(2(N-1) + 11.87 \frac{2}{11.87/2(N-1)} \right) \\ &= \frac{1}{2} m_d \omega_0^2 6(N-1) \quad . \end{aligned} \tag{8.7}$$

Since here only the outer $N-1 = 5$ particles take part in the breathing mode the same breathing mode frequency $\omega = \sqrt{3}\omega_0$ is found also for the (1,5) configuration.

8.4. Structure of 3D Finite Dust Clusters

It is also possible to confine 3D dust clusters under laboratory conditions. The confinement potential is isotropic in 3D and does not lead to void formation. The confinement has been achieved using the combined interaction of thermophoretic levitation and a horizontal boundary due to glass walls (see Fig. 8.6). A glass box is placed onto the lower electrode. The dielectric walls charge negatively and therefore provide an inward electric force on the negative dust particles for horizontal confinement. The lower electrode is heated and induces a temperature gradient in the neutral gas. The temperature gradient provides an upward thermophoretic force that, at least partially, compensates the gravitational force on the particles [119]. By tuning the electrode temperature and plasma properties a 3D isotropic confinement potential is formed to confine the dust particles ($\omega_x^2 = \omega_y^2 = \omega_z^2 =$, i.e. $\alpha_y = \alpha_z = 1$).

The clusters in this three-dimensional confinement also arrange in highly ordered structures [121]. The systems form concentric spheres, arranged in an “onion shell” structure, for which the name “Yukawa ball” has been established [114, 122, 123, 120]. Like 2D finite clusters where the particles arrange in concentric rings, 3D clusters have defined spheres. Since a 3D structure is difficult to visualize, the structure is most clearly seen in cylindrical coordinates (ρ, z) , where the horizontal coordinates (x, y) are mapped onto the radial position $\rho = \sqrt{x^2 + y^2}$ and plotted versus the vertical coordinate z . An experimental dust cluster is shown in Fig. 8.7. The cluster consists of $N = 190$ particles and is arranged in 4 concentric shells in a $(2, 21, 60, 107)$ configuration, i.e. 2 particles are on the innermost shell, followed by 21, 60 and 107 particles on the second, third

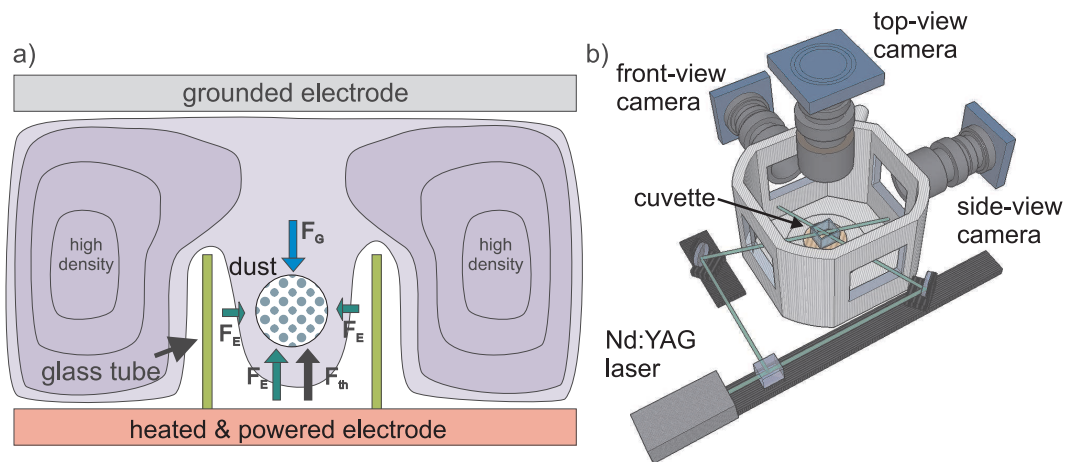


Figure 8.6: a) Scheme of the experimental setup for the confinement of 3D dust clusters. Thermophoretic levitation is used to (partially) compensate the gravitational force. b) Scheme of the 3D stereoscopic imaging unit. From [119, 120].

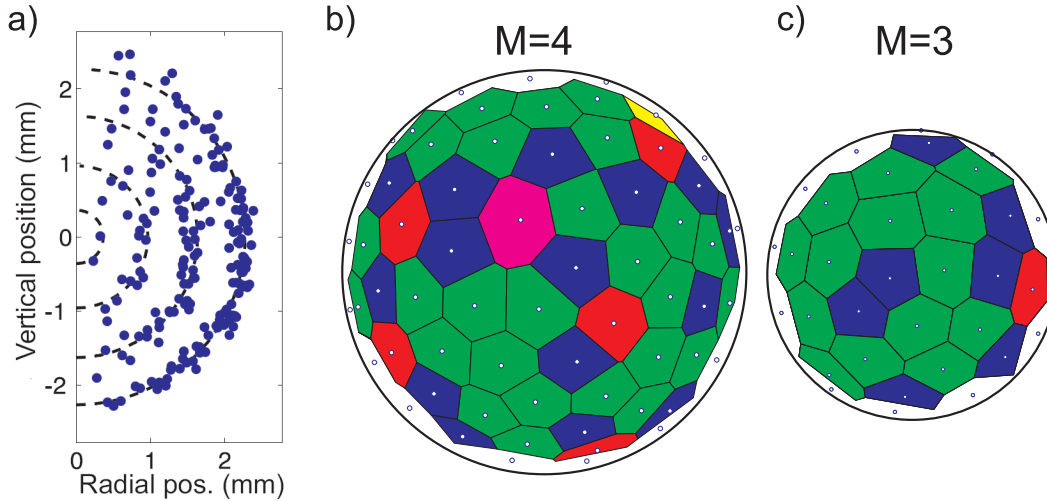


Figure 8.7: 3D dust cluster in an experiment with $N = 190$ particles. a) ρ - z plot. The cluster is seen to have 4 shells. b) Wigner-Seitz-cell analysis of the outer (4th) shell and c) of the 3rd shell. Pentagons are marked blue, hexagons are green. Defect polygons with more than 6 nearest neighbors are colored red. After [114].

and forth shell, respectively. The structure within each shell is visualized in Fig. 8.7b,c) where a Wigner-Seitz-cell construction has been performed on the individual shells. The shells consist of hexagons and pentagons (like the famous C_{60} buckyballs or an ordinary footballs). A certain number of pentagons is needed to ensure the curvature of the sphere and to form closed shells. But also some defects, i.e. particles with more than 6 nearest neighbors are found.

A selection of smaller clusters ($N < 100$) is shown in Fig. 8.8. There, a 3D reconstruction of the structure is shown. Also these clusters arrange in nested spherical shells ranging from one shell with central particle ($N = 17$) to three shells ($N = 91$). From this 3D bond structure also the highly ordered arrangement is readily seen. Analogously to the 2D case, also here a “periodic table”-like construction of the clusters is observed. Typically, a new shell opens up, when the inner shell has 12 particles [124, 125].

However, there is an interesting difference between 2D and 3D clusters concerning the structural properties and screened particle interaction. In 2D, the observed cluster structures (i.e. occupation numbers of the different rings) is nearly independent of the particle interaction: pure Coulomb, Yukawa or even logarithmic interaction potentials (almost) always yield the same cluster structure [126]. In contrast, in 3D, the occupation number for fixed total particle number N of inner shells is higher for Yukawa interaction compared to the pure Coulomb case. Consequently, outer shells have lower particle numbers for Yukawa interaction than for Coulomb interaction. Hence, already the structure of 3D clusters reflects the shielding strength [122, 123, 120] which is found from the experiments

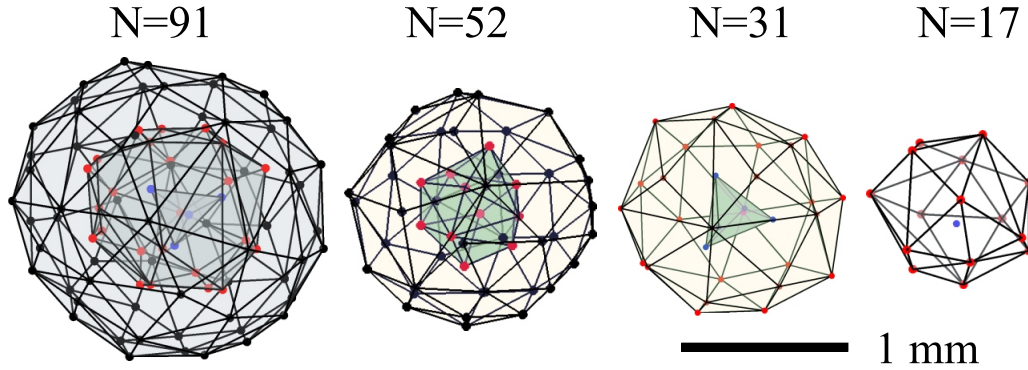


Figure 8.8: Cluster configurations reconstructed from single video snap shots with $N = 91, 52, 31,$ and 17 . The Yukawa balls consist of concentric shells with the configurations $(4, 25, 62)$ for the $N = 91$, $(11, 41)$ for the $N = 52$, $(5, 26)$ for the $N = 31$, and $(1, 16)$ for the $N = 17$ cluster. From [120].

to be of the order of $\kappa \approx 1$. Therefore, the term “Yukawa ball” is fully justified.

8.5. Normal Modes in 2D Finite Clusters

After the discussion of the static equilibrium properties of finite systems we like to delve into the dynamic properties of these systems. The breathing mode discussed above was a first example in that direction.

The dynamic properties of finite systems cannot be described in terms of wave dispersions as in the case of extended systems. First, only a certain number of wavelengths can fit into finite systems. Moreover, due to the boundaries of finite systems, where phase jumps and reflections can occur, the distinction between shear and compressional modes is not possible. The modes that occur in finite systems have both compressional and shear contributions. For small systems the boundaries are important and dominate the dynamic properties of the system. Thus, the dynamic properties of finite clusters are described by their normal modes which replace the dispersion relation of infinite systems [127]. We will treat the problem for the 2D case, here, for simpler visualization. The extension to 3D systems is easily done.

The starting point is the total energy, compare Eq. (8.2),

$$E = \sum_{i=1}^N r_i^2 + \sum_{i>j}^N \frac{\exp(-\kappa r_{ij})}{r_{ij}} \quad , \quad (8.8)$$

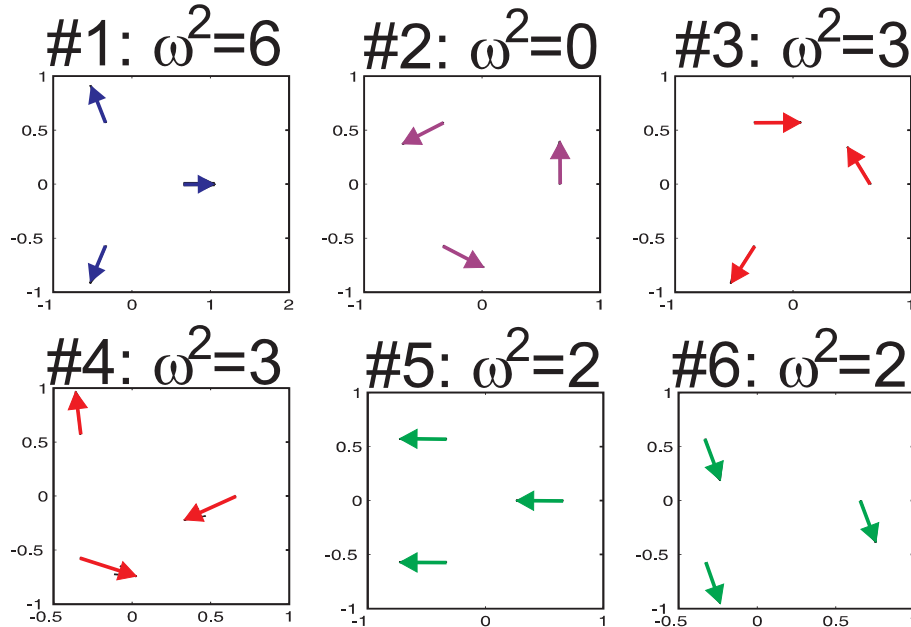


Figure 8.9: The 6 eigen modes of a $N = 3$ cluster with the corresponding mode frequencies ω^2 (in units of $\omega_0^2/2$).

where we have used normalized distances and energies according to Eq. (8.4). The first term is the confinement potential and the second the screened interaction. The screening strength is in these finite clusters accordingly defined as $\kappa = r_0/\lambda_D$.

For multi-particle systems it is known from theoretical mechanics that the normal modes are obtained from the dynamical matrix (for 2D systems)

$$\mathbf{A} = \begin{pmatrix} \left(\frac{\partial^2 E}{\partial x_i \partial x_j} \right) & \left(\frac{\partial^2 E}{\partial x_i \partial y_j} \right) \\ \left(\frac{\partial^2 E}{\partial y_i \partial x_j} \right) & \left(\frac{\partial^2 E}{\partial y_i \partial y_j} \right) \end{pmatrix}, \quad (8.9)$$

that contains the second derivative of the total energy with respect to the particle coordinates x_i and y_i . These second derivatives are similar to that in Eq. (7.10) where we have seen in the determination of the DLW that the effective “spring constant” of the interaction among the different particles is related to the second derivative of the interaction potential. The dynamical matrix \mathbf{A} is just the generalization of this concept for multi-particle systems in more than one dimension.

In extended form, the 4 elements that constitute the dynamical matrix \mathbf{A} are them-

selves $1N \times 1N$ matrices that contain the possible combinations of i and j , namely, e.g.

$$\left(\frac{\partial^2 E}{\partial x_i \partial y_j} \right) = \begin{pmatrix} \frac{\partial^2 E}{\partial x_1 \partial y_1} & \cdots & \frac{\partial^2 E}{\partial x_1 \partial y_N} \\ \vdots & \ddots & \vdots \\ \frac{\partial^2 E}{\partial x_N \partial y_1} & \cdots & \frac{\partial^2 E}{\partial x_N \partial y_N} \end{pmatrix}.$$

Now the eigen value problem

$$\mathbf{A} \begin{pmatrix} x_1 \\ \vdots \\ x_N \\ y_1 \\ \vdots \\ y_N \end{pmatrix} = \lambda \begin{pmatrix} x_1 \\ \vdots \\ x_N \\ y_1 \\ \vdots \\ y_N \end{pmatrix} = \omega^2 \begin{pmatrix} x_1 \\ \vdots \\ x_N \\ y_1 \\ \vdots \\ y_N \end{pmatrix} \quad (8.10)$$

has to be solved*.

The eigen values and eigen vectors of \mathbf{A} describe the normal mode oscillations of the finite clusters. The eigen values λ are the oscillation frequencies ω^2 and the eigen vectors $(x_1, \dots, x_N, y_1, \dots, y_N)^T$ describe the mode oscillation patterns. The matrix \mathbf{A} is $2N \times 2N$, thus there are $2N$ eigen modes for a system with N particles in two dimensions (consequently, in 3D, the matrix \mathbf{A} is $3N \times 3N$ with $3N$ eigen modes).

This is demonstrated for the simple case of $N = 3$ particles in Fig. 8.9 where the $2N$ eigen modes are presented. Modes that occur in any cluster are the two sloshing modes (i.e. oscillations of the entire cluster in the horizontal confining potential, modes number 5 and 6), the rotation of the entire cluster (mode number 2) and the breathing mode (i.e. coherent, purely radial motion of all particles, mode number 1). For the 3-particle cluster also two ‘‘kink’’ modes are found (mode number 3 and 4). Naturally, the mode frequency for the two sloshing modes (5,6) is $\omega_{\text{slosh}} = \omega_0$ since the cluster oscillates in the confinement as a whole, for the rotation (2) of the entire cluster $\omega_{\text{rot}} = 0$ since there are no restoring forces and the cluster is always in equilibrium. The breathing mode (1) has the interesting property that for pure Coulomb interaction, i.e. $\kappa = 0$, its frequency always is $\omega_{\text{breath}} = \sqrt{3}\omega_0$ independent of particle number (see Sec. 8.3.1.). For shielded interaction ($\kappa > 0$) the frequency of the breathing mode increases and slightly depends on particle number N (see Fig. 8.10). Also the frequency of the ‘‘kink’’ mode increases with κ . Of course, the frequencies of the sloshing mode and cluster rotation are independent of κ and stay at their frequencies $\omega_{\text{slosh}} = \omega_0$ and $\omega_{\text{rot}} = 0$, respectively.

*This is easily seen from a simple analogy: Starting from the equation of motion for a simple spring

$$m\ddot{x} = -kx \quad \rightarrow \quad -\omega^2 x = -(k/m)x$$

assuming an oscillatory solution $x \rightarrow x \exp(-i\omega t)$. Now, for the many particle case k/m is replaced by

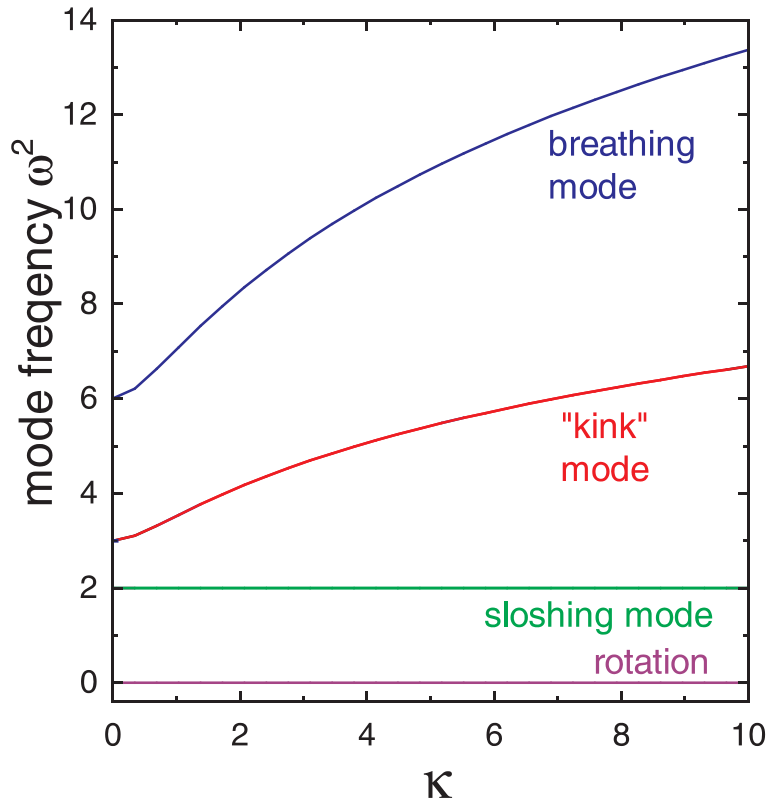


Figure 8.10: Evolution of the mode frequency ω^2 (in units of $\omega_0^2/2$) of the 6 eigen modes of the 3 particle cluster. After [117].

8.6. Modes from Thermal Particle Motion

As for the case of the waves, the normal modes can be extracted experimentally from the thermal Brownian motion of the dust particles [117]. Likewise, first, also for the finite clusters the velocity of the Brownian motion of all particles $\vec{v}_i(\mathbf{t})$ is determined from a video sequence. Then, the contribution of the thermal motion to each of the eigen modes is determined from the projection of the thermal velocities onto the eigen mode pattern by

$$f_\ell(\mathbf{t}) = \sum_{i=1}^N \vec{v}_i(\mathbf{t}) \cdot \vec{e}_{i,\ell} ,$$

where $\vec{e}_{i,\ell}$ is the eigen vector for particle i in mode number ℓ . The function $f_\ell(\mathbf{t})$ is the contribution of the thermal motion to the eigen mode ℓ in the time domain. For

the second derivatives, i.e the dynamical matrix \mathbf{A} , and \mathbf{x} becomes the vector of particle positions in x, y .

comparison, in the wave analysis (Sec. 7.8.), the Brownian particle velocities were projected onto the chosen wave vector \vec{q} . For the clusters, the eigen mode pattern takes the role of the wave vectors.

Finally, the spectral power density of each mode ℓ

$$S_\ell(\omega) = \frac{2}{T} \left| \int_0^T f_\ell(t) e^{i\omega t} dt \right|^2 \quad (8.11)$$

of f_ℓ is calculated. The spectral power density is the square of the Fourier transform of $f_\ell(t)$. The power spectrum contains the contribution of the thermal motion to each of the $2N$ eigen modes in the frequency domain and is proportional to the energy stored in the modes. It can be shown that

$$\int_0^\infty S_\ell(\omega) d\omega = \langle v_\ell^2 \rangle \quad , \text{ thus } \quad \frac{1}{2} m_d \int_0^\infty S_\ell(\omega) d\omega = \frac{1}{2} m_d \langle v_\ell^2 \rangle = E_\ell$$

is the energy stored in mode number ℓ .

For the 3-particle cluster the power spectrum obtained from the thermal motion of the three particles is shown in Fig. 8.11. Darker colors represent higher spectral power density. The measured spectrum is then also compared with the theoretical mode frequencies, i.e. the eigen values of the dynamical matrix. Since the theoretical mode frequencies depend on ω_0 and κ , the theoretical mode frequencies were fitted to the experimental data by changing these two values. It is seen, that the observed power spectrum is in very good agreement with the expected mode frequencies.

This technique can be applied to clusters of any size and has been demonstrated for clusters with several hundred particles. From the analysis of the mode spectra the best-fit parameters ω_0 and κ are derived. Note, that only these two parameters are fitted to match $2N$ modes, thus giving the obtained values a high credibility. Then, from the measured absolute values of cluster size or interparticle distance and by comparison with the scaling parameter $r_0 = [2Z_d^2 e^2 / (4\pi\epsilon_0 m_d \omega_0^2)]^{1/3}$ also the particle charge can be directly extracted. The particle charge was found to be in the presented experiments about 10 000 elementary charges on a $2a = 9.5 \mu\text{m}$ particle and the screening strength κ was found in the range between 0.5 and 2 [117].

8.7. Stability

The claim was made that the power spectrum contains the complete dynamic information on the cluster. This is illustrated here for the very basic dynamic property, the stability against perturbations.

In order to perturb a cluster configuration a force against the restoring forces of the cluster need to be applied. If the forces to induce perturbations are large then the system

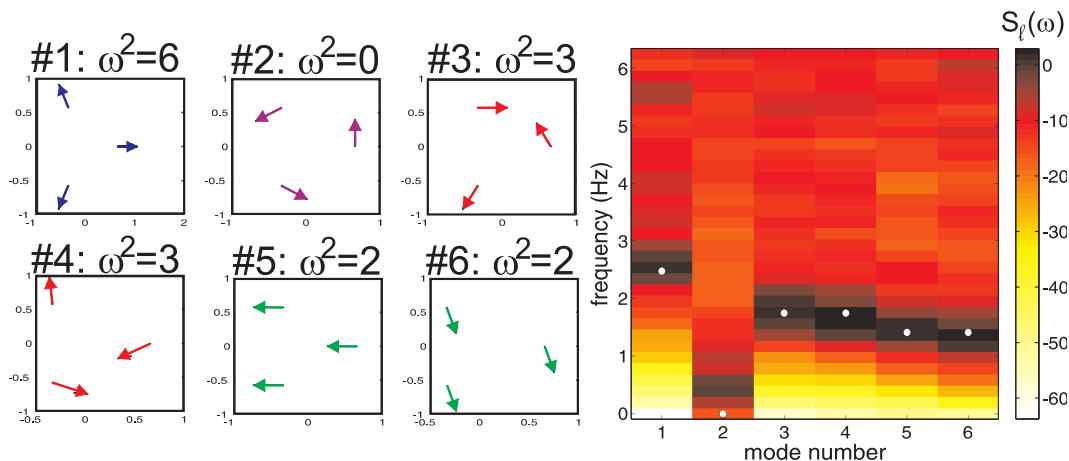


Figure 8.11: (a) The 6 eigen modes of a $N = 3$ cluster with the corresponding mode frequencies ω^2 (in units of ω_0^2). (b) Spectral power density of the 3 particle cluster derived from the thermal motion of the particles. The white dots indicate the best-fit theoretical values of the mode frequencies. After [117].

is more stable than if only small forces are required. In other words, if the restoring forces of the cluster are large against an applied perturbation the cluster is stable. Since the restoring forces directly determine the frequencies of the various modes it is seen that the mode with the lowest eigen frequency is the one that determines the stability of the entire cluster. The easiest way to disturb the cluster is along the mode with the lowest eigen frequency.

The rotational mode always has an eigen frequency of 0 and thus is always the mode with the lowest eigen frequency. However, a rotation of the entire cluster does not change the cluster configuration and thus is not really a perturbation of the cluster. So, the rotation mode is excluded from our following analysis and we seek for the eigen mode with the lowest frequency besides cluster rotation.

As an example we take the 19-particle cluster (see inset in Fig. 8.12a), which is a “magic number” configuration (1,6,12) due to its hexagonal symmetry of inner and outer ring. The particle number in inner and outer ring is commensurable. The inner and outer ring are locked into each other like the teeth of a tooth-wheel. One would expect that this cluster configuration is very stable, justifying the notion of “magic number”. The power spectrum to investigate the stability of the cluster is shown in Fig. 8.12b. One sees that there is a large gap between zero frequency (rotation) and the lowest eigen frequency at about 0.9 Hz. This is indeed a very large frequency gap and shows that the lowest eigen mode already has a quite high frequency which means high restoring forces and thus a high stability.

The corresponding mode patterns are shown in Fig. 8.12a. The already established

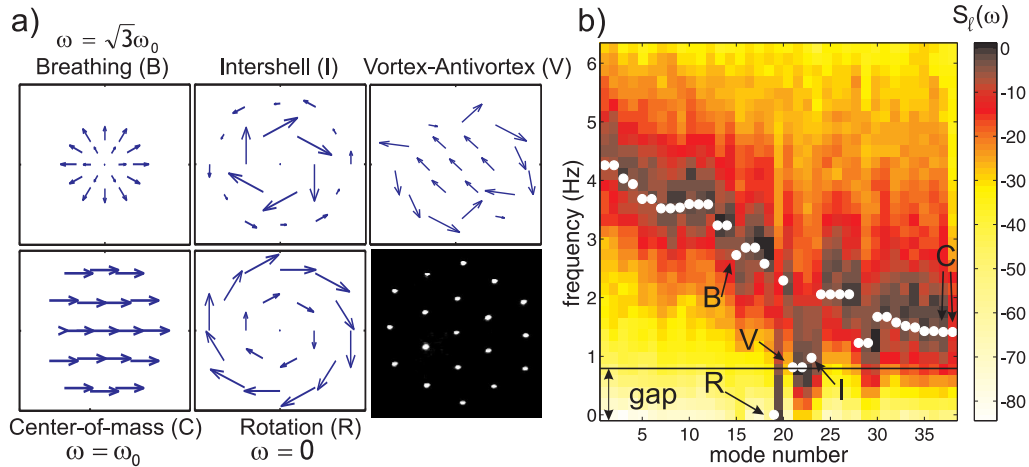


Figure 8.12: *a) Selected modes of a cluster with $N = 19$ particles together with a video snap shot of that cluster. b) Measured mode spectrum of this 19-particle cluster. After [117].*

breathing mode, center-of-mass mode and rotation are indicated. Two modes, that indicate the modes with the lowest frequency are the vortex-antivortex mode and the intershell rotation. The vortex-antivortex mode consists of two vortices, a clockwise and a counter-clockwise rotation within the cluster. This vortex-antivortex pair describes the pattern which results in the easiest disturbance of the 19-particle cluster. Similarly low frequencies are found for the intershell rotation where we find a differential rotation of inner and outer rings. Vortex-antivortex formation and intershell rotation very often are the lowest frequency mode in 2D clusters.

For comparison, the mode spectrum of a $N = 20$ particle cluster is shown in Fig. 8.13. This cluster has a configuration of (1, 7, 12) which is not a magic number configuration, since the number of particles in the inner and outer ring are not commensurate. Hence, inner and outer ring cannot interlock. Consequently, the intershell rotation is found at extremely low frequency of about 0.1 Hz, which is drastically less than for the 19-particle cluster. This demonstrates that the 20-particle cluster is very unstable against this intershell rotation. In contrast, the breathing mode of this cluster is found nearly at the same frequency as for $N = 19$ indicating that the plasma and confinement parameters of these two clusters are nearly identical.

8.8. Phase Transitions

As a final example of modes in 2D clusters, the phase transition by reducing the gas pressure is revisited. The mechanism of the phase transition has been introduced in

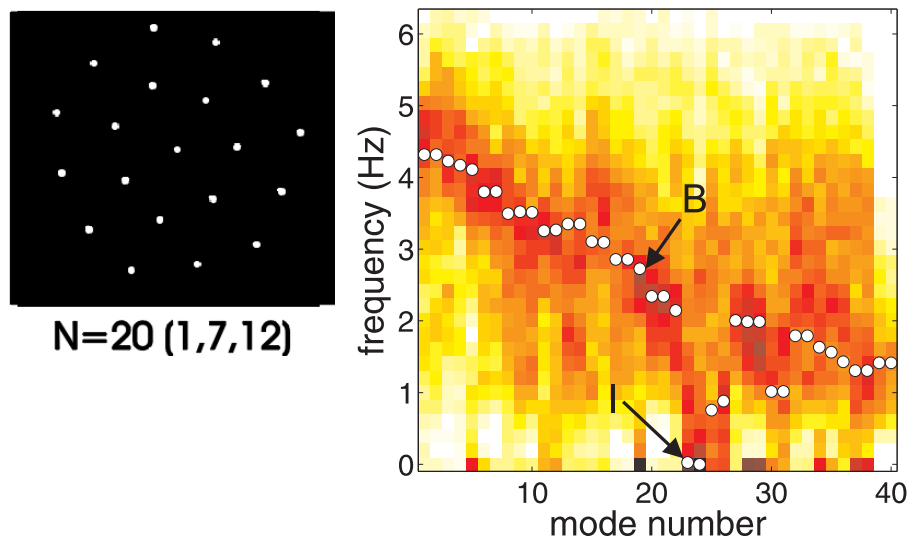


Figure 8.13: *Video snap shot of a cluster with $N = 20$ particles together with the measured mode spectrum. The breathing mode and the intershell rotation are marked by B and I, respectively. After [117].*

Sec. 5.6.

We have seen there that the ion flow in the plasma sheath results in the formation of positive ion space charges (“ion focus”) beneath the dust particles. In addition, the attraction arising from the positive space charge can only be communicated downstream the ion flow. This leads to the formation of the vertically aligned pairs of particles. With reduced gas pressure the vertical alignment becomes unstable (“Schweigert instability”) and gives rise to growing oscillations until a fluid state is reached.

Here, we modify the situation in that we investigate a 2D finite system (with about 40 particles) instead of an extended system [128]. In addition, only one single particle is placed in the layer below the actual cluster (see Fig. 8.14). So there is only a single vertically aligned pair of particles. The advantages of such a system are that, first, the heating effect can be definitely attributed to the single lower-layer particle, and, second, the full dynamics in terms of the normal modes of the cluster is accessible from the mode spectra (the mode spectra are obtained only for the cluster of the upper particles, the lower particle is used as a heat source, only).

As in the case with the extended system, the phase transition is induced by reduction of gas pressure. With decreasing gas pressure, the single lower layer particle starts to oscillate about its vertically aligned equilibrium position due to the instability arising from the non-reciprocal attraction. Due to the mutual Coulomb repulsion, the oscillating lower particle heats the upper particles. At the lowest gas pressures (below 8 Pa) the lower particle is still oscillating below upper layer particles, but from time to time this

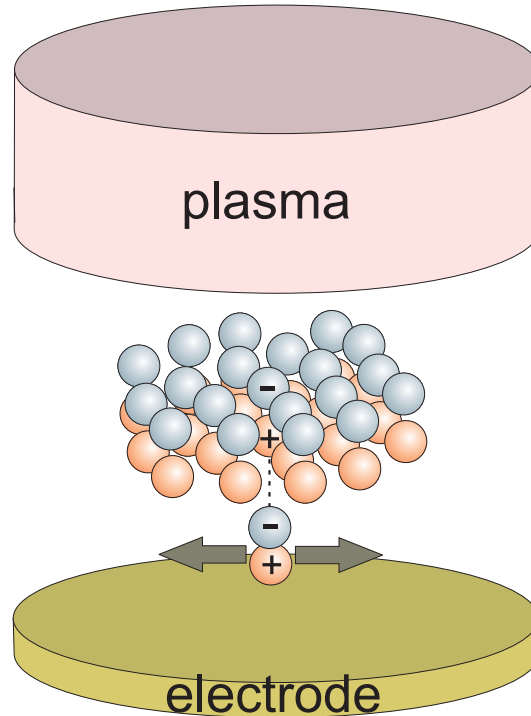


Figure 8.14: *Scheme of the experimental setup to drive a phase transition in finite 2D clusters. A single particle is confined below the actual cluster. By reducing the gas pressure oscillations of the lower particle are excited due to the Schweigert instability.*

particle may jump from one upper particle to another thus heating different particles.

For illustration of the melting transition of the dust cluster, the particle trajectories are shown in Fig. 8.15(a). At the highest gas pressure (12 Pa) the particles only slightly move around their equilibrium positions, at reduced pressure (10 to 11 Pa) the oscillations become visible from the circular particle trajectories in the cluster center. At even lower pressure the particles start to exchange equilibrium positions which is an indication of melting (at 8 Pa an exchange has nearly occurred, at 6 Pa frequent exchanges take place).

The dynamics of the cluster melting process is visible in great detail by analysis of the power spectra, see Fig. 8.15(b). For 12 Pa, the spectral power density of the individual modes is concentrated around a quite narrow band of frequencies that closely follows the mode theoretical frequencies of a solid cluster with a particle charge of $Z = 11\,000 \pm 1000$ and a screening length of $\lambda_D = (1000 \pm 500) \mu\text{m}$.

With reduced gas pressure (10 and 11 Pa), the spectrum changes completely. All modes show a maximum at the same frequency $f_u = 4 \text{ Hz}$ which is apparent from the dark horizontal band in the spectrum. This frequency corresponds to the unstable oscillations. The dominance of this frequency in *all* modes is surprising. In addition to this dominant

frequency, the underlying mode structure of the crystalline state is still faintly observable in the spectrum. From the mode spectra it is seen that the unstable oscillations appear in all the modes although only a single vertically aligned pair exists in this cluster. The pair starts their unstable oscillations at 11 Pa. Upper and lower particle start to oscillate around their equilibrium positions. Due to the Coulomb repulsion between the particles the oscillation is communicated to all particles in the upper layer and is thus visible in all the modes. It is interesting to note, here, that a single aligned pair is sufficient to drive the entire system of 40 particles into the liquid state. That means, that the oscillations of the vertical aligned pair “pump” so much energy into the system that the entire cluster melts in spite of the still relatively large frictional damping.

Below 8 Pa the situation changes again. The spectrum becomes broad for all modes and the close relation to the solid-state mode frequencies is lost. From this, it becomes obvious that the cluster is in a liquid state.

The analysis of the dynamic properties allows to fully substantiate the findings from the extended two-layer system. Here, the situation is simplified as far as possible and detailed information about the onset, the frequencies, the energies and the mechanisms is visualized.

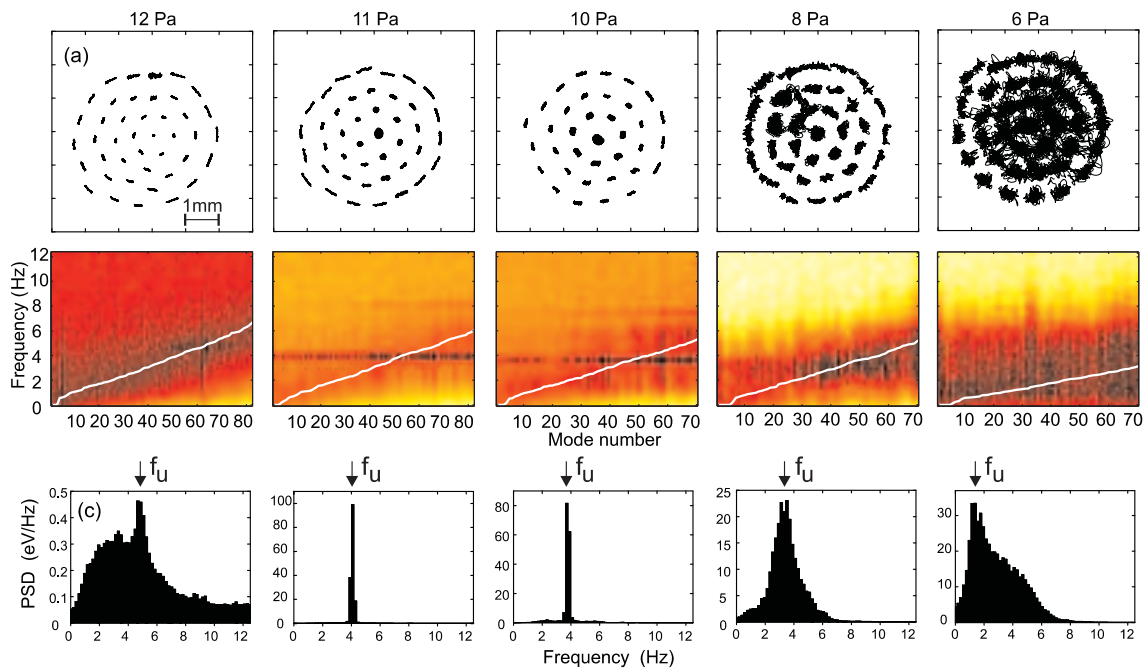


Figure 8.15: *Phase transition of a 2D cluster with one additional particle in the lower layer: a) particle trajectories, b) mode-resolved power spectra, c) mode-integrated power spectra. After [128].*

9. Technical Applications of Dusty Plasmas

After discussing various fundamental aspects of dusty plasmas the next two chapters deal with more “applied” questions. In this chapter, the role of dust in processing plasmas is discussed, in the following chapter dusty plasmas in astrophysical situations are presented.

We start with the description of particle growth in low-temperature plasmas which is followed by the dust removal in processing plasmas and potential issues of dust in fusion devices as well as application of dusty plasmas to the formation of “new” materials.

9.1. Particle Growth Mechanisms

In technological applications the dust particles are not introduced into the plasma, rather the dust particles grow (by wanted or unwanted means) in the discharge itself. This is because typical plasma processes operate in reactive gases, like silane, hydrocarbons, fluorocarbons or organo-silicons. These gases are required to deposit thin films on substrates or to etch into silicon layers, photoresists or protective films. For example, Silane, SiH_4 , is used to deposit thin (amorphous) silicon films. This is needed in computer chip manufacturing or in solar cell production to make use of the properties of silicon as a semiconductor. In the plasma, the silane molecules are dissociated into $\text{SiH}_{0\dots3}$ which is deposited onto suitable substrates. There a hydrogen-rich silicon film is deposited. Hydrocarbons (methane CH_4 , acetylene C_2H_2 or similar) are used to make diamond-like carbon films. There it is intended to grow carbon films that have the properties of diamond, especially in view of hardness. These films are used as covering layers to resist against wear. In addition, HMDSO (Hexamethyldisiloxane) $\text{Si}_2\text{O}(\text{CH}_3)_6$ is used as barrier layers in PET bottles or Tetra packs. HMDSO provides SiO_2 -layers that prevent the carbon-dioxide in beer, lemonade etc. to diffuse through the walls of the container.

All these reactive gases have the tendency to polymerize under plasma conditions. The particle growth mechanisms will be discussed in some more detail, here.

As a model system, we will study the growth mechanism in silane, since it is one of the most investigated systems and is of technological relevance. Silane, SiH_4 , has the same structure as methane (CH_4), where the 4 hydrogen atoms are on the edges of a tetraeder and the silicon atom is sitting in the center. Silane can provide a certain insight into the mechanisms of particle growth. Other reactive gases certainly behave differently due to the different chemical properties involved, but silane shall serve as a paradigm here.

In a plasma discharge (typically rf discharge), the particles grow from molecules (of Å size) to a few hundred nanometer in diameter on the time scale of seconds, see Fig. 9.1. The formation of dust particles works best for high discharge powers and higher gas pressure. The growth is not homogeneous, but one can identify different phases of particle

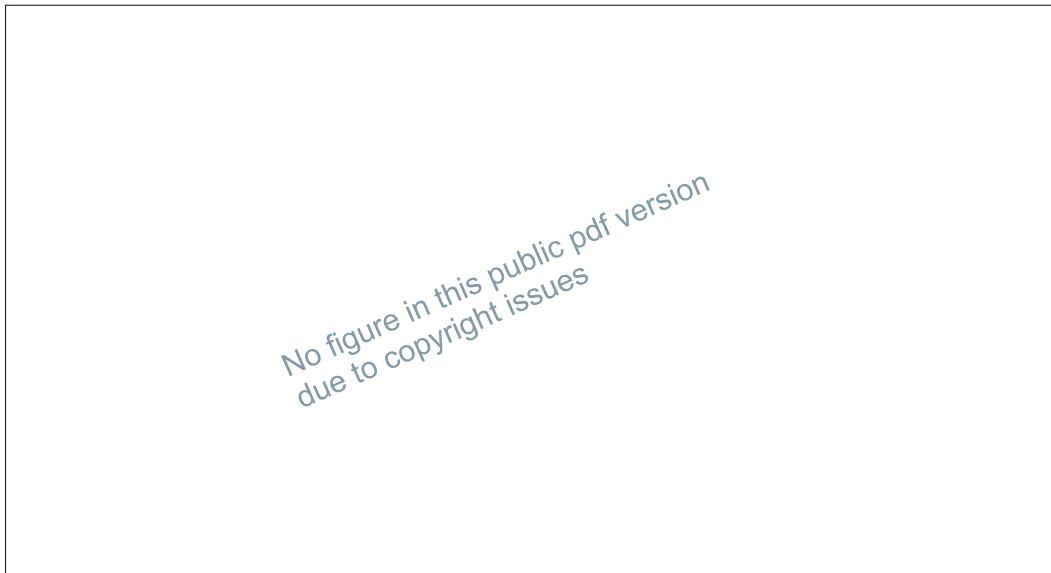


Figure 9.1: *Particle size and particle density in a silane discharge as a function of time. From [2].*

growth:

1. Cluster formation: The particles grow from molecules to clusters of a few nanometer in size. This phase is dominated by plasma chemistry.
2. Agglomeration phase: The particles grow rapidly from a few nanometer to 50 nanometer, say. Correspondingly, the density of particles drops dramatically.
3. Accretion phase: One finds a slow increase in particle size and roughly constant particle density. This phase is dominated by powder dynamics.

The last two phases are observable in Fig. 9.1. These measurements have been obtained using laser light scattering. However, this technique is sensitive only down to particle sizes of about ten nanometer. The initial growth phase, i.e. cluster formation, has to be attacked by different means, e.g. mass spectrometry.

In the following, we will describe the different phases in some more detail.

9.1.1. Cluster Formation

In the cluster formation phase the dust particles grow from the molecule size to clusters of a few nanometer. Nanometer sized particles contain of the order of 100 atoms/molecules. For such small particles (molecules), chemical processes dominate the growth. Possible chemical reactions can be summarized in the form





where reaction pathways are described for neutral, positively charged and negatively charged molecules, respectively.

In this phase, the particles can be measured by mass spectrometry. With modern mass spectrometers, particle masses up to 2000 amu can be measured with high temporal resolution. That means, that clusters with about 60 Si-atoms can be measured with such a device (Si has a mass of 28 amu). Additionally, mass spectra of positively charged particles (ions), negative ions or neutrals can be discriminated by applying opposite voltages at the entrance orifice of the mass spectrometer to repel the unwanted species. The result of such a measurement is shown in Fig. 9.2.

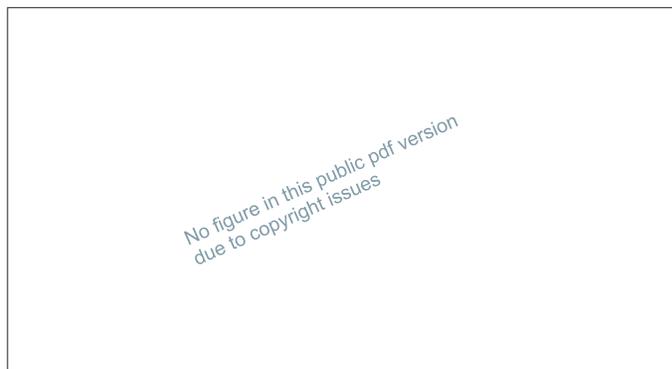


Figure 9.2: *Mass spectrum of negative, positive ions and neutral molecules in a silane discharge. From [2].*

One can easily see that negative ions can be identified up to masses of larger than 1000 amu, whereas positive ions can be seen only up to 400 amu, and neutrals extend only to 100 amu. This finding clearly suggests that the reaction pathway is dominated by negative ions. This can be understood from the fact that the plasma potential is typically positive with respect to the walls. Thus, negative particles, like electrons and the negative silane molecules are trapped in the plasma. Positive ions are readily forced to the walls or electrodes. Thus negative molecules have longer residence times in the plasma and can thus dominate the cluster phase. A further and important reason seems to be the fact that the reaction chain with negative molecules is also favored from chemistry.

When looking closely at the negative ions in Fig. 9.2, one easily sees a periodic structure in the mass spectrum. The peaks correspond to clusters with 1, 2, 3... silicon atoms with some bound hydrogen atoms. In the mass spectrum silicon clusters up to 34 silicon atoms are easily identified. Probably, even larger clusters exist in the discharge, but have not been measured with the mass spectrometer in this particular experiment.

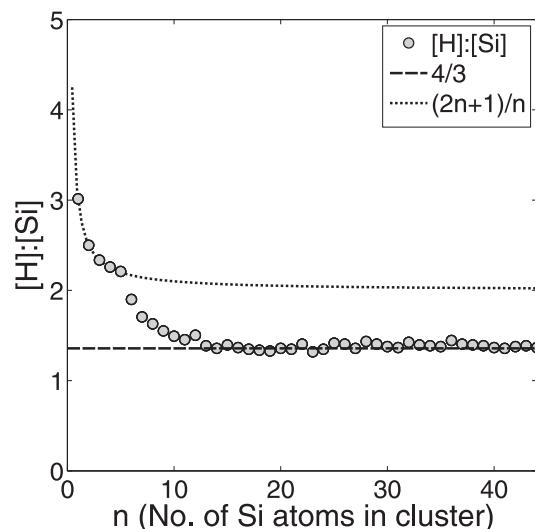


Figure 9.3: *Relative concentration of $[H]:[Si]$ in a molecule (cluster) as a function of the number n of silicon atoms in the cluster. After [2].*

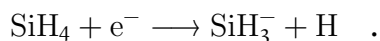
In view of the negative clusters the favored reaction pathway is



...



where SiH_3^- is the precursor of this reaction chain. This ion is formed by dissociative attachment, i.e. an electron attaches to the SiH_4 molecule and a hydrogen ion is removed from the molecule, namely



Following this reaction chain, the ratio of hydrogen to silicon in a cluster then should be $[H]:[Si] = (2n+1)/n$ which is indeed found from the mass spectra for small Si-clusters with up to $n = 5$ or 6 silicon atoms (see Fig. 9.3). For large silicon clusters with $n > 10$ the mass spectra show a concentration of hydrogen to silicon that is very close to $[H]:[Si] = 4:3$. This means that there are equal number of Si-Si and Si-H bonds. Thus, at free bonds randomly hydrogen or silicon is attached. From infrared absorption spectroscopy one knows that there are no double bonds in Si clusters.

The structure of various silicon clusters is shown in Fig. 9.4. The structure of small clusters ($n < 10$) is, of course, dominated by the geometry of their chemical bindings. Larger clusters ($n > 20$) are elongated ellipsoids, whereas yet larger clusters ($n \approx 30$)

become more and more spherical. The radius of a $n = 30$ cluster is about $\sqrt[3]{30} \approx 3$ Si–Si distances wide (a Si–Si bond is about 5 Å). Hence, the cluster is of about 1.5 nm radius (3 nm diameter).

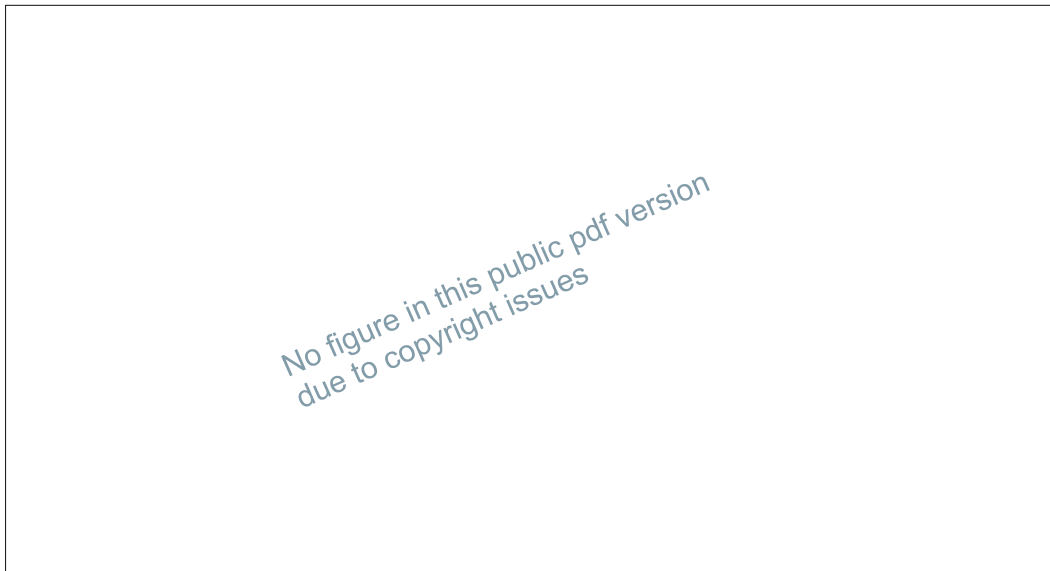


Figure 9.4: Structures of small Si_n clusters. (a) $n = 2$ to 10 and (b) $n = 21$ to 30. From [2].

9.1.2. Agglomeration Phase

In the agglomeration phase, the particles rapidly grow from a few nanometer to several ten nanometers. At the same time, the density of clusters dramatically drops by several orders of magnitude. However, it can be estimated from the measurements (see Fig. 9.1 in the time interval 50 to 60 seconds) that the overall *volume* of the clusters does not change very drastically. From that, it is induced that the large number of small particles agglomerate (stick together) to form a smaller number of larger clusters (see also Fig. 9.5).

Generally speaking, the agglomeration phase is not well understood so far. The problem lies in the fact that clusters of nanometer size are difficult to measure. For smaller clusters one can use, e.g., mass spectrometry (see above), for larger clusters of tens of nanometers light scattering techniques are available. In addition, this growth phase is very fast which makes time resolved measurements difficult.

Thus, one is now in the need for a model to explain that the nanometer particles stick together to form larger clusters. The rapid time scale of agglomeration makes chemical



Figure 9.5: *Electron micrographs of particles grown in an argon-silane discharge a) nanometer sized particles (end of cluster phase), b) and c) agglomerated particles of 45 nm and 100 nm in diameter, respectively. One can see that the particles consist of smaller agglomerated “balls” of about 10 nm in diameter. From [2].*

reactions for this process unlikely. Two alternative agglomeration schemes are discussed, the charged particle agglomeration and the neutral agglomeration model.

The neutral agglomeration model is taken from aerosol science. In that model, particles that collide with each other on their random thermal motion have a certain probability to stick together. From that model, the particle radius r_p is found to increase in time t as

$$r_p = r_0(1 + Ct)^{2/5}$$

and the density n_p drops as

$$n_p = n_0(1 + Ct)^{-6/5}$$

where C is a constant taking into account sticking coefficients, mean free path and further more. The parameters r_0 and n_0 are the particle radius and density at the start of the agglomeration. Such a model fits the experimental results quite well.

The charged particle model brings charging processes into play. In the starting phase of the agglomeration the particle density is very high (more than 10^9 cm^{-3} in Fig. 9.1). The electron density in these discharges is of the order of 10^8 to 10^9 cm^{-3} , thus there are much more clusters (dust particles) than electrons. The electrons are dramatically depleted (see Sec. 2.6.). The average charge on the dust particles is therefore very small,

about 0.1 elementary charges (that means that for a certain fraction of time, e.g. 1 s, the particle has a charge of $1e$ and for another 9 s the particle is neutral). In that case the neutral agglomeration model seems to be reliable.

When the particle density however drops to about 10^7 cm^{-3} , electron depletion is not so dramatic as at the start. Then the particles can have a charge that would correspond to the single particle case. Particles of nanometer size would attain mean charges of the order of a few elementary charges, there are however strong fluctuations of the particle charge for small particles (see Sec. 2.5.2.). In that case, the particles are negatively charged on average, but at certain times they can become neutral or even positive due to the random collection of electrons and ions. The presence of positive *and* negative charged particles at the same time in the plasma strongly enhances the agglomeration rate due to their Coulomb attraction.

In addition, the role of UV photodetachment and secondary electron emission is currently under investigation and might play a considerable role for nanometric dust particles.

9.1.3. Accretion Phase

After the rapid growth in the agglomeration phase it is found that the particles still grow further in size (see Fig. 9.1 at $t > 60$ s). The growth rate in this phase is often found to be close to the growth rate for the corresponding thin-film deposition.

At this stage, the particles have typical sizes of tens of nanometers. They are negatively charged and trapped in the plasma bulk (see Sec. 3.7.). Thus, effectively, the particles behave like small substrates on which additional layers of silicon-hydrogen films are deposited.

The growth of these particles can be continued until the particles reach the micrometer range. The particles are subject to the forces described in Chapter 3. When the particles have grown to several micrometer size the particles experience stronger forces and may eventually drop out of the discharge.

9.2. Technological Impacts of Dusty Plasmas

The technological implications of dusty plasmas can be generalized as twofold: dusty plasmas can have “good” and “bad” impacts on technology. Surface processing technologies are obviously concerned with particle-induced failures and it was recognized only until the end of the 1980’s that (dusty) plasma processes could be involved in such dust contamination problems. Nowadays, dust particles are not only considered as unwanted pollutants, since a number of useful applications have emerged from dusty plasmas. Here, we like to illustrate some of the “good” and “bad” properties of dusty plasmas and we will start with the older problem of contamination by dust.

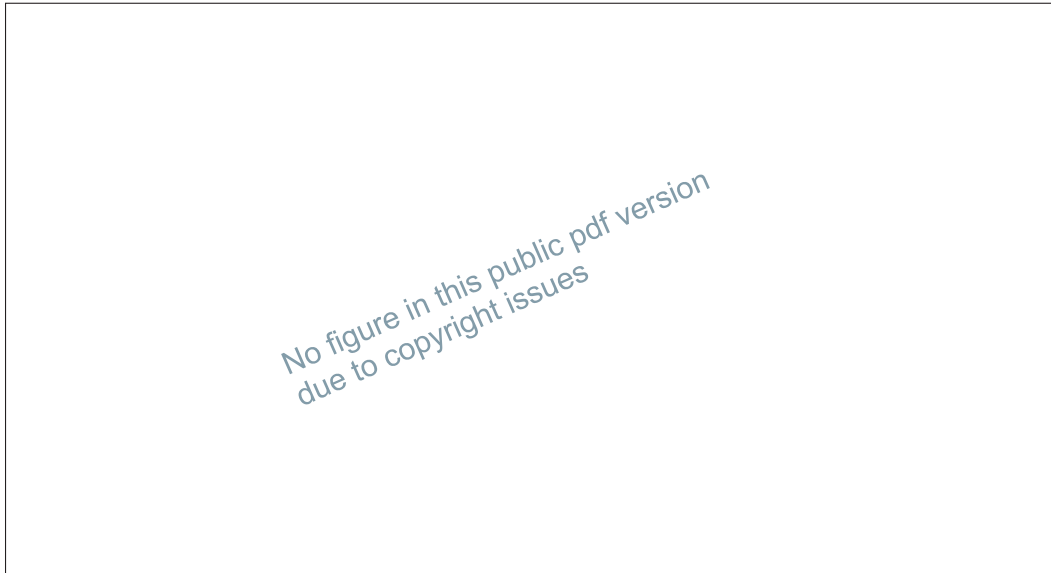


Figure 9.6: *Electron micrographs of a) a trench structure on a silicon wafer. Trenches are used to manufacture capacitors which are buried vertically in the substrate to minimize the occupied wafer space. b) Killer particle lying across several conductor paths. This particle destroys the functionality of the integrated circuit. From Surface Technology Systems Plc.*

9.2.1. Surface Contamination by Dust

Plasma processes are widely used in technological applications such as plasma etching and sputtering or thin-film deposition. It is commonly said that 70 % of the numerous manufacturing steps for computer chip production are plasma processes. Although the plasma conditions are chosen in such a way that dust particle formation is unlikely they are optimized for highest growth rates of the film to be deposited. They are thus close to conditions where growth can occur. In these processing plasmas particles can grow either due to plasma polymerization as described above or particles etched or sputtered from the substrate can arrive in the plasma and can be trapped there (see Fig. 1.3 in the Introduction). When such dust particles are deposited onto the substrate during the discharge cycle or during switch off these particles can do severe damages to the surface properties and can easily destroy integrated circuits. They can cause short circuits or may clog up wafer trenches (see Fig. 9.6).

Roughly speaking, such so-called “killer particles” are dangerous when they have about half the structure size. Current technology works with 300 mm wafers with structure sizes of 32-45 nm. Thus, presently, particles of 20 nm and larger pose a serious problem. As mentioned earlier, particles of that size can just be detected by light scattering, even smaller particles will fall below the detection limit. This causes a severe diagnostic prob-

lem in the future when even smaller structures will be fabricated.

Current technologies to prevent particles from falling onto the substrates make use of the forces that have been discussed in Chapter 3. One possibility is to drill circular grooves in the electrode around the wafer. The grooves then finally lead to the vacuum port. The grooves disturb the sheath potential in such a way that the particles are preferably trapped above the groove and not above the wafer. The grooves duct the dust particles to the vacuum port where the dust is sucked into the vent line.

Additional techniques directly use a gas puff that is blown across the wafer prior to plasma switch-off. The dust particles are blown into regions where they can do no harm to the wafer and when the plasma is switched off the particles settle onto the walls or outer regions of the electrode. For permanent removal of dust by gas flow one of the electrodes has many small holes through which the gas enters the discharge volume, a so-called showerhead configuration. On the other side of the chamber the gas is constantly evacuated. Thus, the discharge works with a constant gas flow through the chamber (most technological applications use discharges with permanent gas flows to remove sputter products and keep the discharge under constant conditions on the molecular level). The gas flow in the chamber is then directed in such way that possible dust particles are constantly washed out of the discharge.

Another way is to heat different parts of the chamber. The thermophoretic force drives the particles to colder plasma regions. Thus by heating the regions where no dust is wanted the particles are removed.

Which technique is applied in a specific discharge strongly depends on the exact conditions and a general statement is not possible here. But one should keep in mind that gas drag or thermophoretic forces scale with the particle radius as α^2 , the electric force proportional to α . Thus, the above described techniques might not work efficiently when smaller and smaller dust particles have to be removed.

9.2.2. Flue Gas Cleaning

Another very important application is very similar to the question discussed above: the removal of dust particles in flue gases, e.g. of coal power plants. The soot particles from the burning process have to be removed very efficiently (more than 99 % of the particles have to be removed), the removal has to be done with low electrical power (otherwise the entire power plant would not work efficiently) and finally large volumes of soot-laden gas have to be treated.

This task can be accomplished by flue gas cleaning using corona discharges, so called electrostatic precipitators. A corona discharge works at air pressure. There a high negative voltage is applied to a wire (similar to a Geiger-Müller counter). The gas near the wire is ionized and the electrons attach to the dust particles. The negatively charged dust particles drift to the positive walls where the dust is collected. From time to time the dust is removed by hammer strokes to the wall. This process is indeed very effective and

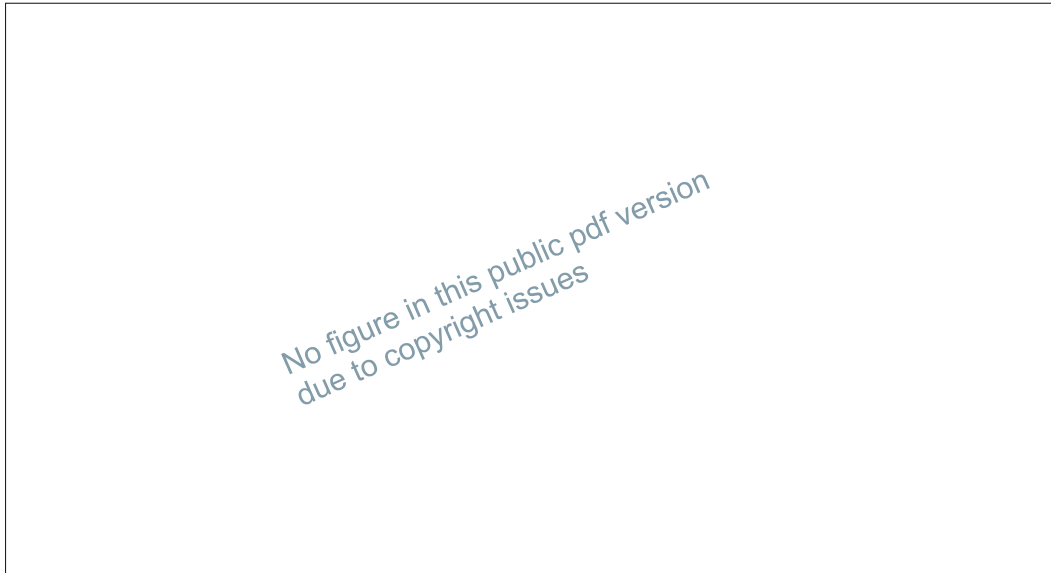


Figure 9.7: *Electrostatic precipitators used in power plants to clean the flue gas from dust particles. Left: Schematic view, right: installed device (Siko Engineering).*

efficient and fulfills the above requirements.

Such a flue gas cleaning device is very large (see Fig. 9.7) and typically cleans 5000 m^3 per hour of flue gas using only several tens to a few hundred kilowatts of electrical power (compared to the 500 MW produced by the power plant).

9.2.3. Dust in Fusion Devices

Dust in fusion devices occurs due to the interaction of the plasma with the plasma facing components (like graphite or CFC (carbon fibre composite) tiles) of the vessel. Dust can be produced by thermal overload of the surfaces leading e.g. to brittle destruction of carbon, to melt layer loss of metals or to desintegration of codeposited layers, see e.g. [129, 130, 131]. Alternatively, dust can grow from sputtered carbon as in the low-temperature plasmas described above. Examples of dust particles collected in existing devices are shown in Fig. 9.8. Particles in active plasmas have also been seen from laser scattering experiments and with fast cameras.

The problems that are associated with dust in fusion devices are the following. First, dust can lead to difficulties with the vacuum vessel and pumping. Second, diagnostics might be covered by dust. For example, mirrors for optical diagnostics of the plasmas might be “blinded” by the dust. More important, material eroded from the wall could enter the core plasma, e.g., in some tokamaks tungsten is used as a plasma facing component. As a high- Z material (the atomic number of tungsten is $Z = 74$), tungsten, when

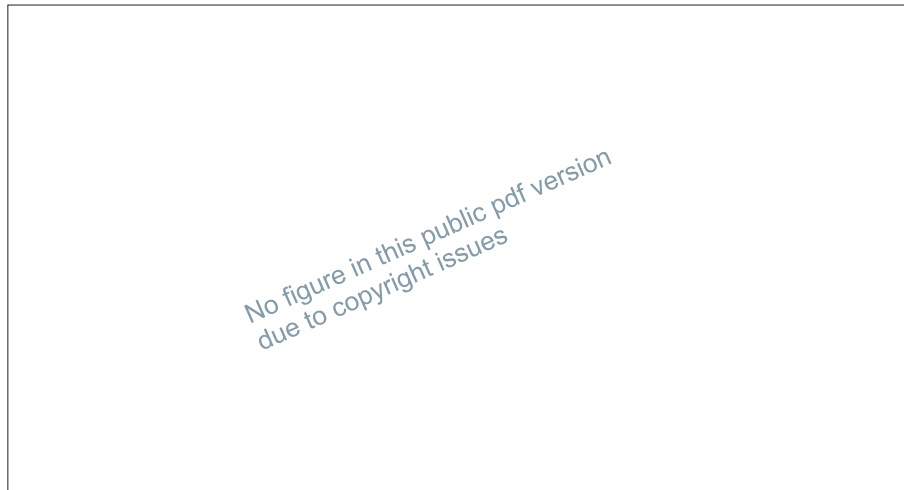


Figure 9.8: *a) REM micrographs of dust collected from fusion devices. From [130, 131].*

eroded from the wall into the core plasma, leads to strong bremsstrahlung losses and thus unwanted cooling of the plasma. Finally, in a real deuterium-tritium fusion plasma, the radioactive tritium can be chemically bound to carbonaceous dust particles (In the edge plasma the plasma conditions are not too different from those of low-temperature plasmas). The dust therefore adds to the radioactive inventory of the fusion device. For an existing tokamak, the density of carbonaceous dust in the edge plasma has been calculated from simulations (see Fig. 9.8). There it has been found highest in the divertor regions where the plasma is relatively cold.

These issues are not problematic for existing devices. The potential implications for safety and operational performance in fusion devices such as ITER are under investigation.

9.2.4. Formation of New Materials

Plasmas in reactive, particle-forming gases are well suited to form new materials. On the one hand, as we have seen, particles can be easily trapped inside the plasma and their positions can be controlled by the various forces acting on them. On the other hand, the chemically active species allow to grow particles or to modify their surface properties.

When using plasmas to modify the surface properties of particles or to grow thin films on substrates one exploits the drastically different temperatures of the various species. The electrons are usually the hottest species with a temperature of a few eV. They are thus able to excite or ionize atoms and molecules, or to dissociate molecules into chemically very active species. Thus, the various radicals or other chemical active species are generated by the electrons. Thus, plasmas provide similar chemically active species as in hot wet-chemical reactants.

The ions and the neutral gas are typically at room temperature or at slightly elevated temperatures. In low-pressure plasmas the species with the highest density is by far the neutral gas. Thus, also the substrate and the particles are kept at low temperatures which is essential for the (thermal) stability of the substrate or the particles.

Consequently, in such reactive discharges one can have the advantage of high-temperature chemistry without the thermal stress on the particles or the substrates. This opens up the road to a large variety of new materials.

Coating of particles can be technologically applied to give the particles desired optical or chemical surface properties, e.g. [132]:

- Iron particles are coated with an optical black surface. These particles then can be used as toner particles which can be handled by magnetic fields which would result in a new type of copy machine.
- Particles are coated with catalytic material. Due to the very large surface area of the particles, such systems provide very efficient catalysts.
- Particles surfaces can be modified so that medical and pharmaceutical agents can attach to the surface of the particles. Again, the very large surface area of the particles leads to an efficient and controlled way to apply the medical drugs.
- Fluorescent particles are coated with a thin layers that keep the particles stable against bombardment from plasma particles. Such fluorescent particles can then be used in as the fluorescent layer in light tubes.

9.2.5. Polymorphous Silicon Films

As a final example for the technical potential of dusty plasmas, the deposition of silicon films with special properties is discussed, namely thin films in solar cell technology.

Solar cells that do not achieve a very high efficiency are often installed in electronic devices like pocket calculators or watches. They can be easily deposited with plasma processes and are quite cheap. These films are deposited in silane discharges on appropriate substrates under conditions where dust particle formation does not occur. This thin silicon film that is responsible for the opto-electric properties of the solar cell is amorphous and a lot of hydrogen is incorporated in the film. These films are denoted as a-Si:H, where the “a” stands for amorphous. The efficiency of such films is of the order of 4 to 6 %, only.

In contrast, solar cells for power production (on the roof of houses or in large solar cell fields) require high efficiency. This is only achieved by crystalline silicon. There, efficiencies above 15 % are standard and up to 22 % have been achieved. However, solar cells from crystalline silicon are very expensive. They are formed from molten silicon at high temperatures and subsequently slow cooling.



Figure 9.9: *Electron micrograph of a silicon film at 50°C in its as-deposited state (left) and after annealing at 425°C for one hour. From [133].*

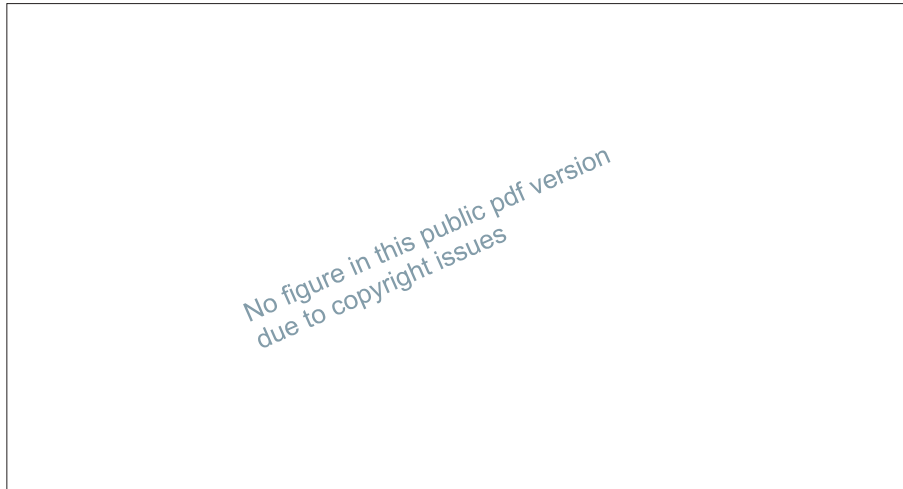


Figure 9.10: *Evolution of the efficiency of solar-cells made from a-Si:H and pm-Si films. From [133].*

Here, an interesting new development has emerged in the last recent years [133]. Solar cells have been deposited in silane discharges just like those that are used to deposit a-Si:H films. However, the discharges are operated under plasma conditions (gas pressure,

gas flow, discharge power, substrate temperature etc.) that are very close to powder formation. Previously, such conditions have been avoided since the formation of dust at thin film deposition was considered as very unfavorable.

Operating the discharge close to powder formation means that no particles larger than 10 nanometers are formed. Thus, in-situ diagnostics will characterize the discharge as dust-free since particles below 10 nanometers cannot be detected. However, it is found that close to the conditions of detectable dust formation already particles of a few nanometers in size are formed. These particles are then incorporated into the film before the particles start to grow in the agglomeration and accretion phase.

Such nanometer clusters are indeed incorporated in the film as can be seen in the micrograph in Fig. 9.9. The dust particles of nanometer size are crystalline and in the film they appear as tiny crystalline patches in the otherwise amorphous silicon matrix. The circles and arrows hint at those crystalline regions. After annealing for one hour the film has much larger crystalline regions. The dust particles serve as a crystalline nucleus where the crystallization can start from. The resulting film is neither crystalline nor amorphous and consists of some larger crystalline patches in a still amorphous matrix. The film is then termed as polymorphous silicon (pm-Si). So, these new type of silicon film is due to the incorporation of nanometer-sized dust.

So, what are the properties of the pm-Si films? Since the film is somewhat crystalline and somewhat amorphous, the efficiency of solar cells made from these films (9 to 10 %) is considerably higher than that of the a-Si:H films (see Fig. 9.10). What is even more, the efficiency stays constant over time, whereas the a-Si:H films tend to degrade, i.e. their efficiency drops with time. So, these dust-incorporated films have decisively improved properties, but essentially use the same technology as the a-Si:H film deposition. Only the parameters of operation are somewhat different and close to the particle formation threshold. It should be noted, here, that the incorporation of larger particles does not lead to improved films.

So with small changes to the manufacturing process a large improvement in the efficiency of solar cells is achieved due to the application of dusty plasmas.

10. Astrophysical Dusty Plasmas

The field of dusty plasma physics has started from the investigations of dusty plasmas in astrophysical situations, from the study of comets, interstellar clouds or the rings of the Great Planets.

In space, dust particles can collect electric charges by various processes, as discussed in Chapter 2, like electron and ion collection, secondary emission, photoelectric charging, sputtering etc. The particles react to the magnetic and electric fields in the plasma environment of planets, the wind of charged particles coming from the Sun and gravitational forces. The combination of these processes give rise to a description of dust processes in astrophysical situations that is sometimes referred to as “gravito-electrodynamics”.

Dusty plasmas represent the most general type of space plasmas. In fact, it is difficult to find astrophysical plasmas that do not include dust particles (maybe except the fusion plasmas in the interior of stars). There is a vast amount of possibilities where astrophysical and extraterrestrial dusty plasmas naturally occur. When starting near the Earth’s surface we find the so-called *Noctilucent Clouds* and *Polar Mesospheric Summer Echoes (PMSE)*. In our solar system we find dust in the rings of the Great Planets like Jupiter and Saturn, in cometary tails and in the zodiacal light. Interstellar dust-containing hydrogen or molecular clouds also add to this list.

From the vast amount of different astrophysical situations we will restrict here to the formation of spokes in the rings of Saturn and dust particle “orbits” at Jupiter and Saturn. These are situations where experimental data are already available (from the spacecraft Galileo at Jupiter) or where they will become available in the near future (Cassini at Saturn, see <http://www.esa.int/SPECIALS/Cassini-Huygens/>). In addition, a few words on the noctilucent clouds will be given here first [134].

10.1. Noctilucent Clouds and PMSE

Noctilucent clouds are “nightly shining” clouds that are observable in the summer months (May to September) at high-latitude regions ($50 - 80^\circ$), like Northern Europe. They can be seen long after sunset. They are thus located at high altitudes of $80 - 110$ km above the surface of the Earth where the sun, although being already below the horizon, still illuminates the clouds (see Fig. 10.1).

The clouds are thus at the lower edge of the ionosphere. They are assumed to consist of water or methane ice particles which are charged by the plasma of the ionosphere. Surprisingly, in the summer months the atmosphere at these altitudes is extremely cold (about 110 K) and is much colder than during winter times (this is the so-called summer anomaly). This low temperature allows the water and the methane to freeze under the



Figure 10.1: *Photo of a noctilucent cloud. From Wikipedia.*

conditions of the upper atmosphere preferably on small condensation nuclei. This explains why the clouds are preferably visible in the summer months.

Noctilucent clouds have first been reported in 1885, a few years after the big explosion of the Krakatoa volcano in 1883. It is not clear whether noctilucent clouds have been present before this explosion, but have not been reported, or whether the Krakatoa has triggered the existence of the noctilucent clouds by blowing large amounts of dust into the atmosphere. Nevertheless, the occurrence and strength of noctilucent clouds have increased since their discovery. It is sometimes argued that the increased methane release on Earth leads to the increased occurrence of noctilucent clouds.

The “dust” particles in the noctilucent clouds can be observed by sounding rockets launched into the ionosphere, by lasers fired into the atmosphere (so-called LIDARs, i.e. Light Detection And Ranging) and by backscatter from radar signal radiated into the atmosphere (see Fig. 10.2). With LIDAR technique the light scattered from particles in the atmosphere is detected at different places on the Earth surface and the height of the scattering particles is found from triangulation. LIDARs are sensitive to dust particles larger than approximately 30 nm due to the use of light scattering (see comments in Chapter 9). Radars do not “see” the dust particles directly, but the radar signal is scattered from the electron and ion clouds around the dust particles. Radar backscatter



Figure 10.2: *Simultaneous occurrence of PMSE and noctilucent clouds over Northern Norway. Color-coded is the radar backscatter signal as a function of time and height. The contour lines denote the noctilucent cloud position determined from the LIDAR. From [135].*

usually is an indication of smaller dust particles of 1-20 nm size. Often during summer months one observes radar backscatter in the mesosphere (up to 100 km altitude), the above mentioned PMSEs. It is reasonable to assume that the PSMEs are related to the presence of noctilucent clouds. Indeed, there are numerous observations that substantiate this reasoning, see Fig. 10.2. However, often one sees noctilucent clouds and no radar backscatter, or vice versa. This might due to the fact that the presence of PMSEs and noctilucent clouds rely on different particle sizes, larger than ≈ 30 nm for the noctilucent clouds and smaller than ≈ 30 nm for radar backscatter. The physics behind the noctilucent clouds and PMSEs is, however, not fully understood so far.

10.2. Dust Streams From Jupiter

We now turn to dusty plasmas in our solar system and will discuss dust properties near Jupiter and Saturn [136].

Jupiter is the largest planet of our solar system (its mean radius is $R_J = 69\,911$ km) and the one with the highest mass ($m_J = 1.898 \cdot 10^{27}$ kg). One would therefore expect that due to gravitational attraction all dust in its vicinity would be “sucked” towards Jupiter. Nevertheless, the Ulysses spacecraft has discovered a high-speed dust flux away from the Jovian system in 1992. This dust stream has been investigated in much more detail by the Galileo spacecraft since 1996. Galileo had a dust detector on board that was able to



Figure 10.3: *Left: Orbits of the Galileo spacecraft from 1996 to 2003. The black circles in the center represent the orbits of the 4 Jovian moons Io, Europa, Ganymed and Callisto. Right: Measured dust impact rate (color coded) on Galileos path near the inner moons. High impact rates are found near the moon Io. From Max-Planck-Institute Heidelberg, E. Grün, <http://www.mpi-hd.mpg.de/dustgroup/galileo/foalien/jupstream.html>.*

measure the velocity and the mass of the arriving dust particles and was calibrated for dust particles in the size range $30 \text{ nm} < a < 100 \text{ nm}$. The dust detector measured a certain fraction of quite large particles ($> 1 \mu\text{m}$). The majority of the particles were very small (smaller than the calibration range, i.e. $a < 30 \text{ nm}$) and very fast. These particles were generally directed away from Jupiter.

On its path, Galileo measured the dust particles arriving at the dust detector (see Fig. 10.3). Very high impact rates were found close to the moon Io. Io is an active volcanic moon and is closest to Jupiter. So, Io was already very early considered to be the source of the dust particles emerging from the Jovian system. Dust from the volcanic eruptions is sent into the magnetosphere of Jupiter and is transported outward. To describe this outward motion the dust particle motion has to be modeled quite accurately.

10.2.1. Model

The equation of motion of a dust particle is given by

$$\ddot{\vec{r}} = \frac{Q_d}{m_d} (\dot{\vec{r}} \times \vec{B} + \vec{E}_c) - Gm_J \frac{1}{r^3} \vec{r} \quad (10.1)$$

where G is the gravitational constant. Hence, electric field force, the Lorentz force and gravitational forces have to be considered. The magnetosphere would rigidly co-rotate with the planet at the rotation frequency Ω_J if the magnetosphere was perfectly conducting. \vec{B} is the magnetic field of Jupiter and $\vec{E}_c = (\vec{r} \times \vec{\Omega}_J) \times \vec{B}$ is the co-rotational electric field. Other forces can be neglected, here.

As the grain moves through the plasma the particle charge is determined by the different currents to the particle (see Eq. (2.1))

$$\frac{dQ_d}{dt} = \sum_i I_i$$

where typically electron and ion collection, secondary emission and photoelectron emission are considered.

The magnetic field \vec{B} (and thus the co-rotational electric field \vec{E}_c) around Jupiter is quite accurately known and is used to calculate the Lorentz force on the dust particles. It is important to note, here, that the magnetic field axis and the rotational axis of Jupiter have a relative angle of about 10° . Thus during Jupiter's rotation the magnetic field precesses, i.e. has a "tumbling" motion.

The equation of motion for the dust particles is then solved numerically. Dust particles of various sizes are considered to originate from Io's orbit and their motion through the Jovian magnetosphere is followed in the simulation.

10.2.2. Model and Experiment

To illustrate their behavior the orbits of particles with fixed charge are considered, see Fig. 10.4. It is seen that negatively charged dust (of fixed charge Z_d) moves on closed orbits. Particles of 80 nm radius are found to have the largest excursions which are still very small compared to the size of the Jovian system. Positively charged dust is found on closed orbits for particles smaller than 20 nm or larger than 120 nm. Positive dust particles in the intermediate size range have no closed orbits and may leave the system. These are the particles that are responsible for the high-speed stream away from Jupiter.

In more sophisticated calculations taking the charging equation into account the trajectories of 10 nm particles emerging from the orbit of the moon Io have been calculated (see Fig. 10.5). One can see that indeed particles are emitted outwards, away from Jupiter. The particles leave Io and form a comet-tail like swarm that spirals outward. One can also see that the particles leave the equatorial plane and acquire positions quite far above and below the equatorial plane (upper right panel). This is due to the inclination of the magnetic field axis relative to Jupiter's rotation axis. So, the dust particles form a pattern around Jupiter like a ballerina skirt. The particles on their way usually have positive charges due to photoelectron emission.

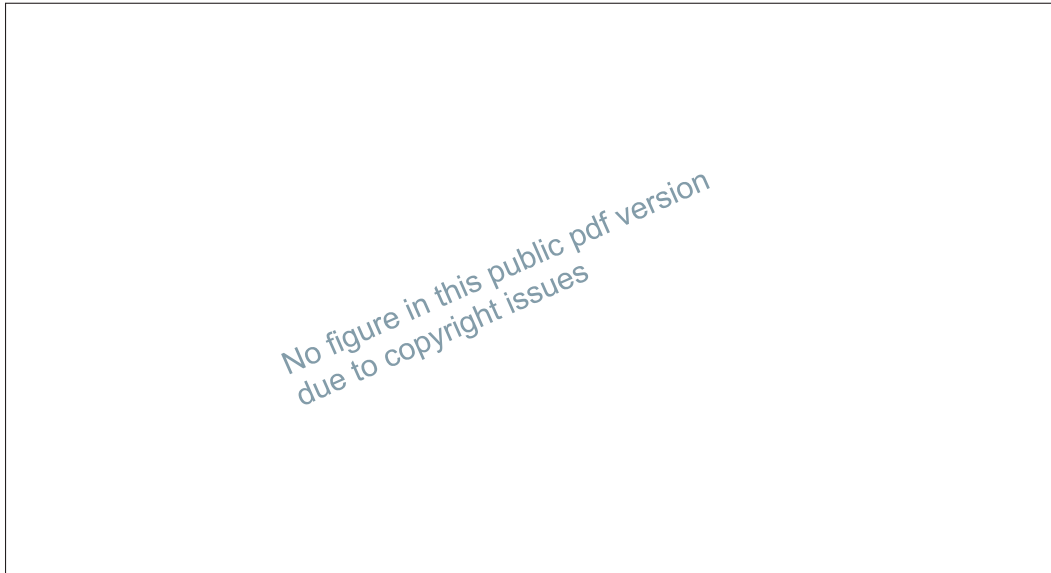


Figure 10.4: *Orbits of dust particles with fixed potential. (a,b) Negatively charged dust with a surface potential of -10 V (corresponding to a charge of $Z_d = 7 \cdot a$ with particle radius a given in nanometers). The considered dust particles range between 20 and 300 nm. (c,d) Positively charged dust at $+10$ V for particles in the size range between 10 and 180 nm. The trajectories are a projection onto the plane of the rotation axis (the rotation is around $x = 0$) and y is the distance above or below the equatorial plane of Jupiter. From [136].*

Finally, to check the reliability of the simulation results the flux of outward-moving dust particles is calculated and compared to the experimental data collected by the dust detector on Galileo. There the number of dust impacts as a function of orientation relative to Jupiter is shown. This comparison is shown in Fig. 10.6. One can see a remarkable agreement between these two curves where the maxima at 5 and 17 h (local time) and the minimum at 10-14 h is modeled very accurately. This gives a lot of confidence in the accuracy of the calculations.

To summarize, the observed dust stream of particles away from Jupiter is believed to be due to positively charged grains of about 10 nm radius that emerge from the volcanic moon Io.

10.3. Dust Orbits at Saturn

The situation of dust particle dynamics at Saturn is very similar to that at Jupiter. Therefore, similar dust streams are expected also for Saturn. There, the source of the



Figure 10.5: *Orbits of dust particles of 10 nm radius. Upper panel: “top view” and “side view” of particle motion at Jupiter. The particles are considered to be emitted from Io’s orbit (the dark ring in the upper left panel). Lower panel: same for the situation at Saturn. The particles are emitted due to disturbances of the magnetosphere by the moons Dione, Helene and Rhea. From [136].*

dust particles can be the moons Dione, Helene and Rhea which orbit in the outskirts of the magnetosphere of Saturn (their distances from Saturn are $6.3R_S$ and $8.7R_S$ with $R_S = 58\,232$ km being the radius of Saturn, $m_S = 568 \cdot 10^{24}$ kg). These moons are not volcanic, but dust may enter the Saturnian magnetosphere by meteoroid bombardment. The simulated dust transport for Saturn is also shown in Fig. 10.5. The particle motion is purely radially outward. The particles stay in the equatorial plane. This is due to the fact that the magnetic field axis of Saturn is closely aligned with the rotation axis.

The aligned magnetic field also gives rise to a new phenomenon that is not observable at Jupiter. Since the aligned situation is very symmetric there exist stable particle orbits that are high above the equatorial plane and that never cross this plane, so-called “halo” orbits, see Fig. 10.7. Particles in these orbits are kept at such positions due to the balance of three forces: the centrally inward gravitational force, the radially outward centrifugal force and the electromagnetic force that points upward under a certain angle (see inset of Fig. 10.7). Such particles might be observed by the spacecraft Cassini that has arrived at Saturn in Summer 2004. At the end of its nominal 4-year mission Cassini will explore high inclination orbits and might then prove the existence of these particles.

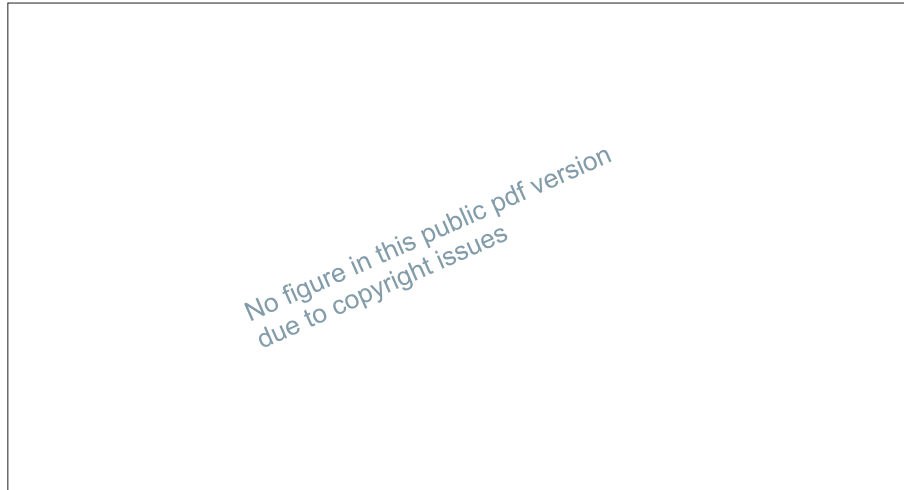


Figure 10.6: *Flux of Jovian stream particles as a function of local time from simulation (upper panel) and experimental data collected from 1995 to 2002 (lower panel). From [136].*

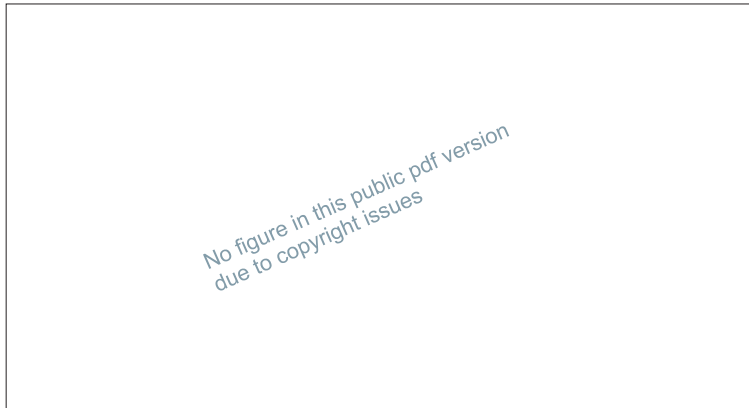


Figure 10.7: *"Halo" orbits of dust particles above the equatorial plane at Saturn. The inset shows the action of the three responsible forces, gravity, centrifugal force and electromagnetic forces (Cover of Geophysical Research Letters, May 2001).*

10.4. Spokes in Saturn's Rings

Next, the formation of spokes will be discussed. We have mentioned this example as a paradigm for dusty plasma physics in astrophysical situations in the Introduction. And, indeed, the problem of spoke formation can only be treated when the various processes in dusty plasmas are taken into account (like charging, forces etc.).

It is interesting to note that at least two different theories exist to explain the formation of spokes and a definite answer cannot be given at the moment. It is expected that also here the spacecraft Cassini will allow a deeper insight into the spoke formation.

Spokes are known since the early 1980's from photos of the spacecrafts Voyager 1 and 2 and they have been rediscovered by Cassini in 2005 (Interestingly, the spokes were not visible when Cassini arrived at Saturn in early 2004). The spokes appear in the B-ring of Saturn which extends from 91 975 km to 117 507 km and is the most opaque ("solid") ring of Saturn and one of the most prominent rings. Spokes are radial features in the B-ring, see Fig. 1.1a). The spokes appear dark when viewed in backscattered light and bright in forward scattered light. This suggests that the spokes consist of sub-micron particles which have such scattering properties. Spokes come into existence in less than 5 minutes and disappear after about 5 hours. The radial elongation of the spokes is a few 10^4 km, their width is between 200 and 1000 km. The spokes are therefore a very dynamical phenomena and are unlikely to be explained by only gravitational effects.

Here, we like to illustrate the problem of spoke formation using the model of Goertz and Morfill [137]. In this model it is assumed that spokes become visible when dust particles are lifted above ring plane. In the ring the small dust particles are not visible due to the larger rocks and boulders (of 10 cm to 10 m size). Above the ring plane the particles become visible and show the scattering properties as described above. To be lifted above the ring plane the dust particles must be accelerated. In this model the acceleration is due to a perpendicular (vertical) electric field. Now the question arises how such an electric field appears and why its appearance is only sporadic (spokes do not appear always and everywhere).

Under normal conditions the plasma density in the ring plane is small ($n_e \leq 10^4 \text{ cm}^{-3}$) and the surface potential of the dust is slightly positive on the sun-facing side, the mean charge of sub-micron dust is expected to be much smaller than one elementary charge. The dust is essentially neutral. In the shadow, it is expected to be around -6 V since there is no photoemission. The ring plane is an equipotential line. Due to the small dust and the small electric fields at the ring surface dust particles cannot be lifted above the ring plane.

It is then assumed that a local increase of plasma density can change this equilibrium situation drastically. Such a local plasma density increase can be due to meteoritic impacts into the ring plane. In the plasma with higher density the surface potential of the dust becomes negative (around -6 V). Furthermore, the equipotential lines become compressed below the local plasma (see Fig 10.8). This can accelerate dust particles above the ring plane where they become visible.

Having now elevated dust particles there is the need to explain the radial motion of the spokes. There, one has to look into the rotation of the different species. The higher-density plasma cloud is coupled to the magnetosphere of Saturn. Since the entire magnetosphere of Saturn rotates at the same frequency Ω_S as Saturn also this plasma cloud will rotate at this speed. The dust particles however will rotate around Saturn

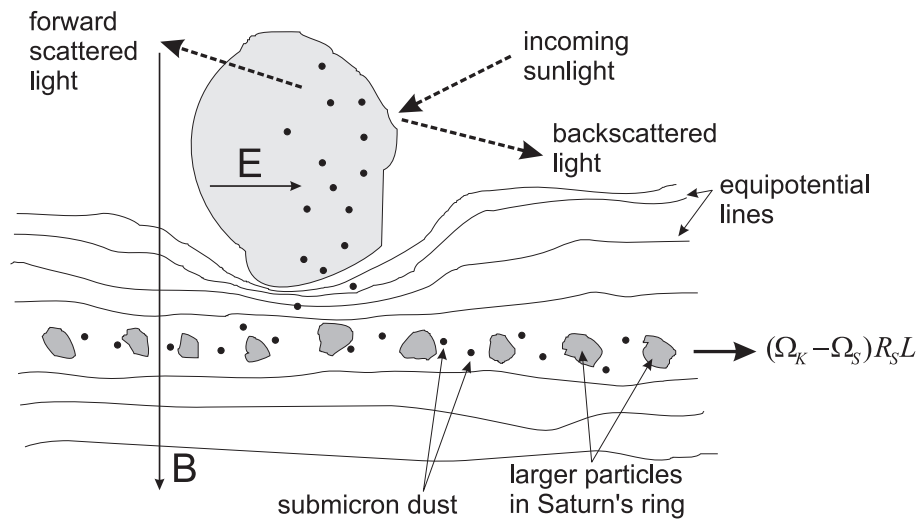


Figure 10.8: *Model for the levitation of dust above the ring plane and the formation of spokes. Under a locally increased plasma density (dark grey) the equipotential lines are compressed leading to an increased electric field. The particles are lifted above the ring plane. There, the particles move on Kepler orbits and accumulate on one side of the local plasma disturbance and are then transported radially (see text). The view in this Figure is radially away from Saturn. After [137].*

on Kepler orbits with the Keplerian frequency $\Omega_K > \Omega_S$.^{*} Thus, the plasma cloud and the particles will rotate at different speeds, so the dust is accumulated on one side of the plasma cloud (see Fig. 10.8). The particles cannot leave the plasma cloud due to confining electric fields at the plasma cloud boundary.

Since the plasma cloud is quasineutral and the negative particles accumulate on one side an electric field arises. This electric field together with the magnetic field of Saturn (which is nearly vertical near the ring plane) leads to an $\mathbf{E} \times \mathbf{B}$ drift in the radial direction. Thus, the plasma cloud with the particles will stretch radially and radially elongated dust structures are formed, which is seen as the spokes.

The particles lifted above the ring plane should have sizes in the range of 100 to 300 nm. Smaller particles need much more time to charge up (the charging time is indirect proportional to particle size, see Eq. 2.20). Larger particles have too large mass and are not accelerated fast enough. This size range is just the one expected from the scattering of the sunlight. Thus the model makes a number of predictions which are in agreement with the findings from the observations.

In a different model, Bliokh and Yaroshenko [138] explain the spoke formation by

^{*}The particles in the B-ring rotate faster than Saturn. Saturn performs one revolution in 10.2 h, the Kepler period at a distance of 100 000 km from Saturn is about 9 h.

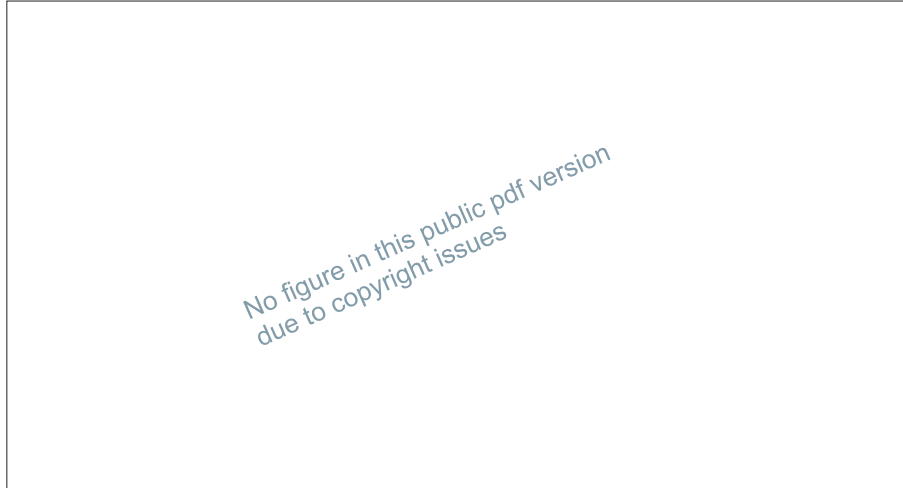


Figure 10.9: *Simulated Mach cone in Saturn's rings. From [139].*

density waves in a multi-stream situation. This approach also allows to account for the very many narrow rings and gaps within the B-ring. Although such dust density waves are probably not strong enough to fully explain the spoke formation they represent an intriguing mechanism. This demonstrates that the question of spoke formation is not settled yet.

10.5. Mach Cones in Saturn's Rings

Finally, we like to address an interesting diagnostic method that might be able to measure plasma properties in the rings of Saturn. This idea was first proposed by O. Havnes in 1995 [105].

There, the effect of Mach cone formation in Saturn's rings is considered. As mentioned above, large boulders of centimeter to meter size move at Keplerian velocities around Saturn. At a radial distance of $R = 100\,000$ km the Keplerian velocity is around 19 km/s. Small dust particles might be coupled to the magnetosphere of Saturn that co-rotates with the planet. At that distance this velocity is around 17 km/s. Thus there is a large relative velocity of larger boulders and small dust particles. This velocity difference might even be larger than the sound speed of dust waves in the ring. Thus, Mach cones might emerge in Saturn's rings. The kind of wave that might be excited there are dust-acoustic waves. Since the dust is expected to be only weakly coupled dust-acoustic waves might be launched. These are the weakly coupled dust waves with the smallest sound speed and thus will be preferably excited by boulders that move with supersonic speed relative to the smaller dust particles. Simulated Mach cones of dust-acoustic waves in the rings of

Saturn are shown in Fig. 10.9.

These Mach cones will be very similar to those observed in strongly coupled dust systems as described in Section 7.6. The main difference is that in strongly coupled systems we find Mach cones due to dust lattice wave excitation whereas in Saturn's rings we expect Mach cones of dust-acoustic waves. As for the DLW Mach cone, the wave pattern of the DAW Mach cone shows a complicated structure with fine details due to the dispersion of the DAW and other effects like spatially and temporally varying dust densities or dust charges. From the Mach cones and its detailed structure the properties of the dusty plasma inside the rings can be derived. Again, it is anticipated that Mach cones might be observed by the Cassini spacecraft.

11. Summary

In these Lecture notes an overview over the various effects in dusty plasmas has been given. Fundamental properties of dusty plasma like particle charging, interaction potentials and forces on the dust have been included. Waves in weakly and strongly coupled dusty plasmas have been discussed and the extension towards normal modes in finite systems has been presented. Finally, a rough description of applications of dusty plasmas in technology has been given, before some examples from the origin of dusty plasma physics, namely astrophysical situations, have been mentioned.

To summarize, the main properties of dusty plasmas compared to “usual” plasmas are compiled below again:

- Dusty plasmas are at least three component plasmas (electrons, ions and dust). In this sense, dusty plasmas are somewhat comparable to negative ion plasmas.
- However, the typical charge on the charge carriers (dust) are of the order of 10 000 elementary charges which leads to strong coupling on the one hand and to strong reactions to electric fields on the other hand.
- The dust charge is variable and depends on the local plasma parameters. The charging time of particles is finite. Thus, the charge becomes a dynamic variable and can lead to novel dynamic phenomena.
- The dust mass is by orders of magnitudes larger than that of electrons and ions. Thus the dominant time scale is that of the dust plasma frequency ω_{pd} which is by orders of magnitude smaller than that of electrons and ions leading to convenient time scales for the observation of dynamic processes in laboratory discharges. Also the separation of time scales leads to new types of waves and dynamical phenomena.
- The slow time scales allow that electrons *and* ions contribute to shielding which should result in different shielding scales.
- The dust size is not negligibly small leading to surface phenomena and forces which are unimportant in “usual” plasmas.

Due to all of these unique properties of dusty plasmas a number of new phenomena occur in dusty plasmas like new force, new types of waves, crystallization processes, phase transitions, observation of processes on the kinetic level and many more. We hope that we have clarified the origin of these phenomena and that we have demonstrated why dusty plasmas have become one of the very interesting fields in plasma physics.

List of symbols

Symbol	Definition
m_d, m_e, m_i, m_n	Mass of dust particles, electrons, ions and neutrals
T_d, T_e, T_i, T_n	Temperature of dust particles, electrons, ions and neutrals
n_d, n_e, n_i, n_n	Density of dust particles, electrons, ions and neutrals
$\lambda_{D,e}, \lambda_{D,i}, \lambda_D$	Electron, ion Debye length and linearized Debye length $\lambda_D^{-2} = \lambda_{D,e}^{-2} + \lambda_{D,i}^{-2}$
$v_{th,e}, v_{th,i}, v_{th,n}$	Thermal velocity of electrons, ions and neutrals: $v_{th,\alpha} = \sqrt{\frac{8kT_\alpha}{\pi m_\alpha}}$
u_i	Ion drift velocity
a	Dust particle radius
b	Nearest neighbor distance in plasma crystals
ϕ_p, ϕ_f	Dust particle potential ϕ_p and floating potential ϕ_f
$Q_d = (-)Z_d e$	Dust particle charge Q_d and charge number Z_d
τ_e, τ_i	Dust charging time scale due to inflow of electrons and ions
β	Epstein friction coefficient
ω_0	Frequency of trapping potential
b_{WS}	Wigner-Seitz radius $b_{WS} = (3/4\pi n)^{1/3}$ (3D) or $b_{WS} = (\pi n)^{-1/2}$
r_0	Size parameter of finite systems $r_0 = (2Z_d^2 e^2 / (4\pi \epsilon_0 m_d \omega_0^2))^{1/3}$
κ	Screening strength $\kappa = b_{WS}/\lambda_D$ (for extended systems) $\kappa = r_0/\lambda_D$ (for finite systems)
ω_{pd}	Dust plasma frequency $\omega_{pd} = \sqrt{\frac{Z_d^2 e^2 n_d}{\epsilon_0 m_d}}$ (for weakly coupled systems) $\omega_{pd} = \sqrt{\frac{Z_d^2 e^2}{\epsilon_0 m_d b^3}}$ (for strongly coupled systems)

Bibliography

- [1] F. Verheest, *Waves in Dusty Space Plasmas* (Kluwer Academic Publishers, Dordrecht, 2000). 1, 87
- [2] *Dusty Plasmas*, edited by A. Bouchoule (John Wiley & Sons, Chichester, 1999). 1, 141, 142, 143, 144, 145
- [3] P. K. Shukla and A. A. Mamun, *Introduction to Dusty Plasma Physics* (Institute of Physics Publishing, Bristol, 2002). 1, 87
- [4] P. Bliokh, V. Sinitin, and V. Yaroshenko, *Dusty and self-gravitational plasma in space* (Kluwer Academic Publ., Dordrecht, 1995). 1
- [5] G. S. Selwyn, J. Singh, and R. S. Bennett, *J. Vac. Sci. Technol. A* **7**, 2758 (1989). 3
- [6] H. M. Mott-Smith and I. Langmuir, *Phys. Rev.* **28**, 727 (1926). 7
- [7] V. R. Ikkurthi, K. Matyash, A. Melzer, and R. Schneider, *Phys. Plasmas* **15**, 123704 (2008). 11
- [8] J. Allen, B. M. Annaratone, and U. deAngelis, *J. Plasma Phys.* **63**, 299 (2000). 11
- [9] M. Lampe, V. Gavrilchaka, G. Ganguli, and G. Joyce, *Phys. Rev. Lett.* **86**, 5278 (2001). 11, 13
- [10] C. T. N. Willis, M. Coppins, M. Bacharis, and J. E. Allen, *Plasma Sources Sci. Technol.* **19**, 065022 (2010). 11
- [11] J. Allen, R. Boyd, and P. Reynolds, *Proc. Phys. Soc.* **70**, 297 (1957). 11
- [12] R. V. Kennedy and J. E. Allen, *J. Plasma Phys.* **67**, 243 (2002). 11
- [13] E. C. Whipple, *Rep. Prog. Phys.* **44**, 1198 (1981). 12
- [14] J. Goree, *Phys. Rev. Lett.* **69**, 277 (1992). 12
- [15] S. A. Khrapak *et al.*, *Phys. Rev. E* **72**, 016406 (2005). 13
- [16] C. K. Goertz, *Rev. Geophys.* **27**, 271 (1989). 13, 14
- [17] A. Zobnin, A. D. Usachev, O. F. Petrov, and V. E. Fortov, *Phys. Plasmas* **15**, 043705 (2008). 18, 19
- [18] S. Khrapak and G. Morfill, *Contrib. Plasma Phys.* **49**, 148 (2009). 18

- [19] N. Meyer-Vernet, *Astronom. Astrophys.* **105**, 98 (1982). 20
- [20] T. Nitter, T. K. Aslaksen, F. Melandsø, and O. Havnes, *IEEE Trans. Plasma Sci.* **22**, 159 (1994). 22
- [21] C. Cui and J. Goree, *IEEE Trans. Plasma Sci.* **22**, 151 (1994). 23
- [22] T. Matsoukas and M. Russell, *J. Appl. Phys.* **77**, 4285 (1995). 23
- [23] I. Goertz, F. Greiner, and A. Piel, *Phys. Plasmas* **18**, 013703 (2011). 25
- [24] O. Havnes *et al.*, *J. Geophys. Res.* **92 A3**, 2281 (1987). 24
- [25] S. Hamaguchi and R. T. Farouki, *Phys. Rev. E* **49**, 4430 (1994). 28, 29
- [26] M. S. Barnes *et al.*, *Phys. Rev. Lett.* **68**, 313 (1992). 32
- [27] M. D. Kilgore, J. E. Daugherty, R. K. Porteous, and D. B. Graves, *J. Appl. Phys.* **73**, 7195 (1993). 32
- [28] S. Khrapak, A. V. Ivlev, G. Morfill, and H. Thomas, *Phys. Rev. E* **66**, 046414 (2002). 33
- [29] S. A. Khrapak, A. V. Ivlev, S. K. Zhdanov, and G. E. Morfill, *Phys. Plasmas* **12**, 042308 (2005). 33, 34, 118
- [30] I. H. Hutchinson, *Plasma Phys. Control. Fusion* **48**, 185 (2006). 33, 34, 118
- [31] L. Patacchini and I. H. Hutchinson, *Phys. Rev. Lett.* **101**, 025001 (2008). 34
- [32] V. R. Ikkurthi, K. Matyash, A. Melzer, and R. Schneider, *Phys. Plasmas* **16**, 043703 (2009). 34, 68
- [33] P. S. Epstein, *Phys. Rev.* **23**, 710 (1924). 35, 43
- [34] B. Liu, J. Goree, V. Nosenko, and L. Boufendi, *Phys. Plasmas* **10**, 9 (2003). 35
- [35] H. Rothermel *et al.*, *Phys. Rev. Lett.* **89**, 175001 (2002). 36
- [36] A. Ashkin, *Phys. Rev. Lett.* **24**, 156 (1970). 36
- [37] A. M. Ignatov and S. G. Amiranashvili, *Phys. Rev. E* **63**, 017402 (2001). 37
- [38] A. Melzer, *Plasma Sources Sci. Technol.* **10**, 303 (2001). 37
- [39] J.-L. Dorier, C. Hollenstein, and A. Howling, *J. Vac. Sci. Technol. A* **13**, 918 (1995). 39

- [40] G. E. Morfill *et al.*, Phys. Rev. Lett. **83**, 1598 (1999). 39
- [41] J. Goree, G. Morfill, V. Tsytovich, and S. V. Vladimirov, Phys. Rev. E **59**, 7055 (1999). 39
- [42] P. Belenguer *et al.*, Phys. Rev. A **46**, 7923 (1992). 41, 42
- [43] E. Tomme, D. Law, B. M. Annaratone, and J. Allen, Phys. Rev. Lett. **85**, 2518 (2000). 41
- [44] A. Melzer, T. Trottenberg, and A. Piel, Phys. Lett. A **191**, 301 (1994). 42
- [45] T. Trottenberg, A. Melzer, and A. Piel, Plasma Sources Sci. Technol. **4**, 450 (1995). 42, 65
- [46] A. Melzer, A. Homann, and A. Piel, Phys. Rev. E **53**, 2757 (1996). 42, 44, 81, 83
- [47] A. Homann, A. Melzer, and A. Piel, Phys. Rev. E **59**, 3835 (1999). 44
- [48] J. Carstensen, H. Jung, F. Greiner, and A. Piel, Phys. Plasmas **18**, 033701 (2011). 44
- [49] A. Sickafoose, J. Colwell, M. Horanyi, and S. Robertson, 367 . 45
- [50] H. Schollmeyer, A. Melzer, A. Homann, and A. Piel, Phys. Plasmas **6**, 2693 (1999). 45
- [51] C. Zafiu, A. Melzer, and A. Piel, Phys. Rev. E **63**, 066403 (2001). 47, 48
- [52] A. Ivlev, U. Konopka, and G. Morfill, Phys. Rev. E **62**, 2739 (2000). 48, 50
- [53] J. Beckers *et al.*, Phys. Rev. Lett. **106**, 115002 (2011). 49
- [54] S. Nunomura, T. Misawa, N. Ohno, and S. Takamura, Phys. Rev. Lett. **83**, 1970 (1999). 49
- [55] E. Wigner, Trans. Faraday Soc. **34**, 678 (1938). 51
- [56] S. Ichimaru, Rev. Mod. Phys. **54**, 1017 (1982). 51, 52, 58
- [57] S. Hamaguchi, R. Farouki, and D. H. E. Dubin, Phys. Rev. E **56**, 4671 (1997). 53
- [58] M. O. Robbins, K. Kremer, and G. S. Grest, J. Chem. Phys. **88**, 3286 (1988). 53
- [59] H. Ikezi, Phys. Fluids **29**, 1764 (1986). 54, 55
- [60] D. Dubin, Phys. Rev. Lett. **71**, 2753 (1993). 56

- [61] H. Totsuji *et al.*, Phys. Lett. A **221**, 215 (1996). 57
- [62] H. Totsuji, T. Kishimoto, and C. Totsuji, Phys. Rev. Lett. **78**, 3113 (1997). 57
- [63] B. Klumov *et al.*, Plasma Phys. Control. Fusion **51**, 124028 (2009). 60, 62
- [64] U. Konopka, G. Morfill, and L. Ratke, Phys. Rev. Lett. **84**, 891 (2000). 63, 64
- [65] J. H. Chu and L. I, Phys. Rev. Lett. **72**, 4009 (1994). 65
- [66] U. Mohideen *et al.*, Phys. Rev. Lett. **81**, 349 (1998). 65
- [67] B. A. Annaratone *et al.*, Phys. Rev. E **63**, 036406 (2001). 65
- [68] S. V. Vladimirov and M. Nambu, Phys. Rev. E **52**, R2172 (1995). 65, 66, 67
- [69] M. Lampe, G. Joyce, and G. Ganguli, Phys. Plasmas **7**, 3851 (2000). 66, 68, 70
- [70] M. Nambu, S. V. Vladimirov, and P. K. Shukla, Phys. Lett. A **203**, 40 (1995). 67
- [71] I. H. Hutchinson, Phys. Rev. Lett. **107**, 095001 (2011). 68
- [72] A. Melzer *et al.*, Phys. Rev. E **54**, R46 (1996). 69, 71, 81, 82
- [73] V. A. Schweigert *et al.*, Phys. Rev. E **54**, 4155 (1996). 68, 69, 70, 74, 76
- [74] V. A. Schweigert *et al.*, JETP **88**, 482 (1999). 68
- [75] W. J. Miloch, M. Kroll, and D. Block, Phys. Plasmas **17**, 103703 (2010). 68
- [76] K. Takahashi *et al.*, Phys. Rev. E **58**, 7805 (1998). 72
- [77] A. Melzer, V. Schweigert, and A. Piel, Phys. Rev. Lett. **83**, 3194 (1999). 72, 73
- [78] A. Melzer, V. Schweigert, and A. Piel, Physica Scripta **61**, 494 (2000). 72, 74
- [79] L. Couédel *et al.*, Phys. Rev. Lett. **104**, 195001 (2010). 74
- [80] H. Thomas and G. E. Morfill, Nature **379**, 806 (1996). 81, 84
- [81] V. A. Schweigert *et al.*, Phys. Rev. Lett. **80**, 5345 (1998). 84
- [82] I. V. Schweigert, V. A. Schweigert, A. Melzer, and A. Piel, Phys. Rev. E **62**, 1238 (2000). 85, 86
- [83] N. N. Rao, P. K. Shukla, and M. Y. Yu, Planet. Space Sci. **38**, 543 (1990). 87
- [84] A. Barkan, R. L. Merlino, and N. D'Angelo, Phys. Plasmas **2**, 3563 (1995). 91, 92

- [85] C. Thompson, A. Barkan, N. D'Angelo, and R. L. Merlino, *Phys. Plasmas* **4**, 2331 (1997). 91, 92
- [86] J. B. Pieper and J. Goree, *Phys. Rev. Lett.* **77**, 3137 (1996). 92, 93
- [87] H. Prabhakara and V. Tanna, *Phys. Plasmas* **3**, 3176 (1996). 92
- [88] J. D. Williams, J. Edward Thomas, and L. Marcus, *Phys. Plasmas* **15**, 043704 (2008). 92, 94
- [89] S. Ratynskaia *et al.*, *Phys. Rev. Lett.* **93**, 085001 (2004). 92, 94
- [90] A. Piel *et al.*, *Phys. Rev. Lett.* **97**, 205009 (2006). 92, 94
- [91] T. M. Flanagan and J. Goree, *Phys. Plasmas* **17**, 123702 (2010). 92
- [92] R. L. Merlino, A. Barkan, C. Thompson, and N. D'Angelo, *Phys. Plasmas* **5**, 1607 (1998). 96, 97, 98
- [93] F. Melandsø, *Phys. Plasmas* **3**, 3890 (1996). 102
- [94] F. M. Peeters and X. Wu, *Phys. Rev. A* **35**, 3109 (1987). 104, 105
- [95] X. Wang, A. Bhattacharjee, and S. Hu, *Phys. Rev. Lett.* **86**, 2569 (2001). 104, 106
- [96] A. Homann *et al.*, *Phys. Rev. E* **56**, 7138 (1997). 107, 108, 109
- [97] A. Homann, A. Melzer, R. Madani, and A. Piel, *Phys. Lett. A* **242**, 173 (1998). 107, 110
- [98] S. Nunomura, D. Samsonov, and J. Goree, *Phys. Rev. Lett.* **84**, 5141 (2000). 111
- [99] S. Nunomura *et al.*, *Phys. Rev. E* **65**, 066402 (2002). 111
- [100] D. Samsonov *et al.*, *Phys. Rev. Lett.* **83**, 3649 (1999). 112
- [101] D. Samsonov, J. Goree, H. Thomas, and G. Morfill, *Phys. Rev. E* **61**, 5557 (2000). 112
- [102] A. Melzer, S. Nunomura, D. Samsonov, and J. Goree, *Phys. Rev. E* **62**, 4162 (2000). 112
- [103] D. H. E. Dubin, *Phys. Plasmas* **7**, 3895 (2000). 112
- [104] V. Nosenko, J. Goree, Z. W. Ma, and A. Piel, *Phys. Rev. Lett.* **88**, 135001 (2002). 113
- [105] O. Havnes *et al.*, *J. Geophys. Res.* **100**, 1731 (1995). 114, 164

- [106] S. V. Vladimirov, P. V. Shevchenko, and N. F. Cramer, Phys. Rev. E **56**, 74 (1997). 115
- [107] T. Misawa *et al.*, Phys. Rev. Lett. **86**, 1219 (2001). 115, 116
- [108] S. Nunomura *et al.*, Phys. Rev. Lett. **89**, 035001 (2002). 116, 117
- [109] B. Liu, K. Avinash, and J. Goree, Phys. Rev. Lett. **91**, 255003 (2003). 116, 117
- [110] J. J. Thomson, Philos. Mag. **39**, 237 (1904). 120
- [111] *Strongly Coupled Coulomb Systems*, edited by G. J. Kalman, J. M. Rommel, and K. Blagoev (Plenum Press, New York, 1998). 120
- [112] W.-T. Juan *et al.*, Phys. Rev. E **58**, 6947 (1998). 120, 123
- [113] M. Klindworth, A. Melzer, A. Piel, and V. Schweigert, Phys. Rev. B **61**, 8404 (2000). 120, 123
- [114] O. Arp, D. Block, A. Piel, and A. Melzer, Phys. Rev. Lett. **93**, 165004 (2004). 120, 128, 129
- [115] A. Melzer, Phys. Rev. E **73**, 056404 (2006). 121, 122
- [116] T. E. Sheridan and K. D. Wells, Phys. Rev. E **81**, 016404 (2010). 121
- [117] A. Melzer, Phys. Rev. E **67**, 016411 (2003). 123, 133, 134, 135, 136, 137
- [118] V. M. Bedanov and F. Peeters, Phys. Rev. B **49**, 2667 (1994). 123
- [119] O. Arp, D. Block, M. Klindworth, and A. Piel, Phys. Plasmas **12**, 122102 (2005). 128
- [120] S. Käding *et al.*, Phys. Plasmas **15**, 073710 (2008). 128, 129, 130
- [121] R. W. Hasse and V. V. Avilov, Phys. Rev. A **44**, 4506 (1991). 128
- [122] M. Bonitz *et al.*, Phys. Rev. Lett. **96**, 075001 (2006). 128, 129
- [123] D. Block *et al.*, Phys. Plasmas **15**, 040701 (2008). 128, 129
- [124] P. Ludwig, S. Kosse, and M. Bonitz, Phys. Rev. E **71**, 046403 (2005). 129
- [125] S. Apolinario, B. Partoens, and F. Peters, New J. Phys. **9**, 283 (2007). 129
- [126] Y.-J. Lai and L. I, Phys. Rev. E **60**, 4743 (1999). 129
- [127] V. A. Schweigert and F. Peeters, Phys. Rev. B **51**, 7700 (1995). 130

- [128] R. Ichiki *et al.*, Phys. Rev. E **70**, 066404 (2004). 137, 139
- [129] J. Winter and G. Gebauer, J. Nucl. Mater. **266-269**, 228 (1999). 149
- [130] J. Sharpe, D. Petti, and H.-W. Bartels, Fusion Engineering and Design **63-64**, 153 (2002). 149, 150
- [131] S. I. Krasheninnikov, A. Y. Pigarov, R. D. Smirnov, and T. K. Soboleva, Contrib. Plasma Phys. **50**, 410 (2010). 149, 150
- [132] H. Kersten *et al.*, New J. Phys. **5**, 93 (2003). 151
- [133] P. Roca i Cabarrocas, in *Advances in Dusty Plasmas*, edited by Y. Nakamura, T. Yokota, and P. Shukla (Elsevier, Amsterdam, 2000), p. 213. 152
- [134] O. Havnes, in *Dusty Plasmas in the new Millenium*, edited by R. Bharuthram, M. A. Hellberg, P. Shukla, and F. Verheest (AIP Conference Proceedings, Melville, New York, 2002), Vol. 649, p. 13. 154
- [135] V. Nussbaumer *et al.*, J. Geophys. Res. **101**, 19161 (1996). 156
- [136] M. Horanyi, in *Dusty Plasmas in the new Millenium*, edited by R. Bharuthram, M. A. Hellberg, P. Shukla, and F. Verheest (AIP Conference Proceedings, Melville, New York, 2002), Vol. 649, p. 22. 156, 159, 160, 161
- [137] C. K. Goertz and G. Morfill, Icarus **53**, 219 (1982). 162, 163
- [138] P. V. Bliokh and V. V. Yaroshenko, Sov. Astron. **29**, 330 (1985). 163
- [139] A. Brattli, O. Havnes, and F. Melandsø, Phys. Plasmas **9**, 958 (2002). 164

Index

- acetylene, 140
- aerosol, 145
- angular correlation function, 59
- Ashkin, 36

- Bohm velocity, 17, 47
- Boltzmann factor, 10, 24, 89, 95
- breathing mode, 126
- Brownian motion, 116, 133

- capacitance, 17, 21
- Cassini spacecraft, 160
- charge, 17, 43
 - position dependent, 49
- charging, 6
 - charging time, 21, 23
 - collisions, 12
 - energy barrier, 11
 - fluctuations, 23
 - impact parameter, 7, 31
 - in rf discharge, 22
 - OML, 7–17
 - photoelectron current, 13
 - secondary electron current, 14, 19
- collisions, 63
- Coulomb cluster, 120, *see* dust cluster
- Coulomb coupling parameter, 51
- Coulomb crystallization, 51, 54
- cross section
 - Coulomb, 31
 - electron collection, 10
 - geometric, 8, 35, 36
 - ion collection, 8

- Debye length, 11, 29, 30, 32, 118
- Debye-Hückel equation, 29
- Debye-Hückel potential, 53, 64
- dipole moment, 29, 65
- drift velocity, 12, 17, 30
- dust cluster, 120
 - 1D, 121
 - 2D, 122
 - 3D, 128
 - magic number, 135
 - normal modes, 130–139
 - periodic table, 122, 129
 - phase transition, 137
 - stability, 134
 - zigzag transition, 121
- dust ion-acoustic wave, 94
 - dispersion relation, 96
 - experiments, 96
- dust ion-cyclotron wave, 97
- dust lattice wave, 100
 - 1D, 101
 - compressional, 104
 - experiments, 107–111
 - shear, 105
 - sound speed, 103, 105
 - transverse, 114
- dust plasma frequency, 87, 103
- dust removal, 148
- dust-acoustic wave, 87
 - dispersion relation, 90
 - experiments, 92
 - wave speed, 90
- dust-cyclotron wave, 96
- dynamical matrix, 131

- electrostatic precipitators, 148
- Epstein friction, 35

- Faraday cup, 44
- floating potential, 6, 15, 16, 26
- force
 - collection, 31
 - Coulomb, 31
 - drag, 30
 - electric field, 27

- friction, 35
 - gravity, 27
 - ion drag, 31
 - neutral drag, 35
 - photophoretic, 37
 - polarization, 29
 - radiation pressure, 36
 - thermophoresis, 35
- Galileo spacecraft, 156
- gravito-electrodynamics, 154
- growth, 140
- halo orbits, 160
- Havnes parameter, 26
- HMDSO, 140
- Jupiter, 156
- Kepler, 12, 163
- killer particle, 147
- Langevin, 85
- Langmuir, 6, 7
- laser manipulation, 36, 43, 72, 107, 110, 111
- Mach cone, 111, 164
- Madelung energy, 52
- mass spectrometry, 142
- Mathieu's equation, 46
- Maxwellian distribution, 9, 14
- methane, 140
- MF particles, 42
- microgravity, 38
- noctilucent clouds, 154
- non-reciprocal attraction, 70, 72
- OCP, 51
- OML current, 9
- one-component plasma, *see* OCP
- pair correlation function, 57
- phase transition, 81–86
 - defects, 85
 - dust cluster, 137
- plasma potential, 24, 26
- Poisson's equation, 88, 95
- polar mesospheric summer echoes, 154
- polymorphous silicon, 153
- quasineutrality, 24, 42, 89, 96
- Saturn, 160
- screening strength, 53, 132
- sheath model, 41
 - matrix sheath, 41
- silane, 140
- silicon clusters, 142
- spectral power density, 134
- Spitzer, 16
- spokes, 161
- strong coupling, 51
- structure factor, 59
- thermal velocity, 9
- vertical alignment, 65
 - instability of, 75–81
- vertical resonance
 - linear, 42
 - nonlinear, 47
 - parametric, 45
 - self-excited, 49
- wakefield, 65
- waves
 - dust ion-acoustic, *see* dust ion-acoustic wave
 - dust ion-cyclotron, *see* dust ion-cyclotron wave
 - dust lattice, *see* dust lattice wave
 - dust-acoustic, *see* dust-acoustic wave
 - dust-cyclotron, *see* dust-cyclotron wave
- Wigner-Seitz cell, 57

Wigner-Seitz radius, 51

Yukawa potential, 53

Yukawa system, 53